

# UC San Diego

## UC San Diego Electronic Theses and Dissertations

### Title

Photochemical and Electrochemical Reduction of Carbon Dioxide

### Permalink

<https://escholarship.org/uc/item/08j33393>

### Author

Cheung, Po Ling

### Publication Date

2019

Peer reviewed|Thesis/dissertation

UNIVERSITY OF CALIFORNIA SAN DIEGO

**Photochemical and Electrochemical Reduction of Carbon Dioxide**

A dissertation submitted in partial satisfaction of the  
requirements for the degree of Doctor of Philosophy

in

Chemistry

by

Po Ling Cheung

Committee in charge:

Professor Clifford P. Kubiak, Chair  
Professor Guy Bertrand  
Professor Judy E. Kim  
Professor Jefferey D. Rinehart  
Professor Jan B. Talbot

2019

Copyright

Po Ling Cheung, 2019

All rights reserved

The dissertation of Po Ling Cheung is approved, and it is acceptable in quality and form for publication on microfilm and electronically:

---

---

---

---

---

Chair

University of California San Diego

2019

## DEDICATION

*This thesis is dedicated to my father and mother,  
and my friends in Hong Kong.*

EPIGRAPH

*Was mich nicht umbringt macht mich stärker.*

*That which does not kill me makes me stronger.*

— *From Twilight of the Idols by Friedrich Nietzsche*

## TABLE OF CONTENTS

SIGNATURE PAGE.....	iii
DEDICATION.....	iv
EPIGRAPH.....	v
TABLE OF CONTENTS.....	vi
LIST OF FIGURES.....	x
LIST OF SCHEMES.....	xv
LIST OF TABLES.....	xvi
ACKNOWLEDGEMENTS.....	xvii
VITA.....	xix
ABSTRACT OF THE DISSERTATION.....	xx
Chapter 1 Energy Storage by Carbon Dioxide Reduction.....	1
1.1 Global Energy Usage and Movement Towards Renewable Energy.....	1
1.2 Problems of Oversupply and Intermittency.....	4
1.3 Role of Carbon Dioxide Utilization in Energy Storage.....	5
1.3.1 Role of Carbon Dioxide Reduction in Grid Management.....	5
1.3.2 Other Impacts Brought by Carbon Dioxide Reduction.....	6
1.4 Catalysts for Carbon Dioxide Reduction.....	7
1.4.1 Photochemical Systems for Carbon Dioxide Reduction.....	8
1.4.2 Electrochemical Systems for Carbon Dioxide Reduction.....	9
1.5 Reference.....	13
Chapter 2 Photochemical Reduction of Carbon Dioxide Using a CN-modified <i>fac</i> -Mn(bpy)(CO) <sub>3</sub> Catalyst.....	17
2.1 Introduction.....	17
2.2 Results and Discussion.....	20
2.2.1 Photocatalytic Experiments.....	20
2.2.2 Disproportionation Mechanism.....	21
2.2.3 Solvent Effects.....	25
2.3 Conclusion.....	29
2.4 Experimental.....	29
2.4.1 General.....	29
2.4.2 Photochemical Reactions.....	30
2.4.3 Product Analysis from Photocatalysis <sup>19</sup> .....	30

2.4.4	Cyclic Voltammetry (CV).....	31
2.4.5	Infrared Spectroelectrochemistry .....	31
2.4.6	Preparation of Ru(dmb) <sub>3</sub> (PF <sub>6</sub> ) <sub>2</sub> .....	32
2.5	Acknowledgement .....	32
2.6	References.....	32
2.7	Appendix.....	37
Chapter 3 Improving Photocatalysis for the Reduction of CO <sub>2</sub> Through Non-Covalent Supramolecular Assembly .....		43
3.1	Introduction.....	43
3.2	Results and Discussion .....	45
3.2.1	Cyclic Voltammetry of Photosensitizers.....	45
3.2.2	Photocatalytic Experiments.....	47
3.2.3	Control Studies of Photocatalytic System.....	49
3.2.4	Analysis of Photocatalytic Products .....	49
3.2.5	Spectroscopic Analysis of the Photocatalytic System .....	51
3.2.6	Further Electrochemical Studies of Photosensitizer Properties .....	52
3.2.7	Spectroelectrochemical Studies of Photocatalytic System.....	53
3.2.8	NMR Studies of the Dimerization Constant .....	54
3.3	Conclusion .....	54
3.4	Experimental.....	55
3.4.1	Preparation and Purification.....	55
3.4.2	Synthesis of Ru(dac)(bpy) <sub>2</sub> (PF <sub>6</sub> ) <sub>2</sub> (RuDAC).....	56
3.4.3	NMR Data Collection and Analysis.....	56
3.4.4	Spectroscopy Data Collection.....	56
3.4.5	Photochemical Reactions. ....	57
3.4.6	Product Analysis from Photocatalysis. ....	57
3.4.7	Cyclic Voltammetry (CV).....	58
3.4.8	Infrared Spectroelectrochemistry.....	58
3.4.9	Time-Related Single Photon Counting.....	58
3.5	Acknowledgement .....	59
3.6	References.....	59
3.7	Appendix.....	63
Chapter 4 Facile Solvent Free Synthesis of Thin Iron Porphyrin COFs on Carbon Cloth Electrodes for CO <sub>2</sub> Reduction .....		68
4.1	Introduction.....	68



4.2	Results and Discussion .....	71
4.2.1	Preparation of FeDhaTph COF electrodes.....	71
4.2.2	X-ray Photoelectron Spectroscopy (XPS) studies.....	72
4.2.3	Stability of COFs by leaching test. ....	74
4.2.4	Cyclic Voltammetry (CV) of homogeneous FeTAPPCl in DMF and MeCN. ....	75
4.2.5	Cyclic Voltammetry of FeTAPPCl and FeDhaTph-COF on carbon cloth in MeCN and DMF. 77	
4.2.6	Controlled Potential Electrolysis (CPE) studies. ....	81
4.2.7	Possible reasons for declined catalytic activities. ....	83
4.3	Conclusion .....	85
4.4	Experimental.....	85
4.4.1	Materials. ....	86
4.4.2	Preparation of carbon cloth electrodes.....	86
4.4.3	Preparation of FeDhaTph-COF on carbon cloth electrodes.....	87
4.4.4	Preparation of SEM samples and SEM measurements .....	87
4.4.5	Preparation of XPS samples.....	87
4.4.6	XPS experiments and analysis. ....	88
4.4.7	Stability leaching test. ....	88
4.4.8	Preparation of Inductively Coupled Plasma Optical Emission Spectroscopy (ICP-OES) samples. 88	
4.4.9	Cyclic voltammetry (CV) studies. ....	89
4.4.10	Controlled-potential electrolysis (CPE) studies. ....	89
4.5	Acknowledgement .....	90
4.6	Reference .....	90
4.7	Appendix.....	98
Chapter 5 Future Directions: New Areas to Be Explored.....		110
5.1	Summary.....	110
5.2	Results and Discussion .....	111
5.2.1	Investigating Electrochemical and Photochemical Activities of Supramolecular Systems Bonded by Guanine-Cytosine Base Pair .....	111
5.2.2	Interrogating the Efficiency and Activity of Electrocatalysts for the Reduction of CO <sub>2</sub> Through Supramolecular Assembly with $\pi$ - $\pi$ Interaction.....	113
5.3	Conclusion and Final Suggestions.....	115
5.4	Experimental.....	116
5.4.1	General.....	117
5.4.2	Synthesis of 4-methyl-4'-methyl(trimethylsilane)-2,2'-bipyridine (dmb-TMS) .....	117

5.4.3	Synthesis of 4-methyl-4'-methylchloro-2,2'-bipyridine (dmb-Cl) .....	118
5.4.4	Synthesis of Re(dmb-cytosine)(CO) <sub>3</sub> Cl.....	119
5.4.5	Synthesis of Re(dmb-guanine)(CO) <sub>3</sub> Cl.....	121
5.4.6	Synthesis of 4-(phenylethynyl)-2,2'-bipyridine.....	123
5.4.7	Synthesis of Re(bpy-PE)(CO) <sub>3</sub> Cl.....	124
5.4.8	Synthesis of Dihydroxypillar[6]arene .....	124
5.4.9	Cyclic Voltammetry .....	125
5.5	Acknowledgments .....	125
5.6	Reference .....	125

## LIST OF FIGURES

<b>Figure 1.1</b> Capacity-weighted average construction costs for electricity generators from 2013 to 2017. Figure reproduced in full from Reference 6. ....	2
<b>Figure 1.2</b> Monthly maximum percent of load served by renewables in California from January 2015 to July 2019. Figure reproduced in full from Reference 3. ....	3
<b>Figure 1.3</b> Global energy-related carbon dioxide emissions by source from 1990 to 2019 recorded by IEA. Figure reproduced in full from Reference 1. ....	3
<b>Figure 1.4</b> The “duck curve” chart published by CAISO in 2016. Figure reproduced in full from Reference 11. ....	4
<b>Figure 1.5</b> Energy density per unit weight or volume of liquid fuels compared to batteries. Figure adapted from Reference 15. ....	6
<b>Figure 1.6</b> Timeline for the number of articles published on photocatalytic and electrocatalytic CO <sub>2</sub> reduction, solar PV production in California on June 20 <sup>th</sup> , and monthly average of seasonally adjusted CO <sub>2</sub> concentration in the atmosphere. ....	7
<b>Figure 2.1</b> Cyclic voltammetry of Mn(CN)(bpy)(CO) <sub>3</sub> under Ar saturation. Conditions: 1 mM Mn(CN)(bpy)(CO) <sub>3</sub> in 0.1 TBAPF <sub>6</sub> /DMF; WE: GC; CE: Pt; RE: Ag/Cl with Fc as internal reference. ....	26
<b>Figure 2.2</b> Infrared spectra of Mn(CN)(bpy)(CO) <sub>3</sub> at controlled potentials (a) in dry MeCN with TEOA under N <sub>2</sub> , and (b) in dry MeCN with TEOA under CO <sub>2</sub> . ....	27
<b>Figure 2.3</b> Infrared spectra of Mn(CN)(bpy)(CO) <sub>3</sub> at controlled potentials (a) in dry DMF under N <sub>2</sub> , (b) in dry DMF with TEOA under N <sub>2</sub> , and (c) in dry DMF with TEOA under CO <sub>2</sub> . ....	28
<b>Figure 2.4</b> A sample <sup>1</sup> H NMR spectrum of the worked-up photocatalytic reaction solution of 1 mM Mn(CN)(bpy)(CO) <sub>3</sub> under CO <sub>2</sub> after 15 h irradiation. The solvent was a DMF-TEOA (4 : 1 v/v) in CD <sub>3</sub> CN solution. The ferrocene reference is at 4.13 ppm while formate is observed at 8.50 ppm. ....	37
<b>Figure 2.5</b> The linear fit lines of HCO <sub>2</sub> H TON vs. catalyst (complex 1) concentration shows high linearity for both 15 h and 6 h irradiation. ....	38
<b>Figure 2.6</b> Linear plots of anodic and cathodic currents against square root of scan rate of CV for 1.0 mM of complex Mn(CN)(bpy)(CO) <sub>3</sub> in 0.1 M TBAPF <sub>6</sub> in dry DMF under Ar. ....	38
<b>Figure 2.7</b> Cyclic voltammetry of Mn(CN)(bpy)(CO) <sub>3</sub> under Ar saturation (black), in the presence of TEOA (blue), and under CO <sub>2</sub> saturation (red) in dry DMF at 100 mVs <sup>-1</sup> . Conditions: 1 mM Mn(CN)(bpy)(CO) <sub>3</sub> in 0.1 TBAPF <sub>6</sub> /DMF; WE: GC; CE: Pt; RE: Ag/Cl with Fc as internal reference. ....	39
<b>Figure 2.8</b> Cyclic voltammetry of Mn(CN)(bpy)(CO) <sub>3</sub> under Ar saturation (black), in the presence of TEOA (blue), and under CO <sub>2</sub> saturation (red) in dry MeCN at 100 mVs <sup>-1</sup> . Conditions: 1 mM	

Mn(CN)(bpy)(CO) <sub>3</sub> in 0.1 TBAPF <sub>6</sub> /MeCN; WE: GC; CE: Pt; RE: Ag/Cl with Fc as internal reference. ....	39
<b>Figure 2.9</b> Infrared spectra of Mn(CN)(bpy)(CO) <sub>3</sub> at controlled potentials in dry MeCN-TEOA under CO <sub>2</sub> . Enlarged spectra of the CO <sub>2</sub> peak at around 2337 cm <sup>-1</sup> shows the decrease in CO <sub>2</sub> concentration under catalytic conditions (ca. -1.9 V vs Fc/Fc+) over the course of 5 min. ....	40
<b>Figure 2.10</b> Infrared spectra of Mn(CN)(bpy)(CO) <sub>3</sub> taken at controlled potentials in dry DMF-TEOA (4:1) under CO <sub>2</sub> . Enlarged spectra of the CO <sub>2</sub> peak at around 2337 cm <sup>-1</sup> shows the decrease in CO <sub>2</sub> concentration at catalytic potentials (ca. -1.9 V vs Fc/Fc+) over the course of 5 min. ....	41
<b>Figure 2.11</b> UV-Vis spectra of Mn(CN)(bpy)(CO) <sub>3</sub> (1) (A) in dry MeCN with and without Vkd base in the absence or presence of TEOA; and (B) in dry DMF with and without Vkd base in the absence or presence of TEOA. ....	42
<b>Figure 3.1</b> Structures of two sacrificial reductants: BIH and BNAH.....	44
<b>Figure 3.2</b> Cyclic voltammograms of 1 mM of RuDAC (red), RuBPY (blue) and RuDMB (black) in dry MeCN containing 0.1 M TBAPF <sub>6</sub> at scan rate 100 mV/s under Ar.....	46
<b>Figure 3.3</b> Turnover number of CO (TON <sub>CO</sub> ) produced by RuDAC/ReDAC (red) and RuBPY/ReDAC (blue) in MeCN (solid line) and DMF (dotted line) solvents. ....	48
<b>Figure 3.4</b> IR spectra of 3 mM ReDAC, 3 mM RuDAC and 0.1 M BIH solution with <sup>12</sup> CO <sub>2</sub> (black) and <sup>13</sup> CO <sub>2</sub> (red) in dry MeCN showing the formation of reduced carbon products upon irradiation of light at 470 nm for 10 min. ....	50
<b>Figure 3.5</b> UV-visible spectra of RuDAC (red), RuBPY (blue) and RuDMB (black) in dry MeCN solution. ....	51
<b>Figure 3.6</b> IRSEC spectrum of 1mM of RuDAC and 1 mM ReDAC in dry MeCN under N <sub>2</sub> . ....	53
<b>Figure 3.7</b> Determination of hydrogen-bonding constant (K <sub>a</sub> ) by fitting to a 1:1 dimerization model using the NMR software WinEQNMR2 <sup>39</sup> . Residuals squared = 3.9 × 10 <sup>-6</sup> . ....	54
<b>Figure 3.8</b> <sup>1</sup> H NMR spectrum of Ru(dac)(bpy) <sub>2</sub> (PF <sub>6</sub> ) <sub>2</sub> in CD <sub>3</sub> CN. The peaks were referenced to residual solvent of CD <sub>3</sub> CN at 1.9400 ppm. ....	63
<b>Figure 3.9</b> Mass spectrum of Ru(dac)(bpy) <sub>2</sub> (PF <sub>6</sub> ) <sub>2</sub> in methanol. ....	63
<b>Figure 3.10</b> FTIR spectra of 10 mM of ReDAC/RuDAC, ReDAC and RuDAC in dry MeCN. ....	64
<b>Figure 3.11</b> Lifetime measurements of RuDAC, RuBPY and RuDMB in dry MeCN (red) and DMF (blue) were collected at room temperature respectively. The excitation wavelength was 405 nm and the emission wavelengths were 609 nm for RuBPY, 613 nm for RuDAC and 618 nm for RuDMB. ....	64
<b>Figure 3.12</b> Stern–Volmer plot measuring the change of fluorescence lifetime of RuDAC and RuBPY in the presence of BIH in dry MeCN and DMF respectively. The excitation wavelength was 405 nm and the emission wavelengths were 609 nm for RuBPY, 613 nm for RuDAC. ....	65
<b>Figure 3.13</b> CV of 1mM of RuDAC in dry MeCN or DMF at different scan rates under N <sub>2</sub> .....	65
<b>Figure 3.14</b> CV of 1mM of RuDAC in dry MeCN or DMF at scan rate 100 mV/s under N <sub>2</sub> or CO <sub>2</sub> . ....	66

<b>Figure 3.15</b> CV of 1mM of RuDAC and 1 mM ReDAC in dry MeCN or DMF at scan rate 100 mV/s under N <sub>2</sub> or CO <sub>2</sub> .	66
<b>Figure 4.1</b> Proposed structure of FeDhaTph-COF.	70
<b>Figure 4.2</b> SEM images of FeDhaTph-COF thin film on Si wafer.	72
<b>Figure 4.3</b> High resolution XPS spectra of N <sub>1s</sub> signals: (a) FeTAPPCl, (b) FeDhaTph-COF and (c) FeDmaTph-COF on Au surfaces.	72
<b>Figure 4.4</b> UV-vis spectra of soaking THF solution of carbon cloth electrodes synthesized with FeTAPPCl only (blue); and with FeTAPPCl and Dha (red).	74
<b>Figure 4.5</b> Scan rate studies of 0.5 mM FeTAPPCl solution in dry DMF and 0.25 mM FeTAPPCl solution in dry MeCN containing 0.1 M TBAPF <sub>6</sub> under Ar respectively.	75
<b>Figure 4.6</b> Cyclic voltammograms of 0.5 mM of FeTAPPCl in dry DMF solution under nitrogen (a) and under CO <sub>2</sub> with added TFE (b) at scan rate 100 mV/s. CVs of 0.25 mM of FeTAPPCl in dry MeCN solution under nitrogen (c) and under CO <sub>2</sub> with added TFE (d) at scan rate 100 mV/s.	76
<b>Figure 4.7</b> (a) Cyclic voltammograms of a FeTAPPCl electrode in dry MeCN solution of 0.1 M TBAPF <sub>6</sub> under nitrogen, and under CO <sub>2</sub> with added TFE at scan rate 100 mV/s. (b) Scan rate studies of the FeTAPPCl electrode under nitrogen. (c) Linear plot of reductive current of Fe(I/0) couple the FeTAPPCl electrode against the scan rate.	78
<b>Figure 4.8</b> (a) Cyclic voltammograms of the FeDhaTph-COF electrode in dry MeCN solution of 0.1 M TBAPF <sub>6</sub> under nitrogen, and under CO <sub>2</sub> with added TFE at scan rate 100 mV/s. (b) Scan rate studies of the FeDhaTph-COF electrode under nitrogen. (c) Linear plot of reductive current of Fe(I/0) couple of the FeDhaTph-COF electrode against the scan rate.	78
<b>Figure 4.9</b> (a) Cyclic voltammograms of a FeTAPPCl electrode in dry DMF solution of 0.1 M TBAPF <sub>6</sub> under nitrogen, and under CO <sub>2</sub> with added TFE at scan rate 100 mV/s. (b) Scan rate studies of the FeTAPPCl electrode under nitrogen. (c) Linear plot of reductive current of Fe(I/0) couple the FeTAPPCl electrode against the scan rate.	79
<b>Figure 4.10</b> (a) Cyclic voltammograms of the FeDhaTph-COF electrode in dry DMF solution of 0.1 M TBAPF <sub>6</sub> under nitrogen, and under CO <sub>2</sub> with added TFE at scan rate 100 mV/s. (b) Scan rate studies of the carbon cloth FeDhaTph-COF electrode under nitrogen. (c) Linear plot of reductive current of Fe(I/0) couple of the FeDhaTph-COF electrode against the scan rate.	80
<b>Figure 4.11</b> Number of mole of CO and H <sub>2</sub> (red for FeDhaTph-COF electrode and blue for FeTAPPCl electrode) in the three hours of CPE in MeCN (a) and DMF (d). FeDhaTph-COF electrode and FeTAPPCl electrode have their Faradaic efficiencies of CO and H <sub>2</sub> plotted during CPE in MeCN (b and c) and DMF (e and f) respectively.	81
<b>Figure 4.12</b> Additional N <sub>1s</sub> XPS spectra of FeDhaTph-COF on carbon cloth (a) before and (b) after 2h CPE at - 2.2 V vs. Ag/AgCl in MeCN under CO <sub>2</sub> . The N <sub>1s</sub> spectrum of TBAPF <sub>6</sub> (c) is also included. Residual TBAPF <sub>6</sub> is found in FeDhaTph-COF electrode after CPE even after thorough rinsing with MeCN. The F <sub>1s</sub> signals overlap with the Fe <sub>2p</sub> signals.	84

<b>Figure 4.13</b> FT-IR spectrum of iron(III) 5,10,15,20-tetrakis-(4'-aminophenyl)porphyrin chloride (FeTAPPCl) in KBr. FT-IR ( $\nu$ ; $\text{cm}^{-1}$ ): 3427, 3370, 1700, 1617, 1606, 1513, 1488, 1286, 1179, 998 ( $\delta_{\text{Fe-N}}$ ), 802, 722.....	98
<b>Figure 4.14</b> ATR-IR spectrum of 2,5-dihydroxyterephthalaldehyde (Dha). ATR-IR ( $\nu$ ; $\text{cm}^{-1}$ ): 3269, 1666, 1477, 1460, 1280, 1129, 888, 833, 795, 674.....	98
<b>Figure 4.15</b> Mass spectrum of 5,10,15,20-tetrakis(4'-aminophenyl)porphyrin (TAPP) m/z calcd for $\text{C}_{44}\text{H}_{34}\text{N}_8$ , 675.30 $[\text{M}+\text{H}]^+$ ; found, 675.37 $[\text{M}+\text{H}]^+$ .....	99
<b>Figure 4.16</b> Mass spectrum of FeTAPPCl m/z calcd for $\text{C}_{44}\text{H}_{32}\text{N}_8\text{Fe}$ , 728.21 $[\text{M}-\text{Cl}]^+$ ; found, 728.15 $[\text{M}-\text{Cl}]^+$ .....	99
<b>Figure 4.17</b> $^1\text{H}$ NMR ( $\text{CDCl}_3$ , 400 MHz) of FeTAPPCl: $\delta$ (ppm) -2.72(s, 2H, NH), 4.02 (s, 8H, $\text{NH}_2$ ), 7.05-.707 (d, 8H, $J = 8.0$ Hz, aromatics), 7.98-8.00 (d, 8H, $J = 8.0$ Hz, aromatics), 8.90 (s, 8H, H-pyrrole). ....	100
<b>Figure 4.18</b> $^1\text{H}$ NMR ( $\text{CDCl}_3$ , 400 MHz) of Dha: $\delta$ (ppm) 10.23 (s, 1H), 9.96 (s, 1H), 7.24 (s, 1H).....	101
<b>Figure 4.19</b> SEM images of FeDhaTph-COF on Si wafer.....	102
<b>Figure 4.20</b> Proposed structure of FeDmaTph-COF.....	103
<b>Figure 4.21</b> Additional XPS spectra of FeTAPPCl on Au slides: (a) survey scan, (b) C1s, (c) O1s and (d) Fe2p. ....	104
<b>Figure 4.22</b> Additional XPS spectra of FeDhaTph-COF on Au slides: (a) survey scan, (b) C1s, (c) O1s and (d) Fe2p.....	104
<b>Figure 4.23</b> Additional XPS spectra of FeDmaTph-COF on Au slides: (a) survey scan, (b) C1s, (c) O1s and (d) Fe2p. The two oxygen peaks correspond to the oxygen in the hemiaminal group and methoxy group. ....	105
<b>Figure 4.24</b> CVs of FeDhaTph-COF electrode in original (black and blue) and new solutions (red) of dry MeCN containing 0.1 M TBAPF <sub>6</sub> under Ar at scan rate 100 mV/s.....	105
<b>Figure 4.25</b> Current of different electrodes during CPE at 2.2 V (vs. Ag/AgCl) in MeCN and 2.1 V in DMF containing 0.1 M TBAPF <sub>6</sub> and 0.5 M TFE under CO <sub>2</sub> for three hours.....	106
<b>Figure 4.26</b> Current of FeDhaTph-COF carbon cloth electrode during CPE at 1.3 V (vs. Ag/AgCl <sub>(3M NaCl)</sub> ) in 0.5 M KHCO <sub>3</sub> under CO <sub>2</sub> for three hours.....	106
<b>Figure 4.27</b> CVs of FeDhaTph-COF electrode in dry MeCN containing 0.1 M TBAPF <sub>6</sub> under Ar (black), CO (blue) and CO <sub>2</sub> (red) at scan rate 100 mV/S.....	107
<b>Figure 4.28</b> Cyclic voltammograms of different electrodes before and after 3 h controlled-potential electrolysis at -2.2 V (vs. Ag/AgCl) in MeCN and at 2.1 V in DMF solutions of 0.1 M TBAPF <sub>6</sub> under CO <sub>2</sub> with added TFE at scan rate 50 mV/s. ....	108
<b>Figure 4.29</b> UV-vis spectra of different concentration of FeTAPPCl in THF solution. ....	109
<b>Figure 4.30</b> Calibration curve of absorbance of soret band at 424 nm against concentration of FeTAPPCl in THF solution.....	109

<b>Figure 5.1</b> Cyclic voltammograms of 1 mM of Re-C, Re-G and mixture of 1 mM Re-C and Re-G in dry MeCN under Ar or CO <sub>2</sub> at a scan rate of 100 mV/s. ....	112
<b>Figure 5.2</b> IR spectrum of 3 mM Re-C, 3 mM Re-G and mixture of 1.5 mM Re-C and Re-G in MeCN upon chemical reduction of bis(pentamethylcyclopentadienyl)cobalt(II) (Co(Cp <sup>*</sup> ) <sub>2</sub> ). ....	112
<b>Figure 5.3</b> Cyclic voltammograms of (a) 0.5 mM of Re(bpy-PE)(CO) <sub>3</sub> Cl, with addition of (b) 0.5 mM calix[6]arene or (c) 0.5 mM of dihydroxypillar[6]arene, in dry MeCN under Ar or CO <sub>2</sub> with or without addition of trifluoroethanol (TFE) at a scan rate of 100 mV/s. ....	114
<b>Figure 5.4</b> Cyclic voltammograms of 0.5 mM of Re(bpy-PE)(CO) <sub>3</sub> Cl, with addition of (a) 0.5 mM calix[6]arene or (b) 0.5 mM of dihydroxypillar[6]arene in dry MeCN under Ar at a scan rate of 100 mV/s.....	115
<b>Figure 5.5</b> <sup>1</sup> H NMR of 4-methyl-4'-methyl(trimethylsilane)-2,2'-bipyridine in CD <sub>3</sub> Cl.....	118
<b>Figure 5.6</b> <sup>1</sup> H NMR of 4-methyl-4'-methylchloro-2,2'-bipyridine in CD <sub>3</sub> Cl.....	119
<b>Figure 5.7</b> <sup>1</sup> H NMR of 4-methyl-4'-methylcytosine-2,2'-bipyridine in CD <sub>3</sub> Cl.....	120
<b>Figure 5.8</b> <sup>1</sup> H NMR of Re(dmb-cytosine)(CO) <sub>3</sub> Cl in CD <sub>3</sub> CN. ....	121
<b>Figure 5.9</b> <sup>1</sup> H NMR of 4-methyl-4'-methylguanine-2,2'-bipyridine in CD <sub>3</sub> Cl. ....	122
<b>Figure 5.10</b> <sup>1</sup> H NMR of Re(dmb-guanine)(CO) <sub>3</sub> Cl in DMSO-d <sub>6</sub> . ....	123
<b>Figure 5.11</b> <sup>1</sup> H NMR of 5 mM Re(bpy-PE)(CO) <sub>3</sub> Cl in CD <sub>3</sub> CN. ....	124

## LIST OF SCHEMES

<b>Scheme 1.1</b> Schematic reaction mechanism of multi-electron photochemical carbon dioxide reduction through reductive quenching. ....	9
<b>Scheme 1.2</b> Schematic representation of electron transfer process of electrocatalysis. ....	10
<b>Scheme 1.3</b> Schematic representation of electrical double layer, which is composed of inner Helmholtz plane (IHP) and outer Helmholtz plane (OHP), diffuse layer, and electroneutral bulk solution. ...	11
<b>Scheme 1.4</b> Schematic representation of homogeneous and heterogenized catalyst for electrocatalysis. .	12
<b>Scheme 2.1</b> Proposed mechanisms for the formation of HCO <sub>2</sub> H and/or CO from the photocatalytic reaction with Mn(CN)(bpy)(CO) <sub>3</sub> and MnBr(bpy)(CO) <sub>3</sub> <sup>18-19</sup> , respectively. ....	23
<b>Scheme 2.2</b> Simplified description of the elementary steps in photochemical reduction of CO <sub>2</sub> by Mn(CN)(bpy)(CO) <sub>3</sub> . ....	24
<b>Scheme 3.1</b> Experimental and control systems for investigation of hydrogen bonding effects on photocatalysis. ....	45
<b>Scheme 3.2</b> A simplified scheme showing reductive quenching of the Ru photosensitizer (Ru) by sacrificial reductant (D) and then the electron transfer from singly reduced Ru to the catalyst (Cat). ....	46
<b>Scheme 3.3</b> A schematic representation of statistical mixture of RuDAC and ReDAC homodimers and RuDAC/ReDAC heterodimers in the ration of 1 : 1 : 2. ....	67
<b>Scheme 5.1</b> Molecular structure of Re(dmb-cytosine)(CO) <sub>3</sub> Cl and Re(dmb-guanine)(CO) <sub>3</sub> Cl. ....	111
<b>Scheme 5.2</b> Schematic representation of proposed photochemical system with specific donor and acceptor pair for hydrogen bonding. ....	113
<b>Scheme 5.3</b> Molecular structure of Re(bpy-PE)(CO) <sub>3</sub> Cl, calix[6]arene and dihydroxypillar[6]arene. ....	113



## LIST OF TABLES

<b>Table 1.1</b> Reduction potentials for electrochemical half-reactions of CO <sub>2</sub> at pH = 7 vs. NHE in aqueous solution. Reproduced from Benson <i>et al.</i> <sup>28</sup> .....	8
<b>Table 2.1</b> Summary of Catalytic Experiments for Photocatalysis.....	20
<b>Table 2.2</b> Summary of Control Experiments for Photocatalysis.....	21
<b>Table 3.1</b> Summary of turnover numbers (TON <sub>CO</sub> and TON <sub>H<sub>2</sub></sub> ), turnover frequency (TOF <sub>CO</sub> ) and quantum yield (Φ <sub>CO</sub> ) of experimental studies of 0.5 mM catalyst (Cat) and 0.5 mM of photosensitizer (PS) under CO <sub>2</sub> . .....	48
<b>Table 3.2</b> Summary of turnover numbers (TON <sub>CO</sub> ) and quantum yield (Φ <sub>CO</sub> ) for control studies of 0.5 mM catalyst (Cat) and 0.5 mM of photosensitizer (PS) after 4 hours of photocatalysis under Ar or CO <sub>2</sub> . .....	49
<b>Table 3.3</b> Photochemical properties of RuDAC, RuBPY and RuDMB.....	52
<b>Table 4.1</b> Concentration of Fe sites of FeDhaTph-COF, FeTAPPCl and blank electrodes before and after 3h electrolysis in MeCN and DMF. <sup>a</sup> The concentrations of Fe are below detection limit. There is no detectable Fe concentration in the blank carbon cloth before and after CPE. ....	83
<b>Table 4.2</b> Percentage contributions of the different nitrogen species for FeTAPPCl, FeDhaTph-COF and FeDmaTph-COF. ....	103

## ACKNOWLEDGEMENTS

I am very fortunate to have so much support from my friends, co-workers, collaborators, advisor and my family. Their sharing, teaching and reflections have made me a better authentic self.

First, I am very grateful that Professor Cliff Kubiak accepted me as a student in his lab and provided support and guidance when I needed them. I felt very fortunate that the lab environment is delighted, supportive, full of humor and bromance. Special thanks to my colleagues in the Kubiak Lab, especially Steven Chabolla and Chris Miller, for brainstorming research ideas, editing my writing, listening to my complaints and providing suggestions. I still enjoy doing research and discussing about science at the end of graduate school. The five years in UC San Diego is the most fruitful, independent and enjoyable period in my life so far.

More thanks to my friends in Hong Kong, including but not limited to Donald Chan, Steven Cheung and Candace Lau. They provided help to me in terms of counselling, emotional support, financial support, editing my writing, sharing cute emojis on Facebook and discussion of science, social and political issues throughout my Ph.D. life.

My parents, even though they only completed elementary school, always support me in pursuing a “dangerous” major with an advanced degree oversea. September 2019 is a memorial time to me as my father has been passed away in peace while I am preparing my dissertation. Last but not least, deepest gratitude to my mother, who is rather open-minded at her age, for her unconditional love and support.

## CHAPTER-SPECIFIC ACKNOWLEDGEMENT

**Chapter 2**, in full, comes directly from a manuscript entitled: “Photochemical Reduction of Carbon Dioxide Using a CN-modified fac-Mn(bpy)(CO)<sub>3</sub> Catalyst.” by Cheung, P.L.; Machan, C.W.; Malkhasian, A.; Agarwal, J. and Kubiak, C.P., which has been published in *Inorg. Chem.* **2016**, *55*, 319–3198. The dissertation author is a primary co-author of this manuscript. This work was supported by the Air Force Office of Scientific Research through AFOSR through a Basic Research Initiative (BRI) Grant (No. FA9550-12-1-0414). J.A. acknowledges support from the NSF (CHE-1361178).

**Chapter 3**, in full, comes directly from a manuscript entitled: “Improving Photocatalysis for the Reduction of CO<sub>2</sub> Through Non-Covalent Supramolecular Assemble.” by Cheung, P.L.; Kapper, S.C.; Zeng, T.; Thompson, M.E. and Kubiak, C.P., which has been published in *J. Am. Chem. Soc.* **2019**, *141*(38), 14961–14965. The dissertation author is a primary co-author of this manuscript. This work was supported by the Air Force Office of Scientific Research through AFOSR through a Basic Research Initiative (BRI) Grant (No. FA9550-12-1-0414).

**Chapter 4**, in full, comes directly from a manuscript entitled: “Facile Solvent-Free Synthesis of Thin Iron Porphyrin COFs on Carbon Cloth Electrodes for CO<sub>2</sub> Reduction.” by Cheung, P.L.; Lee, S.K. and Kubiak, C.P., which has been published in *Chem. Mater.* **2019**, *31*, 1908–1919. The dissertation author is a primary co-author of this manuscript. This work was supported by the Air Force Office of Scientific Research through AFOSR through a Basic Research Initiative (BRI) Grant (No. FA9550-12-1-0414).

**Chapter 5**, in part, consists of unpublished work. This work was supported by the Air Force Office of Scientific Research through AFOSR through a Basic Research Initiative (BRI) Grant (No. FA9550-12-1-0414).

## VITA

2019	Doctor of Philosophy, University of California San Diego
2016	Master of Science, University of California San Diego
2014	Bachelor of Science, The Chinese University of Hong Kong

## PUBLICATIONS

**Cheung, P.L.;** Kapper, S.C.; Zeng, T.; Thompson, M.E.; Kubiak, C.P. Improving Photocatalysis for the Reduction of CO<sub>2</sub> Through Non-Covalent Supramolecular Assemble. *J. Am. Chem. Soc.* **2019**, *141*(38), 14961–14965.

**Cheung, P.L.;** Lee, S.K.; Kubiak, C.P. Facile Solvent-Free Synthesis of Thin Iron Porphyrin COFs on Carbon Cloth Electrodes for CO<sub>2</sub> Reduction. *Chem. Mater.* **2019**, *31*, 1908–1919.

Clark, M.L.; **Cheung, P.L.;** Lessio, M.; Carter, E.A.; Kubiak, C.P. Kinetic and Mechanistic Effects of Bipyridine (bpy) Substituent, Labile Ligand, and Brønsted Acid on Electrocatalytic CO<sub>2</sub> Reduction by Re(bpy) Complexes. *ACS Catal.* **2018**, *8*, 2021–2029.

Sahu, S.; **Cheung, P.L.;** Machan, C.W.; Chabolla, S.A.; Kubiak, C.P.; Gianneschi, N.C. Charged Macromolecular Rhenium Bipyridine Catalysts with Tunable CO<sub>2</sub> Reduction Potentials. *Chem. Eur. J.* **2017**, *23*, 8619–8622.

**Cheung, P.L.;** Machan, C.W.; Malkhasian, A.; Agarwal, J.; Kubiak, C.P. Photochemical Reduction of Carbon Dioxide Using a CN-modified fac-Mn(bpy)(CO)<sub>3</sub> Catalyst, *Inorg. Chem.* **2016**, *55*, 319–3198.

ABSTRACT OF THE DISSERTATION

**Photochemical and Electrochemical Reduction of Carbon Dioxide**

by

Po Ling Cheung

Doctor of Philosophy in Chemistry

University of California San Diego, 2019

Professor Clifford P. Kubiak, Chair

Carbon dioxide reduction has been an increasingly popular research in the renewable energy development as it can be used to store the solar energy in the form of chemical energy in liquid fuels, like gasoline and diesel. There are two main catalytic approaches to overcome the thermodynamically unfavored conversion of carbon dioxide (CO<sub>2</sub>) to carbon-based species, such as carbon monoxide and format:

photochemical reduction using direct sunlight, and electrochemical reduction using electricity generated by solar panels.

In a typical photochemical system using rhenium or manganese bipyridine catalysts, previous work has been done on ligand modification to improve the quantum yield of carbon monoxide (CO) and other carbon species production. The work presented in this dissertation focuses on the structural modification of these catalysts to eliminate dimerization of manganese bipyridine catalyst upon first reduction and facilitate electron transfer from singly reduced photosensitizer to catalyst through non-covalent supramolecular assembly. In the former method, the bromide ligand of the manganese bipyridine catalyst ( $\text{Mnbp}(\text{CO})_3\text{Br}$ ) was replaced with a cyanide ligand ( $\text{Mnbp}(\text{CO})_3\text{CN}$ ) to reach an alternative reaction mechanism, in which disproportionation of two singly reduced manganese bipyridine catalyst occurs to give the active species without dimerization. In the latter method, electron transfer between the singly reduced photosensitizer and the catalyst is facilitated by the closer proximity of the two through non-covalent hydrogen bonding. Both methods, unexpectedly, discovered the role of solvents in photocatalysis on product selectivity.

One of the biggest obstacles of electrochemical reduction of carbon dioxide in large-scale application is the immobilization of catalysts onto electrode surface. Most of the attachment methods in the literature face the issues of catalysts detachment and deactivation, and poor electrical contact between the catalyst and the electrode. A novel solvent-free synthetic method was invented to embed a top carbon dioxide electrocatalyst iron porphyrin into covalent organic frameworks. The COF-modified electrode demonstrated good activity for production of CO under electrocatalytic conditions in acetonitrile (MeCN) compared to the control electrode with only adsorbed iron porphyrins.

# Chapter 1

## Energy Storage by Carbon Dioxide Reduction

### 1.1 Global Energy Usage and Movement Towards Renewable Energy

With increasing demand in energy, there is a growing need for finding renewable energy resources to offset or stabilize the emissions of carbon dioxide. Energy consumption worldwide grew by 2.3 % in 2018, nearly twice the average rate of growth since 2010.<sup>1-2</sup> It was spurred by increased consumption in China and the United States. Chinese energy consumption, being the largest in the world since 2009, was mainly driven by power generation, strong industrial demand, and increasing transport fuel consumption encouraged by a growing vehicle fleet. The United States has consumed a record-high of 2.3 giga tonne of oil equivalent of energy in 2018 (3.5 % increase from 2017).<sup>2</sup> In contrast, energy consumption decreased in the European Union ( 1 %), and in particular Germany ( 3.5 %), partly due to decreasing consumption in the power industry, a milder winter, reducing commercial consumption, and energy efficiency improvements.<sup>3</sup> Natural gas accounted for nearly 45 % of the increase in total energy demand. Demand for all fuels rose, with fossil fuels meeting nearly 70 % of the growth for the second year energy consumption.<sup>1</sup> Modeled projections from different groups suggest that the consumption of fossil fuels is likely to continue to grow due to increased energy demand in the future.<sup>2, 4-5</sup>

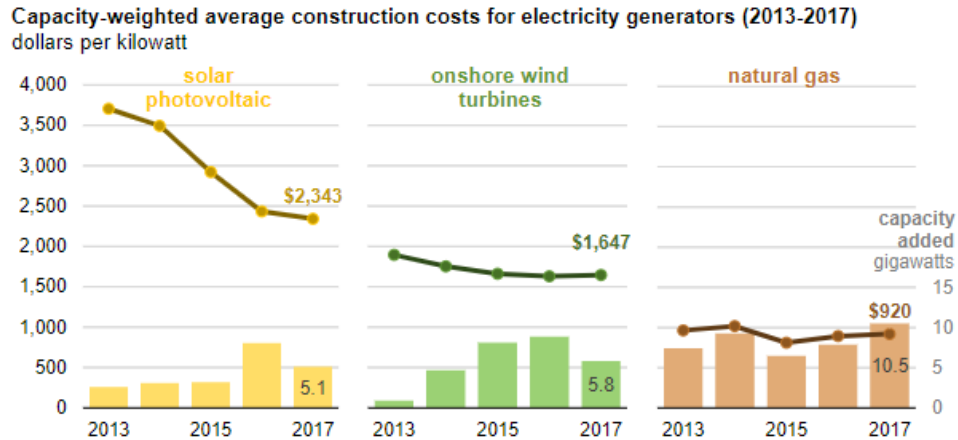


**Figure 1.1** Capacity-weighted average construction costs for electricity generators from 2013 to 2017. Figure reproduced in full from Reference 6.

Global energy demands and climate change have increased interest in the renewable energy development in the world, making it more cost-competitive compared to conventional fossil fuel power plants.<sup>4-6</sup> From 2013 to 2017, average costs for solar photovoltaic (PV) generators have fallen by 37 %, wind by 13 %, and natural gas by 4.7 % in the United States (**Figure 1.1**).<sup>6</sup> Renewables 2019 Global Status Report<sup>5</sup> showed that renewable energy accounted for an estimated 18.1 % of total global final energy consumption. The electricity generated from new solar PV plants had become more economical than power from fossil fuel plants in many countries, such as China, Germany, and Italy.<sup>7</sup> The increased popularity of solar PV plants is due to the decreased global total installation cost of utility-scale solar PV projects, which have fallen more than 70% since 2010 (1210/kW in 2018 and 4621/kW in 2010)<sup>7</sup> due to competition, continued improvements in manufacturing, and module efficiency.<sup>5</sup> In the U.S., California is on the track to meet its goal of 33 % of its energy produced from renewable sources, such as solar, wind, and geothermal energy by 2020 (**Figure 1.2**);<sup>8</sup> it has also set an additional goal of reaching 50 % of its electrical needs by renewable energy by 2030.<sup>9</sup> The lowering of building cost makes renewable energy a bigger section of global energy supply.



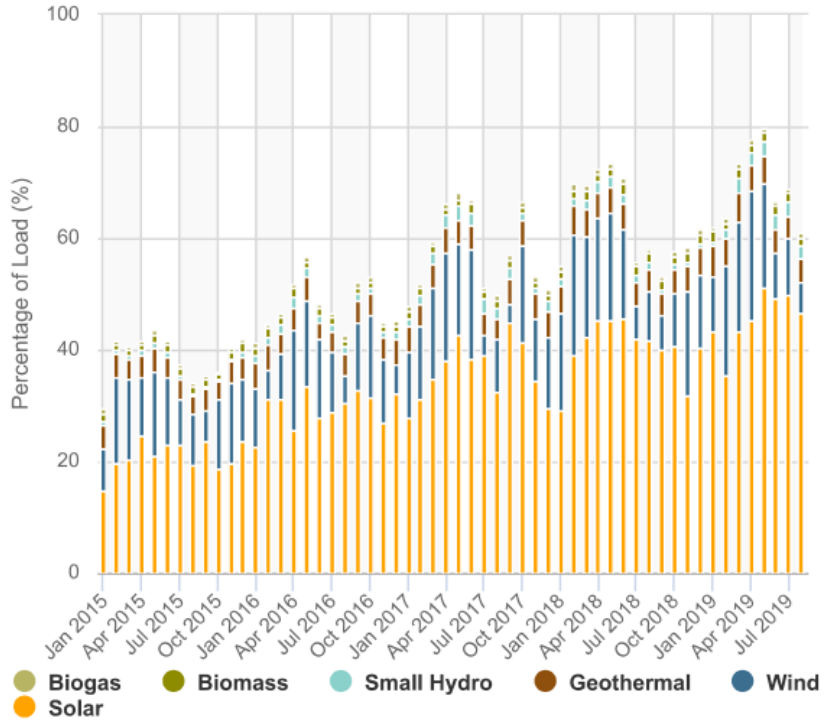


**Figure 1.2** Monthly maximum percent of load served by renewables in California from January 2015 to July 2019. Figure reproduced in full from Reference 3.

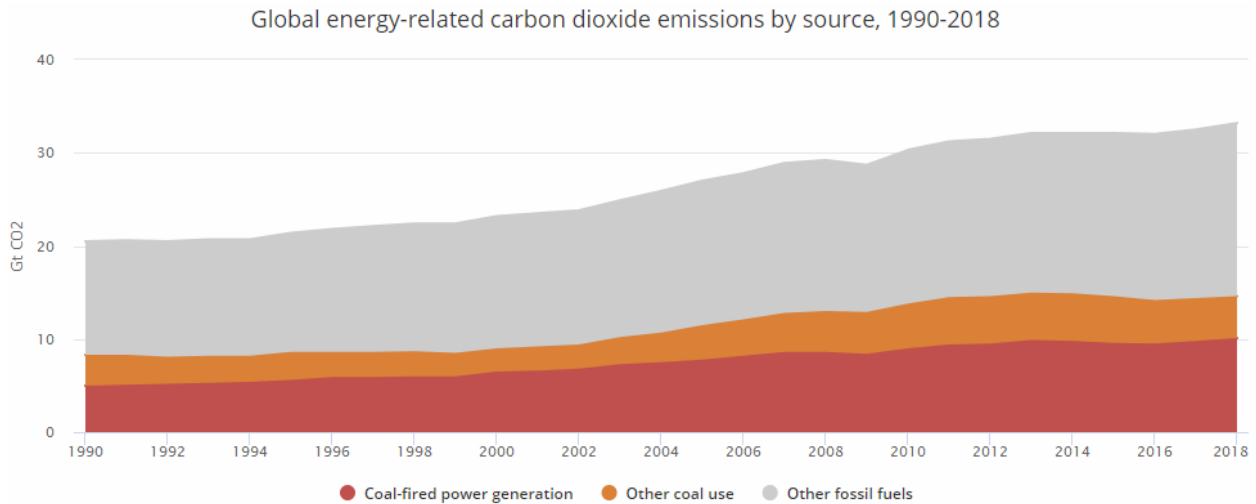


**Figure 1.3** Global energy-related carbon dioxide emissions by source from 1990 to 2019 recorded by IEA. Figure reproduced in full from Reference 1.

Despite progress in renewables generation, energy efficiency, and energy access, the world is not on track to meet the targets of the Paris Agreement, which aims to limit the global temperature rise in this century to 1.5 °C above pre-industrial levels via increased renewable energy usage and a decrease in global

carbon emissions.<sup>10</sup> Due to increased fossil fuel consumption global energy-related carbon dioxide (CO<sub>2</sub>) emissions rose 1.7 % to a historic high of 33.1 gigatonne (Gt) of CO<sub>2</sub> in 2018. **(Figure 1.3).**<sup>1,5</sup> In the new global economy, reduction of carbon dioxide emissions has become a central issue for economic growth and environmental sustainable development.

## 1.2 Problems of Oversupply and Intermittency

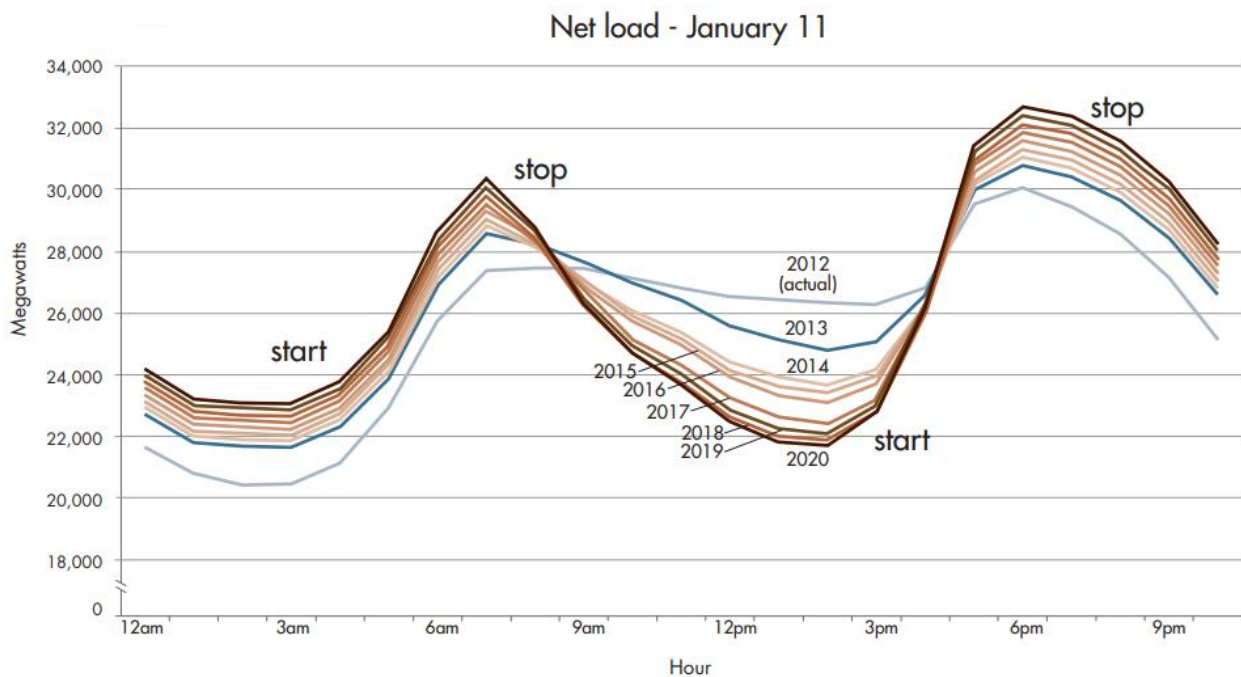


**Figure 1.4** The “duck curve” chart published by CAISO in 2016. Figure reproduced in full from Reference 11.

In February 2008, a team of analysts at the National Renewable Energy Laboratory (NREL) led by Paul Denholm published work<sup>12</sup> that examined future large-scale integration of solar photovoltaic (PV) generation on the electric grid. Their recognition of a unique change in the shape of the electric load met by conventional power plants when increasing levels of PV are added to the system is consistent with the “duck curve” phenomenon **(Figure 1.4)** observed by the California Independent System Operator (CAISO) in their real-time monitor of daily net electricity demand from 2012 to 2020.<sup>11, 13</sup> Since its discovery, the duck curve has become an emblem of the challenges faced by power system operators when integrating

variable renewables on the grid. On a particular sunny day, especially when the temperature is cool, system operators have to turn off some of the solar panels as conventional plants are too slow to turn on and off to accommodate the spike of solar energy during daytime. Moreover, the intermittent nature of solar and wind energies makes them unreliable supply of energy for long term utilization. To cope with these problems, energy storage is the ultimate solution to renewable energies.

### **1.3 Role of Carbon Dioxide Utilization in Energy Storage**

#### **1.3.1 Role of Carbon Dioxide Reduction in Grid Management**

Without cost-effective storage, solar electricity can never be a primary energy source for society, due to the diurnal variation in local insolation. In principle, storage of electricity could be obtained using batteries, but at present no battery technology meets the needs for large scale storage applications. A second approach is to store the electrical energy mechanically, for instance, by pumping water uphill. This method is relatively inexpensive for storing large amounts of energy, but it is not well matched to being charged and discharged every 24 h to compensate for the diurnal cycle. A third way of storage is to store the solar electrical energy into chemical energy in the form of chemical bonding in artificial photosynthesis, as a mimic of natural photosynthesis.<sup>14</sup> One of the best end products that can be produced from artificial photosynthesis is liquid fuels, such as gasoline and diesel, by using carbon dioxide as a raw material. Carbon dioxide is a very thermodynamically stable form of carbon. As a result, conversion of carbon dioxide into a more energetic product involves transfer of electrons to carbon, reducing its oxidation state. The processes by which carbon dioxide is converted to a more reduced product is called carbon dioxide reduction. As a comparison to energy storage in batteries or hydrogen gas, liquid hydrocarbon fuels have much higher energy density per unit weight or volume (**Figure 1.5**). Together with their low density and liquid state, liquid fuels are still the best form of energy storage that is already well incorporated into our current society.

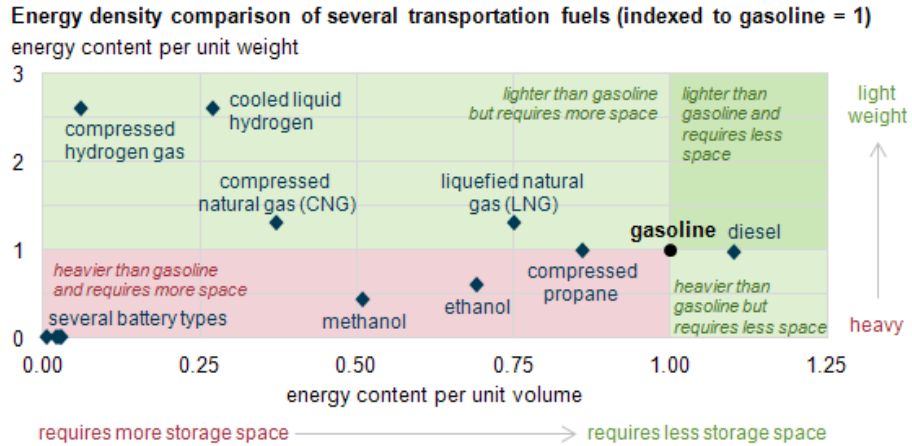


**Figure 1.5** Energy density per unit weight or volume of liquid fuels compared to batteries. Figure adapted from Reference 15.

### 1.3.2 Other Impacts Brought by Carbon Dioxide Reduction

By coupling carbon dioxide reduction to micro-grids of renewable energy, liquid fuels can be produced using sunlight or wind, carbon dioxide, and water. Such technology is not only important to the development of renewable energy, but also essential to the national security<sup>16</sup> and Mars exploration<sup>17</sup>. According to a Department of Defense (DOD) report<sup>18</sup>, U.S. military facilities had 701 power outages in 2016 that lasted eight hours or longer, with an average cost of \$500,000 per day. These power outages are mainly due to mechanical failures and the loss of electricity through the public power grid. In cases where continuity of power supply is vital for national defense operations, renewable power and energy storage technology, can be combined to form self-sustaining microgrids. Renewable energy generators can be constructed within a short timeframe throughout different regions and terrains, and enhance the reliability and resilience of the entire electrical grid during high-impact events.<sup>16</sup>

The Keck Institute for Space Sciences (KISS) has studied the viability of the photoelectrochemical (PEC) or electrochemical (EC) production of fuel (e.g., carbon monoxide or methane) and oxygen from atmospheric carbon dioxide on Mars. The Martian atmosphere consists of more than 95 % of carbon dioxide. Due to the complexity, site dependency, and mission risk currently on Mars, utilization of atmospheric CO<sub>2</sub> is deemed the preferred way to produce oxygen and fuels for human missions.<sup>17</sup>

## 1.4 Catalysts for Carbon Dioxide Reduction

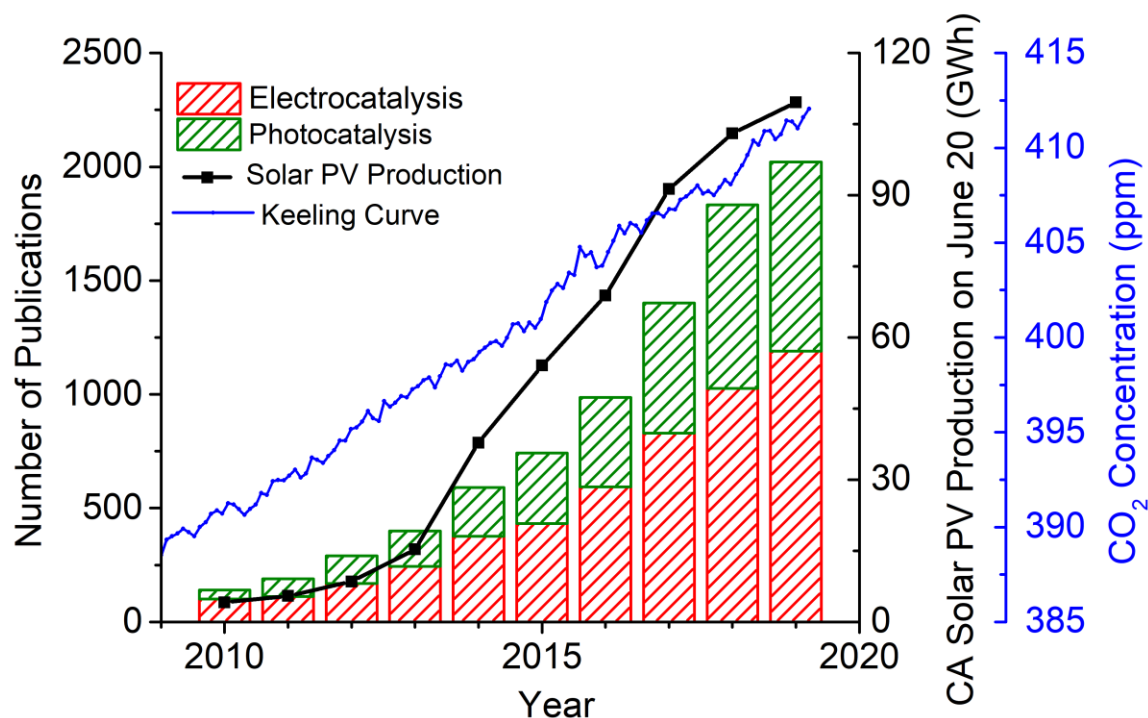


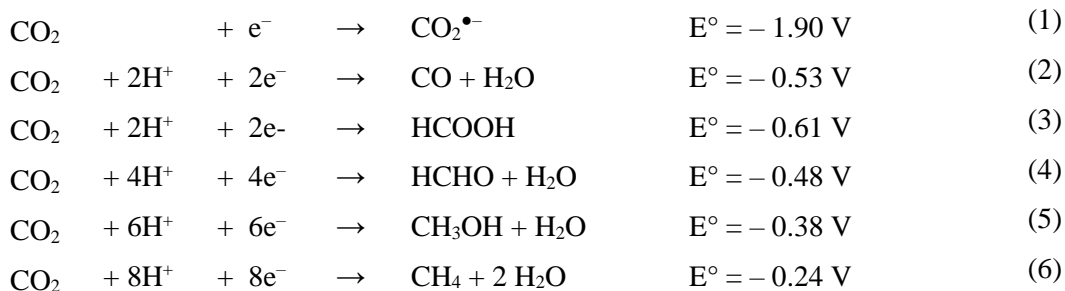
**Figure 1.6** Timeline for the number of articles published on photocatalytic and electrocatalytic CO<sub>2</sub> reduction, solar PV production in California on June 20<sup>th</sup>, and monthly average of seasonally adjusted CO<sub>2</sub> concentration in the atmosphere.

The search of catalytic systems for carbon dioxide reduction has started since the oil crisis in 1970s.<sup>19</sup> Despite the drop in oil prices since, there has been an increase of solar PV production (**Figure 1.6**) that has led to more and more work has been done on photocatalysis and electrocatalysis for carbon dioxide reduction. The plot was made from the article numbers (Web of Science, Clarivate Analytics)<sup>20</sup>, solar PV production (CAISO Daily Renewables Watch)<sup>21</sup>, and CO<sub>2</sub> concentration (the Scripps CO<sub>2</sub> measurements at Mauna Loa)<sup>22</sup> respectively. All data were updated on November 12, 2019. In the past few decades, useful catalytic systems were developed mostly using semiconductors, transition metal complexes, and enzymes. In this work, we focus on the development of transition metal complexes as electrocatalysts and photocatalysts for carbon dioxide reduction.

### 1.4.1 Photochemical Systems for Carbon Dioxide Reduction

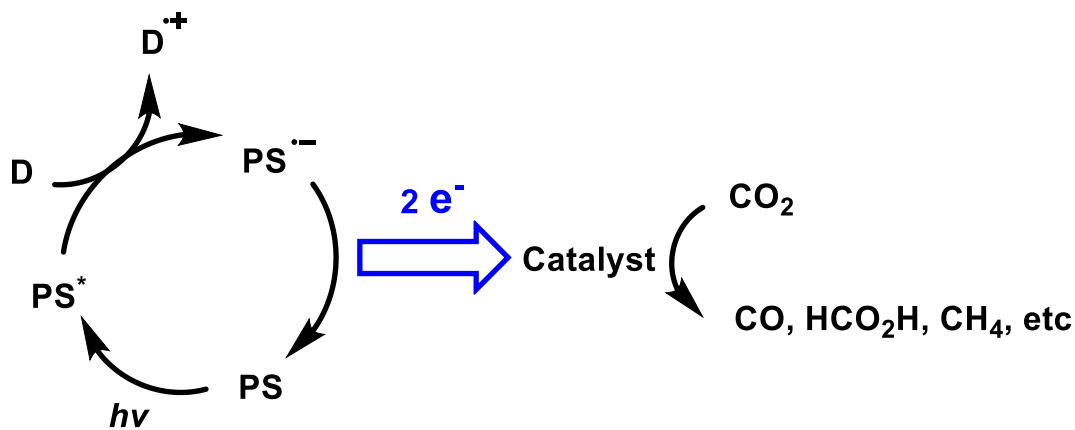
The one-electron reduction of carbon dioxide is a highly endergonic reaction (eqn. (1) in **Table 1.1**) because carbon dioxide is a very thermodynamically stable form of carbon. Only a few studies have reported this process by photocatalysis. For instance, Yanagida et al showed that poly-*p*-phenylene serves as redox photosensitizer to reduce CO<sub>2</sub> to CO<sub>2</sub><sup>•-</sup> in the presence of trimethylamine as reductant<sup>23</sup>. However, to have better product control and utilize low energy light, the multi-electron reduction of carbon dioxide via chemical reactions is a more promising process. As shown in eqn. (2) and (3), the two-electron two-proton reduction of carbon dioxide is thermodynamically more favorable. Carbon monoxide (CO) is a useful chemical precursor that can be converted into liquid hydrocarbon fuels through Fischer-Tropsch process.<sup>24</sup> Formic acid can act as a hydrogen carrier<sup>25</sup> and as use in a formic acid fuel cell.<sup>26-27</sup>

**Table 1.1** Reduction potentials for electrochemical half-reactions of CO<sub>2</sub> at pH = 7 vs. NHE in aqueous solution. Reproduced from Benson *et al.*<sup>28</sup>



A typical multi-electron system for photocatalytic reduction of carbon dioxide via reductive quenching usually consists of a sacrificial reductant (D), a photosensitizer (PS), and a catalyst (**Scheme 1.1**). In this work, we concentrate on reductive quenching process as photosensitizer and catalyst are two isolated molecules, not being linked by covalent bonds. In most photocatalytic systems, the catalytic cycles were initiated by the reductive quenching process, in which an electron was transferred from sacrificial reductant to the photoexcited PS\* to give the singly reduced photosensitizer (PS<sup>•-</sup>). The reductant sometimes has drastic impacts on the photocatalytic activity of the system. Photosensitizer is a redox mediator transferring electrons from sacrificial reductant to catalyst after photoexcitation. Catalyst accepts

one or multiple electrons from  $PS^{\bullet-}$  or ( $PS^*$ ) to reduce  $CO_2$  molecule by making one or multiple bonds. The driving force of electron transfer between photosensitizer and catalyst is determined by the redox potential difference between  $PS^{\bullet-}$  and the catalyst.<sup>19</sup>



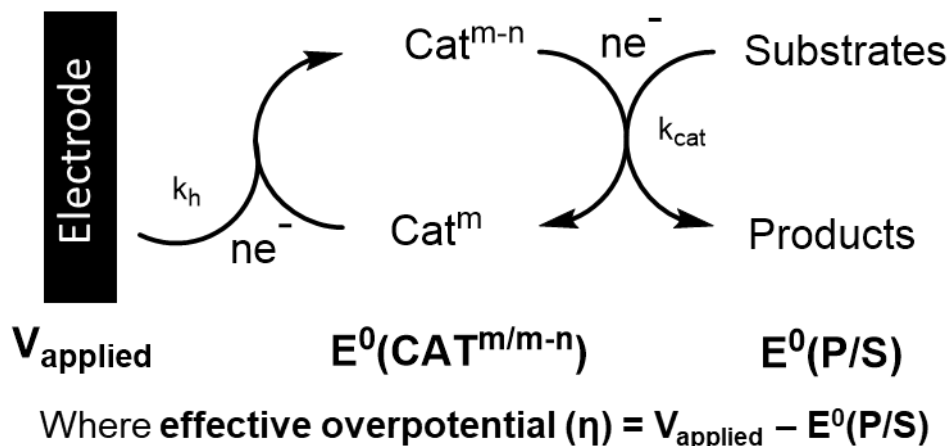
**Scheme 1.1** Schematic reaction mechanism of multi-electron photochemical carbon dioxide reduction through reductive quenching.

The most studied photochemical systems include rhenium, manganese and ruthenium bipyridyl complexes, iron and cobalt porphyrins, as well as cobalt and nickel cyclams<sup>29</sup>. Current work has been focused on synthesizing novel photosensitizer for longer excited state lifetime<sup>30-31</sup> and visible light excitation<sup>32-33</sup>, replacement of scarce metals to earth abundant metals in catalysts<sup>34-35</sup> and photosensitizers<sup>32, 35</sup>, acceleration of electron transfer from  $PS^{\bullet-}$  to catalyst,<sup>31, 36</sup> and usage of better sacrificial reductants<sup>37</sup> to further improve catalytic performance. Most of these works were done through modification of ligands of the organometallic complexes,<sup>31-32, 36</sup> but there is still room for study by alternating the reaction mechanism for photocatalysis.<sup>38-39</sup> Hence, this work shows two projects alternating the reaction mechanisms by changing the ligand directly attached to the metal center<sup>39</sup> and installing hydrogen bonding groups to ligands<sup>38</sup>.

#### 1.4.2 Electrochemical Systems for Carbon Dioxide Reduction

The electrochemical reduction of carbon dioxide was studied for the first time by Royer<sup>40</sup> in 1870. Similar to photocatalytic reduction of carbon dioxide, there was a growing body of literature that recognizes

the importance of electrochemical studies started since 1970s.<sup>41</sup> As shown in **Scheme 1.2**, electrocatalysts receive one or more electrons from electrode to reach the reduced state ( $\text{Cat}^{m-n}$ ), then they pass the electrons to the substrate to give the products and regenerate the oxidized catalyst ( $\text{Cat}^m$ ). An electrocatalytic process is therefore dependent on the relationship between the applied voltage,  $V_{\text{applied}}$ , and the thermodynamic potential of the reaction,  $E^0(\text{P/S})$ , which can be used to determine the effective overpotential,  $\eta$  [ $V_{\text{applied}} - E^0(\text{P/S})$ ]. Ideal molecular electrocatalysts have a high heterogeneous electron transfer rate constant,  $k_h$ , at  $V_{\text{applied}}$  in addition to a redox couple,  $E^0(\text{CAT}^{m/m-n})$ , that is well-matched with  $E^0(\text{P/S})$  so that  $\eta$  is minimal. Ideal catalysts will have high catalytic rate constants,  $k_{\text{cat}}$ , with low  $\eta$  values (**Scheme 1.2**).<sup>42</sup> To study these reactions, isolation of catalytically relevant species is of the utmost importance to understanding the catalytic mechanism and gives insight into how electronic structures can be manipulated to improve catalytic activity.

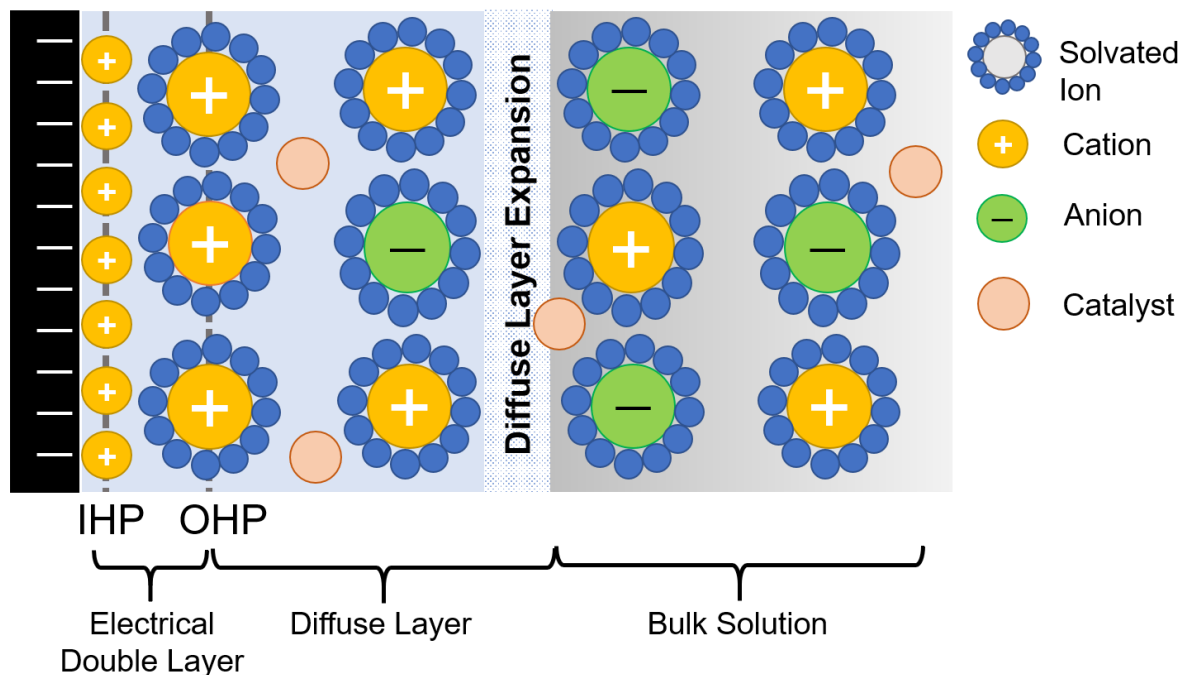


**Scheme 1.2** Schematic representation of electron transfer process of electrocatalysis.

The direct electrochemical reduction of carbon dioxide results in a variety of products which depend mainly on catalyst materials and the reaction medium. Electrochemical reduction of carbon dioxide can mainly proceed through two-, four-, six-, and eight-electron reduction pathways in gaseous, aqueous, and non-aqueous phases at different cell and electrode configurations (**Table 1.1**). In this work, we focus on molecular electrocatalysts, which are mostly molecular transition metal complexes. Based on their



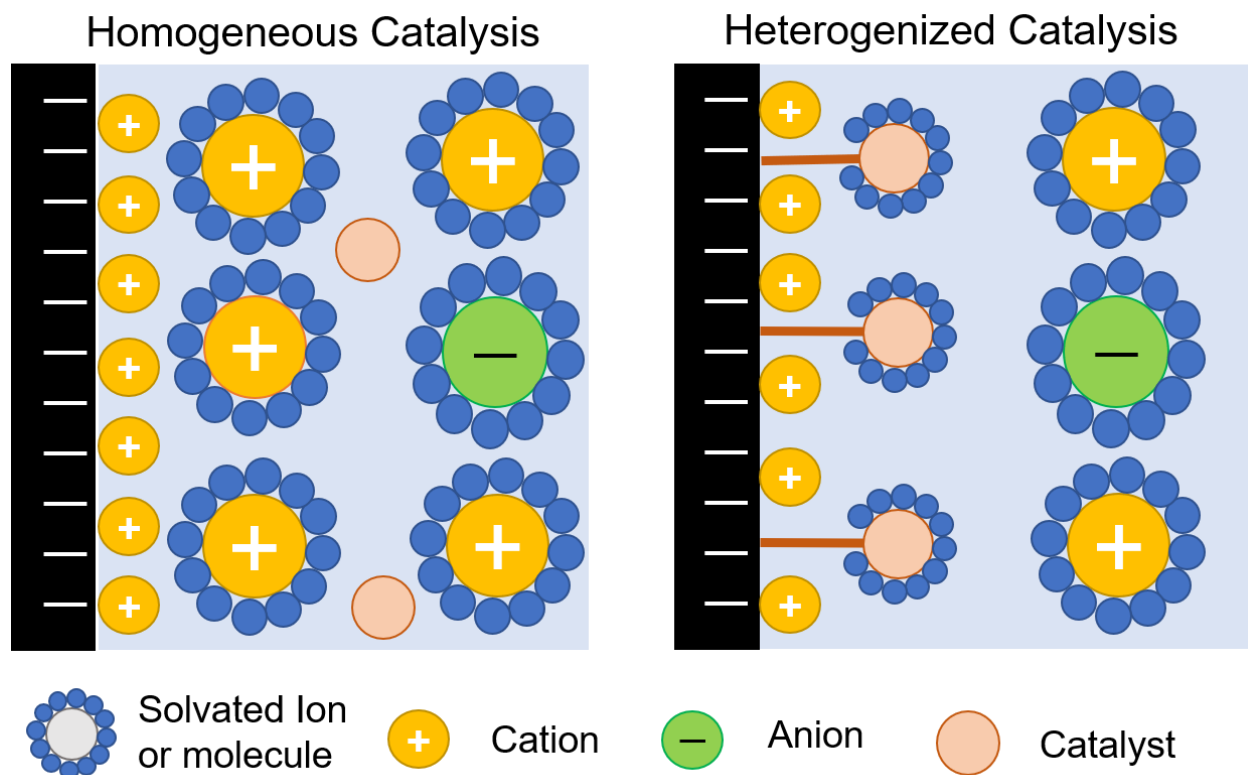
physical states during catalysis, molecular electrocatalysts can be categorized into two groups: homogeneous catalysts and heterogenized catalysts.



**Scheme 1.3** Schematic representation of electrical double layer, which is composed of inner Helmholtz plane (IHP) and outer Helmholtz plane (OHP), diffuse layer, and electroneutral bulk solution.

Homogeneous catalysts dissolve in solution during catalysis. When a negative potential is applied at the electrode, there is a space-charged region composed of electrical double layer and a diffuse layer. The former contains exclusively cations of the supporting electrolyte on the electrode surface (and vice versa if the electrode is positive). The inner Helmholtz plane (IHP) is the layer of adsorbed charged solvent or supporting electrolyte molecules, while the outer Helmholtz plane (OHP) consists of ions and solvated ions of opposite charges to the electrode attracted to the electrode surface via long range coulombic forces (**Scheme 1.3**).<sup>43</sup> The electrical double layer extends to the bulk solution via a diffuse layer in which the excess of positive charges over negative charges gradually decreases with distance until electroneutrality is reached. Since the concentration of supporting electrolyte is usually a hundred times higher than the concentration of the electroactive species, the presence of the electroactive species, the catalyst in this case, does not perturb the double layer significantly. The migration of charged electroactive species and

convection of solution is minimized during cyclic voltammetry, therefore, the electroactive molecules are transported solely by diffusion.<sup>42</sup> Because catalysts work only when they receive electrons, only the small fraction of catalysts present at the electrical double layer or diffuse layer can be reduced and reactive. Therefore, the rate of catalysis is limited by the rate of diffusion of catalyst to electrode surface.



**Scheme 1.4** Schematic representation of homogeneous and heterogenized catalyst for electrocatalysis.

To solve this problem, heterogenization of homogeneous molecular catalyst by immobilizing them onto electrode surfaces becomes a viable solution (**Scheme 1.4**). The molecular catalysts are attached to electrode surfaces via physical and chemical interactions. For example, molecular catalysts with aromatic rings are commonly deposited onto carbon nanotubes on carbon electrodes and then used in aqueous solution in which the catalysts are insoluble.<sup>44-47</sup> In the ideal situation, the heterogenized catalysts at the electrode surface receives electrons rapidly to drive catalysis, of which their rate is not limited by diffusion of catalysts. Heterogenization of catalysts also favors large scale applications due to lower catalyst loading, higher compatibility of various solvents, and easier handling of processes.

Rhenium and manganese bipyridine systems, iron and cobalt porphyrins, nickel cyclams, iron carbonyl clusters, and iron and cobalt cyclopentadienones are some of the most well-studied electrocatalysts for carbon dioxide reduction.<sup>28, 48-49</sup> A lot of studies have been done on attaching these catalysts onto electrode surfaces. Due to low cost, easy modification, and diversity in morphology, carbon electrodes are most commonly used for modification with catalysts. The attachment methods on carbon electrodes can be categorized as covalent immobilization and non-covalent immobilization. However, most of these attachments suffer from catalyst detachment, catalyst deactivation, low catalyst loading, and poor electrical contact.<sup>50</sup> More work needs to be done to build an ideal system with inexpensive catalyst, low catalyst loading, high catalytic activity, and long term stability. For example, monolayers or ultrathin films of catalysts made from earth-abundant metals, such as iron, manganese, and nickel, can be deposited or chemically linked to electrodes to decrease the catalyst loading. The molecular structure and morphology of catalysts is likely to affect the way they attach onto electrode surface, and hence their catalytic activity and long-term attachment.

## 1.5 Reference

1. *Global Energy & CO<sub>2</sub> Status Report The latest trends in energy and emissions in 2018*; International Energy Agency: Paris (France), March 26, 2019, 2019.
2. *Global Energy Statistical Yearbook 2019*; 2019.
3. *Total energy consumption*; Enerdata: Global Energy Statistical Yearbook 2019, 2019.
4. Annual Energy Outlook 2019. Energy, U. S. D. o., Ed. U.S. Energy Information Administration: Washington, DC 20585, 2019.
5. *Renewables 2019 Global Status Report*; REN21: Paris (France), 2019.
6. Mey, Alex Average U.S. construction costs for solar generation continue to decrease. [www.eia.gov/todayinenergy/detail.php?id=41153](http://www.eia.gov/todayinenergy/detail.php?id=41153) (accessed October 15, 2019).
7. IRENA *Renewable Power Generation Costs in 2018*; Abu Dhabi, 2019.
8. Monthly Renewables Performance Report - Aug 2019. [www.caiso.com/Documents/MonthlyRenewablesPerformanceReport-Aug2019.html](http://www.caiso.com/Documents/MonthlyRenewablesPerformanceReport-Aug2019.html) (accessed October 15, 2019).

9. Managing an Evolving Grid - Fast Facts. California Independent System Operator: Folsom, California, 2018; Vol. 2019.
10. Paris Agreement. Nations, U., Ed. 2019 United Nations Framework Convention on Climate Change: 2015; Vol. 2019.
11. What the duck curve tells us about managing a green grid - Fast Facts. California Independent System Operator: Folsom, California, 2013; Vol. 2019.
12. Denholm, P.;Margolis, R.; Milford, J. *Production Cost Modeling for High Levels of Photovoltaics Penetration*; The National Renewable Energy Laboratory: 2008.
13. Ten Years of Analyzing the Duck Chart: How an NREL Discovery in 2008 Is Helping Enable More Solar on the Grid Today. The National Renewable Energy Laboratory: 2018.
14. Lewis, N. S.; Nocera, D. G., Powering the planet: chemical challenges in solar energy utilization. *Proc. Natl. Acad. Sci. U.S.A* **2006**, *103* (43), 15729–15735.
15. Few transportation fuels surpass the energy densities of gasoline and diesel. [www.eia.gov/todayinenergy/detail.php?id=9991](http://www.eia.gov/todayinenergy/detail.php?id=9991) (accessed October 15, 2019).
16. The Role of Renewable Energy in National Security American Council On Renewable Energy: Washington, D.C. 20036, 2018.
17. *Addressing the Mars ISRU Challenge: Production of Oxygen and Fuel from CO<sub>2</sub> Using Sunlight*; the Keck Institute for Space Studies: 2018.
18. *Department of Defense Annual Energy Management and Resilience (AEMR) Report Fiscal Year 2016*; Office of the Assistant Secretary of Defense for Energy Installations, and Environment: 2017.
19. Yamazaki, Y.;Takeda, H.; Ishitani, O., Photocatalytic reduction of CO<sub>2</sub> using metal complexes. *J. Photochem. Photobiol. C: Photochemistry Reviews* **2015**, *25*, 106–137.
20. Web of Science. [apps.webofknowledge.com](http://apps.webofknowledge.com) (accessed July 2019).
21. Renewables and emissions reports. [www.caiso.com/market/Pages/ReportsBulletins/RenewablesReporting.aspx](http://www.caiso.com/market/Pages/ReportsBulletins/RenewablesReporting.aspx) (accessed July 2019).
22. Atmospheric CO<sub>2</sub> Data Primary Mauna Loa CO<sub>2</sub> Record. [scrippsco2.ucsd.edu/data/atmospheric\\_co2/primary\\_mlo\\_co2\\_record.html](http://scrippsco2.ucsd.edu/data/atmospheric_co2/primary_mlo_co2_record.html) (accessed July 2019).
23. Matsuoka, S.;Kohzuki, T.;Pac, C.;Ishida, A.;Takamuku, S.;Kusaba, M.;Nakashima, N.; Yanagida, S., Photocatalysis of oligo(p-phenylenes): photochemical reduction of carbon dioxide with triethylamine. *J. Phys. Chem.* **1992**, *96* (11), 4437–4442.
24. Dry, M.E., The Fischer–Tropsch process: 1950–2000. *Catal. Today* **2002**, *71* (3-4), 227–241.
25. Hull, J.F.;Himeda, Y. ;Wang, W.H.;Hashiguchi, B.;Periana, R.;Szalda, D.J.;Muckerman, J.T.; Fujita, E., Reversible hydrogen storage using CO<sub>2</sub> and a proton-switchable iridium catalyst in aqueous media under mild temperatures and pressures. *Nat. Chem.* **2012**, *4* (5), 383–388.
26. Zhu, Y.;Ha, S.Y.; Masel, R.I., High power density direct formic acid fuel cells. *J. Power Sources* **2004**, *130* (1–2), 8–14.

27. Rees, N.V.; Compton, R.G., Sustainable energy: a review of formic acid electrochemical fuel cells. *J. Solid State Electr.* **2011**, *15* (10), 2095–2100.
28. Benson, E. E.; Kubiak, C. P.; Sathrum, A. J.; Smieja, J. M., Electrocatalytic and homogeneous approaches to conversion of CO<sub>2</sub> to liquid fuels. *Chem. Soc. Rev.* **2009**, *38* (1), 89–99.
29. Yamazaki, Y.; Takeda, H.; Ishitani, O., Photocatalytic Reduction of CO<sub>2</sub> Using Metal Complexes. *J. Photochem. Photobiol. C: Photochem. Rev.* **2015**, *25*, 106–137.
30. Hamze, R.; Peltier, J.L.; Sylvinson, D.; Jung, M.; Cardenas, J.; Haiges, R.; Soleilhavoup, M.; Jazzar, R.; Djurovich, P.I.; Bertrand, G.; Thompson, M.E., Eliminating nonradiative decay in Cu(I) emitters: > 99% quantum efficiency and microsecond lifetime. *Science* **2019**, *363* (6427), 601–606.
31. Yamazaki, Y.; Ohkubo, K.; Saito, D.; Yatsu, T.; Tamaki, Y.; Tanaka, S.; Koike, K.; Onda, K.; Ishitani, O., Kinetics and Mechanism of Intramolecular Electron Transfer in Ru(II)–Re(I) Supramolecular CO<sub>2</sub>–Reduction Photocatalysts: Effects of Bridging Ligands. *Inorg. Chem.* **2019**, *58* (17), 11480–11492.
32. Takeda, H.; Monma, Y.; Sugiyama, H.; Uekusa, H.; Ishitani, O., Development of Visible-Light Driven Cu(I) Complex Photosensitizers for Photocatalytic CO<sub>2</sub> Reduction. *Front. Chem.* **2019**, *7*, 418.
33. Kuramochi, Y.; Ishitani, O., An Ir(III)-Complex Photosensitizer with Strong Visible-Light Absorption for Photocatalytic CO<sub>2</sub> Reduction. *Front. Chem.* **2019**, *7*, 259.
34. Takeda, H.; Koizumi, H.; Okamoto, K.; Ishitani, O., Photocatalytic CO<sub>2</sub> reduction using a Mn complex as a catalyst. *Chem. Commun.* **2014**, *50*, 1491–1493.
35. Takeda, H.; Kamiyama, H.; Okamoto, K.; Irimajiri, M.; Mizutani, T.; Koike, K.; Sekine, A.; Ishitani, O., Highly Efficient and Robust Photocatalytic Systems for CO<sub>2</sub> Reduction Consisting of a Cu(I) Photosensitizer and Mn(I) Catalysts. *J. Am. Chem. Soc.* **2018**, *140*, 17241–17254.
36. Gholamkhash, B.; Mametsuka, H.; Koike, K.; Furue, M.; Ishitani, O., Architecture of Supramolecular Metal Complexes for Photocatalytic CO<sub>2</sub> Reduction: Ruthenium-Rhenium Bi- and Tetranuclear Complexes. *Inorg. Chem.* **2005**, *44*, 2326–2336.
37. Tamaki, Y.; Koike, K.; Ishitani, O., Highly efficient, selective, and durable photocatalytic system for CO<sub>2</sub> reduction to formic acid. *Chem. Sci.* **2015**, *6*, 7213–7221.
38. Cheung, P.L.; Kapper, S.C.; Zeng, T.; Thompson, M.E.; Kubiak, C.P., Improving Photocatalysis for the Reduction of CO<sub>2</sub> Through Non-Covalent Supramolecular Assemble. *J. Am. Chem. Soc.* **2019**, *141* (38), 14961–14965.
39. Cheung, P.L.; Machan, C.W.; Malkhasian, A.; Agarwal, J.; Kubiak, C.P., Photochemical Reduction of Carbon Dioxide Using a CN-modified fac-Mn(bpy)(CO)<sub>3</sub> Catalyst. *Inorg. Chem.* **2016**, *55*, 319–3198.
40. Royer, M.E., Electrochemistry - Reduction from carbonic acid to formic acid. *C. R. Hebd. Seances Acad. Sci* **1870**, *70*, 731–732.
41. Meshitsuka, S.; Ichikawa, M.; Tamaru, K., Electrocatalysis by metal phthalocyanines in the reduction of carbon dioxide. *J. Chem. Soc. Chem. Commun.* **1974**, 158–159.

42. Savéant, J.-M., Single Electron Transfer At An Electrode. In *Elements of Molecular and Biomolecular Electrochemistry*, John Wiley & Sons, Inc.: Hoboken, N.J., 2006.
43. Wang, J., *Analytical Electrochemistry*. 3rd ed.; Wiley-VCH: Hoboken, N.J., 2006.
44. Reuillard, B.; Ly, K.H.; Rosser, T.E.; Kuehne, M.F.; Zebger, I.; Reisner, E., Tuning Product Selectivity for Aqueous CO<sub>2</sub> Reduction with a Mn(bipyridine)-pyrene Catalyst Immobilized on a Carbon Nanotube Electrode. *J. Am. Chem. Soc.* **2017**, *139* (41), 14425–14435.
45. Zhanaidarova, A.; Jones, S.C.; Despagnet-Ayoub, E.; Pimentel, B.R.; Kubiak, C.P., Re(tBu-bpy)(CO)<sub>3</sub>Cl supported on multi-walled carbon nanotubes selectively reduces CO<sub>2</sub> in water. *J. Am. Chem. Soc.* **2019**.
46. Sinha, S.; Sonea, A.; Shen, W.; Hanson, S.S.; Warren, J.J, Heterogeneous Aqueous CO<sub>2</sub> Reduction Using a Pyrene-Modified Rhenium(I) Diimine Complex. *Inorg. Chem.* **2019**, *58* (16), 10454–10461.
47. Leung, J.J.; Warnan, J.; Ly, K.H.; Heidary, N.; Nam, D.H.; Kuehnel, M.F.; Reisner, E., Solar-driven reduction of aqueous CO<sub>2</sub> with a cobalt bis(terpyridine)-based photocathode. *Nat. Catal.* **2019**, *2* (4), 354–365.
48. Franck, R.; Schille, B.; Roemelt, M., Homogeneously Catalyzed Electroreduction of Carbon Dioxide—Methods, Mechanisms, and Catalysts. *Chem. Rev.* **2018**, *118* (9), 4631–4701.
49. Albo, J.; Alvarez-Guerra, M. ; Castaño, P.; Irabienb, A. , Towards the electrochemical conversion of carbon dioxide into methanol. *Green Chem.* **2015**, *17*, 2304–2324.
50. Zhang, B.; Sun, L., Artificial photosynthesis: opportunities and challenges of molecular catalysts. *Chem. Soc. Rev.* **2019**, *48*, 2216–2264.

## Chapter 2

# Photochemical Reduction of Carbon Dioxide Using a CN-modified *fac*-Mn(bpy)(CO)<sub>3</sub> Catalyst

### 2.1 Introduction

The development of systems to harness renewable energy for conversion of carbon dioxide attracted attention as an artificial means of photosynthesis since the energy crisis from 1970s to 1990s. Three systems have been developed using semiconductors, transition metal complexes and enzymes during this period. Fujishima and Honda et al reported the photochemical reduction of carbon dioxide using semiconductor photocatalysts, e.g. titanium dioxide (TiO<sub>2</sub>) and cadmium sulfide (CdS).<sup>1</sup> Lehn's catalyst, *fac*-Re(bpy)(CO)<sub>3</sub>Cl, was also reported to be a very selective carbon dioxide photocatalyst in 1980s.<sup>2-4</sup> Willner and his coworkers also presented their development of photocatalytic CO<sub>2</sub>-fixation systems into organic products using enzymes in 1986.<sup>5</sup> Despite the decrease of oil price in recent years and the difficulty in developing technologies for industrial usage, the development of photocatalytic reduction of carbon dioxide continues to receive plenty of interest.

In this work, we focus on the photocatalytic reduction of carbon dioxide using transition metal complexes as catalysts and redox photosensitizers, especially molecular catalysts with Ru- and Re-carbonyl cores and ligands based on 2,2'-bipyridine (bpy).<sup>6-11</sup> Complexes of this type have been used to convert CO<sub>2</sub> to carbon monoxide (CO) and/or formic acid (HCO<sub>2</sub>H) by using a photosensitizer (PS) to initiate photochemical electron transfer along with a sacrificial reductant to donate electrons and sustain catalysis. However, the cost of ruthenium (Ru) and rhenium (Re) precludes their use on a large scale, underscoring the need for earth-abundant alternatives, e.g., manganese (Mn).<sup>12-13</sup> Although it is not the focus of the present work, we note that there is a complementary focus on the development of photosensitizers which do not use heavy metals for similar reasons.<sup>14-16</sup>

Prior reports have focused on the electrochemical<sup>17</sup> and photosensitizer-driven<sup>18-19</sup> reactions of *fac*-MnBr(bpy)(CO)<sub>3</sub> (the *fac*- label will be omitted from here on). During electrocatalysis, MnBr(bpy)(CO)<sub>3</sub> is first reduced by a single electron, after which the Br<sup>-</sup> ligand dissociates and a metal-metal bonded dimer, [Mn(bpy)(CO)<sub>3</sub>]<sub>2</sub>, is formed.<sup>20-21</sup> Further reduction of the dimer with two electrons yields two equivalents of the proposed active species, [Mn(bpy)(CO)<sub>3</sub>]<sup>-</sup>; this reduced species can react with CO<sub>2</sub> in the presence of added Brønsted acids to produce CO in non-aqueous media.<sup>20, 22-23</sup> The intermediate steps are proposed to involve a hydroxycarbonyl species, [Mn(η<sup>1</sup>-COOH)(bpy)(CO)<sub>3</sub>], which forms from the initial reaction of the [Mn(bpy)(CO)<sub>3</sub>]<sup>-</sup> anion with CO<sub>2</sub>/H<sup>+</sup> and requires an additional reduction to achieve the highest rate of catalysis.<sup>22, 24</sup> Consistent with the electrochemical mechanism detailed above, Takeda *et al.*<sup>18</sup> found that, as a catalyst, MnBr(bpy)(CO)<sub>3</sub> forms the [Mn(bpy)(CO)<sub>3</sub>]<sub>2</sub> dimer rapidly following a photo-induced one-electron reduction by a photosensitized [Ru(dmb)<sub>3</sub>]<sup>2+</sup> complex. Time-resolved experiments estimate the dimerization rate constant to be rapid, with  $2k_{\text{dim}} = 1.3 \pm 0.1 \times 10^9 \text{ M}^{-1}\text{s}^{-1}$ .<sup>21</sup> The authors<sup>18</sup> suggested a monomeric, five-coordinate manganese radical species [Mn(bpy)(CO)<sub>3</sub>]<sup>•</sup> results from photoinduced homolytic dimer cleavage; this radical is also proposed to be the active catalyst for reduction of CO<sub>2</sub>, with HCO<sub>2</sub>H as the major product. Analogous Mn radical species have been previously detected as a product of the photoassisted cleavage of Mn–Mn bonds.<sup>25-27</sup>



In a recent report we described the electrocatalytic behavior of  $\text{Mn}(\text{CN})(\text{bpy})(\text{CO})_3$ , which was found to be a competent catalyst for the electrocatalytic reduction of  $\text{CO}_2$  with high Faradaic yield for CO ( $98 \pm 3\%$ ).<sup>28</sup> With the substitution of the  $\text{Br}^-$  ligand for the pseudohalogen cyanide ( $\text{CN}^-$ ), the mechanism of catalytic  $\text{CO}_2$  reduction was altered from that described above. Specifically,  $\text{CN}^-$  did not readily dissociate like  $\text{Br}^-$  following a one-electron reduction, mitigating the formation of the Mn–Mn dimer species as an intermediate to the active state,  $[\text{Mn}(\text{bpy})(\text{CO})_3]^-$ , which was instead generated after a disproportionation reaction. As a result, we were interested in investigating the photocatalytic properties of  $\text{Mn}(\text{CN})(\text{bpy})(\text{CO})_3$  to see if the alternate reduction mechanism would also impact the distribution of two-electron products ( $\text{H}_2$ , CO and  $\text{HCO}_2\text{H}$ ).<sup>18</sup>

Herein, the use of  $\text{Mn}(\text{CN})(\text{bpy})(\text{CO})_3$  as part of a photocatalytic system for the reduction of  $\text{CO}_2$  is reported. The results suggest that, similar to the previously described electrochemical mechanism,  $\text{Mn}(\text{CN})(\text{bpy})(\text{CO})_3$  undergoes a disproportionation reaction involving two singly reduced species,  $[\text{Mn}(\text{CN})(\text{bpy})(\text{CO})_3]^-$ , to produce one equivalent of the catalytically active species  $[\text{Mn}(\text{bpy})(\text{CO})_3]^-$  and one equivalent of  $\text{Mn}(\text{CN})(\text{bpy})(\text{CO})_3$ . Indeed, under a variety of experimental conditions  $\text{Mn}(\text{CN})(\text{bpy})(\text{CO})_3$  is capable of photocatalytically converting  $\text{CO}_2$  to both CO and  $\text{HCO}_2\text{H}$ , although at lower rates than previously reported for  $\text{MnBr}(\text{bpy})(\text{CO})_3$ . Interestingly, the preferred catalytic product shifts from CO to  $\text{HCO}_2\text{H}$  when changing the solvent from MeCN to DMF. Supplementary electrochemical and infrared spectroelectrochemical studies support the disproportionation mechanism, and indicate that the DMF-TEOA mixture is non-innocent with respect to the production of  $\text{HCO}_2\text{H}$ . This is noteworthy because many studies have focused on the electro- and photocatalytic performance of molecular catalysts related to  $\text{MnX}(\text{bpy})(\text{CO})_3$ <sup>6-11, 18-19</sup>, but few studies investigate the role of solvent.<sup>10, 29-30</sup> Indeed, some reports note that DMF can be hydrolyzed to produce formate either during photocatalysis or during analysis if significant amounts of water are present.<sup>29-30</sup> Some studies suggest that dimethylacetamide (DMA) is a better alternative of DMF for photocatalytic reduction of  $\text{CO}_2$  as DMA does not hydrolyze to give formate.

## 2.2 Results and Discussion

### 2.2.1 Photocatalytic Experiments

Thirty one photocatalytic experiments with different reaction conditions were conducted and the results are summarized in **Table 2.1** and **Table 2.2**. In a typical photocatalytic experiment – adapted from a previous report<sup>19</sup> – a quartz cell of known volume was charged with solvent mixtures of acetonitrile (MeCN) and triethanolamine (TEOA) (4:1 v/v) or dimethylformamide (DMF) and TEOA (4:1 v/v) that contained Mn(CN)(bpy)(CO)<sub>3</sub>, [Ru(dmb)<sub>3</sub>]<sup>2+</sup> as a photosensitizer, and 1-benzyl-1,4-dihydronicotinamide (BNAH) as a sacrificial reductant. After irradiation at 470 nm with an LED laser, the gaseous products (CO, H<sub>2</sub>) were quantified by GC and liquid products (HCO<sub>2</sub>H) with <sup>1</sup>H NMR (See Experimental Methods). A key finding is that the main product of the photochemical reaction was HCO<sub>2</sub>H in the DMF-TEOA solvent system, while CO was the primary product in MeCN-TEOA, *vide infra*.

**Table 2.1** Summary of Catalytic Experiments for Photocatalysis.

Entry	Mn Catalyst/ mM	Ru Photosensitizer/ mM	Irradiation Time / h	HCO <sub>2</sub> H- TON	CO- TON	H <sub>2</sub> - TON	HCO <sub>2</sub> H- Φ	CO- Φ
Catalytic Experiments in DMF-TEOA								
1	0.1	0.1	15	36.29	3.90	0.64	0.0096	0.001
2	0.5	0.5	15	21.16	3.17	0.45	0.0312	0.0047
3	1.0	1.0	15	9.50	2.28	0.37	0.0272	0.0065
4	0.1	0.1	6	16.46	2.76	0.20	0.011	0.0018
5	0.5	0.5	6	10.92	0.92	0.25	0.0387	0.0033
6	1.0	1.0	6	5.18	0.83	0.07	0.033	0.0053
Catalytic Experiments in MeCN-TEOA								
7	0.1	0.1	15	4.52	7.87	0.56	0.0011	0.002
8	0.5	0.5	15	2.05	5.26	0.24	0.0027	0.0069
9	1.0	1.0	15	1.16	3.21	0.17	0.0029	0.008
10	0.1	0.1	6	0.00	4.65	0.27	0.00	0.0032
11	0.5	0.5	6	0.00	3.35	0.14	0.00	0.0112
12	1.0	1.0	6	0.00	3.14	0.14	0.00	0.0207
Variable Concentration Studies in DMF-TEOA								
13	0.1	0.5	15	129.87	9.08	1.20	0.0262	0.0018
14	0.1	1.0	15	127.36	7.10	1.55	0.0318	0.0018
15	1.0	0.5	15	5.79	3.03	0.24	0.0144	0.007
Variable Concentration Studies in MeCN-TEOA								
16	0.1	0.5	15	8.08	19.02	1.42	0.0021	0.0048
17	0.1	1.0	15	9.01	21.47	1.31	0.0022	0.0053
18	1.0	0.5	15	1.38	4.20	0.18	0.003	0.01

All runs were sparged with CO<sub>2</sub> for 30 mins prior irradiation with 470 nm monochromatic light for 15 h.

**Table 2.2** Summary of Control Experiments for Photocatalysis.

Entry	Mn Catalyst/ mM	Ru Photosensitizer/ mM	Irradiation Time / h	HCO <sub>2</sub> H- TON	CO- TON	H <sub>2</sub> - TON	HCO <sub>2</sub> H- Φ	CO- Φ
Control Reactions in DMF								
19	0.5	0	CO <sub>2</sub>	1.89	2.10	0.00	0.0022	0.0025
20	0	0.5	CO <sub>2</sub>	5.66	1.49	2.84	0.0069	0.0018
21 <sup>#</sup>	0.5	0.5	CO <sub>2</sub>	0.00	5.81	0.26	0.00	0.0082
22 <sup>@</sup>	0.5	0.5	Ar	2.63	/	/	/	/
23	0.5	0.5	Ar	3.82	1.54	7.82	0.0047	0.0018
24	0	0.5	Ar	3.15	0.87	1.32	0.004	0.0011
25	0.5	0	Ar	2.19	2.25	0.00	0.003	0.003
26 <sup>#</sup>	0.5	0.5	Ar	0.00	2.44	1.40	0.00	0.0021
Control Reactions in MeCN								
27	0.5	0	CO <sub>2</sub>	0.00	2.04	0.00	0.00	0.0024
28	0	0.5	CO <sub>2</sub>	0.72	0.60	1.23	0.0009	0.0008
29 <sup>#</sup>	0.5	0.5	CO <sub>2</sub>	0.00	2.18	0.00	0.00	0.0025
30	0.5	0.5	Ar	0.55	2.20	4.40	0.0007	0.0026
31 <sup>#</sup>	0.5	0.5	Ar	0.00	2.39	1.37	0.00	0.002

All runs were irradiated with 470 nm monochromatic light for 15 h. <sup>#</sup> TEOA is not used in the solvent system. <sup>@</sup> Irradiation time = 0 h.

In the following sections we highlight two conclusions that are supported by these experimental results: i) Mn(CN)(bpy)(CO)<sub>3</sub> follows a disproportionation mechanism under photocatalytic conditions, and ii) varying the solvent system from DMF-TEOA to MeCN-TEOA affects the product distribution between HCO<sub>2</sub>H and CO. We discuss the origin of these conclusions and introduce further experimental results in support.

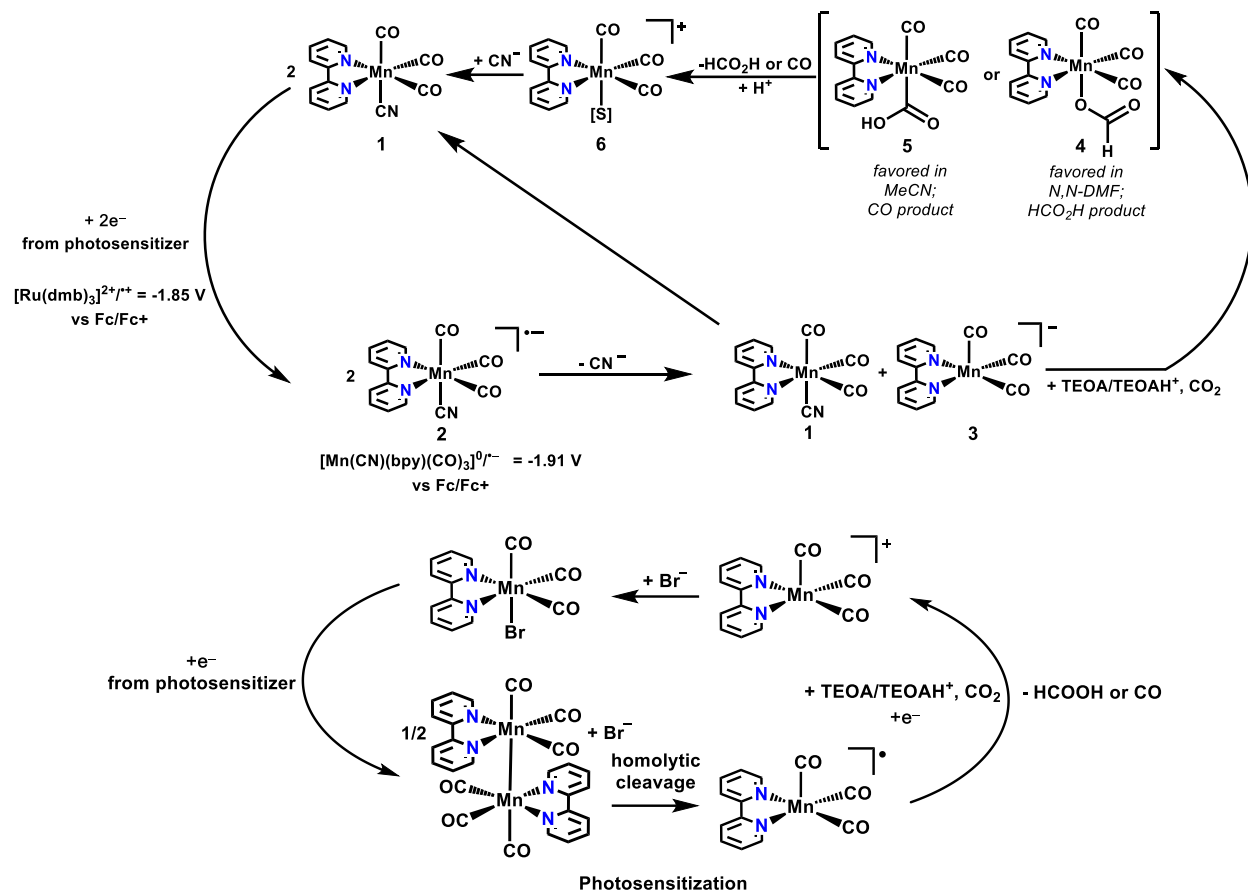
## 2.2.2 Disproportionation Mechanism

In **Scheme 2.1**, we present a proposed mechanism for the photocatalytic reduction of CO<sub>2</sub> by Mn(CN)(bpy)(CO)<sub>3</sub> based on the photocatalytic results presented above and additional experiments detailed below. In the photosensitization step, the reduced [Ru(dmb)<sub>3</sub>]<sup>1+</sup> ([Ru(dmb)<sub>3</sub>]<sup>2+\*/+</sup> = -1.85 V vs Fc/Fc+) transfers an electron to the ligand of Mn(CN)(bpy)(CO)<sub>3</sub> (species **1**), forming a [Mn(CN)(bpy)(CO)<sub>3</sub>]<sup>1-</sup> species, **2** [eqn. 1 in **Scheme 2.2**; [Mn(CN)(bpy)(CO)<sub>3</sub>]<sup>0/\*-</sup> = -1.91 V vs Fc/Fc+].<sup>1 28, 31-34</sup> The reduced photosensitizer [Ru(dmb)<sub>3</sub>]<sup>1+</sup> is capable of driving catalysis at this potential, but at a diminished rate. Indeed,

<sup>1</sup> [Ru(dmb)<sub>3</sub>]<sup>2+\*/+</sup> = 0.24 V; BNAH<sup>0/\*+</sup> = 0.20 V vs Fc/Fc+

in comparison to  $\text{MnBr}(\text{bpy})(\text{CO})_3$  much lower rates are observed.<sup>18</sup> Two equivalents of **2** can undergo disproportionation to generate the active  $[\text{Mn}(\text{bpy})(\text{CO})_3]^-$  anion, **3**, and the starting material  $\text{Mn}(\text{CN})(\text{bpy})(\text{CO})_3$  [eqn. 2 in **Scheme 2.2**]. It is presumed that  $\text{HCO}_2\text{H}$  formation in this mechanism results from the protonation of species **3** (by TEOA,  $\text{TEOA}^{*+}$ , or TEOAH) to generate a Mn hydride, an expected intermediate before  $\text{CO}_2$  insertion, during catalysis.<sup>19, 35-39</sup> A preference for  $\text{HCO}_2\text{H}$  is observed in DMF-TEOA solution, indicating that the formation of an intermediate hydride species may be favored relative to MeCN.<sup>19</sup> It is also possible for species **3** to form a hydroxycarbonyl species (preferred in MeCN-TEOA) through a direct attack of  $\text{CO}_2$  with subsequent protonation by TEOA or  $\text{TEOAH}^+$  (generated by the deprotonation of  $\text{BNAH}^{*+}$ , the expected sacrificial co-product from photosensitization).<sup>40-41</sup> The resulting  $\eta^1\text{-COOH}$  coordination mode generally yields CO as a product.<sup>42-44</sup> We note another formate formation pathway. It is possible that species **2** may abstract a hydrogen atom from TEOA or  $\text{BNAH}^{*+}$  to generate a hydride species (with presumptive  $\text{CN}^-$  loss) and that the photosensitizer is observed to generate formate in control reactions by an ostensibly analogous mechanism.<sup>45</sup> This presumptive hydride species generated by **2** could also then react with  $\text{CO}_2$  to give  $\text{HCO}_2\text{H}$ . Such reaction pathways are expected to be in competition with the disproportionation mechanism and eventual catalysis by **3**.

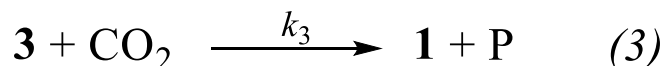
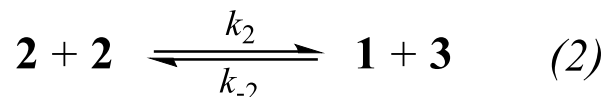
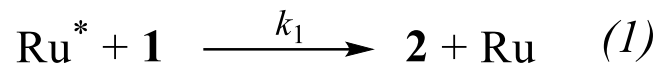
The proposed mechanism for the photocatalytic reduction of  $\text{CO}_2$  by  $\text{MnBr}(\text{bpy})(\text{CO})_3$  based on the previous literature<sup>18-19</sup> is also presented for comparison (**Scheme 2.1**). In this reaction scheme, the formation of a Mn–Mn bonded dimer is an intermediate step to the formation of a neutral five-coordinate radical species from photoassisted bond cleavage. It is likely at this point in the reaction that the photosensitizer provides the additional electron required to complete the reduction of  $\text{CO}_2$ . The redox potential for  $[\text{Mn}(\text{bpy})(\text{CO})_3]^{*+}$  has not been directly measured, but when using the structural analogue  $\text{MnBr}(6,6'\text{-dimesityl-2,2'-bipyridine})(\text{CO})_3$ , the first reduction becomes a two electron process at  $-1.55$  V vs  $\text{Fc}/\text{Fc}^+$  by the prevention of dimerization, suggesting this can be considered the approximate maximum potential required to generate the anion.<sup>24</sup>



**Scheme 2.1** Proposed mechanisms for the formation of  $\text{HCO}_2\text{H}$  and/or  $\text{CO}$  from the photocatalytic reaction with  $\text{Mn}(\text{CN})(\text{bpy})(\text{CO})_3$  and  $\text{MnBr}(\text{bpy})(\text{CO})_3$ <sup>18-19</sup>, respectively.

In both the DMF-TEOA and MeCN-TEOA solvent systems, the turnover number (TON) for  $\text{HCO}_2\text{H}$ ,  $\text{CO}$ , and  $\text{H}_2$  decreased as the concentration of the Mn complex increased (entries 2, 8, 15, and 18). This observation is consistent with the proposed mechanism of photocatalytic  $\text{CO}_2$  reduction involving an intermediate disproportionation step, *vide infra*.<sup>28</sup> Two equivalents of  $\text{Mn}(\text{CN})(\text{bpy})(\text{CO})_3$  are required to be reduced by one electron each from  $[\text{Ru}(\text{dmb})_3]^{2+}$  before a disproportionation reaction yields one equivalent each of the active catalyst  $[\text{Mn}(\text{bpy})(\text{CO})_3]^-$  and  $\text{Mn}(\text{CN})(\text{bpy})(\text{CO})_3$ . At high concentrations of  $\text{Mn}(\text{CN})(\text{bpy})(\text{CO})_3$  and  $[\text{Ru}(\text{dmb})_3]^{2+}$ , mass transport limitations would be expected to affect this process, and limit the overall efficiency. This can be shown in a simplified kinetic description of the overall reaction as shown in Scheme 2.2 below. Inhibition by increasing concentration of  $\text{Mn}(\text{CN})(\text{bpy})(\text{CO})_3$  is an expected

consequence of the disproportionation reaction in eqn. 2, if it is assumed to be the rate-limiting step for the formation of **3** and the reaction of **3** with CO<sub>2</sub> is assumed to be fast relative to  $k_{-2}$ .



**Scheme 2.2** Simplified description of the elementary steps in photochemical reduction of CO<sub>2</sub> by Mn(CN)(bpy)(CO)<sub>3</sub>.

This mechanism is further validated by the observation that the TON increases when the ratio of Ru photosensitizer to Mn complex (entries 1, 2, 7, 8, 13 – 18) is increased. The observed increase in catalysis levels off after the ratio of [Ru(dmb)<sub>3</sub>]<sup>2+</sup> : Mn(CN)(bpy)(CO)<sub>3</sub> reaches 5 : 1. At this ratio, relative to experiments with equimolar amounts of photosensitizer and catalyst (entries 1 – 12), there is a 3.6× enhancement in the HCO<sub>2</sub>H-TON and 2.3× in the CO-TON in the DMF-TEOA system. Likewise, the MeCN-TEOA system shows a 1.8× increase in the HCO<sub>2</sub>H-TON and 2.4× in the CO-TON. As shown in Eqn (1) of **Scheme 2.2**, an increased amount of photosensitized Ru (Ru<sup>\*</sup>) relative to Mn(CN)(bpy)(CO)<sub>3</sub> in solution could generate more equivalents of the singly reduced species [Mn(CN)(bpy)(CO)<sub>3</sub>]<sup>-</sup> **2** (**Scheme 2.2**). Therefore, more equivalents of the active anion [Mn(bpy)(CO)<sub>3</sub>]<sup>-</sup> **3**, would be formed in Eqn (2), resulting in an increase in catalyst TONs [Eqn (3)]. After the optimized ratio is reached, the concentration of photosensitizer is no longer a limiting factor and the observed TONs do not change at higher ratios of [Ru(dmb)<sub>3</sub>]<sup>2+</sup> : **1**.

Lastly, photodecomposition (mole equivalent of CO ≈ 2 relative to [Mn(CN)(bpy)(CO)<sub>3</sub>]) in both the MeCN-TEOA and DMF-TEOA solvent systems was observed when there was no [Ru(dmb)<sub>3</sub>]<sup>2+</sup>, CO<sub>2</sub>, or TEOA present (entries 19 – 31 in Table 2.2). These experiments also showed that [Ru(dmb)<sub>3</sub>]<sup>2+</sup> contributed to H<sub>2</sub>, HCO<sub>2</sub>H, and CO production, although in a much lower quantity than Mn(CN)(bpy)(CO)<sub>3</sub> (entries 20, 24 and 28).<sup>18-19, 46</sup>

### 2.2.3 Solvent Effects

The observation that the photocatalytic system is more selective for CO in MeCN-TEOA than in DMF-TEOA (which produces more HCO<sub>2</sub>H) suggests the possibility of solvent interactions during the photochemical mechanism. In control reactions with the DMF-TEOA solvent system (entries 19 – 20, 22 – 25), we note that there is always a small amount of residual HCO<sub>2</sub>H which is independent of photocatalysis. The lack of residual HCO<sub>2</sub>H in the absence of TEOA (entries 21 and 26) suggests the TEOA is vital for the production of HCO<sub>2</sub>H in DMF. Furthermore, in the case of entry 22 (a control work-up of entry 23 before any irradiation occurred), HCO<sub>2</sub>H was detected by <sup>1</sup>H NMR immediately after mixing the solution in the dark. No HCO<sub>2</sub>H was found in the MeCN-TEOA system in analogous experiments. Residual HCO<sub>2</sub>H is *only* observed from the interaction between DMF and TEOA; this observation is consistent with some recent reports: Vos<sup>29</sup> and Ishida<sup>30</sup> pointed out that DMF hydrolyzes spontaneously to give HCO<sub>2</sub>H in the presence of water or TEOA. A plot (**Figure 2.5**) of HCO<sub>2</sub>H-TON vs. the concentration of Mn(CN)(bpy)(CO)<sub>3</sub> shows high linearity for both the 15 h and 6 h irradiation times in the DMF-TEOA solvent system, suggesting that the amount of HCO<sub>2</sub>H formed from DMF and TEOA interaction is insignificant under catalytic conditions. Solvent decomposition alone does not explain the large difference in product distribution between the two solvent systems.

To further understand the role of solvent in product selectivity, cyclic voltammetry (CV) was performed both under Ar and CO<sub>2</sub> saturation. In **Figure 2.1**, scans were performed with Mn(CN)(bpy)(CO)<sub>3</sub> (1 mM) and tetrabutylammonium hexafluorophosphate (TBAPF<sub>6</sub>; 0.1 M) as the supporting electrolyte in DMF under argon (Ar) at scan rates from 100 mV/s to 2000 mV/s. The first one-electron, quasireversible redox feature is observed at -1.95 V vs. Fc/Fc+ (E<sub>pc</sub>) with peak-to-peak separation (ΔE<sub>p</sub>) of 74 mV. As shown in **Figure 2.7**, the addition of TEOA to the solution under Ar showed a slight current attenuation (0.7×) of the peak current of the first reduction wave (ca. -1.95 V vs Fc/Fc+), which is attributed to dilution. When CO<sub>2</sub> is present, the peak current increased to 2.1× that observed under Ar. The current enhancement is consistent with the catalytic reduction of CO<sub>2</sub> by a [Mn(bpy)(CO)<sub>3</sub>]<sup>-</sup> active species.<sup>28</sup> The process is

diffusion-limited as indicated by the linear relationship between the square root of the scan rate and the peak current (**Figure 2.6**).

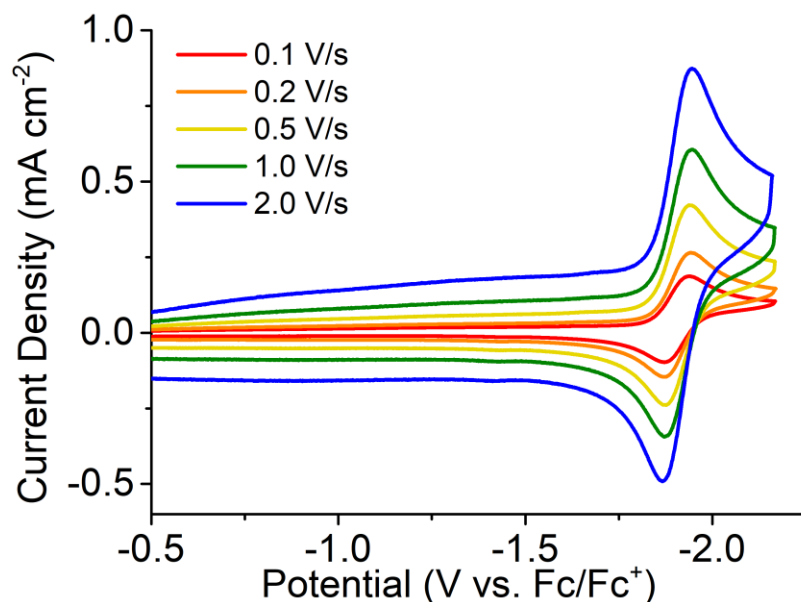


**Figure 2.1** Cyclic voltammetry of  $\text{Mn}(\text{CN})(\text{bpy})(\text{CO})_3$  under Ar saturation. Conditions: 1 mM  $\text{Mn}(\text{CN})(\text{bpy})(\text{CO})_3$  in 0.1 TBAPF<sub>6</sub>/DMF; WE: GC; CE: Pt; RE: Ag/Cl with Fc as internal reference.

Interestingly, when TEOA was added to dry MeCN, the redox feature became less reversible and the peak current showed a slight enhancement (2×) under Ar (**Figure 2.8**). Such irreversibility is not observed in the absence of TEOA.<sup>28</sup> The presence of CO<sub>2</sub> increased both the irreversibility of the wave and the peak current, suggesting that the interaction of MeCN with TEOA and the reduced species is relevant at this potential, but not for DMF. This provides important clues for the different product distributions between two solvent systems observed during photocatalysis.



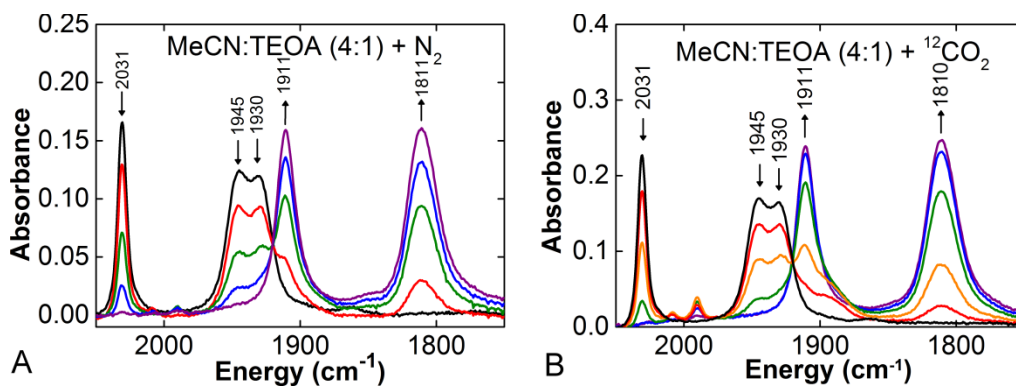


**Figure 2.2** Infrared spectra of  $\text{Mn}(\text{CN})(\text{bpy})(\text{CO})_3$  at controlled potentials (a) in dry MeCN with TEOA under  $\text{N}_2$ , and (b) in dry MeCN with TEOA under  $\text{CO}_2$ .

Infrared spectroelectrochemistry (IR-SEC) was used to monitor the microscale electrolysis of  $\text{Mn}(\text{CN})(\text{bpy})(\text{CO})_3$  in the DMF-TEOA and MeCN-TEOA solvent systems by IR spectroscopy. IR-SEC allows the starting, intermediate, and product species in solution to be characterized as a function of potential and time.<sup>20, 28</sup> In the experiment, a solution of 4 mM  $\text{Mn}(\text{CN})(\text{bpy})(\text{CO})_3$  in 0.1 M TBAPF<sub>6</sub>/MeCN or DMF-TEOA (4 : 1) inside the IR-SEC cell was put under catalytic conditions (ca.  $-1.9$  V vs Fc/Fc+) over the course of 5 min under Ar or  $\text{CO}_2$  with glassy carbon as working electrode, platinum as counter electrode and silver as pseudoreference electrode. When the potential of the IR-SEC cell is shifted stepwise from resting to that of the first reduction in MeCN with added TEOA and  $\text{Mn}(\text{CN})(\text{bpy})(\text{CO})_3$  ( $\sim -1.9$  V vs Fc/Fc+), two new bands appear at  $1911\text{ cm}^{-1}$  and  $1810\text{ cm}^{-1}$  with the concomitant disappearance of the original bands (**Figure 2.2a**), which are assigned to  $[\text{Mn}(\text{bpy})(\text{CO})_3]^-$ . A band of low intensity appears during reduction at  $1990\text{ cm}^{-1}$ , corresponding to the high frequency carbonyl mode of  $[\text{Mn}(\text{CN})(\text{bpy})(\text{CO})_3]^-$ . When the MeCN-TEOA solution of  $\text{Mn}(\text{CN})(\text{bpy})(\text{CO})_3$  is sparged briefly with  $\text{CO}_2$  and this experiment is repeated, a band for  $\text{CO}_2$  is observed at  $2337\text{ cm}^{-1}$ . At the potential of the first reduction this band decreases in intensity, consistent with catalytic consumption of  $\text{CO}_2$  (**Figure 2.9**). Similar to the case when TEOA is present under  $\text{N}_2$  saturation conditions, the only Mn carbonyl bands observed are at  $1911\text{ cm}^{-1}$  and  $1810\text{ cm}^{-1}$ , consistent with the formation of the active catalyst species  $[\text{Mn}(\text{bpy})(\text{CO})_3]^-$ .

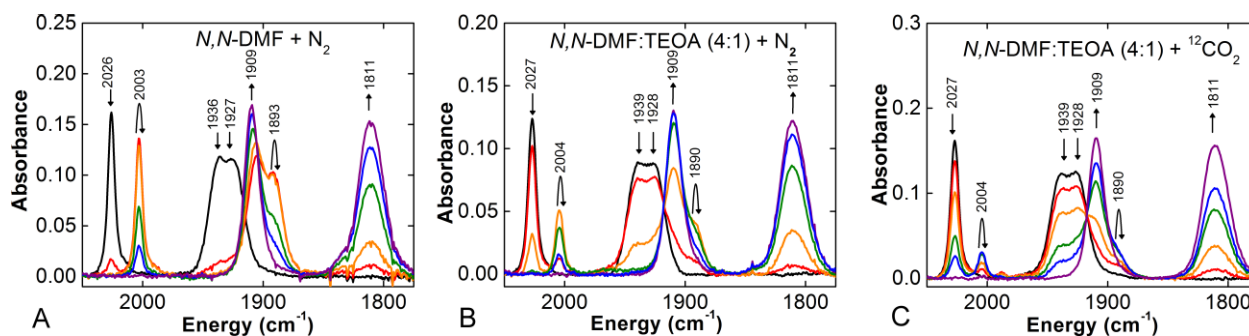


**Figure 2.3** Infrared spectra of  $\text{Mn}(\text{CN})(\text{bpy})(\text{CO})_3$  at controlled potentials (a) in dry DMF under  $\text{N}_2$ , (b) in dry DMF with TEOA under  $\text{N}_2$ , and (c) in dry DMF with TEOA under  $\text{CO}_2$ .

By comparison, conducting the same experiments in DMF showed a similar redshift of the Mn carbonyl stretching modes to the active catalyst at the potential of the first reduction, albeit at a slower rate on the experimental timescale ( $\sim 5$  minutes, **Figure 2.10** and **Figure 2.3a**). The singly reduced species,  $[\text{Mn}(\text{CN})(\text{bpy})(\text{CO})_3]^{-}$ , is more stable under these conditions relative to the results in MeCN. The IR bands visible at resting potential (2026, 1936, and 1927  $\text{cm}^{-1}$ ) almost completely shift to lower frequencies (2003, 1905, and 1893  $\text{cm}^{-1}$ ) when the cell potential is changed from resting to that of the first reduction ( $\sim -1.9$  V vs Fc/Fc $^{+}$ ;  $\sim 1$  min). Previous computations predicted that in MeCN  $[\text{Mn}(\text{CN})(\text{bpy})(\text{CO})_3]^{-}$  would have observable IR modes at 2010, 1909, and 1895  $\text{cm}^{-1}$ ; the high frequency mode was experimentally observed at 2007  $\text{cm}^{-1}$ .<sup>28</sup> The presence of TEOA and  $\text{CO}_2$  decreases the stability of  $[\text{Mn}(\text{CN})(\text{bpy})(\text{CO})_3]^{-}$ , as evidenced by a more rapid shift to  $[\text{Mn}(\text{bpy})(\text{CO})_3]^{-}$  on this timescale (1909 and 1811  $\text{cm}^{-1}$ ;  $\sim 5$  minutes). In comparison to MeCN-TEOA, however, a more significant amount (as estimated by IR intensity) of the singly reduced species is still observed under these conditions.<sup>19</sup> This difference in the relative stability of  $[\text{Mn}(\text{CN})(\text{bpy})(\text{CO})_3]^{-}$  in the MeCN- and DMF-based solvent systems could explain the observed product selectivities. The higher stability of species **2** observed in DMF would allow more time for competing hydrogen atom abstraction pathways involving TEOA or  $\text{BNAH}^{+}$  to generate  $\text{HCO}_2\text{H}$  via a Mn hydride species.

The UV-Vis spectra of  $\text{Mn}(\text{CN})(\text{bpy})(\text{CO})_3$  also revealed the difference of interaction of the catalyst and the solvent. As shown in **Figure 2.11**, upon the addition of Verkade's base (Vkd base) to

solution in the absence of TEOA, the band at ~370 nm diminishes in intensity and broadens, indicating the disappearance of  $\text{Mn}(\text{CN})(\text{bpy})(\text{CO})_3$ . On the other hand, there is a slight diminishment observed with the addition of TEOA only, likely due to a decrease in the concentration of  $\text{Mn}(\text{CN})(\text{bpy})(\text{CO})_3$  from dilution. Such observation is seen in both MeCN and DMF solvent systems. This is another piece of evidence showing the presence of TEOA affecting the reaction of catalyst.

## 2.3 Conclusion

Using  $[\text{Ru}(\text{dmb})_3]^{2+}$  as a photosensitizer in dry DMF-TEOA or MeCN-TEOA solvent mixtures with  $\text{Mn}(\text{CN})(\text{bpy})(\text{CO})_3$  as a catalyst results in photocatalytic  $\text{CO}_2$  reduction through an intermediate disproportionation mechanism. The formation of  $\text{HCO}_2\text{H}$  and  $\text{CO}$  from  $\text{CO}_2$  decreases with increasing concentration of the Mn complex from 0.1 mM to 1.0 mM, while the formation of products increases with a higher ratio of  $[\text{Ru}(\text{dmb})_3]^{2+} : \text{Mn}(\text{CN})(\text{bpy})(\text{CO})_3$ . Control reactions have also demonstrated that the DMF solvent is not innocent in the formation of  $\text{HCO}_2\text{H}$  in the presence of TEOA. Even in the dark, DMF and TEOA generate a measurable amount of  $\text{HCO}_2\text{H}$ . Supplemental CV and IR-SEC studies indicate that although the reduction mechanism in MeCN and DMF is similar, there is an observable difference in stability of the  $[\text{Mn}(\text{CN})(\text{bpy})(\text{CO})_3]^-$ . It is clear from these studies that the process of photosensitization by  $[\text{Ru}(\text{dmb})_3]^{2+}$  with BNAH as a sacrificial reductant and the role of TEOA are mechanistically complex and require further investigation to rationally optimize the overall reaction.

## 2.4 Experimental

### 2.4.1 General.

All reagents were obtained from commercial suppliers and used as received unless otherwise noted. Acetonitrile (MeCN) was obtained from a solvent system under argon (Ar); dimethylformamide (DMF) and methanol were dried over molecular sieves (3 Å) for three days under  $\text{N}_2$  prior to use. Triethanolamine (TEOA) was stored under  $\text{N}_2$ . Tetrabutylammonium hexafluorophosphate ( $\text{TBAPF}_6$ ) was recrystallized in

MeOH twice and dried at 90°C before use.  $\text{Mn}(\text{CN})(\text{bpy})(\text{CO})_3$  was synthesized according to literature procedure.<sup>28</sup>

<sup>1</sup>H NMR spectra were recorded on a Varian Mercury Plus 400 MHz spectrometer and NMR chemical shifts were referenced to the proton signal of ferrocene. Fourier transform infrared (FTIR) spectra were recorded on a ThermoNicolet 6700 spectrophotometer running OMNIC software. Absorption spectra were recorded on a CARY 300 Bio UV–Vis spectrophotometer with a quartz cuvette (1 cm pathlength).

#### 2.4.2 Photochemical Reactions

A solution of acetonitrile (MeCN) and triethanolamine (TEOA) (~20 mL; 4:1 v/v) or dimethylformamide (DMF) and TEOA (~20 mL; 4:1 v/v), which contained  $\text{Mn}(\text{CN})(\text{bpy})(\text{CO})_3$ ,  $[\text{Ru}(\text{dmb})_3]^{2+}$  as a photosensitizer, and 1-benzyl-1,4-dihydronicotinamide (BNAH, 0.1 M) as a sacrificial reductant was prepared in a 36 mL quartz cell (NSG Precision Cell, Inc.; pathlength = 2 cm) sealed with a rubber septum. In the concentration study, solutions containing 0.1 mM, 0.5 mM and 1.0 mM of both  $\text{Mn}(\text{CN})(\text{bpy})(\text{CO})_3$  and  $[\text{Ru}(\text{dmb})_3]^{2+}$  were prepared and measured. The solution was sparged with dry Ar or CO<sub>2</sub> gases for 30 minutes prior to irradiation. The solution was irradiated with a 470 nm LED (ThorLabs, Inc.; bandwidth FWHM = 25 nm) with temperature maintained at  $25.0 \pm 0.1^\circ\text{C}$  and constant stirring throughout the experiment. The light intensity was measured using a NOVA II power meter.

#### 2.4.3 Product Analysis from Photocatalysis<sup>19</sup>

The gaseous products, H<sub>2</sub> and CO, were analyzed by GC-TCD (Hewlett-Packard 7890A Series gas chromatograph) with two molsieve columns (30 m × 0.53 mm × 25 μm film). The 1 mL injection was split between two columns, which use N<sub>2</sub> and He as carrier gases to measure the quantity of H<sub>2</sub> and CO, respectively. Turnover numbers (TON) for the product were calculated as the moles of product divided by the moles of catalyst.

The liquid products were analyzed by a previously reported <sup>1</sup>H NMR (400 MHz Mercury NMR Instrument) method<sup>12</sup>: a known amount of ferrocene (5-8 mg) was added to the irradiated solution in a 5.0 mL volumetric flask to serve as an internal standard, and the solution was sonicated for 10 minutes. A 1.0

mL syringe was used to transfer a 0.8 mL aliquot of the resulting solution to a 2.0 mL volumetric flask containing 0.1 mmol of Verkade's base (2,8,9-Triisopropyl-2,5,8,9-tetraaza-1-phosphabicyclo[3,3,3]undecane, Vkd base). CD<sub>3</sub>CN was added to the 2.0 mL mark and the resulting solution was sonicated for another 10 minutes. The solution was divided into three NMR samples and each one was run for 128 scans on a Mercury 400 MHz spectrometer at 298K. The whole work-up process was carried out in the dark. The ferrocene peak is usually found at 4.13 ppm while the formate peak is at around 8.50 ppm (**Figure 2.4**). The areas of the peaks were integrated using the software Origin. The concentration of formate is calculated using a calibration curve made from various ratio of 99% formic acid and ferrocene with the same workup procedure (**Figure 2.5**).

#### 2.4.4 Cyclic Voltammetry (CV)

A series of CV studies were performed using a BASi Epsilon potentiostat. A 3 mm diameter glassy carbon working electrode (BASi), a platinum (Pt) wire counter electrode and a silver/silver chloride (Ag/AgCl) wire separated from the bulk solution by a CoralPor tip as a pseudoreference electrode were used in a single compartment cell for all experiments. Experiments were run with and without ferrocene as an internal reference. Electrolyte solutions were composed of dry MeCN or DMF, containing 1 mM of catalyst, 0.1 M TBAPF<sub>6</sub> as supporting electrolyte, and with or without 1.88 M TEOA (solvent : TEOA = 4 : 1 v/v) unless otherwise noted. The electrolyte was purged with Ar or CO<sub>2</sub> for before cyclic voltammograms were recorded and stirred between successive experiments.

#### 2.4.5 Infrared Spectroelectrochemistry

The experimental method, cell design and setup of the IR-SEC cell have been reported previously.<sup>20</sup> All measurements were made with a Pine Instrument Company model AFCBP1 bipotentiostat. The IR-SEC cell is composed of GC working electrode, Ag pseudoreference electrode, and Pt counter electrode. All potentials were referenced to the pseudoreference Ag/Ag<sup>+</sup>, ~+200 mV higher than the Fc/Fc<sup>+</sup> couple. The solution containing 4 mM Mn complex and 0.1 M TBAPF<sub>6</sub> in dry MeCN or DMF with or without TEOA (solvent : TEOA = 4 : 1 v/v) was sparged with N<sub>2</sub> or CO<sub>2</sub> and then injected into the IR-SEC cell to

form a thin liquid layer for bulk electrolysis. The potential was changed stepwise and the solution was monitored with Fourier transform reflectance IR off the electrode surface over time.

#### 2.4.6 Preparation of Ru(dmb)<sub>3</sub>(PF<sub>6</sub>)<sub>2</sub>

The photosensitizer, Ru(dmb)<sub>3</sub>(PF<sub>6</sub>)<sub>2</sub> (dmb = 4,4'-dimethyl-2,2'-bipyridine) was synthesized from RuCl<sub>3</sub>·xH<sub>2</sub>O (91.7 mg, 0.169 mmol) and dmb (46.5 mg, 0.255 mmol) according to literature<sup>47</sup> and further purified by recrystallization with acetone-diethyl ether. All characterization was consistent with previous reports; yield: 55.2 mg (34.6%).

### 2.5 Acknowledgement

**Chapter 2**, in full, comes directly from a manuscript entitled: “Photochemical Reduction of Carbon Dioxide Using a CN-modified fac-Mn(bpy)(CO)<sub>3</sub> Catalyst.” by Cheung, P.L.; Machan, C.W.; Malkhasian, A.; Agarwal, J. and Kubiak, C.P., which has been published in *Inorg. Chem.* **2016**, *55*, 319–3198. The dissertation author is a primary co-author of this manuscript. This work was supported by the Air Force Office of Scientific Research through AFOSR through a Basic Research Initiative (BRI) Grant (No. FA9550-12-1-0414). J.A. acknowledges support from the NSF (CHE-1361178).

### 2.6 References

1. Inoue, T.;Fujishima, A.;Konishi, S.; Honda, K., Photoelectrocatalytic reduction of carbon dioxide in aqueous suspensions of semiconductor powders. *Nature* **1979**, *277*, 637–638.
2. Hawecker, J.;Lehn, J.-M.; Ziessel, R., Photochemical and Electrochemical Reduction of Carbon Dioxide to Carbon Monoxide Mediated by (2,2' - Bipyridine)tricarbonylchlororhenium(I) and Related Complexes as Homogeneous Catalysts. *Helv. Chim. Acta* **1986**, *69* (8), 1990-2012.
3. Hawecker, J.;Lehn, J. M.; Ziessel, R., Photochemical Reduction of Carbon-Dioxide to Formate Mediated by Ruthenium Bipyridine Complexes as Homogeneous Catalysts. *J. Chem. Soc., Chem. Comm.* **1985**, (2), 56–58.
4. Hawecker, J.;Lehn, J.-M.; Ziessel, R., Efficient photochemical reduction of CO<sub>2</sub> to CO by visible light irradiation of systems containing Re(bipy)(CO)<sub>3</sub>X or Ru(bipy)<sub>3</sub><sup>2+</sup>-Co<sup>2+</sup> combinations as homogeneous catalysts. *J. Chem. Soc., Chem. Commun.* **1983**, 536–538.

5. Willner, I.; Mandler, D.; Riklin, A., Photoinduced carbon dioxide fixation forming malic and isocitric acid. *J. Chem. Soc., Chem. Commun.* **1986**, 1022–1024.
6. Ishida, H.; Terada, T.; Tanaka, K.; Tanaka, T., Photochemical CO<sub>2</sub> Reduction Catalyzed by [Ru(Bpy)<sub>2</sub>(CO)<sub>2</sub>]<sup>2+</sup> Using Triethanolamine and 1-Benzyl-1,4-Dihydronicotinamide as an Electron-Donor. *Inorg. Chem.* **1990**, 29 (5), 905–911.
7. Lehn, J.-M.; Ziessel, R., Photochemical Reduction of Carbon-Dioxide to Formate Catalyzed by 2,2'-Bipyridine-Ruthenium(II) or 1,10-Phenanthroline-Ruthenium(II) Complexes. *J. Organomet. Chem.* **1990**, 382 (1-2), 157–173.
8. Kumar, B.; Smieja, J. M.; Kubiak, C. P., Photoreduction of CO<sub>2</sub> on p-type Silicon Using Re(bipy-Bu<sup>t</sup>)(CO)<sub>3</sub>Cl: Photovoltages Exceeding 600 mV for the Selective Reduction of CO<sub>2</sub> to CO. *J. Phys. Chem. C* **2010**, 114 (33), 14220–14223.
9. Tamaki, Y.; Morimoto, T.; Koike, K.; Ishitani, O., Photocatalytic CO<sub>2</sub> reduction with high turnover frequency and selectivity of formic acid formation using Ru(II) multinuclear complexes. *Proc. Nat. Acad. Sci. U.S.A.* **2012**, 109 (39), 15673–15678.
10. Morimoto, T.; Nakajima, T.; Sawa, S.; Nakanishi, R.; Imori, D.; Ishitani, O., CO<sub>2</sub> Capture by a Rhenium(I) Complex with the Aid of Triethanolamine. *J. Am. Chem. Soc.* **2013**, 135 (45), 16825–16828.
11. Shakeri, J.; Farrokhpour, H.; Hadadzadeh, H.; Joshaghani, M., Photoreduction of CO<sub>2</sub> to CO by a mononuclear Re(I) complex and DFT evaluation of the photocatalytic mechanism. *RSC Adv.* **2015**, 5 (51), 41125–41134.
12. Smieja, J. M.; Sampson, M. D.; Grice, K. A.; Benson, E. E.; Froehlich, J. D.; Kubiak, C. P., Manganese as a Substitute for Rhenium in CO<sub>2</sub> Reduction Catalysts: The Importance of Acids. *Inorg. Chem.* **2013**, 52 (5), 2484–2491.
13. In *CRC Handbook of Chemistry and Physics*, 92nd ed.; Haynes, W. M., Ed. CRC Press: Boca Raton: FL, 2011; pp 2011–2012.
14. Juris, A.; Balzani, V.; Barigelletti, F.; Campagna, S.; Belser, P.; von Zelewsky, A., Ru(II) polypyridine complexes: photophysics, photochemistry, electrochemistry, and chemiluminescence. *Coord. Chem. Rev.* **1988**, 84, 85–277.
15. Matsuoka, S.; Yamamoto, K.; Ogata, T.; Kusaba, M.; Nakashima, N.; Fujita, E.; Yanagida, S., Efficient and selective electron mediation of cobalt complexes with cyclam and related macrocycles in the p-terphenyl-catalyzed photoreduction of carbon dioxide. *J. Am. Chem. Soc.* **1993**, 115 (2), 601–609.
16. Loudet, A.; Burgess, K., BODIPY Dyes and Their Derivatives: Syntheses and Spectroscopic Properties. *Chem. Rev.* **2007**, 107 (11), 4891–4932.
17. Bourrez, M.; Molton, F.; Chardon-Noblat, S.; Deronzier, A., [Mn(bipyridyl)(CO)<sub>3</sub>Br]: An Abundant Metal Carbonyl Complex as Efficient Electrocatalyst for CO<sub>2</sub> Reduction. *Angew. Chem. Int. Ed.* **2011**, 50 (42), 9903–9906.
18. Takeda, H.; Koizumi, H.; Okamoto, K.; Ishitani, O., Photocatalytic CO<sub>2</sub> reduction using a Mn complex as a catalyst. *Chem. Commun.* **2014**, 50 (12), 1491–1493.

19. Fei, H. H.; Sampson, M. D.; Lee, Y.; Kubiak, C. P.; Cohen, S. M., Photocatalytic CO<sub>2</sub> Reduction to Formate Using a Mn(I) Molecular Catalyst in a Robust Metal-Organic Framework. *Inorg. Chem.* **2015**, *54* (14), 6821–6828.
20. Machan, C. W.; Sampson, M. D.; Chabolla, S. A.; Dang, T.; Kubiak, C. P., Developing a Mechanistic Understanding of Molecular Electrocatalysts for CO<sub>2</sub> Reduction using Infrared Spectroelectrochemistry. *Organometallics* **2014**, *33* (18), 4550–4559.
21. Grills, D. C.; Farrington, J. A.; Layne, B. H.; Lyman, S. V.; Mello, B. A.; Preses, J. M.; Wishart, J. F., Mechanism of the Formation of a Mn-Based CO<sub>2</sub> Reduction Catalyst Revealed by Pulse Radiolysis with Time-Resolved Infrared Detection. *J. Am. Chem. Soc.* **2014**, *136* (15), 5563–5566.
22. Riplinger, C.; Sampson, M. D.; Ritzmann, A. M.; Kubiak, C. P.; Carter, E. A., Mechanistic Contrasts between Manganese and Rhenium Bipyridine Electrocatalysts for the Reduction of Carbon Dioxide. *J. Am. Chem. Soc.* **2014**, *136* (46), 16285–16298.
23. Riplinger, C.; Carter, E. A., Influence of Weak Bronsted Acids on Electrocatalytic CO<sub>2</sub> Reduction by Manganese and Rhenium Bipyridine Catalysts. *ACS Catal.* **2015**, *5* (2), 900–908.
24. Sampson, M. D.; Nguyen, A. D.; Grice, K. A.; Moore, C. E.; Rheingold, A. L.; Kubiak, C. P., Manganese Catalysts with Bulky Bipyridine Ligands for the Electrocatalytic Reduction of Carbon Dioxide: Eliminating Dimerization and Altering Catalysis. *J. Am. Chem. Soc.* **2014**, *136* (14), 5460–5471.
25. Meyer, T. J.; Caspar, J. V., Photochemistry of Metal Metal Bonds. *Chem. Rev.* **1985**, *85* (3), 187–218.
26. Allen, D. M.; Cox, A.; Kemp, T. J.; Sultana, Q.; Pitts, R. B., Photochemistry of Some Binuclear Carbonyl-Compounds of Manganese, Rhenium, Molybdenum, and Tungsten, and of Some Related Pentacarbonylmetal Halides in N-Donor Solvents. *J. Chem. Soc., Dalton Trans.* **1976**, (13), 1189–1193.
27. Van der Graaf, T.; Hofstra, R. M. J.; Schilder, P. G. M.; Rijkhoff, M.; Stufkens, D. J.; Vanderlinden, J. G. M., Metal to Ligand Charge-Transfer Photochemistry of Metal Metal-Bonded Complexes .10. Photochemical and Electrochemical Study of the Electron-Transfer Reactions of Mn(CO)<sub>3</sub>(.alpha.-diimine)(L) (L = N-, P-donor) radicals formed by irradiation of (CO)<sub>5</sub>MnMn(CO)<sub>3</sub>(.alpha.-diimine) complexes in the presence of L. *Organometallics* **1991**, *10* (10), 3668–3679.
28. Machan, C. W.; Stanton, C. J.; Vandezande, J. E.; Majetich, G. F.; Schaefer, H. F.; Kubiak, C. P.; Agarwal, J., Electrocatalytic Reduction of Carbon Dioxide by Mn(CN)(2,2'-bipyridine)(CO)<sub>3</sub>: CN Coordination Alters Mechanism. *Inorg. Chem.* **2015**, *54* (17), 8849–8856.
29. Paul, A.; Connolly, D.; Schulz, M.; Pryce, M. T.; Vos, J. G., Effect of Water during the Quantitation of Formate in Photocatalytic Studies on CO<sub>2</sub> Reduction in Dimethylformamide. *Inorg. Chem.* **2012**, *51* (4), 1977–1979.
30. Kuramochi, Y.; Kamiya, M.; Ishida, H., Photocatalytic CO<sub>2</sub> Reduction in N,N-Dimethylacetamide/Water as an Alternative Solvent System. *Inorg. Chem.* **2014**, *53* (7), 3326–3332.
31. Kitamura, N.; Rajagopal, S.; Tazuke, S., Does Nonadiabaticity Play a Role in the Photoinduced Electron-Transfer Reactions of Tris(4,4'-Dialkyl-2,2'-Bipyridine)Ruthenium(Ii) Complexes. *J. Chem. Phys.* **1987**, *91* (14), 3767–3771.



32. Connelly, N. G.; Geiger, W. E., Chemical redox agents for organometallic chemistry. *Chem. Rev.* **1996**, *96* (2), 877–910.
33. Ross, H. B.; Boldaji, M.; Rillema, D. P.; Blanton, C. B.; White, R. P., Photosubstitution in Tris Chelate Complexes of Ruthenium(II) Containing the Ligands 2,2'-Bipyrazine, 2,2'-Bipyrimidine, 2,2'-Bipyridine, and 4,4'-Dimethyl-2,2'-Bipyridine - Energy-Gap Control. *Inorg. Chem.* **1989**, *28* (6), 1013–1021.
34. Fukuzumi, S.; Hironaka, K.; Nishizawa, N.; Tanaka, T., One-Electron Oxidation Potentials of an NADH Model-Compound and a Dimeric Rhodium(I) Complex in Irreversible Systems - a Convenient Determination from the Fluorescence Quenching by Electron-Acceptors. *Bull. Chem. Soc. Jpn.* **1983**, *56* (8), 2220–2227.
35. Sullivan, B. P.; Meyer, T. J., Kinetics and Mechanism of CO<sub>2</sub> Insertion into a Metal-Hydride Bond - a Large Solvent Effect and an Inverse Kinetic Isotope Effect. *Organometallics* **1986**, *5* (7), 1500–1502.
36. Agarwal, J.; Johnson, R. P.; Li, G. H., Reduction of CO<sub>2</sub> on a Tricarbonyl Rhenium(I) Complex: Modeling a Catalytic Cycle. *J. Phys. Chem. A* **2011**, *115* (13), 2877–2881.
37. Chan, S. F.; Chou, M.; Creutz, C.; Matsubara, T.; Sutin, N., Mechanism of the Formation of Dihydrogen from the Photoinduced Reactions of Poly(Pyridine)Ruthenium(II) and Poly(Pyridine)Rhodium(III) Complexes. *J. Am. Chem. Soc.* **1981**, *103* (2), 369–379.
38. Koike, K.; Hori, H.; Ishizuka, M.; Westwell, J. R.; Takeuchi, K.; Ibusuki, T.; Enjouji, K.; Konno, H.; Sakamoto, K.; Ishitani, O., Key process of the photocatalytic reduction of CO<sub>2</sub> using [Re(4,4'-X-2-bipyridine)(CO)<sub>3</sub>PR<sub>3</sub>](+) (X = CH<sub>3</sub>, H, CF<sub>3</sub>; PR<sub>3</sub> = phosphorus ligands): Dark reaction of the one-electron-reduced complexes with CO<sub>2</sub>. *Organometallics* **1997**, *16* (26), 5724–5729.
39. Franco, F.; Cometto, C.; Ferrero Vallana, F.; Sordello, F.; Priola, E.; Minero, C.; Nervi, C.; Gobetto, R., A local proton source in a [Mn(bpy-R)(CO)<sub>3</sub>Br]-type redox catalyst enables CO<sub>2</sub> reduction even in the absence of Bronsted acids. *Chem. Commun.* **2014**, *50* (93), 14670–14673.
40. Tamaki, Y.; Watanabe, K.; Koike, K.; Inoue, H.; Morimoto, T.; Ishitani, O., Development of highly efficient supramolecular CO<sub>2</sub> reduction photocatalysts with high turnover frequency and durability. *Faraday Discuss.* **2012**, *155*, 115–127.
41. Gholamkhash, B.; Mametsuka, H.; Koike, K.; Tanabe, T.; Furue, M.; Ishitani, O., Architecture of supramolecular metal complexes for photocatalytic CO<sub>2</sub> reduction: Ruthenium-rhenium bi- and tetranuclear complexes. *Inorg. Chem.* **2005**, *44* (7), 2326–2336.
42. Keith, J. A.; Grice, K. A.; Kubiak, C. P.; Carter, E. A., Elucidation of the Selectivity of Proton-Dependent Electrocatalytic CO<sub>2</sub> Reduction by fac-Re(bpy)(CO)<sub>3</sub>Cl. *J. Am. Chem. Soc.* **2013**, *135* (42), 15823–15829.
43. Agarwal, J.; Shaw, T. W.; Schaefer, H. F.; Bocarsly, A. B., Design of a Catalytic Active Site for Electrochemical CO<sub>2</sub> Reduction with Mn(I)-Tricarbonyl Species. *Inorg. Chem.* **2015**, *54* (11), 5285–5294.
44. Keene, F. R.; Sullivan, B. P., In *Electrochemical and Electrocatalytic Reactions of Carbon Dioxide*, Sullivan, B. P., Krist, K., Guard, H. E., Ed. Elsevier: Amsterdam, 1993; pp 118–144.

45. Gerasimov, O. V.; Parmon, V. N., Photocatalysis by the Transition-Metal Complexes. *Russ. Chem. Rev* **1992**, *61* (2), 154–167.
46. Priyadarshani, N.; Liang, Y. N.; Suriboot, J.; Bazzi, H. S.; Bergbreiter, D. E., Recoverable Reusable Polyisobutylene (PIB)-Bound Ruthenium Bipyridine (Ru(PIB-bpy)<sub>3</sub>Cl<sub>2</sub>) Photoredox Polymerization Catalysts. *ACS Macro Lett.* **2013**, *2* (7), 571–574.
47. Hawecker, J.; Lehn, J.-M.; Ziessel, R., Photochemical Reduction of Carbon-Dioxide to Formate Mediated by Ruthenium Bipyridine Complexes as Homogeneous Catalysts. *J. Chem. Soc., Chem. Comm.* **1985**, (2), 56–58.

## 2.7 Appendix

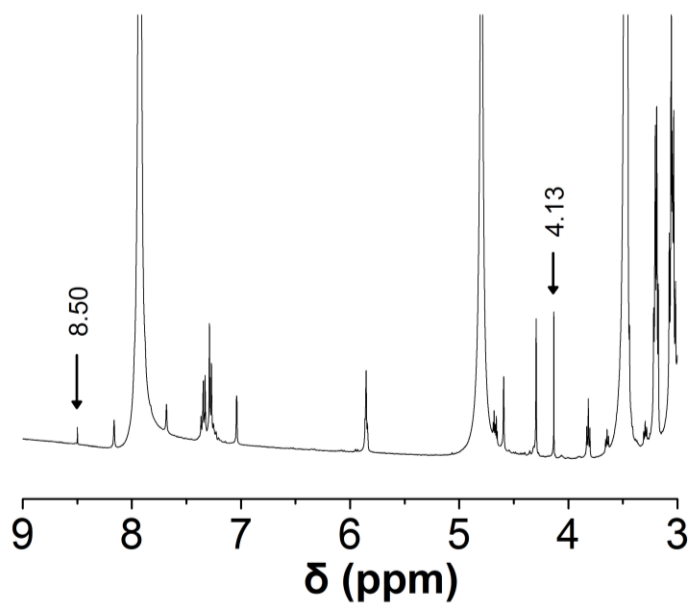


**Figure 2.4** A sample  $^1\text{H}$  NMR spectrum of the worked-up photocatalytic reaction solution of 1 mM  $\text{Mn}(\text{CN})(\text{bpy})(\text{CO})_3$  under  $\text{CO}_2$  after 15 h irradiation. The solvent was a DMF-TEOA (4 : 1 v/v) in  $\text{CD}_3\text{CN}$  solution. The ferrocene reference is at 4.13 ppm while formate is observed at 8.50 ppm.

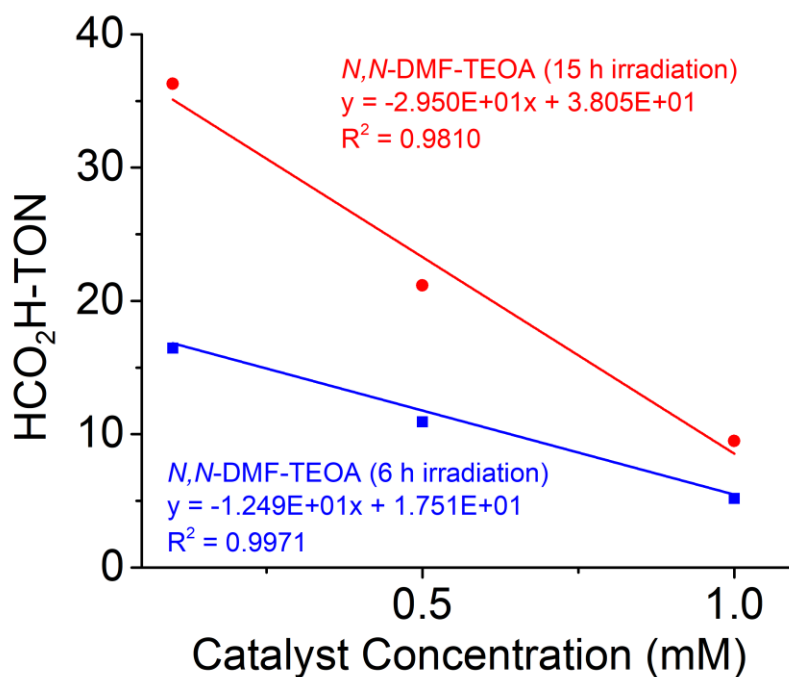


**Figure 2.5** The linear fit lines of HCO<sub>2</sub>H TON vs. catalyst (complex 1) concentration shows high linearity for both 15 h and 6 h irradiation.

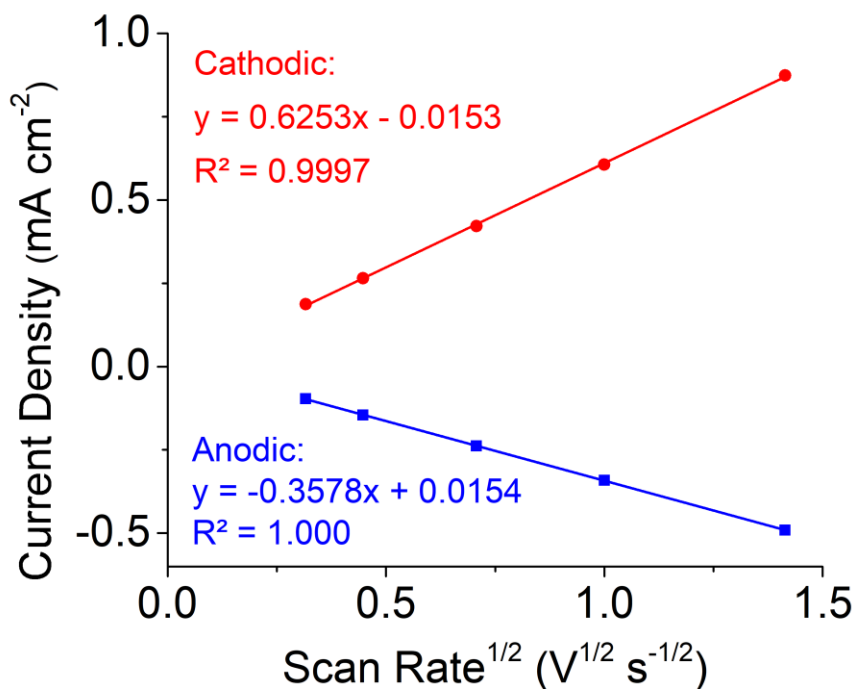


**Figure 2.6** Linear plots of anodic and cathodic currents against square root of scan rate of CV for 1.0 mM of complex Mn(CN)(bpy)(CO)<sub>3</sub> in 0.1 M TBAPF<sub>6</sub> in dry DMF under Ar.

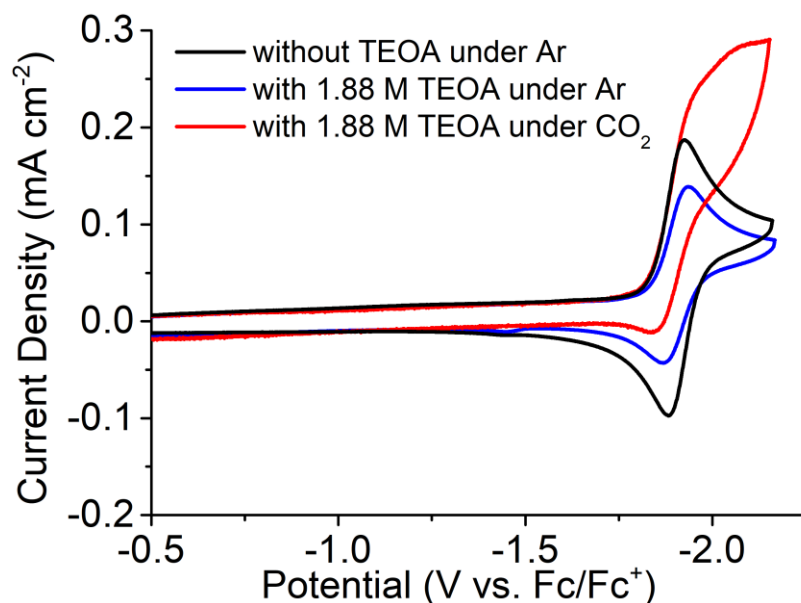


**Figure 2.7** Cyclic voltammety of  $\text{Mn}(\text{CN})(\text{bpy})(\text{CO})_3$  under Ar saturation (black), in the presence of TEOA (blue), and under  $\text{CO}_2$  saturation (red) in dry DMF at  $100 \text{ mVs}^{-1}$ . Conditions:  $1 \text{ mM Mn}(\text{CN})(\text{bpy})(\text{CO})_3$  in  $0.1 \text{ TBAPF}_6/\text{DMF}$ ; WE: GC; CE: Pt; RE: Ag/Cl with Fc as internal reference.

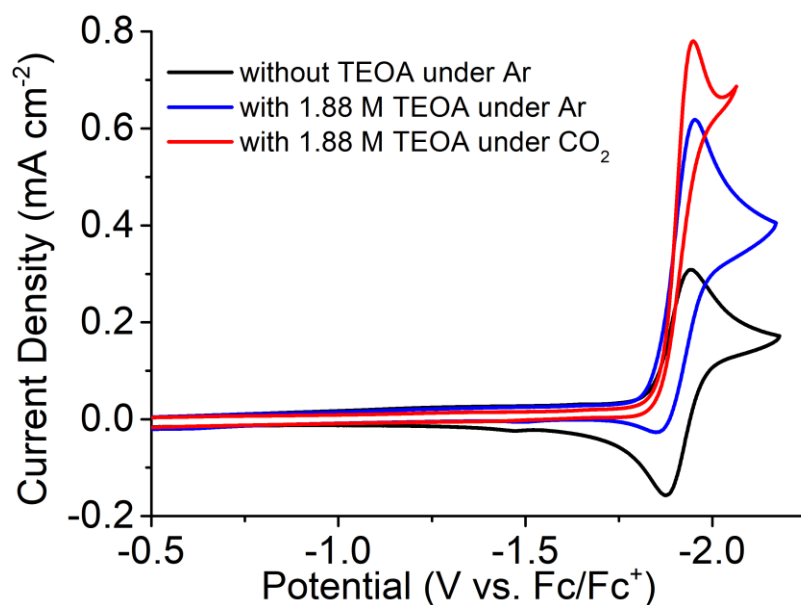


**Figure 2.8** Cyclic voltammety of  $\text{Mn}(\text{CN})(\text{bpy})(\text{CO})_3$  under Ar saturation (black), in the presence of TEOA (blue), and under  $\text{CO}_2$  saturation (red) in dry MeCN at  $100 \text{ mVs}^{-1}$ . Conditions:  $1 \text{ mM Mn}(\text{CN})(\text{bpy})(\text{CO})_3$  in  $0.1 \text{ TBAPF}_6/\text{MeCN}$ ; WE: GC; CE: Pt; RE: Ag/Cl with Fc as internal reference.

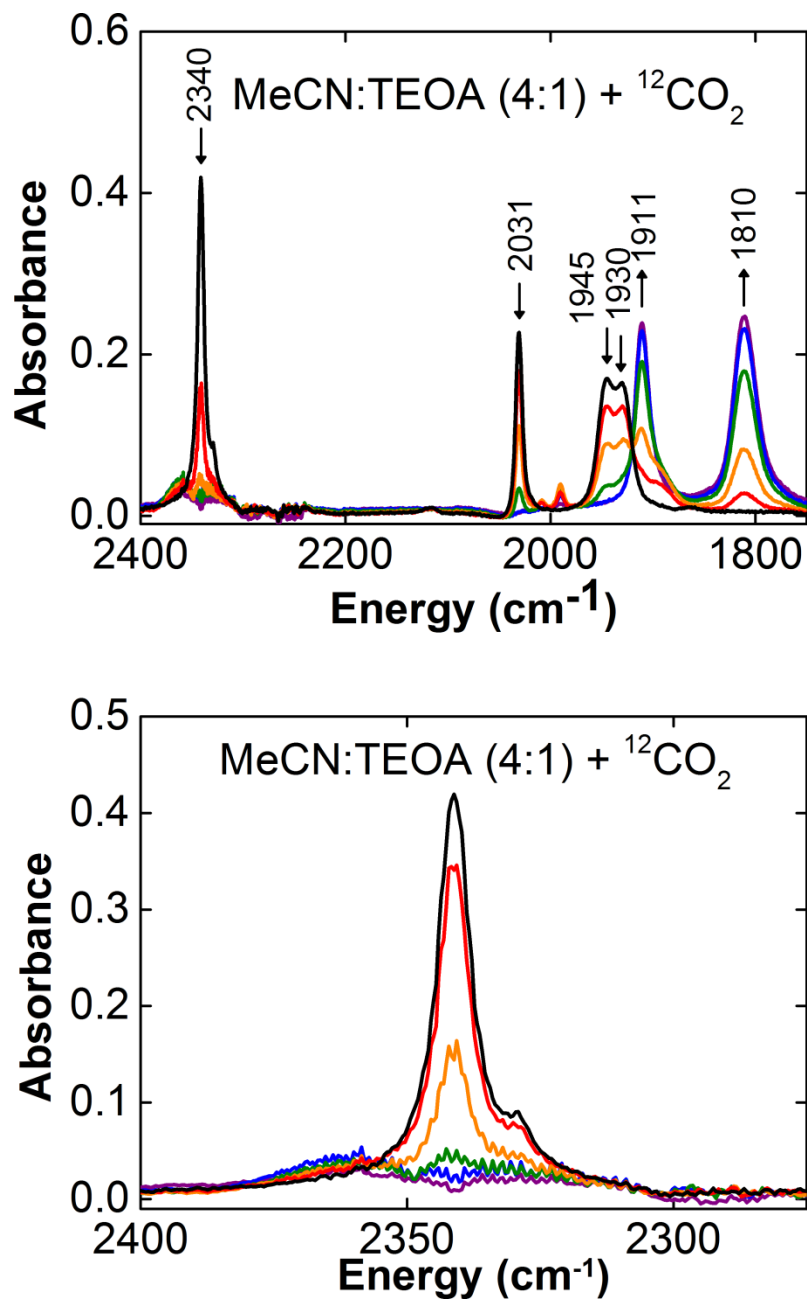


**Figure 2.9** Infrared spectra of  $\text{Mn}(\text{CN})(\text{bpy})(\text{CO})_3$  at controlled potentials in dry MeCN-TEOA under  $\text{CO}_2$ . Enlarged spectra of the  $\text{CO}_2$  peak at around  $2337\text{ cm}^{-1}$  shows the decrease in  $\text{CO}_2$  concentration under catalytic conditions (ca.  $-1.9\text{ V}$  vs  $\text{Fc}/\text{Fc}^+$ ) over the course of 5 min.

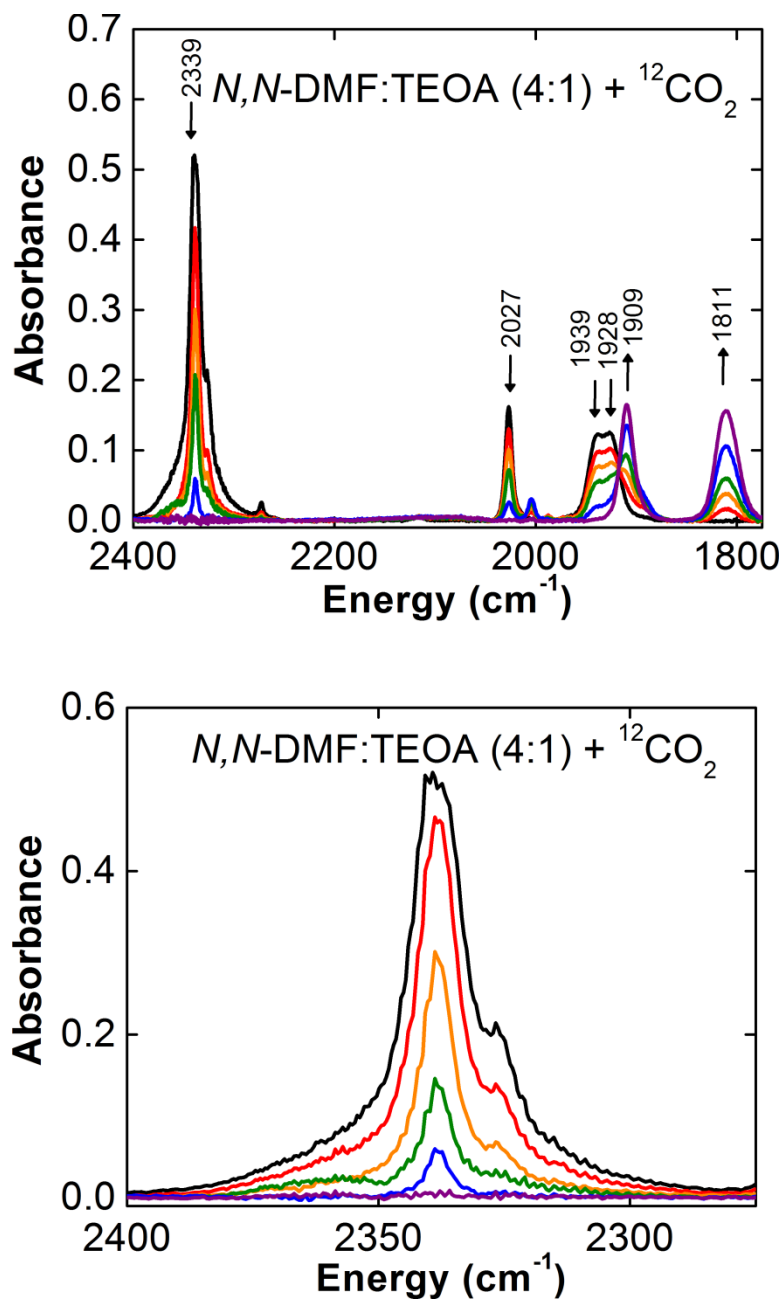


**Figure 2.10** Infrared spectra of  $\text{Mn}(\text{CN})(\text{bpy})(\text{CO})_3$  taken at controlled potentials in dry DMF-TEOA (4:1) under  $\text{CO}_2$ . Enlarged spectra of the  $\text{CO}_2$  peak at around  $2337 \text{ cm}^{-1}$  shows the decrease in  $\text{CO}_2$  concentration at catalytic potentials (ca.  $-1.9 \text{ V}$  vs  $\text{Fc}/\text{Fc}^+$ ) over the course of 5 min.

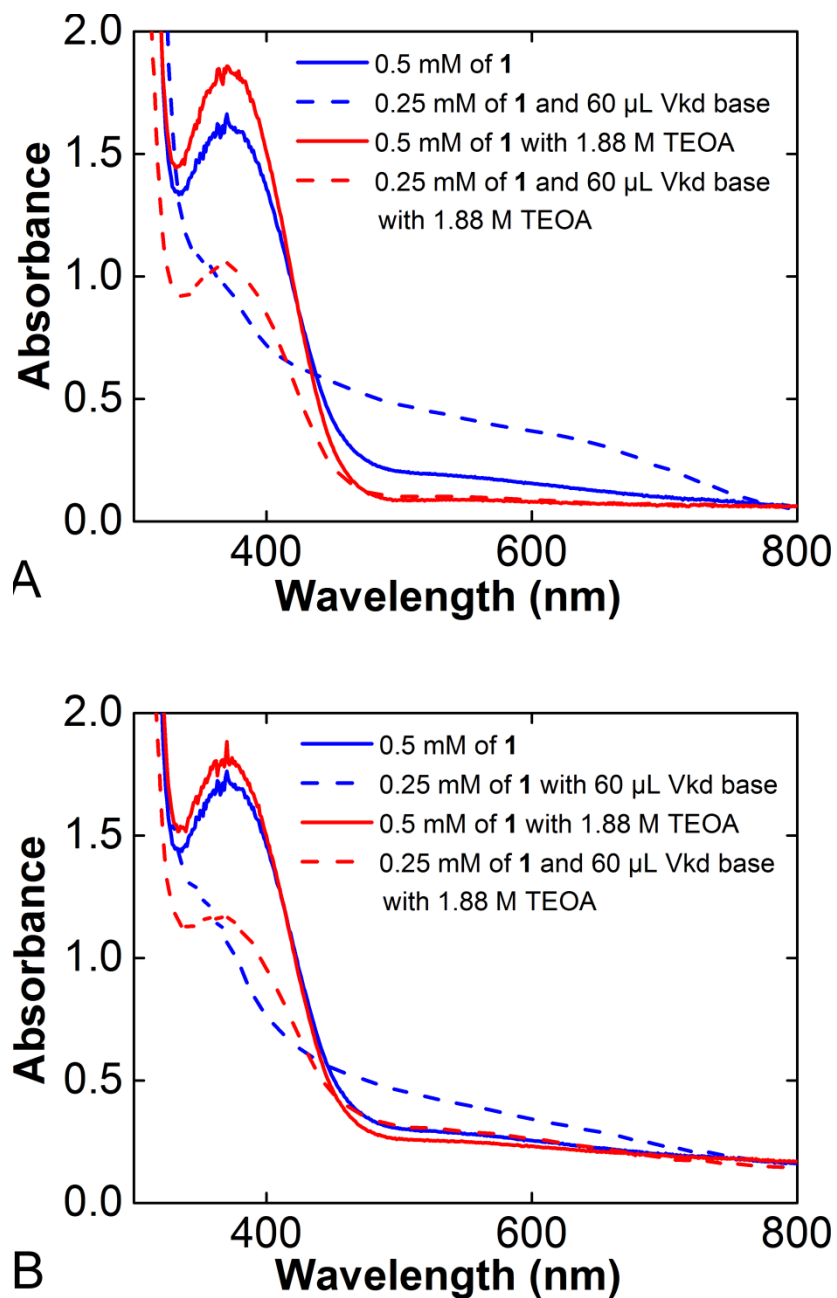


**Figure 2.11** UV-Vis spectra of Mn(CN)(bpy)(CO)<sub>3</sub> (**1**) (A) in dry MeCN with and without Vkd base in the absence or presence of TEOA; and (B) in dry DMF with and without Vkd base in the absence or presence of TEOA.



## Chapter 3

# Improving Photocatalysis for the Reduction of CO<sub>2</sub> Through Non-Covalent Supramolecular Assembly

### 3.1 Introduction

To mimic natural photosynthesis, photocatalytic reduction of CO<sub>2</sub> has been extensively investigated using transition metal complexes that can act as redox photosensitizers (PS) by transferring electrons upon photon excitation and as catalysts (Cat) by accepting electrons and reducing CO<sub>2</sub>. Re bipyridine catalysts have been shown to be excellent electrocatalysts<sup>1-3</sup> and photocatalysts<sup>4-5</sup> when coupled with photosensitizers. In a typical photocatalytic system using Re(dmb)(CO)<sub>3</sub>Cl (ReDMB, where 4,4'-dimethyl-2,2'-bipyridine = dmb) as catalyst, Ru(dmb)<sub>3</sub>(PF<sub>6</sub>)<sub>2</sub> (RuDMB) as photosensitizer, and 1-Benzyl-1,4-dihydronicotinamide (BNAH) as sacrificial reductant in a solution of *N,N*-dimethylformamide/triethanolamine (DMF : TEOA, 5 : 1), the quantum yield is 6.2 % for carbon monoxide ( $\Phi_{\text{CO}}$ ) and the turnover number for CO (TON<sub>CO</sub>) is 101 in 16 h<sup>6</sup>. In order to improve the quantum yield of photocatalytic systems, the Ishitani group has studied extensively supramolecular photocatalysts by linking different photosensitizers and Re catalysts using short, covalent bridging ligands since 2005<sup>7-15</sup>. They also

switched the sacrificial reductant to 1,3-dimethyl-2-phenyl-2,3-dihydro-1*H*-benzo[*d*]imidazole (BIH), which can serve as a two-electron donor with stronger reducing power compare to BNAH<sup>16</sup> (**Figure 3.1**). The catalytic performance of these new systems is greatly improved compared to the separated systems due to the acceleration and higher yield of intramolecular electron transfer between the two components, with the rate of electron transfer as fast as  $k_{\text{ET}} = (1.4 \pm 0.1) \times 10^9 \text{ s}^{-1}$ <sup>8</sup>. Recently, our laboratory estimated that the rates of electron transfer ( $k_{\text{ET}}$ ) between Ru<sub>3</sub>O clusters linked by hydrogen bonded pyrimidinones were on the order of  $10^{11} \text{ s}^{-1}$ <sup>17</sup>. There are several reports of the influence of second coordination sphere effects, such as hydrogen bonding interactions, on catalysis<sup>18-21</sup>. Consequently, in this work, we investigate a bimolecular system, in which the photosensitizer and the catalyst form hydrogen bonding pairs, to determine the effects of non-covalent interactions on photocatalytic performance.

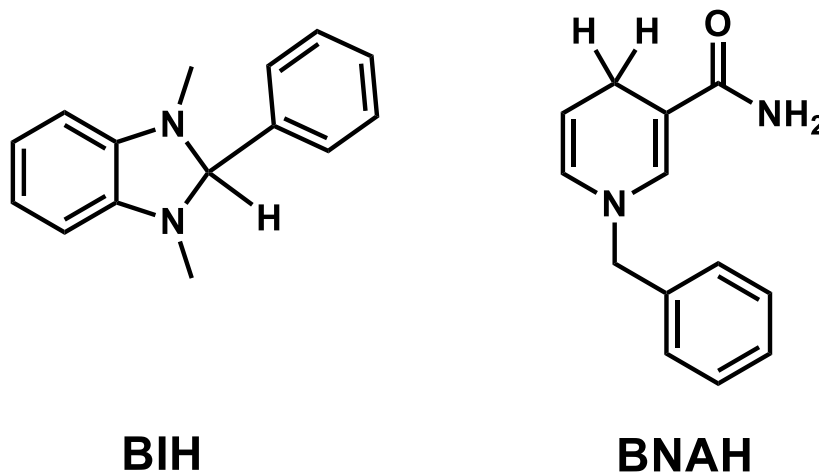
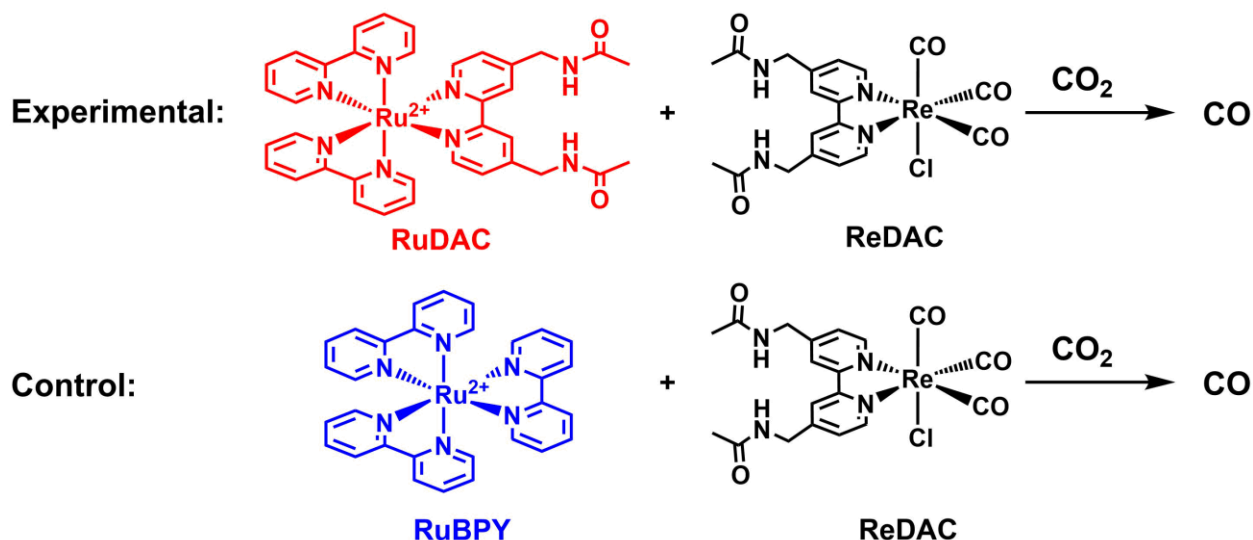


**Figure 3.1** Structures of two sacrificial reductants: BIH and BNAH.

The system composed of Ru(dac)(bpy)<sub>2</sub>(PF<sub>6</sub>)<sub>2</sub> (RuDAC) (4,4'-bis(methyl acetamidomethyl)-2,2'-bipyridine = dac, 2,2'-bipyridine = bpy) as the photosensitizer and Re(dac)(CO)<sub>3</sub>Cl (ReDAC) as the catalyst was chosen for this study (**Scheme 3.1**). A previous electrochemical study of ReDAC indicated the formation of a hydrogen-bonded Re–Re dimer in acetonitrile (MeCN)<sup>22</sup>. In order to fairly assess the effects of hydrogen bonding interactions on photocatalysis, a control system composed of Ru(bpy)<sub>3</sub>(PF<sub>6</sub>)<sub>2</sub> (RuBPY) and ReDAC was used for comparison (**Scheme 3.1**). More control experiments were run using

Re(bpy)(CO)<sub>3</sub>Cl (ReBPY) as catalyst with RuDAC and RuBPY as photosensitizers respectively to further investigate the influence of hydrogen bonding on photocatalysis. RuBPY has similar reduction potentials, UV-vis absorption spectrum, and excited state lifetime as RuDAC.



**Scheme 3.1** Experimental and control systems for investigation of hydrogen bonding effects on photocatalysis.

## 3.2 Results and Discussion

### 3.2.1 Cyclic Voltammetry of Photosensitizers

ReDAC<sup>22</sup> and BIH<sup>23</sup> were synthesized as reported and RuDAC was synthesized by adapting methods in the literature<sup>24</sup>. In a typical mixed system with the Ru photosensitizer and catalyst as separate components, the Ru photosensitizer (Ru<sup>2+</sup>) is first excited by light and then reduced by a sacrificial reductant (D), followed by electron transfer from the singly reduced Ru photosensitizer (Ru<sup>+</sup>) to the catalyst<sup>25-26</sup>(**Scheme 3.2**). The latter step (eq. 2 in **Scheme 3.2**) is driven by the difference between the redox potential of Ru<sup>+</sup> and catalyst. To better demonstrate the impact of hydrogen bonding on photocatalysis, the first reduction potential of the photosensitizer should be comparable to that of the catalyst so that there is a low driving force for electron transfer. In the previous study, ReDAC was reported to display its first reduction at  $-1.77$  V (vs. Fe<sup>+0</sup>)<sup>22</sup>. Cyclic voltammograms (CVs) of RuDAC, RuBPY and RuDMB were taken under Ar in dry MeCN solutions containing 0.1 M tetrabutylammonium hexafluorophosphate (TBAPF<sub>6</sub>). Within

experimental error, the CVs of RuDAC and RuBPY display first reduction potentials at  $-1.76$  V, making them excellent trial systems comparing hydrogen bonding effects in this study. Another commonly used photosensitizer, RuDMB, has a more negative reduction potential at  $-1.88$  V. The increased driving force for electron transfer could mask hydrogen bonding effects. Therefore, RuBPY was chosen to be the control for comparison of catalytic performance without a hydrogen bonding interaction.

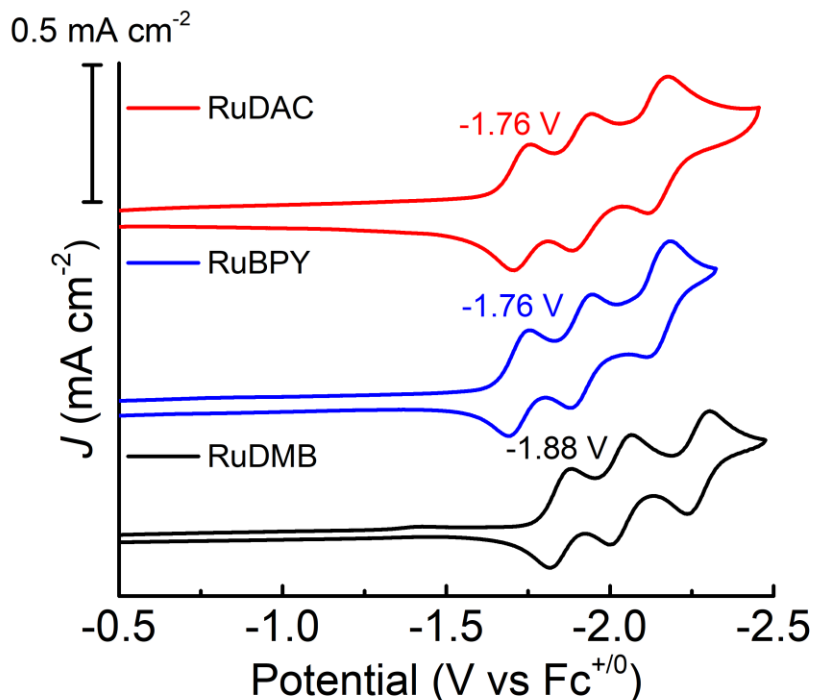


**Figure 3.2** Cyclic voltammograms of 1 mM of RuDAC (red), RuBPY (blue) and RuDMB (black) in dry MeCN containing 0.1 M TBAPF<sub>6</sub> at scan rate 100 mV/s under Ar.



**Scheme 3.2** A simplified scheme showing reductive quenching of the Ru photosensitizer (Ru) by sacrificial reductant (D) and then the electron transfer from singly reduced Ru to the catalyst (Cat).

### 3.2.2 Photocatalytic Experiments

A series of photocatalytic studies were performed by irradiating solutions that were 0.5 mM in photosensitizer, 0.5 mM in catalyst, 0.1 M in 1,3-dimethyl-2-phenyl-2,3-dihydro-1*H*-benzo[*d*]imidazole (BIH) in dry MeCN or DMF under CO<sub>2</sub> or Ar at 470 nm for 4 h. The common practice of using triethanolamine (TEOA) as proton source and 1-benzyl-1,4-dihydropyridin-2(1*H*)-one (BNAH) as sacrificial reductant was not adopted in this study as these have hydroxyl or amide groups which are capable of interrupting the hydrogen bonding between the photosensitizer and the catalyst. A benzimidazole derivative, BIH, was used as sacrificial reductant in this work as it does not interfere with hydrogen bonds (**Figure 3.1**). The systems in this study work surprisingly well without the added proton source, and it is likely due to the disproportionation mechanism of  $2 \text{CO}_2 + 2 e^-$  to CO and  $\text{CO}_3^{2-}$  or  $\text{HCO}_3^-$  ( $[\text{H}]\text{CO}_3^{[2]-}$ ) by the ReDAC catalyst<sup>22</sup>. In MeCN solutions, hydrogen bonds can be formed between amide substituents as demonstrated in previous electrochemical studies of ReDAC<sup>22</sup>. The photocatalytic reactions were run for 4 hours only because over half of the BIH was consumed. After 4 hours of irradiation, the RuDAC/ReDAC system exhibits a more-than-threefold increase in photocatalytic reduction of CO<sub>2</sub> with a higher turnover number ( $\text{TON}_{\text{CO}} = 100 \pm 4$ ) and quantum yield ( $\Phi_{\text{CO}} = 23.3 \pm 0.8 \%$ ) for CO production compared to the RuBPY/ReDAC control system ( $\text{TON}_{\text{CO}} = 28 \pm 4$  and  $\Phi_{\text{CO}} = 7 \pm 1 \%$ ) as shown in **Figure 3.3** and **Table 3.1**. To further test hydrogen bonding as the principal cause for these observations, similar photocatalytic studies were done in DMF, a solvent that interrupts hydrogen bond formation. In D (**Table 3.1**), the RuBPY/ReDAC control system displays improvement in catalysis ( $\text{TON}_{\text{CO}} = 43 \pm 9$  and  $\Phi_{\text{CO}} = 11 \pm 1 \%$ ) while the RuDAC/ReDAC system displays a decrease in catalysis ( $\text{TON}_{\text{CO}} = 79 \pm 8$  and  $\Phi_{\text{CO}} = 18 \pm 1 \%$ ), but it still outperforms the RuBPY/ReDAC system. Thus, the two systems exhibit opposite responses to different solvents. The higher activity of the RuDAC/ReDAC system compared to the control system in DMF is unexpected, but it is likely due to increased contact surface area between photosensitizer and catalyst<sup>27</sup>. The reason for higher activity of RuBPY/ReDAC in DMF compared to MeCN remains unclear, but previous studies show that solvents play important roles in controlling catalytic rates and selectivity<sup>25</sup>.

<sup>28-32</sup>. Since the RuDAC/ReDAC system behaves in a trend opposite to the control, it is reasonable to conclude that hydrogen bonding is the dominant factor influencing differences in performance.

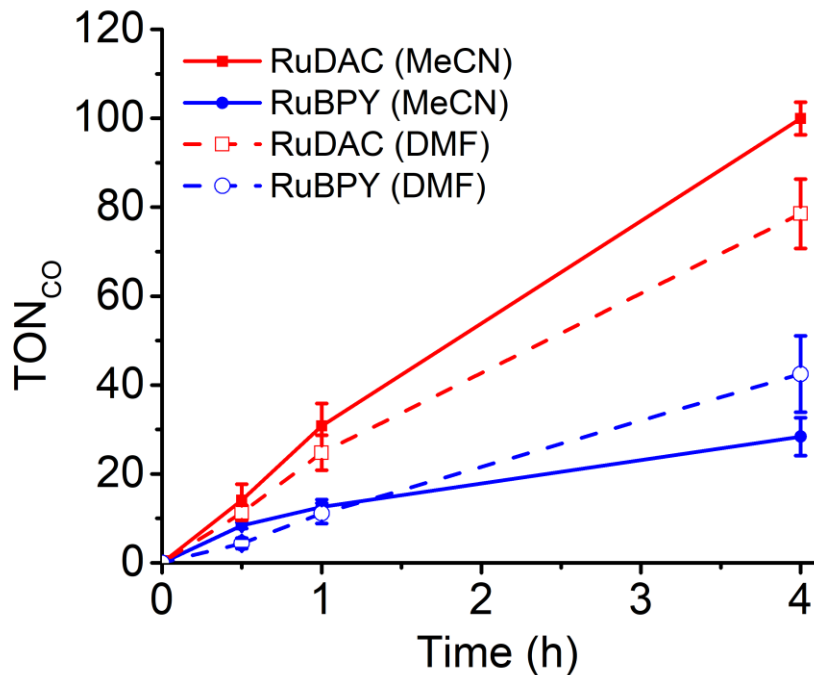


**Figure 3.3** Turnover number of CO ( $\text{TON}_{\text{CO}}$ ) produced by RuDAC/ReDAC (red) and RuBPY/ReDAC (blue) in MeCN (solid line) and DMF (dotted line) solvents.

**Table 3.1** Summary of turnover numbers ( $\text{TON}_{\text{CO}}$  and  $\text{TON}_{\text{H}_2}$ ), turnover frequency ( $\text{TOF}_{\text{CO}}$ ) and quantum yield ( $\Phi_{\text{CO}}$ ) of experimental studies of 0.5 mM catalyst (Cat) and 0.5 mM of photosensitizer (PS) under  $\text{CO}_2$ .

0.5 mM RuDAC and 0.5 mM ReDAC						
Solvent	Time (h)	$\text{TON}_{\text{CO}}$	$\text{TOF}_{\text{CO}}$ (per h)	$\Phi_{\text{CO}}$	$\text{TON}_{\text{H}_2}$	$\text{TON}_{\text{HCO}_2^-}$
MeCN	0.5	$14 \pm 4$	$28 \pm 7$	$26 \pm 6 \%$	NA	NA
	1	$31 \pm 5$	$31 \pm 5$	$29 \pm 4 \%$	NA	NA
	4	$100 \pm 4$	$25.0 \pm 0.9$	$23.3 \pm 0.8 \%$	NA	NA
DMF	0.5	$11 \pm 2$	$22 \pm 4$	$21 \pm 3 \%$	NA	NA
	1	$25 \pm 4$	$25 \pm 4$	$23 \pm 3 \%$	NA	NA
	4	$78 \pm 8$	$20 \pm 2$	$18 \pm 1 \%$	NA	NA
0.5 mM RuBPY and 0.5 mM ReDAC						
Solvent	Time (h)	$\text{TON}_{\text{CO}}$	$\text{TOF}_{\text{CO}}$ (per h)	$\Phi_{\text{CO}}$	$\text{TON}_{\text{H}_2}$	$\text{TON}_{\text{HCO}_2^-}$
MeCN	0.5	$8.4 \pm 0.7$	$17 \pm 1$	$15 \pm 3 \%$	NA	NA
	1	$13 \pm 2$	$13 \pm 2$	$12 \pm 2 \%$	NA	NA
	4	$28 \pm 4$	$7 \pm 1$	$7 \pm 1 \%$	NA	NA
DMF	0.5	$4 \pm 1$	$9 \pm 2$	$9 \pm 1 \%$	NA	NA
	1	$11 \pm 2$	$11 \pm 2$	$11 \pm 1 \%$	NA	NA
	4	$42 \pm 8$	$11 \pm 2$	$11 \pm 1 \%$	NA	NA

The formate concentration was below detectable limit of the NMR.

### 3.2.3 Control Studies of Photocatalytic System

Control studies under Ar reveal no CO or H<sub>2</sub> production upon irradiation (**Table 3.2**). In addition, control reactions without ReDAC reveal that RuDAC is a better catalyst than RuBPY in both solvents and it performed better in MeCN than in DMF. These observations are similar to the trend seen in the RuDAC/ReDAC system, but the absence of the Re catalyst significantly slows down the rate of CO formation (**Table 3.2**). Several control experiments were run using ReBPY as catalyst with RuDAC or RuBPY as photosensitizer respectively under catalytic conditions (**Table 3.2**). The use of RuDAC as photosensitizer with ReBPY demonstrates much higher turnover number ( $72 \pm 3$  in MeCN and  $50 \pm 20$  in DMF) and quantum yields ( $17.3 \pm 0.3$  % in MeCN and  $12 \pm 3$  % in DMF) for CO compares to the use of RuBPY with ReBPY. Similar to the RuDAC/ReDAC and RuBPY/ReDAC systems mentioned above, this is likely due to increased contact surface area between photosensitizer and catalyst<sup>27</sup>.

**Table 3.2** Summary of turnover numbers (TON<sub>CO</sub>) and quantum yield ( $\Phi_{CO}$ ) for control studies of 0.5 mM catalyst (Cat) and 0.5 mM of photosensitizer (PS) after 4 hours of photocatalysis under Ar or CO<sub>2</sub>.

Cat / PS	Solvent	Gas	TON <sub>CO</sub>	TON <sub>H<sub>2</sub></sub>	TON <sub>HCO<sub>2</sub><sup>-</sup></sub>	$\Phi_{CO}$
ReDAC/RuDAC	MeCN	Ar	NA	NA	NA	NA
ReDAC/RuBPY	MeCN	Ar	NA	NA	NA	NA
RuDAC only	MeCN	CO <sub>2</sub>	$23 \pm 2$	0.02	NA	$6.0 \pm 0.7$ %
RuBPY only	MeCN	CO <sub>2</sub>	$9.7 \pm 0.4$	0.02	NA	$2.5 \pm 0.1$ %
ReBPY/RuDAC <sup>a</sup>	MeCN	CO <sub>2</sub>	$72 \pm 3$	NA	NA	$17.3 \pm 0.3$ %
ReBPY/RuBPY <sup>a</sup>	MeCN	CO <sub>2</sub>	$32 \pm 5$	NA	NA	$7.3 \pm 0.9$ %
ReDAC/RuDAC	DMF	Ar	NA	NA	NA	NA
ReDAC/RuBPY	DMF	Ar	NA	NA	NA	NA
RuDAC only	DMF	CO <sub>2</sub>	$17.6 \pm 0.9$	NA	NA	$4.4 \pm 0.4$ %
RuBPY only	DMF	CO <sub>2</sub>	$11 \pm 2$	0.01	NA	$2.7 \pm 0.4$ %
ReBPY/RuDAC <sup>a</sup>	DMF	CO <sub>2</sub>	$50 \pm 20$	NA	NA	$12 \pm 3$ %
ReBPY/RuBPY <sup>a</sup>	DMF	CO <sub>2</sub>	$18 \pm 4$	NA	NA	$5 \pm 1$ %

Products below detectable limit are labelled as NA. <sup>a</sup> Re(bpy)(CO)<sub>3</sub>Cl (ReBPY) was used as a catalyst with RuDAC or RuBPY as photosensitizer. <sup>12</sup>C<sup>18</sup>O (2137 cm<sup>-1</sup>) and [H]<sup>12</sup>CO<sub>3</sub><sup>[21]-</sup> (1672 and 1635 cm<sup>-1</sup>) were detected in irradiation condition in **Figure 3.4**. The higher activity of the RuDAC/ReBPY system compared to the control system in DMF is likely due to increased contact surface area between photosensitizer and catalyst.

### 3.2.4 Analysis of Photocatalytic Products

In addition to gaseous products, the liquid mixtures were analyzed. No formate is detected with <sup>1</sup>H NMR (**Table 3.2**) but appreciable [H]CO<sub>3</sub><sup>[21]-</sup> are observed with IR. It is known that ReDAC undergoes the disproportionation mechanism of  $2 \text{CO}_2 + 2 \text{e}^- \rightleftharpoons \text{CO} + \text{CO}_3^{2-}$  in electrocatalysis<sup>22</sup>. Upon irradiation

without a proton source (**Figure 3.4**), ReDAC is reduced to give the acetonitrile adduct (2020, 1913, and 1892  $\text{cm}^{-1}$  for  $^{12}\text{CO}_2$  and 1972, 1869, and 1849  $\text{cm}^{-1}$  for  $^{13}\text{CO}_2$ ). IR stretches assigned to  $^{12}\text{CO}$  (2138  $\text{cm}^{-1}$ ) and  $^{12}\text{CO}_3^{2-}$  or  $\text{H}^{12}\text{CO}_3^-$  ( $[\text{H}]\text{CO}_3^{[2]-}$ : 1672 and 1637  $\text{cm}^{-1}$ ) were observed as well. Repeating these experiments with  $^{13}\text{CO}_2$  showed shifts in these bands ( $[\text{H}]\text{CO}_3^{[2]-}$ : 1625 and 1598  $\text{cm}^{-1}$  and  $^{13}\text{CO}$ : 2090  $\text{cm}^{-1}$ ), consistent with isotopic labeling<sup>22, 33</sup>. Similar [bi]carbonate products are observed with RuDAC/ReBPY, RuBPY/ReBPY and RuDAC only systems. At the end of 4 h photocatalysis, orange powder, which is insoluble in MeCN but soluble in methanol (MeOH), were observed in solution. By dissolving it in MeOH and measuring its UV-vis absorption and fluorescence, the orange powder is likely to be some kind of Ru photosensitizer[bi]carbonate products. The observation of formation of [bi]carbonate products is an important evidence that the choice of solvent significantly influences the type of production formation.

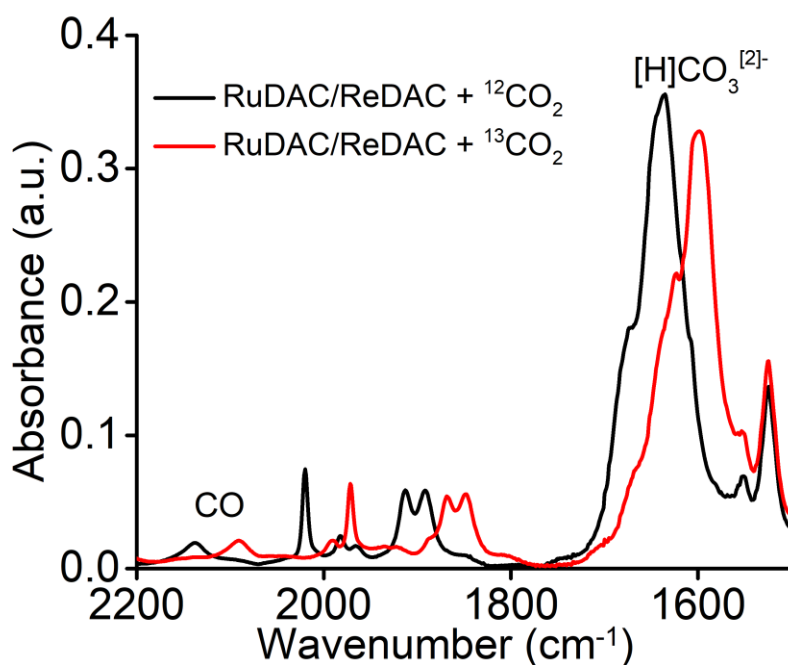


**Figure 3.4** IR spectra of 3 mM ReDAC, 3 mM RuDAC and 0.1 M BIH solution with  $^{12}\text{CO}_2$  (black) and  $^{13}\text{CO}_2$  (red) in dry MeCN showing the formation of reduced carbon products upon irradiation of light at 470 nm for 10 min.



### 3.2.5 Spectroscopic Analysis of the Photocatalytic System

Several additional experiments were carried out to understand the origin of the enhancement in photocatalytic activity in the RuDAC/ReDAC system compared to RuBPY/ReDAC. Further support for hydrogen bonding interactions was gained as contributions arising from discrepancies in light absorption by the photosensitizers, faster electron transfer from BIH to the photosensitizer, and other interactions of the photosensitizer with the catalyst were ruled out. First, the photochemical properties of the photosensitizers were investigated. The UV-visible absorption measurements of the three photosensitizers show comparable molar absorptivity at 470 nm, which is the wavelength used for photocatalysis (**Table 3.3** and **Figure 3.5**).

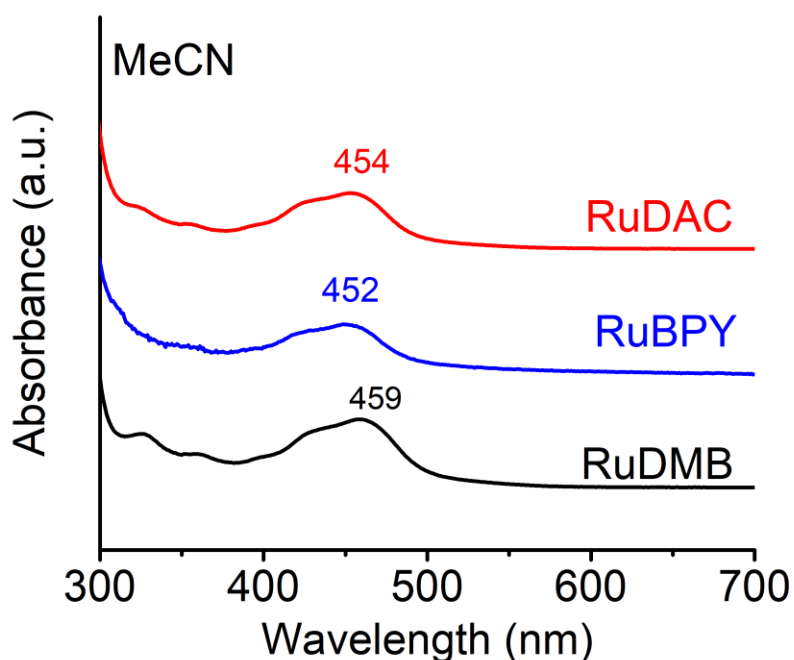


**Figure 3.5** UV-visible spectra of RuDAC (red), RuBPY (blue) and RuDMB (black) in dry MeCN solution.

The lifetimes of the excited states were measured by Time-Correlated Single Photon Counting (TCSPC) with excitation wavelength at 405 nm at room temperature. The lifetimes of excited RuDAC were found to be 980 ns and 910 ns in MeCN and DMF respectively (**Table 3.3** and **Figure 3.11**). Since there is a range of values for the reported lifetimes of RuBPY<sup>34</sup> and RuDMB<sup>14, 35</sup>, we measured them in this work

for consistency (**Table 3.3**). The photoinduced electron transfer from BIH to Ru photosensitizers is the initial process in the photocatalytic CO<sub>2</sub> reduction<sup>36</sup>. To determine the rate of this process, the quenching constant ( $k_q$ ) was found by fluorescence lifetime measurements and the following equation<sup>37</sup>:

$$\frac{\tau_0}{\tau} = 1 + \tau_0 \kappa_q [Q] = 1 + K_D [Q] \quad (\text{Equation 3.1})$$

Here,  $\tau_0$  and  $\tau$  are the fluorescence lifetimes without and with the quencher respectively,  $k_q$  is the biomolecular quenching constant,  $K_D$  is the Stern–Volmer constant for dynamic quenching, and  $Q$  is the quencher. By plotting the Stern–Volmer relationship (**Figure 3.12**), the slope was used to calculate the quenching rate constant ( $k_q$ ) using  $\frac{\tau_0}{\tau} = 1 + \tau_0 \kappa_q [Q] = 1 + K_D [Q]$  (**Equation**

**3.1**). The non-zero slope from the plots suggests dynamic quenching between BIH and the Ru photosensitizers. While the quenching rates of RuDAC and RuBPY are comparable to each other in MeCN and DMF respectively, the rates in MeCN are two to three times higher than those in DMF, indicating a faster electron transfer process in MeCN (**Table 3.3**).

**Table 3.3** Photochemical properties of RuDAC, RuBPY and RuDMB.

complex	$\lambda_{em}$ (MeCN) (nm) <sup>a</sup>	$\lambda_{em}$ (DMF) (nm) <sup>a</sup>	$\epsilon_{470}$ (L mol <sup>-1</sup> cm <sup>-1</sup> )	$\tau_{MeCN}$ (ns) <sup>b</sup>	$\tau_{DMF}$ (ns) <sup>b</sup>	$\kappa_q$ (MeCN) (M <sup>-1</sup> s <sup>-1</sup> ) <sup>c</sup>	$\kappa_q$ (DMF) (M <sup>-1</sup> s <sup>-1</sup> ) <sup>c</sup>
RuDAC	613	620	7200	980	910	$5.9 \pm 0.2 \times 10^9$	$1.8 \pm 0.2 \times 10^9$
RuBPY	609	618	9000	930	930	$7.2 \pm 0.2 \times 10^9$	$2.6 \pm 0.2 \times 10^9$
RuDMB	618	624	8100	900	790		

<sup>a</sup> A dry MeCN or DMF solution containing the Ru complex was measured using fluorometer. <sup>b</sup> The fluorescence lifetimes were measured in dry MeCN or DMF using TCSPC with excitation wavelength at 405 nm at room temperature. <sup>c</sup> The quenching constants were obtained by the Stern–Volmer plot of reductive quenching with BIH in dry MeCN or DMF (**Figure 3.12**)

### 3.2.6 Further Electrochemical Studies of Photosensitizer Properties

Further electrochemical studies were carried out to examine the interaction between photosensitizer and catalyst. RuDAC has three quasi-reversible reduction peaks at  $-1.76$  V,  $-1.52$  V and  $-2.18$  V in MeCN and DMF (**Figure 3.13**) respectively. Similar to other Ru bipyridine complexes<sup>38</sup>, RuDAC itself exhibits current enhancement under a CO<sub>2</sub> atmosphere in both solvent systems (**Figure 3.14**). Addition of ReDAC to the cell causes no significant changes to the three reversible reductions of RuDAC. However, as revealed

in the CV of RuDAC/ReDAC in MeCN under CO<sub>2</sub> (**Figure 3.15**), the characteristic catalytic peak at around -1.8 V vs. Fc<sup>+0</sup> is similar to ReDAC alone in MeCN<sup>22</sup>, suggesting the formation of the ReDAC dimer. This indicates that the presence of RuDAC does not interfere in the catalytic reaction of ReDAC. The absence of the ReDAC hydrogen bonded dimer feature in the CV under catalytic conditions in DMF (**Figure 3.15**) also provides clear evidence that DMF disrupts hydrogen bonding.<sup>22</sup>

### 3.2.7 Spectroelectrochemical Studies of Photocatalytic System

To further test this hypothesis, IR spectroelectrochemistry (IR-SEC) studies were conducted on the RuDAC/ReDAC system in MeCN under N<sub>2</sub>. The complex [Re<sup>I</sup>(dac)(CO)<sub>3</sub>Cl] (black) is taken to the first reduction potential, the IR exhibits bands consistent with [Re<sup>I</sup>(dac•)(CO)<sub>3</sub>Cl]<sup>-</sup>, [Re<sup>0</sup>(dac)(CO)<sub>3</sub>], and [Re<sup>0</sup>(dac)(CO)<sub>3</sub>]<sub>2</sub> (red). If the cell is held at this potential, the dimer [Re<sup>0</sup>(dac)(CO)<sub>3</sub>]<sub>2</sub> (blue) is formed. The IR spectra of **Figure 3.6** indicate the formation of the Re–Re dimer from ReDAC as reported in a previous electrochemical study<sup>22</sup>, indicating that RuDAC is unlikely to affect the catalytic mechanism of ReDAC.

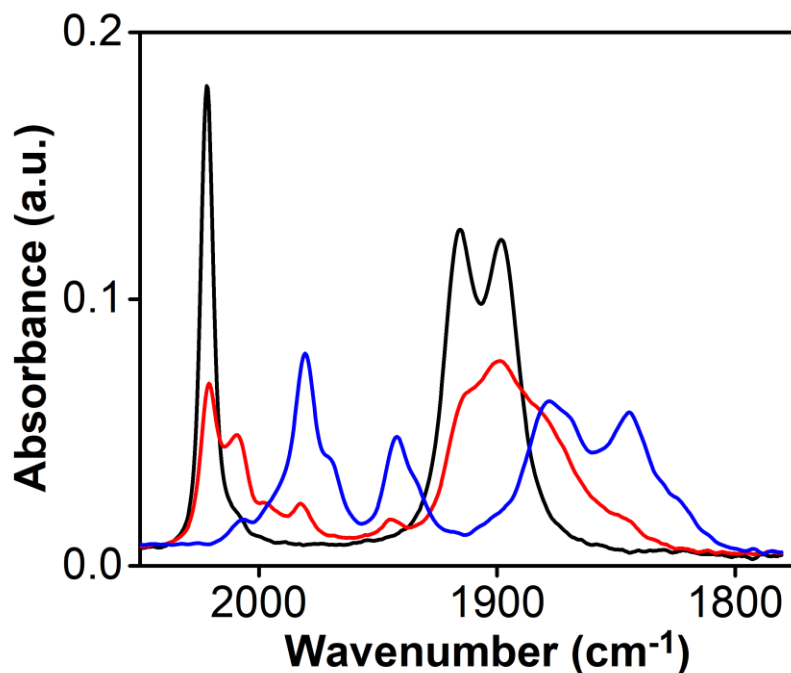


**Figure 3.6** IRSEC spectrum of 1mM of RuDAC and 1 mM ReDAC in dry MeCN under N<sub>2</sub>.

### 3.2.8 NMR Studies of the Dimerization Constant

Using NMR concentration studies, we estimate the association constant ( $K_a$ ) for the hetero-dimer of [ReDAC $\cdots$ RuDAC] to be approximately  $300\text{ M}^{-1}$  in MeCN (**Figure 3.8**)<sup>39</sup>, which is close to the self-dimerization constant ( $290\text{ M}^{-1}$ ) of ReDAC<sup>22</sup>. Although an approximately statistical mixture of homo- and hetero-dimers is expected in the RuDAC/ReDAC system (**Scheme 3.3**), the hydrogen bonding interaction is strong enough to boost catalysis significantly.

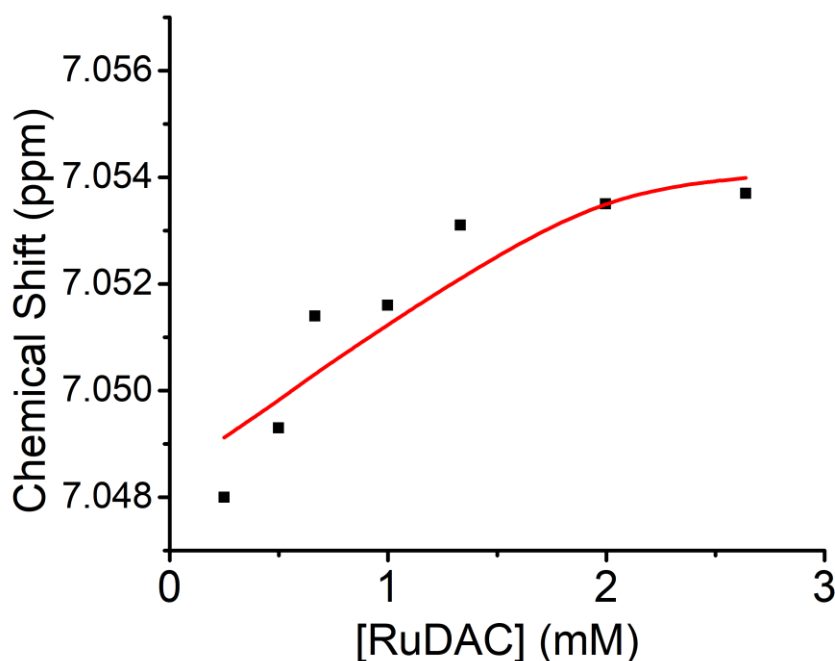


**Figure 3.7** Determination of hydrogen-bonding constant ( $K_a$ ) by fitting to a 1:1 dimerization model using the NMR software WinEQNMR2<sup>39</sup>. Residuals squared =  $3.9 \times 10^{-6}$ .

### 3.3 Conclusion

In conclusion, the findings reported here taken together demonstrate that appending amide groups to photosensitizer and catalyst significantly improves photocatalysis in MeCN by enabling hydrogen bonding interactions. To the best of our knowledge, this constitutes the first report of successfully utilizing hydrogen bonding groups on photosensitizers and catalysts to improve photocatalytic  $\text{CO}_2$  reduction.

In addition to the significance of non-covalent interactions between photosensitizer and catalyst on photocatalysis, several extra important findings were also shown in this work. First, photocatalytic systems are able to perform CO<sub>2</sub> reduction even with the absence of the Brønsted Acid or Lewis acid. This is because an alternate reaction mechanism is able to disproportionate two CO<sub>2</sub> molecules to a carbonate molecule and a CO molecule. This is an interesting finding since most of photocatalytic CO<sub>2</sub> reduction studies were performed with proton source<sup>4, 6-16, 26, 28-29, 35-36</sup>. By simply changing the solvent system, different reduction products are obtained. Second, the larger surface area of photosensitizer is likely able to improve the electron transfer between itself and the catalyst. As evidence by the cases of ReBPY and ReDAC, the use of bulkier RuDAC as photosensitizer considerably outperforms the use of less bulky RuBPY in MeCN or DMF.

A forthcoming study will employ specific hydrogen bond donor and acceptors on photosensitizers and catalysts to eliminate self-dimerization effects. Moreover, more work should be done on investigation of impacts of solvent choices and surface area of photosensitizers on photocatalysis of CO<sub>2</sub> reduction.

## **3.4 Experimental**

### **3.4.1 Preparation and Purification.**

All solvents were obtained from Fisher Scientific. All solvents were deoxygenated and dried over alumina columns on a Grubbs style solvent system under an argon atmosphere. All compounds were obtained from Fisher Scientific or Sigma-Aldrich and used as obtained unless otherwise specified. The 200 proof pure ethanol was purchased from Koptec. The ferrocene was sublimed prior to use. 4,4'-dicyano-2,2'-bipyridine was obtained from HetCat and used without further purification. Tetrabutylammonium hexafluorophosphate (TBAPF<sub>6</sub>, Aldrich, 98%) was recrystallized from EtOH and dried at 90 °C overnight before use in electrochemical experiments. CD<sub>3</sub>CN was purchased from Cambridge Isotope Laboratories, deoxygenated by sparging with argon for 5 minutes, and stored over 3 Å molecular sieves in a nitrogen filled glove box.

### 3.4.2 Synthesis of Ru(dac)(bpy)<sub>2</sub>(PF<sub>6</sub>)<sub>2</sub> (RuDAC).

Ru(bpy)<sub>2</sub>Cl<sub>2</sub><sup>24</sup> and 4,4'-bis(methyl acetamidomethyl)-2,2'-bipyridine<sup>22</sup> were synthesized according to the literature. The synthesis of RuDAC was adapted from the literature<sup>24</sup>. A 100 mL of round bottomed flask was charged with Ru(bpy)<sub>2</sub>Cl<sub>2</sub> (357 mg, 0.74 mmol), 4,4'-bis(methyl acetamidomethyl)-2,2'-bipyridine (100 mg, 0.67 mmol) and 20 mL of ethanol. The solution was refluxed overnight in dark under N<sub>2</sub> and then cooled to room temperature. An ethanol solution containing AgPF<sub>6</sub> (203 mg, 0.80 mmol) was added to the mixture and the solution was refluxed for two hours. The resulted solution was filtered through basic alumina to remove AgCl and excess AgPF<sub>6</sub>. The filtrate was evaporated to dryness under vacuum. The orange red solid was dissolved in minimal amount (~ 3 mL) of dichloromethane. The concentrated solution was added dropwisely with constant stirring to large excess of diethyl ether (~ 100 mL). The precipitated solid was obtained by filtration several times in small fractions and then dried under vacuum in a desiccator at room temperature overnight. The product was obtained as deep orange powder (64% yield). <sup>1</sup>H NMR (CD<sub>3</sub>CN) δ 8.87 (2H, s, dac ArH), 8.59 (2H, br s, dac ArCH<sub>2</sub>NHC(O)CH<sub>3</sub>), 8.53-8.50 (4H, d, bpy ArH), 8.06-8.00 (4H, m, bpy ArH), 7.76-7.70 (4H, dd, bpy ArH), 7.58-7.57 (2H, d, dac ArH), 7.42-7.35 (4H, dt, bpy ArH), 7.30-7.28 (2H, d, dac ArH), 4.49-4.48 (2H, d, dac ArCH<sub>2</sub>NHC(O)CH<sub>3</sub>), 1.98 (6H, s, dac ArCH<sub>2</sub>NHC(O)CH<sub>3</sub>). ESI-MS (m/z) [M - (PF<sub>6</sub>)<sub>2</sub>]<sup>2+</sup>: calcd 356.09; found: 356.02.

### 3.4.3 NMR Data Collection and Analysis.

<sup>1</sup>H NMR spectra were recorded on a Varian Mercury plus 400 MHz NMR spectrometer and <sup>13</sup>C NMR spectra were recorded on a Varian VX 500MHz NMR spectrometer. All NMR data were analyzed using MestReNova software. Samples were prepared in acetonitrile-d<sub>3</sub> and referenced to solvent residuals for <sup>1</sup>H and <sup>13</sup>C.

### 3.4.4 Spectroscopy Data Collection.

The identity and purity of compounds synthesized were confirmed by Fourier transform infrared (FTIR) (Thermo Scientific Nicolet 6700), attenuated total reflection-infrared (ATR-IR) (Bruker Alpha), NMR (Varian Mercury 400), and UV-vis (Shimadzu UV-3600 UV-vis-NIR spectrometer).

### 3.4.5 Photochemical Reactions.

A 10 mL solution of MeCN or DMF, in which contained 0.5 mM of  $\text{Re}(\text{dac})(\text{CO})_3\text{Cl}$  as a catalyst, 0.5mM of  $[\text{Ru}(\text{bpy})_3]^{2+}$  or  $[\text{Ru}(\text{dac})(\text{bpy})_2]^{2+}$  as a photosensitizer, and 0.1M of 1,3-dimethyl-2-phenyl-2,3-dihydro-1H-benzo[d]imidazole (BIH) as a sacrificial reductant, was prepared in a 36 mL quartz cell (NSG Precision Cell, Inc.; path length = 2 cm) sealed with a rubber septum. The solution was sparged with dry Ar or  $\text{CO}_2$  gases through a vial containing MeCN or DMF over molecular sieves and a bubbler for 15 min prior to irradiation. The solution was irradiated with a 470 nm LED (ThorLabs, Inc.; bandwidth fwhm = 25 nm) with temperature maintained at  $25.0 \pm 0.1$  °C, and constant stirring throughout the experiment. The light intensity was measured using a NOVA II power meter. The light power was stabilized by turning on 15 minutes prior to photocatalysis and controlled within  $1.3 - 1.7 \times 10^{-7}$  Einstein/s. Each experimental condition was repeated three times to obtain the average and standard deviation of the results.

### 3.4.6 Product Analysis from Photocatalysis.

The gas in the headspace of the quartz cell was analyzed at different time points. The gaseous products,  $\text{H}_2$  and  $\text{CO}$ , were analyzed by GC-TCD (Hewlett-Packard 7890A Series gas chromatograph) with two molsieve columns ( $30 \text{ m} \times 0.53 \text{ mm} \times 25 \mu\text{m}$  film). The 1 mL injection was split between two columns, which use  $\text{N}_2$  and He as carrier gases to measure the quantity of  $\text{H}_2$  and  $\text{CO}$ , respectively. On the other hand, the concentration of formate was determined using  $^1\text{H}$  NMR as reported in literature.<sup>25</sup> Turnover numbers (TONs) for the product were calculated as the moles of product divided by the moles of catalyst.

The carbonate product was detected using a SPECAC flow through optical cryostat (model, 21525) with a 1.12 mm path length (determined from infringing pattern),  $\text{CaF}_2$  windowed cell enclosed in a vacuum jacketed housing. For solution with  $^{12}\text{CO}_2$ , it was purged with  $^{12}\text{CO}_2$  and then brought in a glove box under a nitrogen atmosphere. For solution with  $^{13}\text{CO}_2$ , it was freeze-pump-thaw twice with  $^{13}\text{CO}_2$  with a Schlenk line and then brought in the glove box. The solutions were transferred to the SPECAC cell and then irradiated with the 470 nm LED system for 10 min. The irradiated solution was analyzed using the FTIR.

### 3.4.7 Cyclic Voltammetry (CV).

CV studies were performed using a BASi Epsilon potentiostat. A 3 mm diameter glassy carbon working electrode (BASi), a platinum (Pt) wire counter electrode, and a silver/ silver chloride (Ag/AgCl) wire separated from the bulk solution by a CoralPor tip as a pseudoreference electrode were used in a single compartment cell for all experiments. Experiments were run with and without ferrocene as an internal reference. Electrolyte solutions were composed of dry MeCN or DMF, containing 1 mM of analyte, 0.1 M TBAPF<sub>6</sub> as supporting electrolyte. The electrolyte was purged with N<sub>2</sub> or CO<sub>2</sub> for before cyclic voltammograms were recorded and stirred between successive experiments.

### 3.4.8 Infrared Spectroelectrochemistry.

The experimental method, cell design, and setup of the IR-SEC cell have been reported previously<sup>22, 40</sup>. All measurements were made with a Pine Instrument Company model AFCBP1 bipotentiostat. The IR-SEC cell is composed of GC working electrode, Ag pseudoreference electrode and Pt counter electrode. All potentials were referenced to the pseudoreference Ag/Ag<sup>+</sup>, ~+200 mV higher than the Fc/Fc<sup>+</sup> couple. The electrolyte was 0.1 M TBAPF<sub>6</sub> MeCN solution. The solution was sparged with N<sub>2</sub> or CO<sub>2</sub> and then injected into the IR-SEC cell to form a thin liquid layer for bulk electrolysis. The potential was changed stepwise and the solution was monitored with Fourier transform reflectance IR off the electrode surface over time.

### 3.4.9 Time-Correlated Single Photon Counting.

Lifetime quenching of RuBPY and RuDAC with BIH was done by taking 2 mL of ~20 μM stock solution of the corresponding ruthenium complex and diluting it with various concentrations of BIH to a total volume of 4 mL. An 8 mM of BIH stock solution was made and diluted to obtain a total concentration of 0.1, 0.2, 0.3, and 0.4 mM in the 4 mL solution. Lifetime measurements were obtained using an IBH Fluorocube instrument with a time-correlated single photon counting (TCSPC) method. A 405 nm laser excitation source was used for all lifetime measurements at room temperature.



### 3.5 Acknowledgement

**Chapter 3**, in full, comes directly from a manuscript entitled: “Improving Photocatalysis for the Reduction of CO<sub>2</sub> Through Non-Covalent Supramolecular Assemble.” by Cheung, P.L.; Kapper, S.C.; Zeng, T.; Thompson, M.E. and Kubiak, C.P., which has been published in *J. Am. Chem. Soc.* **2019**, *141*(38), 14961–14965. The dissertation author is a primary co-author of this manuscript. This work was supported by the Air Force Office of Scientific Research through AFOSR through a Basic Research Initiative (BRI) Grant (No. FA9550-12-1-0414).

### 3.6 References

1. Clark, M. L.; Cheung, P. L.; Lessio, M.; Carter, E. A.; Kubiak, C. P., Kinetic and Mechanistic Effects of Bipyridine (bpy) Substituent, Labile Ligand, and Brønsted Acid on Electrocatalytic CO<sub>2</sub> Reduction by Re(bpy) Complexes. *ACS Catal.* **2018**, *8* (3), 2021–2029.
2. Hawecker, J.; Lehn, J. M.; Ziesel, R., Electrocatalytic reduction of carbon dioxide mediated by Re(bipy)(CO)<sub>3</sub>Cl (bipy = 2,2'-bipyridine). *J. Chem. Soc., Chem. Commun.* **1984**, 328–330.
3. Hawecker, J.; Lehn, J. M.; Ziesel, R., Photochemical and Electrochemical Reduction of Carbon Dioxide to Carbon Monoxide Mediated by (2,2' - Bipyridine)tricarbonylchlororhenium(I) and Related Complexes as Homogeneous Catalysts. *Helv. Chim. Acta* **1990**, *69*, 1990–2013.
4. Koike, K.; Hori, H.; Ishizuka, M.; Westwell, J.R.; Takeuchi, K.; Ibusuki, T.; Enjouji, K.; Konno, H.; Sakamoto, K.; Ishitani, O., Key Process of the Photocatalytic Reduction of CO<sub>2</sub> Using [Re(4,4'-X<sub>2</sub>-bipyridine)(CO)<sub>3</sub>PR<sub>3</sub>]<sup>+</sup> (X = CH<sub>3</sub>, H, CF<sub>3</sub>; PR<sub>3</sub> = Phosphorus Ligands): Dark Reaction of the One-Electron-Reduced Complexes with CO<sub>2</sub>. *Organometallics* **1997**, *16*, 5724–5729.
5. Agarwal, J.; Fujita, E.; Schaefer, H.F.; Muckerman, J.T., Mechanisms for CO Production from CO<sub>2</sub> Using Reduced Rhenium Tricarbonyl Catalysts. *J. Am. Chem. Soc.* **2012**, *134*, 5180–5186.
6. Gholamkhash, B.; Mametsuka, H.; Koike, K.; Tanabe, T.; Furue, M.; Ishitani, O., Architecture of Supramolecular Metal Complexes for Photocatalytic CO<sub>2</sub> Reduction: Ruthenium–Rhenium Bi- and Tetranuclear Complexes. *Inorg. Chem.* **2005**, *44*, 2326–2336.
7. Kamata, R.; Kumagai, H.; Yamazaki, Y.; Sahara, G.; Ishitani, O., Photoelectrochemical CO<sub>2</sub> Reduction Using a Ru(II)-Re(I) Supramolecular Photocatalyst Connected to a Vinyl Polymer on a NiO Electrode. *ACS Appl. Mater. Interfaces* **2019**, *11* (6), 5632–5641.
8. Koike, K.; Grills, D.C.; Tamaki, Y.; Fujita, E.; Okubo, K.; Yamazaki, Y.; Saigo, M.; Mukuta, T.; Onda, K.; Ishitani, O., Investigation of excited state, reductive quenching, and intramolecular electron transfer

- of Ru(II)-Re(I) supramolecular photocatalysts for CO<sub>2</sub> reduction using time-resolved IR measurements. *Chem. Sci.* **2018**, *9*, 2961–2974.
9. Kumagai, H.;Sahara, G.;Maeda, K.;Higashi, M.;Abe, R.; Ishitani, O., Hybrid Photocathode Consisting of CuGaO<sub>2</sub> *p*-Type Semiconductor and a Ru(II)-Re(I) Supramolecular Photocatalyst: Non-Biased Visible-Light-Driven CO<sub>2</sub> Reduction with Water Oxidation. *Chem. Sci.* **2017**, *8*, 4242–4249.
  10. Kuramochi, Y.; Ishitani, O., Iridium(III) 1-Phenylisoquinoline Complexes as a Photosensitizer for Photocatalytic CO<sub>2</sub> Reduction: A Mixed System with a Re(I) Catalyst and a Supramolecular Photocatalyst. *Inorg. Chem.* **2016**, *55*, 5702–5709.
  11. Sato, S.;Koike, K.;Inoue, H.; Ishitani, O., Highly efficient supramolecular photocatalysts for CO<sub>2</sub> reduction using visible light. *Photochem. Photobiol. Sci.* **2007**, *6* (4), 454–461.
  12. Tamaki, Y.; Ishitani, O., Supramolecular Photocatalysts for the Reduction of CO<sub>2</sub>. *ACS Catal.* **2017**, *7* (5), 3394–3409.
  13. Tamaki, Y.;Koike, K.;Morimoto, T.;Yamazaki, Y.; Ishitani, O., Red-Light-Driven Photocatalytic Reduction of CO<sub>2</sub> using Os(II)-Re(I) Supramolecular Complexes. *Inorg. Chem.* **2013**, *52*, 11902–11909.
  14. Tamaki, Y.;Watanabe, K.;Koike, K.;Inoue, H.;Morimoto, T.; Ishitani, O., Development of highly efficient supramolecular CO<sub>2</sub> reduction photocatalysts with high turnover frequency and durability. *Faraday Discuss.* **2012**, *155*, 115–127.
  15. Ueda, Y.;Takeda, H.;Yui, T.;Koike, K.;Goto, Y.;Inagaki, S.; Ishitani, O., A Visible-Light Harvesting System for Efficient CO<sub>2</sub> Reduction Using a Supramolecular Ru(II)-Re(I) Photocatalyst Adsorbed in Periodic Mesoporous Organosilica. *ChemSusChem.* **2015**, *8*, 439–442.
  16. Tamaki, Y.;Koike, K.; Ishitani, O., Highly efficient, selective, and durable photocatalytic system for CO<sub>2</sub> reduction to formic acid. *Chem. Sci.* **2015**, *6*, 7213–7221.
  17. Porter, T. M.;Heim, G. P.; Kubiak, C. P., Stable Mixed-Valent Complexes Formed by Electron Delocalization Across Hydrogen Bonds of Pyrimidinone-Linked Metal Clusters. *J. Am. Chem. Soc.* **2018**, *140* (40), 12756–12759.
  18. Sahu, S.;Cheung, P.L.;Machan, C. W.;Chabolla, S. A.;Kubiak, C. P.; Gianneschi, N. C., Charged Macromolecular Rhenium Bipyridine Catalysts with Tunable CO<sub>2</sub> Reduction Potentials. *Chem. Eur. J.* **2017**, *23*, 8619–8622.
  19. Azcarate, I.;Costentin, C.;Robert, M.; Savéant, J.-M., Through-Space Charge Interaction Substituent Effects in Molecular Catalysis Leading to the Design of the Most Efficient Catalyst of CO<sub>2</sub>-to-CO Electrochemical Conversion. *J. Am. Chem. Soc.* **2016**, *138*, 16639–16644.
  20. Doud, M.D.;Grice, K.A.;Lilio, A.M.;Seu, C.S.; Kubiak, C. P., Versatile Synthesis of PR<sub>2</sub>NR'<sub>2</sub> Ligands for Molecular Electrocatalysts with Pendant Bases in the Second Coordination Sphere. *Organometallics* **2012**, *31*, 779–782.

21. Bays, J.T.;Priyadarshani, N.;Jeletic, M.S.;Hulley, E.B.;Miller, D.L.;Linehan, J.C.; Shaw, W.J., The Influence of the Second and Outer Coordination Spheres on Rh(diphosphine)<sub>2</sub> CO<sub>2</sub> Hydrogenation Catalysts. *ACS Catal.* **2014**, *4*, 3663–3670.
22. Machan, C. W.;Chabolla, S. A.;Yin, J.;Gilson, M. K.;Tezcan, F. A.; Kubiak, C. P., Supramolecular assembly promotes the electrocatalytic reduction of carbon dioxide by Re(I) bipyridine catalysts at a lower overpotential. *J. Am. Chem. Soc.* **2014**, *136* (41), 14598–14607.
23. Hong, D.;Tsukakoshi, Y.;Kotani, H.;Ishizuka, T.; Kojima, T., Visible-Light-Driven Photocatalytic CO<sub>2</sub> Reduction by a Ni(II) Complex Bearing a Bioinspired Tetradentate Ligand for Selective CO Production. *J. Am. Chem. Soc.* **2017**, *139* (19), 6538–6541.
24. Aranyos, V.;Hagfeldt, A.;Grennberg, H.; Figgemeier, E., Electropolymerisable bipyridine ruthenium(II) complexes: synthesis, spectroscopic and electrochemical characterisation of 4-((2-thienyl) ethenyl)- and 4,4'-di((2-thienyl) ethenyl)-2,2'-bipyridine ruthenium complexes. *Polyhedron* **2004**, *23* (4), 589-598.
25. Cheung, P. L.;Machan, C. W.;Malkhasian, A. Y.;Agarwal, J.; Kubiak, C. P., Photocatalytic Reduction of Carbon Dioxide to CO and HCO<sub>2</sub>H Using *fac*-Mn(CN)(bpy)(CO)<sub>3</sub>. *Inorg. Chem.* **2016**, *55* (6), 3192–3198.
26. Yamazaki, Y.;Takeda, H.; Ishitani, O., Photocatalytic reduction of CO<sub>2</sub> using metal complexes. *J. Photochem. Photobiol. C: Photochemistry Reviews* **2015**, *25*, 106–137.
27. Porter, T.M.;Canzi, G.C.;Chabolla, S.A.; Kubiak, C.P., Tuning Electron Delocalization and Transfer Rates in Mixed-Valent Ru<sub>3</sub>O Complexes through “Push–Pull” Effects. *J. Phys. Chem. A* **2016**, *120* (32), 6309–6316.
28. Takeda, H.;Kamiyama, H.;Okamoto, K.;Irimajiri, M.;Mizutani, T.;Koike, K.;Sekine, A.; Ishitani, O., Highly Efficient and Robust Photocatalytic Systems for CO<sub>2</sub> Reduction Consisting of a Cu(I) Photosensitiser and Mn(I) Catalysts. *J. Am. Chem. Soc.* **2018**, *140*, 17241–17254.
29. Morimoto, T.;Nakajima, T.;Sawa, S.;Nakanishi, R.;Imori, D.; Ishitani, O., CO<sub>2</sub> capture by a rhenium(I) complex with the aid of triethanolamine. *J. Am. Chem. Soc.* **2013**, *135* (45), 16825–16828.
30. Paul, A.;Connolly, D.;Schulz, M.;Pryce, M. T.; Vos, J. G. , Effect of Water during the Quantitation of Formate in Photocatalytic Studies on CO<sub>2</sub> Reduction in Dimethylformamide. *Inorg. Chem.* **2012**, *51*, 1977–1979.
31. Kuramochi, Y.;Kamiya, M.; Ishida, H., Photocatalytic CO<sub>2</sub> Reduction in *N,N*-Dimethylacetamide/Water as an Alternative Solvent System. *Inorg. Chem.* **2014**, *53*, 3326–3332.
32. Lee, S. K.;Kondo, M.;Okamura, M.;Enomoto, T.;Nakamura, G.; Masaoka, S., Function-Integrated Ru Catalyst for Photochemical CO<sub>2</sub> Reduction. *J. Am. Chem. Soc.* **2018**, *140* (49), 16899–16903.
33. Sampson, M.D.; Kubiak, C.P., Manganese Electrocatalysts with Bulky Bipyridine Ligands: Utilizing Lewis Acids To Promote Carbon Dioxide Reduction at Low Overpotentials. *J. Am. Chem. Soc.* **2016**, *138* (4), 1386–1393.

34. Arias-Rotondo, D. M.; McCusker, J. K., The photophysics of photoredox catalysis: a roadmap for catalyst design. *Chem. Soc. Rev.* **2016**, *45* (21), 5803–5820.
35. Kato, E.; Takeda, H.; Koike, K.; Ohkubo, K.; Ishitani, O., Ru(II)–Re(I) binuclear photocatalysts connected by –CH<sub>2</sub>XCH<sub>2</sub>– (X = O, S, CH<sub>2</sub>) for CO<sub>2</sub> reduction. *Chem. Sci.* **2015**, *6*, 3003–3012.
36. Kuramochi, Y.; Ishitani, O.; Ishida, H., Reaction mechanisms of catalytic photochemical CO<sub>2</sub> reduction using Re(I) and Ru(II) complexes. *Coord. Chem. Rev.* **2018**, *373*, 333–356.
37. Fraiji, L. K.; Hayes, D.M.; Werner, T.C., Static and dynamic fluorescence quenching experiments for the physical chemistry laboratory. *J. Chem. Educ.* **1992**, *69*, 424–428.
38. Ishida, H.; Tanaka, K.; Tanaka, T., Electrochemical CO<sub>2</sub> reduction catalyzed by ruthenium complexes [Ru(bpy)<sub>2</sub>(CO)<sub>2</sub>]<sup>2+</sup> and [Ru(bpy)<sub>2</sub>(CO)Cl]<sup>+</sup>. Effect of pH on the formation of CO and HCOO<sup>•</sup>. *Organometallics* **1987**, *6* (1), 181–186.
39. Hynes, M.J., EQNMR: A computer program for the calculation of stability constants from nuclear magnetic resonance chemical shift data. *J. Chem. Soc., Dalton Trans.* **1993**, 311–312.
40. Machan, C.W.; Sampson, M.D.; Chabolla, S.A.; Dang, T.; Kubiak, C.P., Developing a Mechanistic Understanding of Molecular Electrocatalysts for CO<sub>2</sub> Reduction using Infrared Spectroelectrochemistry. *Organometallics* **2014**, *33* (18), 4550–4559.

### 3.7 Appendix

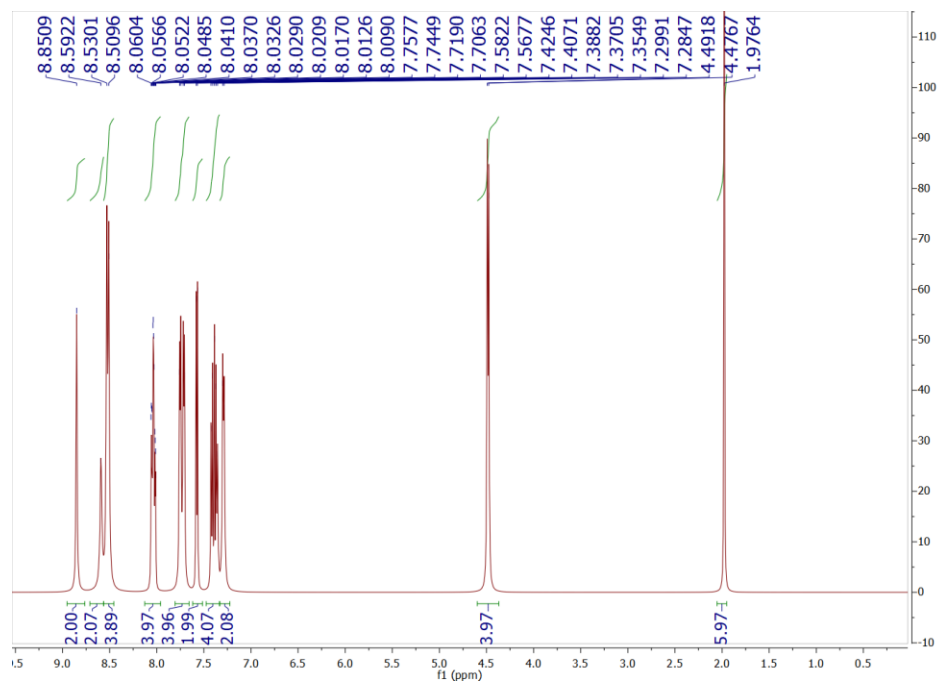


**Figure 3.8**  $^1\text{H}$  NMR spectrum of  $\text{Ru}(\text{dac})(\text{bpy})_2(\text{PF}_6)_2$  in  $\text{CD}_3\text{CN}$ . The peaks were referenced to residual solvent of  $\text{CD}_3\text{CN}$  at 1.9400 ppm.

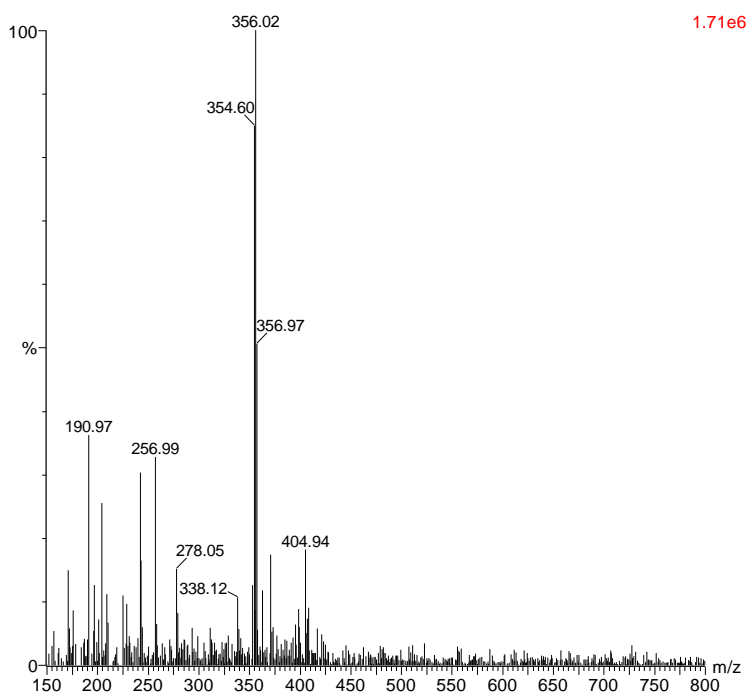


**Figure 3.9** Mass spectrum of  $\text{Ru}(\text{dac})(\text{bpy})_2(\text{PF}_6)_2$  in methanol.

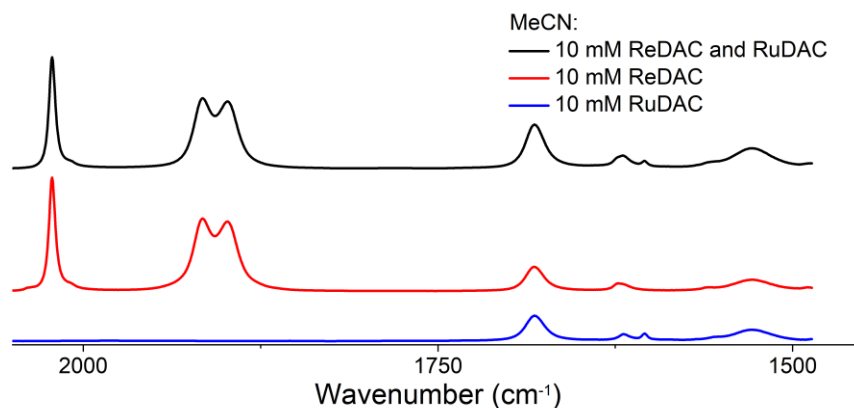


**Figure 3.10** FTIR spectra of 10 mM of ReDAC/RuDAC, ReDAC and RuDAC in dry MeCN.

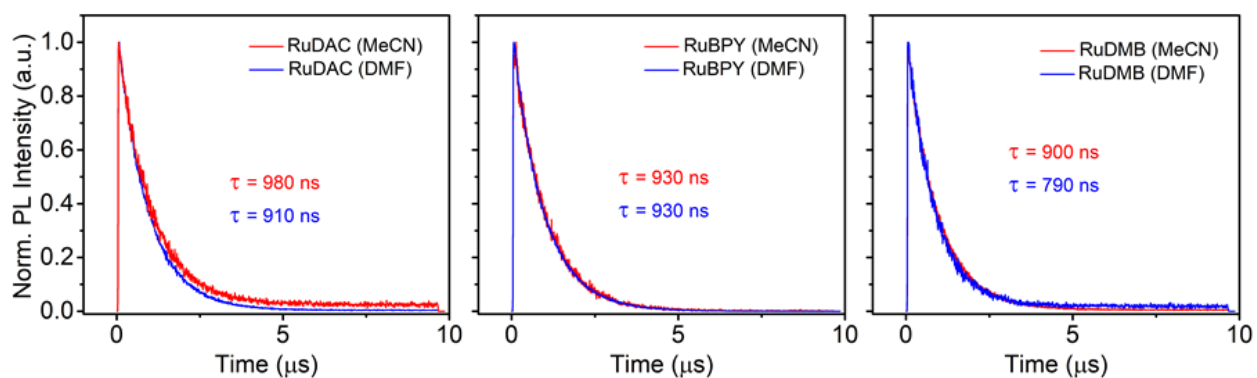


**Figure 3.11** Lifetime measurements of RuDAC, RuBPY and RuDMB in dry MeCN (red) and DMF (blue) were collected at room temperature respectively. The excitation wavelength was 405 nm and the emission wavelengths were 609 nm for RuBPY, 613 nm for RuDAC and 618 nm for RuDMB.

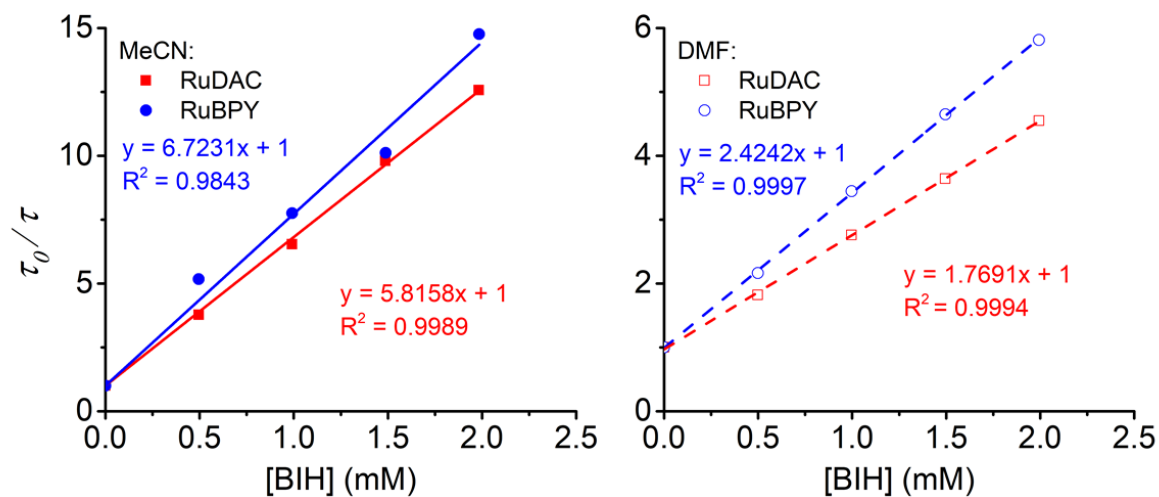


**Figure 3.12** Stern–Volmer plot measuring the change of fluorescence lifetime of RuDAC and RuBPY in the presence of BIH in dry MeCN and DMF respectively. The excitation wavelength was 405 nm and the emission wavelengths were 609 nm for RuBPY, 613 nm for RuDAC.

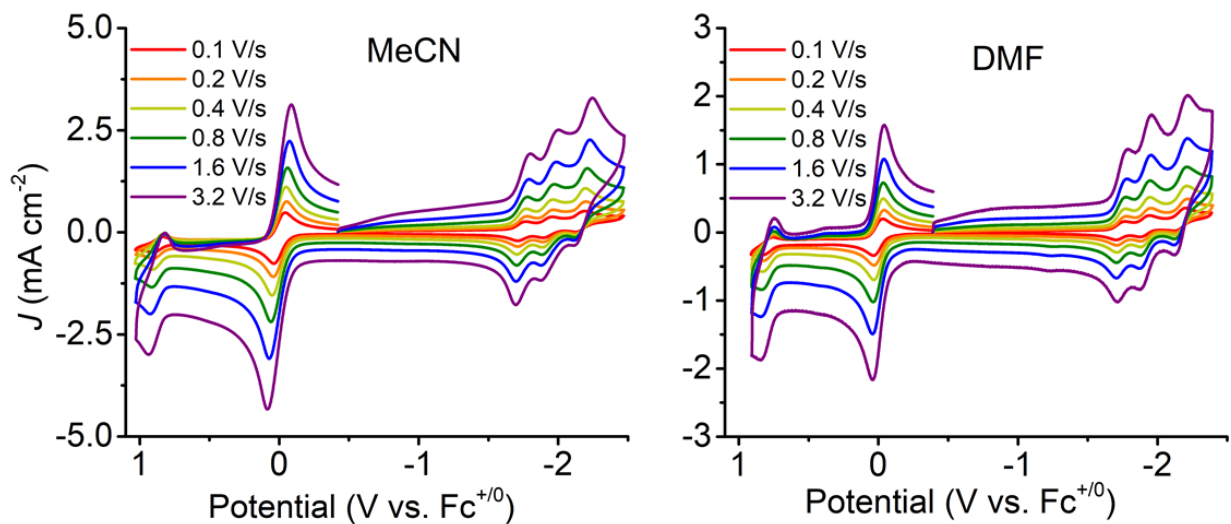


**Figure 3.13** CV of 1mM of RuDAC in dry MeCN or DMF at different scan rates under  $N_2$ .

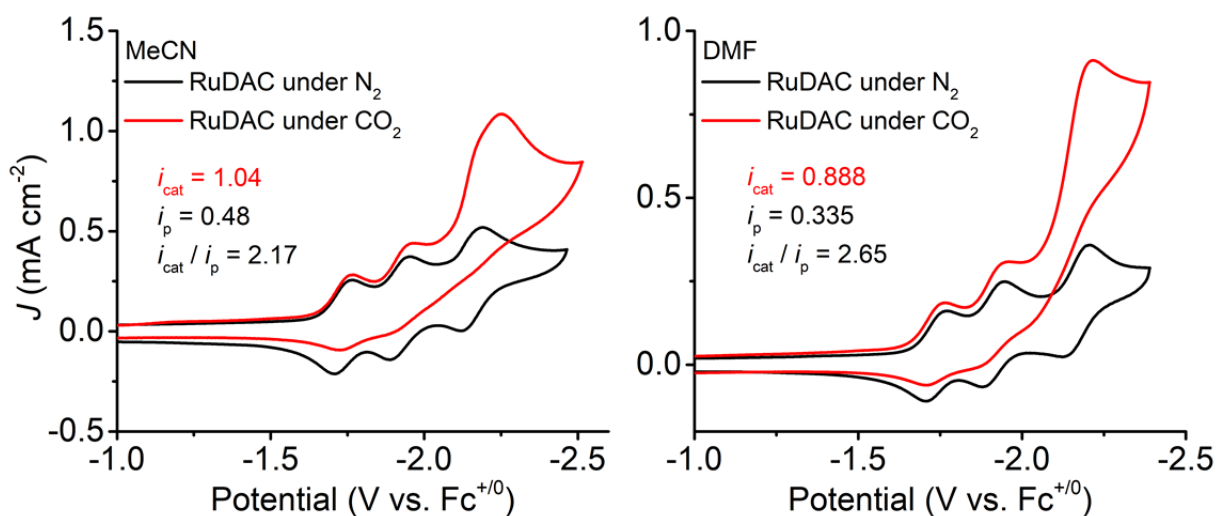


**Figure 3.14** CV of 1mM of RuDAC in dry MeCN or DMF at scan rate 100 mV/s under N<sub>2</sub> or CO<sub>2</sub>.

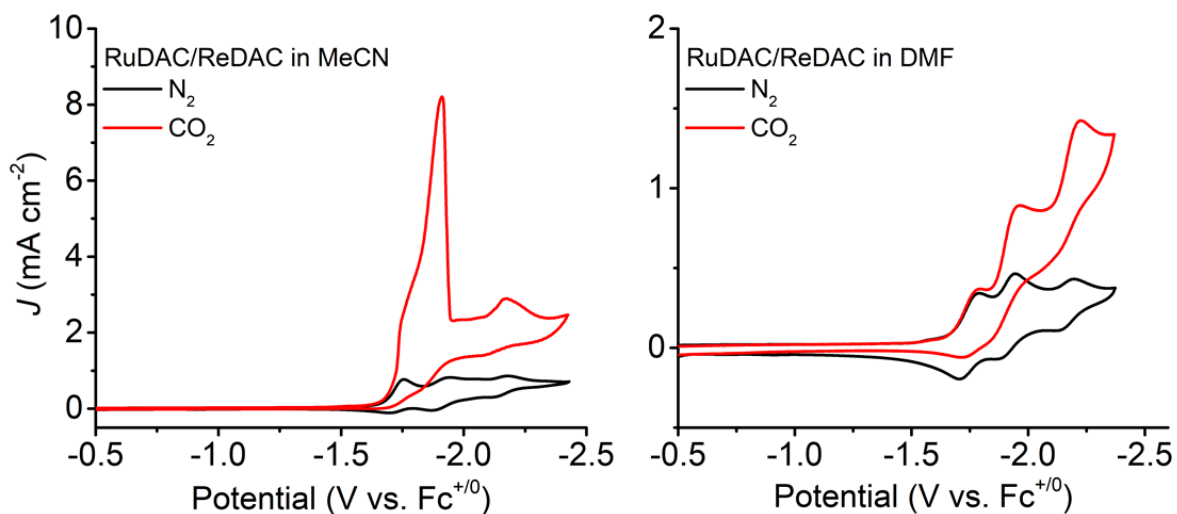
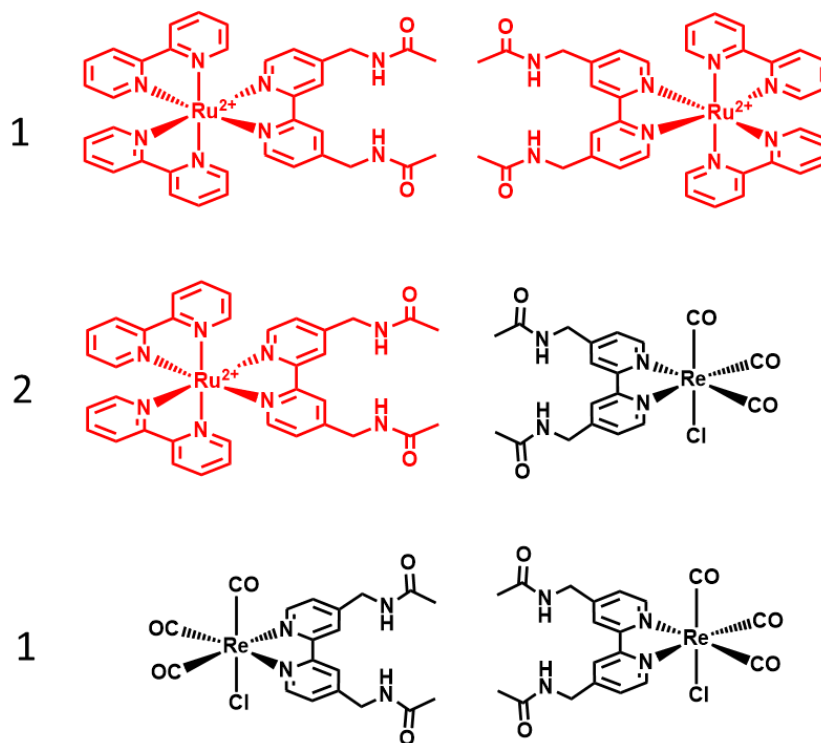


**Figure 3.15** CV of 1mM of RuDAC and 1 mM ReDAC in dry MeCN or DMF at scan rate 100 mV/s under N<sub>2</sub> or CO<sub>2</sub>.



Statistical mixture:



**Scheme 3.3** A schematic representation of statistical mixture of RuDAC and ReDAC homodimers and RuDAC/ReDAC heterodimers in the ratio of 1 : 1 : 2.

## Chapter 4

# Facile Solvent Free Synthesis of Thin Iron Porphyrin COFs on Carbon Cloth Electrodes for CO<sub>2</sub>

## Reduction

### 4.1 Introduction

Global energy demands and climate change have increased interest in the sustainable conversion of carbon dioxide (CO<sub>2</sub>) to liquid fuel precursors like carbon monoxide (CO) via electrochemical reduction<sup>1</sup>, in addition to the photochemical catalysis stated in previous chapters. Since CO<sub>2</sub> is both thermodynamically and kinetically stable, many molecular catalysts have been explored to reduce CO<sub>2</sub> at low overpotentials.<sup>2-5</sup>

Apart from manganese and rhenium bipyridine catalysts mentioned before, iron porphyrins have also been extensively studied in *N, N*-dimethylformamide (DMF) and shown to be one of the most active and selective catalysts for electrochemical CO<sub>2</sub> reduction to CO.<sup>6-8</sup> Iron(0) porphyrins, which are electrochemically generated from iron(III) porphyrins by three successive one-electron reductions, undergo

an electron-push-pull mechanism with weak Brønsted<sup>2</sup> or Lewis acids<sup>3</sup> to reduce CO<sub>2</sub> at an overpotential as low as 220 mV (Fe-*o*-TMA).<sup>9</sup> While molecular catalysts offer the advantage of synthetic tunability to optimize the thermodynamics and/or kinetics of substrate activation,<sup>4, 10-11</sup> heterogeneous catalysts are more readily incorporated into devices such as electrolyzers and fuel cells for large scale applications. Therefore, facile, tunable, and robust approaches for immobilizing molecular catalysts such as iron porphyrins to electrode surfaces represents a significant goal.

Numerous methods of attaching molecular catalysts to electrode surfaces have been explored, including covalent linkages,<sup>12-18</sup> weak physisorption, and electrostatic interactions.<sup>19-22</sup> Among these methods,  $\pi$ - $\pi$  physisorption of the aromatic molecular catalysts to carbonaceous materials are of particular interest due to the high stability, conductivity and surface area of these electrodes.<sup>22-26</sup> Recently, two-dimensional covalent organic frameworks (COFs), which are composed of covalently linked organic molecules, have been shown to be a promising platform for supporting molecular catalysts for CO<sub>2</sub> reduction in aqueous KHCO<sub>3</sub> solution.<sup>26-30</sup> COFs, designed with careful considerations of size, shape and connectivity of building blocks, have high versatility in tuning the porosity of structures and tend to exhibit high charge carrier mobilities.<sup>31-34</sup> Extensive research has been devoted to the use of cobalt(II) porphyrins as the building block for the COFs due to their planarity, high activity, and selectivity.<sup>23, 26-27, 35-39</sup> However, among the first row transition elements, cobalt metal has relatively low abundance in Earth's crust and is used heavily in the battery industry.<sup>40</sup> Iron, being the most abundant transition metal on the Earth, should generally be a more sustainable alternative to cobalt in industrial applications.<sup>41</sup> Iron(III) porphyrin COFs have been used for organic catalysis<sup>42</sup>, oxygen evolution<sup>43</sup> and hydrogen evolution<sup>44-45</sup>, but have not yet been reported for CO<sub>2</sub> reduction.

Schiff base condensations are commonly used to form strong covalent imine bonds between the amino group of the porphyrin and aldehyde group of the organic linkers.<sup>46-53</sup> Studies have shown that intramolecular hydrogen bonding strengthens the imine group of the COF network, making the COF more resistant towards hydrolysis during catalysis.<sup>33, 54</sup> Therefore, we chose 5,10,15,20-*tetra*-(4-

aminophenyl)porphyrine Fe(III) chloride (FeTAPPCI) and 2,5-dihydroxyterephthalaldehyde (Dha) to be the two component building blocks of the COF for our study (**Figure 4.1**).

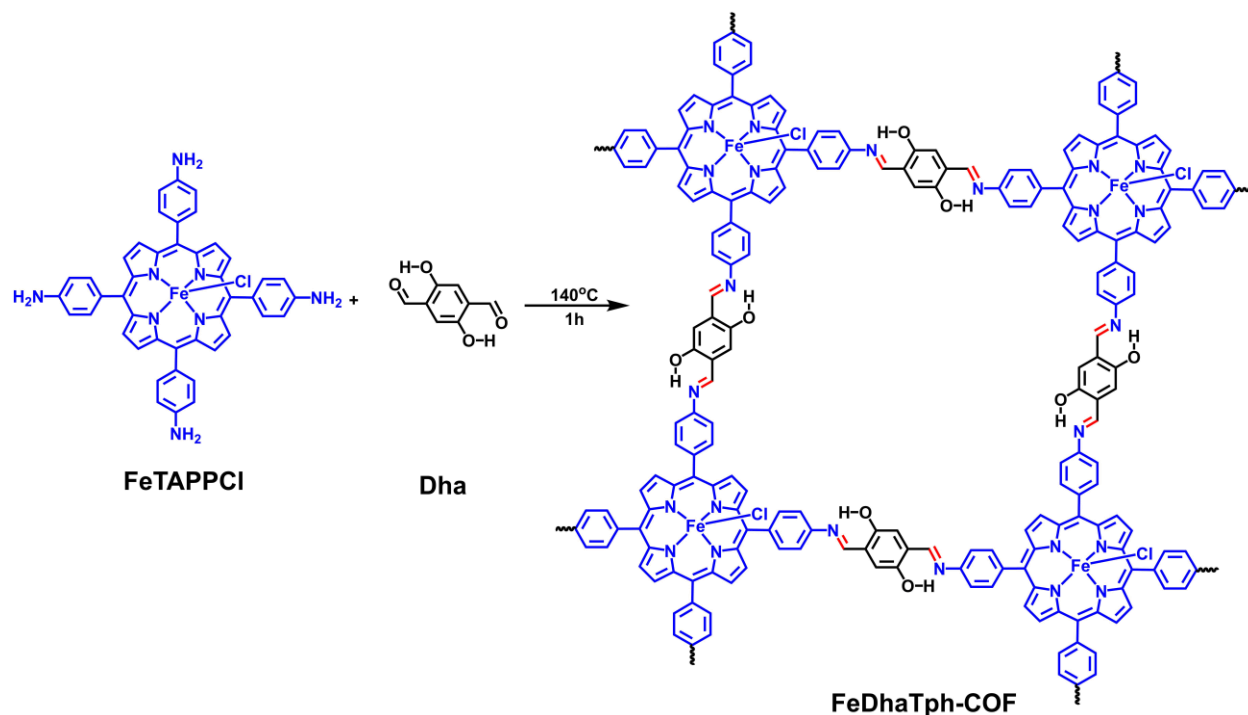


**Figure 4.1** Proposed structure of FeDhaTph-COF.

Several previous studies have explored methods to control the thickness, degree of defects, and coverage of COFs on surfaces.<sup>26-27, 55</sup> Most COFs are synthesized as powders by solvothermal methods and then drop-casted onto electrode surface for catalysis.<sup>26-27, 52</sup> In Chang's earlier work<sup>26</sup>, only 4% of the cobalt sites in the powder were found to be electroactive. Later, thin films of COF-366-Co with 250 nm thickness on highly oriented pyrolytic graphite (HOPG) substrates were prepared to ensure that the majority of the metal centers in the frameworks were electroactive.<sup>27</sup> However, the authors didn't report the cyclic voltammograms of the thin film. Thinner COFs or similar polymeric materials have been shown to exhibit properties than the thicker films.<sup>25, 56-59</sup> Homogeneous electrocatalysis usually is performed using millimolar concentrations of catalyst, of which only a small portion in the diffusion layer participates in the electrochemical process. Thin films of heterogenized electrocatalysts offer lower loading on the order of nanomoles of catalyst per square centimeter, and almost all of this can be electroactive on the surface.<sup>25</sup> As

such, catalysis is then no longer dependent on the diffusion of catalyst, but only limited by the diffusion of substrate to the electrode surface. Furthermore, heterogenized electrocatalysts are not limited by solubility of the catalysts and can be used in a variety of solvents.

In order to make thin films of COFs from iron porphyrins, we employed a facile, solvent free synthesis method adapted from other COF syntheses for STM studies.<sup>51, 60-66</sup> This ‘bottom-up’ approach offers the possibility to fabricate highly ordered COFs with controlled pore size and orientation.<sup>64</sup> In this method, the precursor molecules are introduced to the substrate surface dissolved in compatible volatile solvents, and then air-dried. At this point, the precursor molecules have not reacted chemically to produce COF. The dry samples are then heated to assemble the COFs. Since no solvent is involved during synthesis, precursors with various solvent solubilities are able to combine to form layers of COF networks on smooth surfaces like gold or HOPG<sup>51, 60-66</sup> as well as more complex surfaces like carbon cloth, as reported here. This work demonstrates a potential application of monolayer COF films coating surfaces of electrical devices, *e.g.* photovoltaic cells and fuel cells, for other electrochemical processes.

## **4.2 Results and Discussion**

### **4.2.1 Preparation of FeDhaTph COF electrodes.**

In this study, FeDhaTph-COF coated electrodes were prepared according to previously established methods.<sup>51, 60-66</sup> The optimal concentrations of iron(III) porphyrins and Dha solutions to form the COF with strongest electrochemical signals are found to be in  $10^{-3}$  M range instead of  $10^{-4}$  M suggested in many other studies. This is likely attributable to the high surface area of carbon cloth compared to smooth surfaces of gold and HOPG. The stoichiometric ratio of iron(III) porphyrins and Dha is approximately 1 : 2 and excess Dha has no significant improvement on the electrochemical performance of the COF. In addition, significant excess heating time leads to deactivation in catalytic activities of the FeTAPPCl and COF electrodes. A lower heating temperature ( $\sim 120$  °C) required longer heating time (3 hours). Therefore, all the electrodes used in chemical and electrochemical studies were synthesized by the optimal conditions

described in the experimental section. It can be seen from the SEM images (**Figure 4.2**) that FeDhaTph-COF formed a homogeneous thin film on the Si wafer.

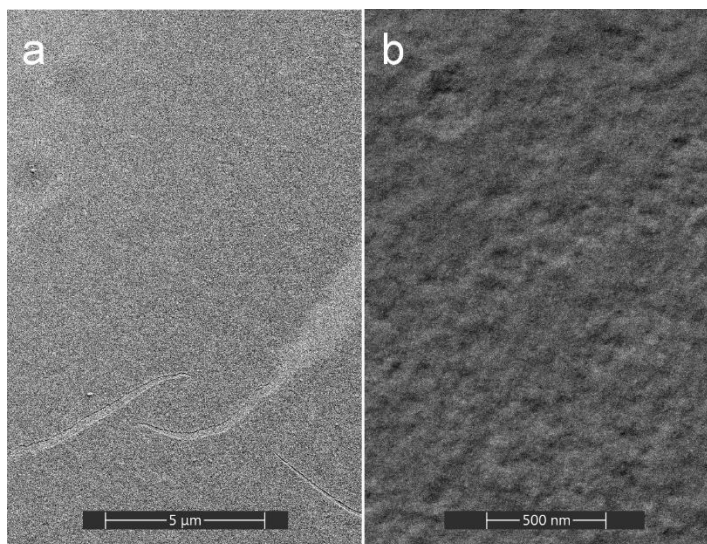


**Figure 4.2** SEM images of FeDhaTph-COF thin film on Si wafer.

#### 4.2.2 X-ray Photoelectron Spectroscopy (XPS) studies.

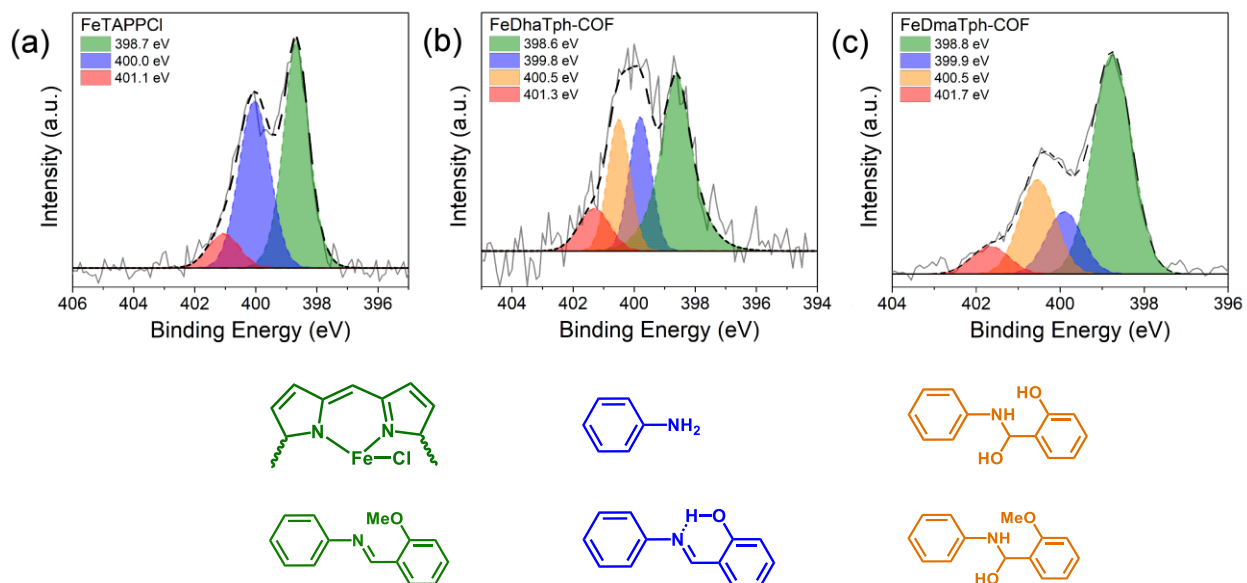


**Figure 4.3** High resolution XPS spectra of N<sub>1s</sub> signals: (a) FeTAPPCl, (b) FeDhaTph-COF and (c) FeDmaTph-COF on Au surfaces.

XPS yields N1s spectra with the binding energy specific to the nitrogen chemical and local electronic environment and hence studies the formation of 2D-COF structures. In **Figure 4.3**, the gray lines represent experimental data after background subtraction. The black dashed lines represent the simulated envelope resulting from the colored overlapping components. The molecular structures of N species are shown below the figure depict the molecular configurations of the different N electronic environments. **Figure 4.3a** shows the N1s spectrum of a film of unreacted FeTAPPCl on gold surface. This control sample is modelled with two components at 398.7 and 400.0 eV respectively. The green component (398.6 – 398.8 eV) is in agreement with the four N atoms coordinated to the central Fe<sup>III</sup> <sup>67-68</sup>, while the blue component (399.8 – 400.0 eV) is consistent with amine groups<sup>69-70</sup>. The red component observed at 401.1 – 401.7 eV corresponds to the satellite peaks of porphyrins (401 – 402 eV)<sup>70-71</sup>.

Figure 3b shows XPS spectra of FeDhaTph-COF. There is a new intense peak apparent at 400.5 eV, which indicates the hemiaminal formation<sup>69-70</sup>. The blue component has a moderate decrease from 48% to 25%, while the green component remains at around 51% (**Table 4.2**). This drop in the amine groups is consistent with the formation of hemiaminal groups in FeDhaTph-COF. Despite the imine groups having a similar range of energy (398.5 eV)<sup>72</sup> as pyrrolic nitrogens, there is no increase in the green component in FeDhaTph-COF. One possible reason is that the nitrogen in the imine bond has shifted to higher energy due to the intramolecular hydrogen bonding with the hydroxyl group. To test this hypothesis, FeDmaTph-COF (**Figure 4.20**) was synthesized and analyzed by XPS. The only difference between FeDmaTph-COF and FeDhaTph-COF is the replacement of the hydroxyl group with a methoxy group, eliminating the formation of intramolecular hydrogen bonds in FeDmaTph-COF. As expected, Figure 3c shows a decrease in peak area of the amine groups from 48% to 16%, which corresponds to the increase in the green component from around 51% to 61% and the appearance of the orange component (24%). The peak components of FeDmaTph-COF are in close agreement with those reported by Hu et al<sup>70</sup>. The XPS spectrum of FeDmaTph-COF (**Figure 4.3c**) shows that a large portion of the amine groups of FeTAPPCl are converted to imine bonds and hemiaminal groups. In the case of FeDhaTph-COF (**Figure 4.3b**), the intramolecular hydrogen-bonded imine groups have binding energies shifted by around 1 eV to around

399.8 eV, leading to a smaller reduction in the blue component compared to FeDmaTph-COF (**Figure 4.3c**). Such energy shifts by intramolecular hydrogen bonds is larger than intermolecular hydrogen bonding ( $\sim 0.6$  eV)<sup>73</sup> and smaller than protonated imine bonds ( $\sim 2$  eV)<sup>73-74</sup> as reported in literature.

#### 4.2.3 Stability of COFs by leaching test.

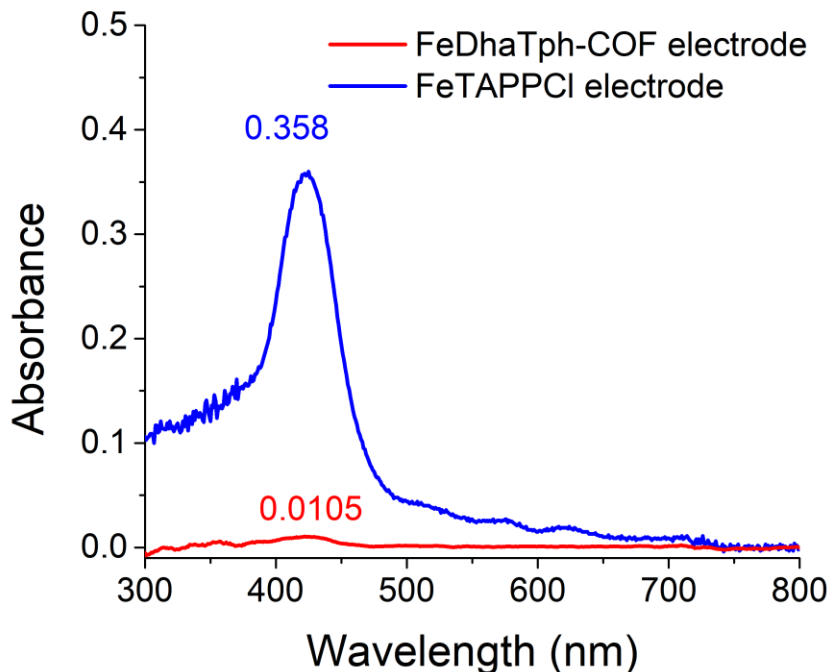


**Figure 4.4** UV-vis spectra of soaking THF solution of carbon cloth electrodes synthesized with FeTAPPCI only (blue); and with FeTAPPCI and Dha (red).

A goal of this study was to show that the formation of COFs by FeTAPPCI and Dha would prevent FeTAPPCI molecules from detaching from the surface of carbon cloth. Hence, FeTAPPCI coated carbon cloth electrodes with and without Dha, respectively, were re-soaked in a THF solution to measure the amount of leached FeTAPPCI. At the peak of the Soret band (424 nm), the absorbance of the solution exposed to carbon cloth with only FeTAPPCI is 0.424 while that of carbon cloth with FeTAPPCI and Dha is 0.00818. Using Beer's law, the concentrations of FeTAPPCI were determined to be 4.3  $\mu$ M and 0.086  $\mu$ M, respectively. As a total of 40  $\mu$ L of 1 mM of FeTAPPCI solution was added to each of the electrodes, 3.2% of FeTAPPCI is detached from the carbon cloth electrode without Dha linkers while only 0.061% of



FeTAPPCI is leached from the electrode with added Dha solution. The trace amount of FeTAPPCI leached from the COF is likely due to incomplete COF formation. Therefore, in the presence of Dha linkers, FeTAPPCI films are at least 50 times more stable on carbon cloth electrodes. This is indirect evidence of the formation of COFs on the electrode surface, whereas common characterization methods for COFs, *e.g.* powder XRD, SEM and FTIR, are not sensitive enough to observe the very thin layers of COFs, that were the subjects of this study.

#### 4.2.4 Cyclic Voltammetry (CV) of homogeneous FeTAPPCI in DMF and MeCN.

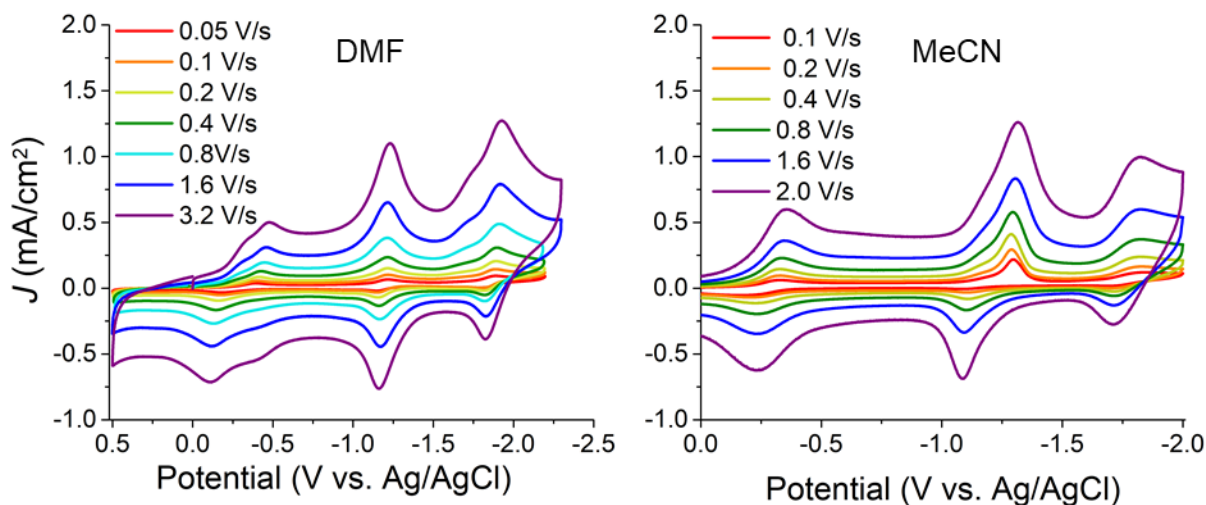


**Figure 4.5** Scan rate studies of 0.5 mM FeTAPPCI solution in dry DMF and 0.25 mM FeTAPPCI solution in dry MeCN containing 0.1 M TBAPF<sub>6</sub> under Ar respectively.

The polymerization of FeTAPPCI has been reported by repeated CV scanning,<sup>75</sup> thus, the glassy carbon electrode was polished and the counter Pt wire was heated to red-hot to remove any possible porphyrin deposition on the electrodes before each scan. The peak current is obtained by subtracting the capacitive current from the peak of current. In the absence of CO<sub>2</sub> in dry DMF, FeTAPPCI displays three successive peaks at -0.284 V, -1.177 V and -1.843 V, assigned as the Fe(III/II), Fe(II/I) and Fe(I/0) redox couples, respectively (**Figure 4.6a**). The Fe(III/II) couple has a peak-to-peak separation of 226 mV, larger than the separation of other two couples (56 mV and 66 mV respectively). This is likely due to chloride dissociation and association and is affected by scan rate and solvent environment. As shown in scan rate

studies (**Figure 4.5**), this separation increases with higher scan rate. Under CO<sub>2</sub> (**Figure 4.6b**), FeTAPPCl exhibits a slight current enhancement at the third reduction with  $i_{\text{cat}}/i_{\text{p}} = 1.4$ . When 4 % TFE was added into the CO<sub>2</sub>-saturated solution (**Figure 4.6b**), FeTAPPCl shows augmented catalytic current ( $i_{\text{cat}}/i_{\text{p}} = 63$ ). This observation is consistent with reported behavior of other iron porphyrin complexes.<sup>2, 7-9, 76-77</sup>

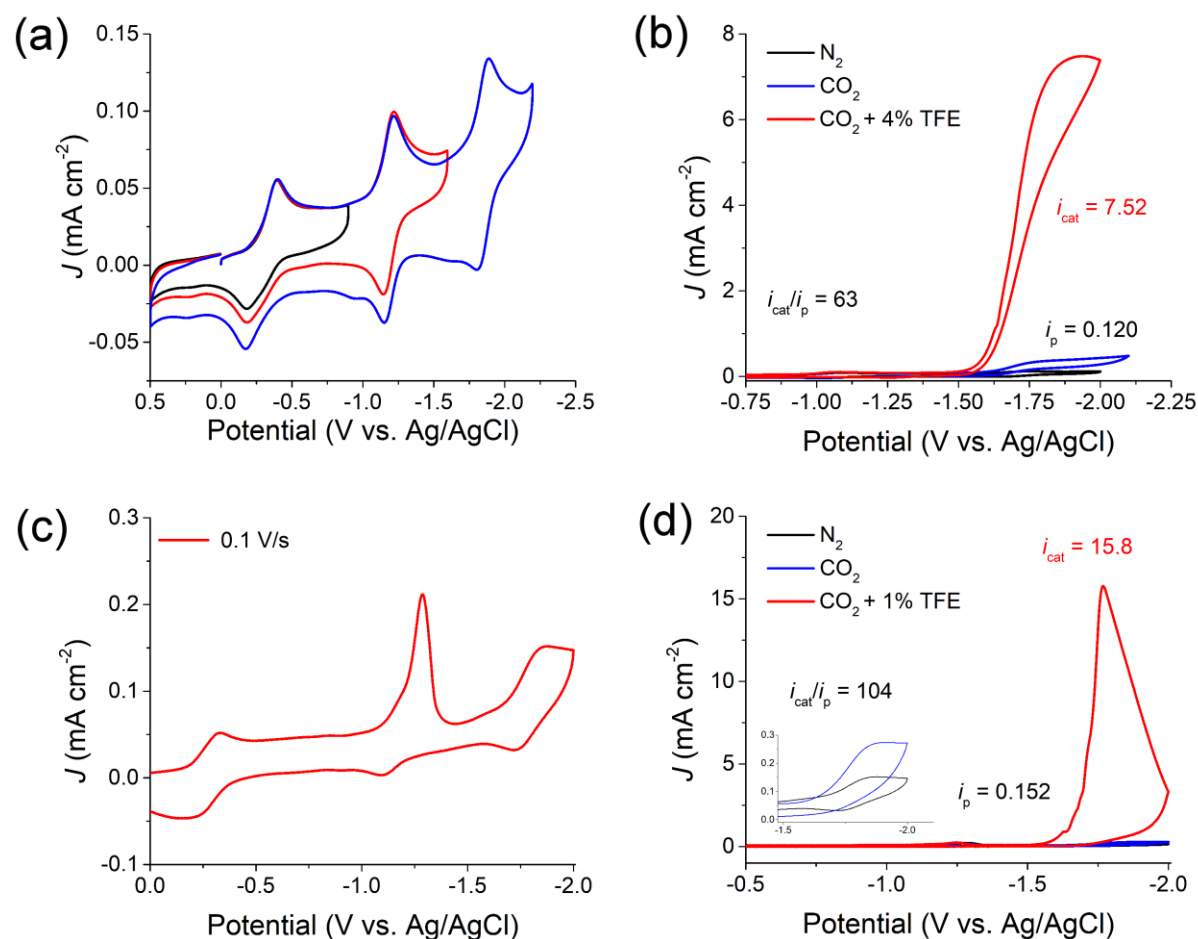


**Figure 4.6** Cyclic voltammograms of 0.5 mM of FeTAPPCl in dry DMF solution under nitrogen (a) and under CO<sub>2</sub> with added TFE (b) at scan rate 100 mV/s. CVs of 0.25 mM of FeTAPPCl in dry MeCN solution under nitrogen (c) and under CO<sub>2</sub> with added TFE (d) at scan rate 100 mV/s.

CV studies of FeTAPPCl were also performed in dry MeCN. Due to limited solubility of FeTAPPCl in MeCN, a solution of only 0.25 mM FeTAPPCl was used. Similar to CVs in dry DMF, three peaks at -0.257 V, -1.20 V and -1.81 V are assigned to be the three successive Fe(III/II), Fe(II/I) and Fe(I/0) redox couples, respectively (**Figure 4.6c**). Despite the irreversibility of the second redox couple, there is no observable polymerization upon several scans under Ar and the internal standard ferrocene peak was

fully reversible. Surprisingly, FeTAPPCl reaches maximal current enhancement ( $i_{cat} / i_p = 104$ ) at -1.77 V (vs Ag/AgCl) in the presence of only 1% TFE under CO<sub>2</sub> (**Figure 4.6d**). The rapidly decaying peak rather than stable plateau of the catalytic current (**Figure 4.6d**) is observed, which is also shown by other iron(III) porphyrin catalysts<sup>8, 78</sup>, because of secondary phenomena such as the rapid substrate depletion, inhibition by products, and deactivation of the catalysts<sup>8, 79-80</sup>. In agreement with recent work by Warren group<sup>81</sup>, MeCN appears to be a very good solvent for CO<sub>2</sub> reduction by iron porphyrins.

#### 4.2.5 Cyclic Voltammetry of FeTAPPCl and FeDhaTph-COF on carbon cloth in MeCN and DMF.

MeCN was chosen as the solvent due to lower solubility of FeTAPPCl in MeCN and higher observed catalytic CO<sub>2</sub> reduction current densities in MeCN compared to DMF. In order to remove the loosely bound FeTAPPCl molecules on the electrode surface, the electrode was transferred to a fresh electrolyte solution after three CV scans at 100 mV/s in the first electrolyte solution. The current is stable after the second CV scan without further decrease (**Figure 4.24**). All of the CV data shown in **Figure 4.7** were collected in the fresh electrolyte solution. The three typical redox couples of the FeTAPPCl electrode are observed as in homogeneous solutions (**Figure 4.7b**). Fe(II/I) and Fe(I/0) redox couples here are very similar to the homogeneous case, however, the Fe(III/II) potential shifts from -0.284 V to ~ -0.450 V, and the peak-to-peak separation increases to 640 mV. A possible reason for such a shift and separation might be chloride dissociation/association during the Fe(III/II) redox process when the FeTAPPCl molecules are on the electrode surface. Scan rate studies were performed with an increment of 25 mV/s (**Figure 4.7b**). The linear plot of reductive current of the Fe(I/0) couple against scan rate suggests that the Fe sites are attached to the electrode surface. The discrepancy in the slope also suggests quasi-reversibility. The FeTAPPCl electrode shows current enhancement under CO<sub>2</sub> and a larger current ( $i_{cat} / i_p = 33$ ) at -1.91 V vs. Ag/AgCl in the presence of TFE under CO<sub>2</sub>. However, the catalytic peak current drops notably in the second scan (**Figure 4.7a**), implying instability of the attached FeTAPPCl molecules under catalytic conditions.

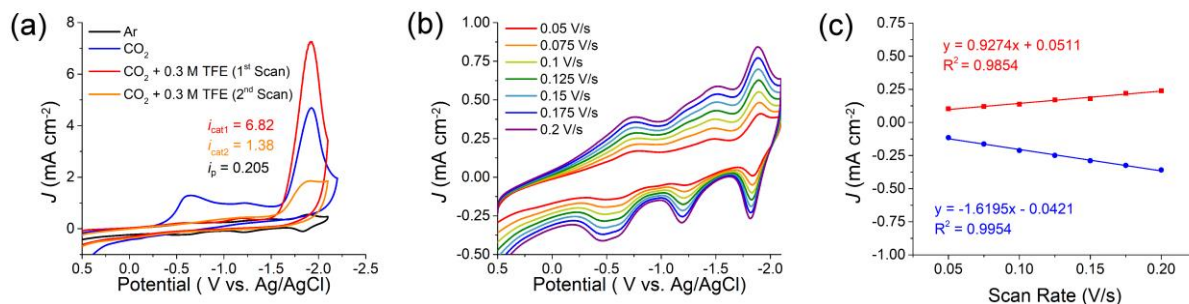


**Figure 4.7** (a) Cyclic voltammograms of a FeTAPPCI electrode in dry MeCN solution of 0.1 M TBAPF<sub>6</sub> under nitrogen, and under CO<sub>2</sub> with added TFE at scan rate 100 mV/s. (b) Scan rate studies of the FeTAPPCI electrode under nitrogen. (c) Linear plot of reductive current of Fe(I/0) couple the FeTAPPCI electrode against the scan rate.

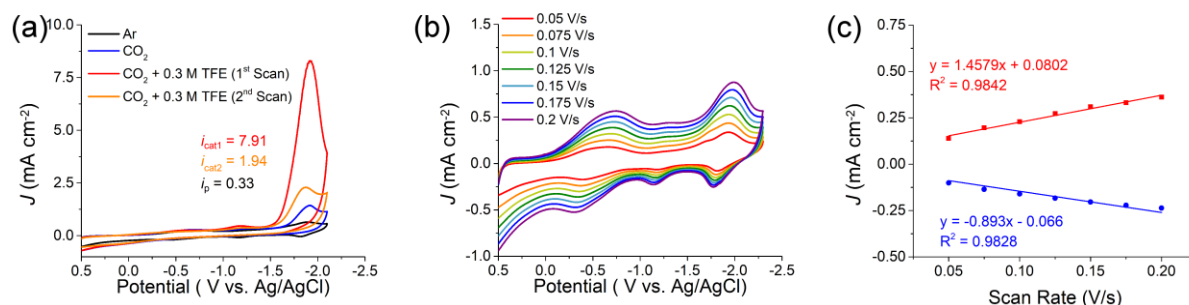


**Figure 4.8** (a) Cyclic voltammograms of the FeDhaTph-COF electrode in dry MeCN solution of 0.1 M TBAPF<sub>6</sub> under nitrogen, and under CO<sub>2</sub> with added TFE at scan rate 100 mV/s. (b) Scan rate studies of the FeDhaTph-COF electrode under nitrogen. (c) Linear plot of reductive current of Fe(I/0) couple of the FeDhaTph-COF electrode against the scan rate.

As a comparison, similar CV measurements were performed on the FeDhaTph-COF electrode in a new vial of electrolyte solution (**Figure 4.8**). The peak sizes of the three redox couples are significantly larger than those of the FeTAPP coated electrode, indicating the presence of more Fe centers on the electrode surface. The scan rate studies also reveal the linear relationship of the reductive and oxidative peak currents of the Fe(I/0) couple and the corresponding scan rates, which is indicative of a non-diffusive surface bound species. However, the quasi-reversible Fe(I/0) couple indicates that the oxidation takes place at a lower rate than reduction. We attribute this observation to side reactions such as residual proton reduction or differences in electron transfer kinetics in the film. The FeDhaTph-COF electrode shows comparable catalytic currents than the FeTAPPCI electrode. Interestingly, its catalytic activity ( $i_{cat}/i_p = 24$ )

is lower than that of the FeTAPPCl electrode despite its slightly higher current density. One possible explanation is that the rigidity of the COF framework hinders the structural changes of FeTAPPCl during catalysis, leading to lower activity. Surprisingly, most DFT calculations are focused on the electronic configurations of iron porphyrins during catalysis<sup>82-84</sup>, and no work has been done on the structural changes of porphyrin rings. In addition, greater numbers of layers of the COF compared to adsorbed FeTAPPCl, as revealed in  $i_p$  value, obstruct the accessibility to substrate in bulk solution. It therefore follows that with the addition of Dha and FeTAPPCl on carbon cloth, the result is a higher number of electroactive Fe centers compared to the addition of FeTAPPCl alone to the electrode. The Fe centers of the FeDhaTph-COF survive on the surface of the electrode even with the structural changes of the porphyrins during redox reactions, e.g. the disturbance of ring planarity and chloride dissociation.<sup>6, 82, 85-87</sup> However, the higher catalytic activity of the FeTAPPCl electrodes suggests that both quantity and activity play important roles in overall electrocatalytic properties.

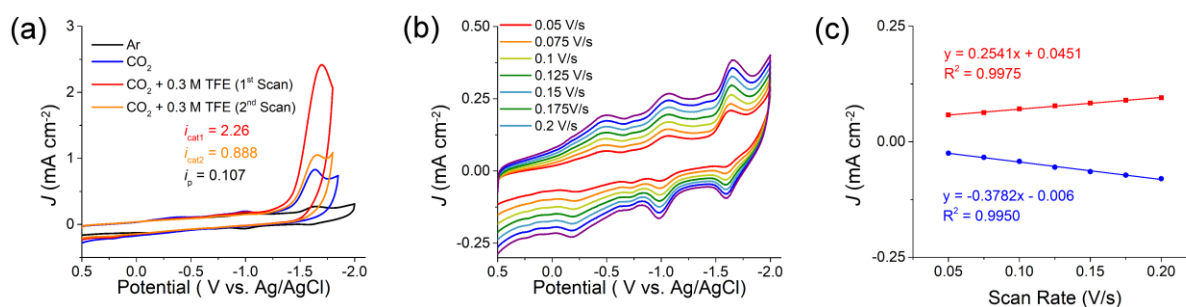


**Figure 4.9** (a) Cyclic voltammograms of a FeTAPPCl electrode in dry DMF solution of 0.1 M TBAPF<sub>6</sub> under nitrogen, and under CO<sub>2</sub> with added TFE at scan rate 100 mV/s. (b) Scan rate studies of the FeTAPPCl electrode under nitrogen. (c) Linear plot of reductive current of Fe(I/0) couple the FeTAPPCl electrode against the scan rate.

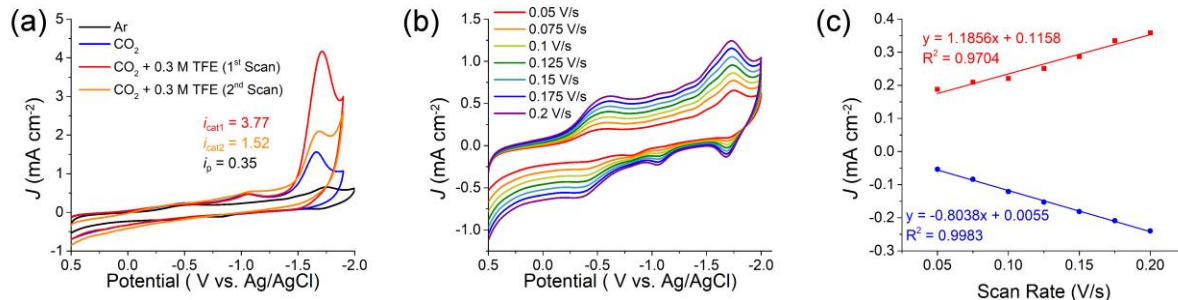


**Figure 4.10** (a) Cyclic voltammograms of the FeDhaTph-COF electrode in dry DMF solution of 0.1 M TBAPF<sub>6</sub> under nitrogen, and under CO<sub>2</sub> with added TFE at scan rate 100 mV/s. (b) Scan rate studies of the carbon cloth FeDhaTph-COF electrode under nitrogen. (c) Linear plot of reductive current of Fe(I/0) couple of the FeDhaTph-COF electrode against the scan rate.

To investigate the solvent effects on the behavior of the electrodes, analogous CV studies were conducted in DMF (**Figure 4.9** and **Figure 4.10**). A larger portion of FeTAPPCl could be washed off by rinsing the electrodes with DMF, which was also reflected in the diminished  $i_p$  of Fe (I/0) couple. In DMF, the FeTAPPCl electrode displayed a lower catalytic current ( $i_{cat} / i_p = 21$ ) than the MeCN system. Similar to the MeCN system, the FeDhaTph-COF electrode had higher peak current density but lower  $i_{cat} / i_p$  (~11) than the FeTAPPCl electrode. While there is a 200 mV positive shift of the catalytic potential in DMF (–1.70 V vs. Ag/AgCl), the electrodes exhibit lower catalytic current than those in MeCN.

The surface concentration of electroactive Fe sites was determined by cyclic voltammetry at slow scan rate (50 mV/s). The surface concentration,  $\Gamma$ , is calculated using the following equation:

$$\Gamma = \frac{Q_{CV}}{nFA} \quad \text{(Equation 4.1)}$$

Where  $n$  is the number electrons transferred for the redox couple ( $n = 1$ ),  $F$  is the Faraday constant, and  $A$  is the surface area of the electrode. Integration of the peak area in CV under the Fe(I/0) reduction wave gives the charge passed,  $Q_{CV}$  to reduce Fe (I) to Fe (0). The electroactive surface area of carbon cloth was determined by a scan rate study of Fc (I/0) couple in dry MeCN. Using the above method, the surface concentrations of Fe sites of the FeDhaTph-COF electrodes in MeCN and DMF are determined to be  $1.2 \pm 0.2$  nmol cm<sup>-2</sup> and  $1.0 \pm 0.6$  nmol cm<sup>-2</sup> respectively. Considering the size of one unit of FeDhaTph-COF to

be ca.  $6.25 \text{ nm}^{2,63,66}$ , there is approximately 40 to 50 layers of COF on the electrode in MeCN and DMF respectively. Unsurprisingly, the FeTAPPCI electrodes, which have smaller peak size of redox couples in CVs, has a lower surface concentration of  $2.2 \pm 0.4 \times 10^{-10} \text{ mol cm}^{-2}$  and  $9 \pm 2 \times 10^{-11} \text{ mol cm}^{-2}$  in MeCN and DMF respectively. As the size of FeTAPPCI molecule can be  $1.69 \text{ nm}^2$  or  $3.24 \text{ nm}^2$  depending on packing direction, there are only one to four layers of electrochemically active FeTAPPCI molecules.

#### 4.2.6 Controlled Potential Electrolysis (CPE) studies.

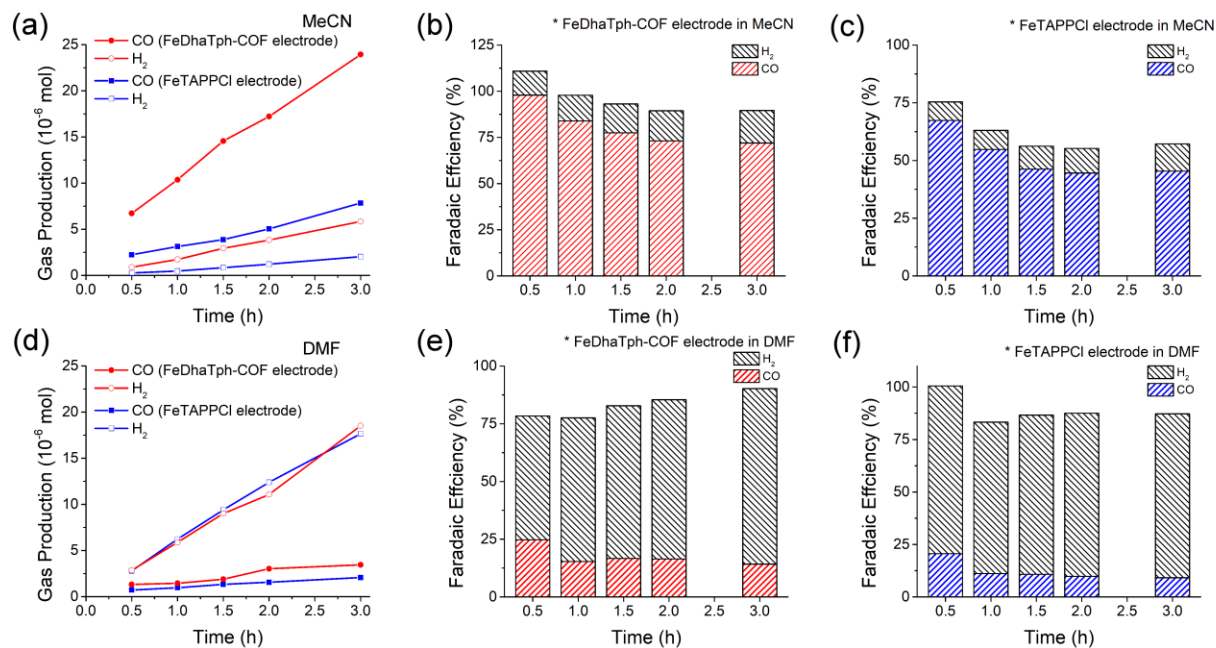


**Figure 4.11** Number of mole of CO and H<sub>2</sub> (red for FeDhaTph-COF electrode and blue for FeTAPPCI electrode) in the three hours of CPE in MeCN (a) and DMF (d). FeDhaTph-COF electrode and FeTAPPCI electrode have their Faradaic efficiencies of CO and H<sub>2</sub> plotted during CPE in MeCN (b and c) and DMF (e and f) respectively.

In controlled potential electrolysis performed in CO<sub>2</sub>-saturated MeCN solution with 0.5 M TFE under applied potential at 2.2 V (vs. Ag/AgCl), CO and H<sub>2</sub> are observed as the major products. The blank carbon cloth electrode gives 30% Faradaic efficiency for hydrogen and no observable CO production. A less negative applied potential (− 2.1 V compared to − 1.9V to vs. Ag/AgCl) leads to more hydrogen production. The average electrolysis current density is approximately 0.5 mA per cm<sup>2</sup> (geometric area) of carbon cloth electrode, with a gradual drop in current over time (**Figure 4.25**). Both of the COF electrode

and control electrode show significant decrease in catalytic current density after three hours of CPE in MeCN (**Figure 4.28**). Turnover frequency (TOF) was calculated by the number of moles of gas product produced over the number of moles of electroactive Fe centers on the electrode surface per hour. Initially, a FeDhaTph-COF electrode displays a  $\text{TOF}_{\text{CO}}$  of  $800 \text{ h}^{-1}$  per mole of Fe site in the first half hour and an average of  $600 \text{ h}^{-1}$  over three hours. The COF is rather selective for  $\text{CO}_2$  reduction over hydrogen production, with high Faradaic efficiency for CO ( $\text{FE} > 90\%$  initially and  $\text{FE} > 70\%$  after 3 hours). Even with the decrease in performance in prolonged electrolysis, it is still an efficient electrochemical carbon dioxide reduction catalyst. To date, this is the first reported COF used for  $\text{CO}_2$  reduction in MeCN. The FeTAPPCL electrode, owing to lower loading and easier detachment of Fe sites on the surface, has higher  $\text{TOF}_{\text{CO}}$  (an average of  $1300 \text{ h}^{-1}$  per mole of Fe site over three hours) but lower  $\text{FE}_{\text{CO}}$  ( $\sim 50\%$  over three hours) than the FeDhaTph-COF electrode during electrolysis. This suggests that free FeTAPPCL on carbon cloth is an active  $\text{CO}_2$  reduction catalyst. Incorporating FeTAPPCL into the COF increases the catalyst loading on the electrode surface and hence total amount of product produced (**Figure 4.11a**).

CPE experiments conducted in DMF at  $-2.1 \text{ V}$  vs. Ag/AgCl revealed an overall decreased selectivity for CO production (**Figure 4.11e f**). Both electrolysis of FeDhaTph-COF and FeTAPPCL electrodes generates more hydrogen than CO and also leads to significant decrease in catalytic current density after CPE in DMF (**Figure 4.28**). We explored the cause for this observation by ICP-OES in the following section. Lowering the applied reduction potential to less than  $-2.1 \text{ V}$  vs. Ag/AgCl also disfavors CO production. Considering the overall yield of  $\text{CO}_2$  reduction to CO, the FeDhaTph-COF electrode works better in MeCN than in DMF. The blank carbon cloth electrode under the same catalytic conditions has 100% Faradaic efficiency for hydrogen production.

Controlled potential electrolysis of the FeDhaTph-COF electrode was also performed in aqueous solution of  $0.5 \text{ M KHCO}_3$  at  $-1.3 \text{ V}$  (vs Ag/AgCl<sub>(3M NaCl)</sub>) (**Figure 4.26**). However,  $\text{H}_2$  is the major product ( $\text{FE}_{\text{H}_2} > 80\%$  and  $\text{FE}_{\text{CO}} < 20\%$ ) and CO production decreases at a faster pace than electrolysis in MeCN under these conditions. Hydrogen production prevails in water possibly because of proton reduction by the exposed carbon cloth at the center of COF unit cells outcompeting Fe COF based reduction of  $\text{CO}_2$ .



In view of the significant differences in product selectivity in MeCN and DMF, as well as the declination in catalytic activity over time, several experiments were conducted to explore the reasons leading to these observations.

#### 4.2.7 Possible reasons for declined catalytic activities.

ICP-OES analysis (**Table 4.1**) was carried out on different electrodes before and after 3 h electrolysis to determine leaching problems. With  $2.22 \pm 0.02$  nmol / cm<sup>2</sup> of Fe on the FeDhaTph-COF electrodes and  $1.2 \pm 0.2$  nmol cm<sup>-2</sup> of them being electroactive in MeCN, roughly half of the Fe sites in the COF are electroactive, which is a significant improvement compared to 4 – 8% of electroactive Co in powder form<sup>26</sup>.

**Table 4.1** Concentration of Fe sites of FeDhaTph-COF, FeTAPPCl and blank electrodes before and after 3h electrolysis in MeCN and DMF. <sup>a</sup> The concentrations of Fe are below detection limit. There is no detectable Fe concentration in the blank carbon cloth before and after CPE.

Solvent	Sample	Concentration per mg carbon cloth (ppb / mg)	Concentration per cm <sup>2</sup> carbon cloth (nmol / cm <sup>2</sup> )
MeCN	FeDhaTph-COF_beforeCPE	$11.3 \pm 0.1$	$2.41 \pm 0.02$
	FeDhaTph-COF_afterCPE	$10.4 \pm 0.1$	$2.22 \pm 0.02$
	FeTAPPCl_beforeCPE	$10.34 \pm 0.09$	$2.22 \pm 0.02$
	FeTAPPCl_afterCPE	$2.84 \pm 0.04$	$0.608 \pm 0.008$
DMF	FeDhaTph-COF_beforeCPE	$11.5 \pm 0.1$	$2.47 \pm 0.03$
	FeDhaTph-COF_afterCPE	$3.55 \pm 0.03$	$0.760 \pm 0.007$
	FeTAPPCl_beforeCPE	$7.91 \pm 0.09$	$1.70 \pm 0.02$
	FeTAPPCl_afterCPE	$0.4 \pm 0.1$	$0.08 \pm 0.02$

It is clear that the adsorbed FeTAPPCl adheres to electrodes better in MeCN than in DMF as both rinsing by DMF and electrolysis in DMF caused greater drops in Fe concentration compared to the samples treated with MeCN. This discrepancy in solubility explains the distinct difference in Faradaic efficiency for CO and H<sub>2</sub> by the FeTAPPCl electrode in DMF and MeCN (**Figure 4.11c** and **Figure 4.11f**). Interestingly, with the estimated concentration of electroactive Fe sites, 30% (MeCN) to almost all of the FeTAPPCl (DMF) that remained on the electrode surface are electroactive. In general, the FeDhaTph-COF electrodes retain more Fe than the FeTAPPCl electrodes in both MeCN and DMF (**Table 4.1**). The FeDhaTph-COF electrode shows a much smaller reduction in Fe concentration after electrolysis in MeCN compared to

DMF, likely due to lower solubility of FeTAPPCl and/or higher stability of the COF network in MeCN. We attribute these observations to be the reasons for higher CO production by the FeDhaTph-COF electrodes in MeCN.

The possibility of catalyst poisoning was ruled out by a cyclic voltammetry study under carbon monoxide. In **Figure 4.27**, the FeDhaTph electrode displayed good catalytic activity under CO<sub>2</sub> after repeated scans from 500 mV to –2200 mV after 5 min purging with CO in dry MeCN. There is also no significant current drop during CV scans under CO compared to that under Ar. Along with the ICP-OES results, a likely explanation for the decreased catalytic activity of the FeDhaTph-COF electrodes is the degradation of the organic portion of the COF network.

N1s XPS analysis of the post-CPE electrodes (**Figure 4.12b**) shows substantial decrease in the pyrrolic nitrogens. While the amine groups and hemiaminal groups remained persistent after electrolysis, the COF network seems to be able to survive the catalytic conditions. The exact reason for the loss of catalytic activity remains unclear, but it appears to be the degradation of the porphyrin part of the COF network<sup>88</sup>. DFT calculations may be helpful to determine the effects of restricted flexibility on the stability of iron porphyrins during catalysis.

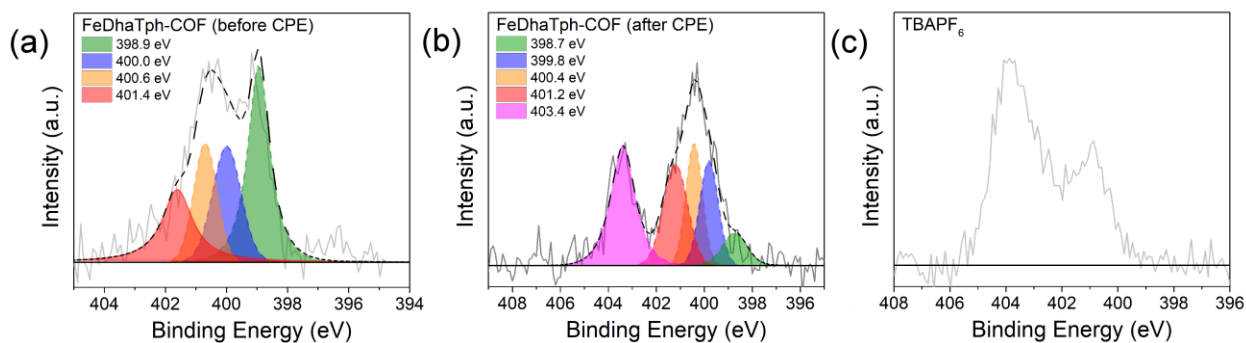


**Figure 4.12** Additional N1s XPS spectra of FeDhaTph-COF on carbon cloth (a) before and (b) after 2h CPE at –2.2 V vs. Ag/AgCl in MeCN under CO<sub>2</sub>. The N1s spectrum of TBAPF<sub>6</sub> (c) is also included. Residual TBAPF<sub>6</sub> is found in FeDhaTph-COF electrode after CPE even after thorough rinsing with MeCN. The F1s signals overlap with the Fe2p signals.

Further research should be undertaken to investigate on the degradation of COF networks and develop more robust COF thin films on electrodes. More planar metal porphyrins, *e.g.* cobalt (II)

porphyrins and copper (II) porphyrins, may be better choices for generating stronger COFs attached to electrode surfaces, as there is less puckering of the porphyrin ring upon reduction during catalysis, and this may improve structural integrity. Bimetallic systems may also be prepared by incorporating organometallic species as the linker group, providing extra sites for catalysis.<sup>53</sup> Diercks et al<sup>27</sup> attempted to grow COF-366-Co on HOPG, the study showed that the COF prefers the perpendicular orientation rather than the coplanar orientation relative to the graphite layers. Methods should be developed to control the orientation of the COF for better conductivity and structural stability.<sup>89</sup>

### 4.3 Conclusion

We have carried out an investigation of electrochemical properties of COFs consisting of iron(III) porphyrins synthesized with a facile and green solvent-free method on carbon cloth electrodes. Electrochemical characterizations of the FeDhaTph-COF electrode reveal the resemblance of the three redox couples of Fe(III/II), Fe(II/I) and Fe(I/0) to the molecular FeTAPPCl catalyst in MeCN solution, and considerable catalytic activity in the presence of 4% TFE under CO<sub>2</sub>. The FeTAPPCl electrodes show higher catalytic activity in cyclic voltammetry but the COF network helped retaining the FeTAPPCl molecules, leading to greater CO production during electrolysis in both MeCN and DMF systems. In controlled-potential studies, the FeDhaTph-COF electrode exhibits catalytic activity for CO<sub>2</sub> reduction to CO, with good TOF (> 600 h<sup>-1</sup> per mol of electroactive Fe) and fair Faradaic efficiency (average of 80%) when observed over three hours in MeCN with 0.5 M TFE. Surface XPS and ICP-OES studies demonstrate that the COF network retains FeTAPPCl molecules on the electrodes and then survives the catalytic conditions. This is the first study showing the use of COF thin films for CO<sub>2</sub> reduction in MeCN or DMF, opening a door for coating COF films on electronic devices for electrochemical applications.

### 4.4 Experimental

#### 4.4.1 Materials.

*N, N*-dimethylformamide was stored over 4 Å molecular sieves under nitrogen. Other solvents were obtained from Fisher Scientific and were degassed with argon, dried over alumina, and dispensed by a custom solvent system.

Pyrrole (Aldrich), *p*-nitrobenzaldehyde (Aldrich), SnCl<sub>2</sub>·2H<sub>2</sub>O (Alfa Aesar), sodium hydroxide (Fisher), 37% HCl (Fisher), 70% trace metal grade HNO<sub>3</sub> (Fisher Chemical), ACS Grade 30% H<sub>2</sub>O<sub>2</sub> (Columbus Chemical Industries, INC), 2,5-dimethoxyterephthalaldehyde (Aldrich), carbon monoxide (Praxair) and trifluoroethanol (Sigma Aldrich) were purchased from commercial sources and used without further purification. Silver paint 503 was purchased from Electron Microscopy Sciences. Loctite 9460 Hysol Epoxy Adhesive was purchased from Loctite. Carbon cloth (99.5% carbon) was purchased from Fuel Cell Earth LLC. Carbon dioxide and argon were purchased from Airgas. Si wafers were purchased from Silicon Valley Microelectronics, Inc.

Electrochemical measurements were collected with a BASi Epsilon electrochemical system. Ag/AgCl reference electrodes were purchased from BASi and stored in a MeCN or DMF solution containing 0.1M tetrabutylammonium hexafluorophosphate (TBAPF<sub>6</sub>) before use. The identity and purity of compounds synthesized were confirmed by FT-IR (Thermo Scientific Nicolet 6700), ATR-IR (Bruker Alpha), NMR (Varian Mercury 400) and UV-vis (Shimadzu UV-3600 UV/ vis/NIR spectrometer). Inductively coupled plasma optical emission spectroscopy (ICP-OES) data were collected with Perkin Elmer Optima 3000 DV ICP-OES. X-Ray Photoelectron Spectroscopy (XPS) were measured with SSF-Kratos AXIS-SUPRA.

#### 4.4.2 Preparation of carbon cloth electrodes.

The carbon cloth was soaked in 6 M HCl overnight to remove trace metal impurities, rinsed thoroughly with Milli-Q water, sonicated in THF for 15 minutes, and then dried in an oven at 140 °C before use. Silver paint was used to attach the Sn/Cu wire to the carbon cloth and an epoxy was used to insulate the Sn/Cu wire and the silver paste. The electrodes were air-dried overnight.

#### 4.4.3 Preparation of FeDhaTph-COF on carbon cloth electrodes.

FeTAPPCl<sup>42, 90-91</sup> and 2,5-Dihydroxyterephthalaldehyde (Dha)<sup>92-93</sup> were synthesized according to literature procedures. The synthesis of FeDhaTph-COF on carbon cloth electrodes was adapted from the literature.<sup>51, 60-66</sup> A carbon cloth electrode was dipped into a THF solution of 1 mM FeTAPPCl and air dried. Then a THF solution of 2 mM Dha was added to the electrode until it was fully wet. The electrode was air dried and heated in an oven at 140 °C for 1 hour in air and then rinsed with 1 mL of dry MeCN prior to electrochemical studies.

#### 4.4.4 Preparation of SEM samples and SEM measurements

The Si wafers ( $\sim 0.75 \times 0.5 \text{ cm}^2$ ) were cleaned with piranha solution for 15 minutes, then they were rinsed thoroughly with deionized water and finally with MilliQ water. The wafers were oven-dried at 140 °C. 5  $\mu\text{L}$  of THF solution of 1 mM FeTAPPCl and then 5  $\mu\text{L}$  of THF solution of 2 mM Dha were added to one Si wafer and then air-dried. The wafers were heated at 140 °C for 1 h.

The silica wafers were attached to a flat aluminum sample holder, and then further coated with iridium. Samples were analyzed on a FEI Apreo SEM operating at 3.0 kV.

#### 4.4.5 Preparation of XPS samples.

The microscopy glass slides ( $\sim 0.5 \times 0.5 \text{ cm}^2$ ) coated with gold (150 nm thickness) were cleaned with piranha solution for 15 minutes, then they were rinsed thoroughly with deionized water and finally with MilliQ water. The slides were oven-dried at 140 °C. 10  $\mu\text{L}$  of a THF solution of 1 mM FeTAPPCl was added to one gold slide and then air-dried. Then, 10  $\mu\text{L}$  of a THF solution of 2 mM Dha or 2,5-dimethoxyterephthalaldehyde (Dma) was added to the gold slide and then air-dried. The gold slides were heated in an oven at 140 °C for 1 hour in air. The sample coated with FeTAPPCl only was prepared using the same method but no aldehyde solution added, and no heating was applied.

#### 4.4.6 XPS experiments and analysis.

XPS experiments were performed using a Kratos AXIS-SUPRA instrument equipped with an AL K-alpha monochromatic X-ray source operating at 225W. A pass energy of 160 eV was used for survey spectrum with 1 eV step size and a pass energy of 20 eV was used for details spectra, averaged over 5 scans, with 0.1 eV step size. A charge neutralizer was used to remove build-up charge on the sample surface during XPS experiments.

XPS data were analyzed with the Casa XPS program with settings adapted from Hu's work<sup>70</sup>. Background subtraction of all XPS spectra were performed with Shirley background. All the peaks were calibrated by the intense adventitious carbon C1s peak (284.8 eV). The N1s XPS spectra were fitted with full-width-half-maximum (FWHM) values constrained within the range 0.8 – 1.2 eV, using components with Gaussian/Lorentzian line shapes. There were no constraints on energy or relative area.

#### 4.4.7 Stability leaching test.

The FeDhaTph-COF electrode was prepared in the same way described above except that a fixed amount of 40  $\mu$ L of 1 mM FeTAPPCl solution and 60  $\mu$ L of 2 mM Dha solution were used. The other electrode was covered with 40  $\mu$ L of 1 mM FeTAPPCl solution without Dha. After the two electrodes were heated, they were each soaked in 3 mL of THF for one minute. UV-vis spectra (**Figure 4.29**) were collected with these THF solutions and the peak maxima of the Soret band were compared to the calibration curve of FeTAPPCl in THF solutions (**Figure 4.30**) to calculate the concentration of FeTAPPCl released into THF solutions.

#### 4.4.8 Preparation of Inductively Coupled Plasma Optical Emission Spectroscopy (ICP-OES) samples.

The carbon cloth electrodes were rinsed with the solvent used in CPE, oven-dried, cut and weighed. Each piece of electrode was added to a pre-cleaned Teflon tube, where 1.000 mL of 70% HNO<sub>3</sub> was added. The tube was sealed and heated in an oil bath at 110 °C for 20 h. The solution was cooled and followed by addition of 0.5 mL of 30 % H<sub>2</sub>O<sub>2</sub>, the reaction was sealed and heated to 110 °C for half an hour. The

treatment with H<sub>2</sub>O<sub>2</sub> was repeated one more time. The solution was then diluted with MiliQ water and filtered to give a colorless 5% HNO<sub>3</sub> solution for ICP-OES analysis.

Samples were analyzed on a Perkin Elmer Optima 3000 DV ICP-OES in axial mode. Samples were introduced via a concentric nebulizer in conjunction with a standard cyclonic spray chamber. Samples were quantified using a five-point calibration curve.

#### **4.4.9 Cyclic voltammetry (CV) studies.**

CVs were performed using a one-compartment cell with a three-electrode configuration, which consisted of a freshly prepared carbon cloth working electrode, a Ag/AgCl reference electrode with CoralPor™ tip, and a Pt wire counter electrode in a 5 mL solution of dry MeCN containing 0.1 M TBAPF<sub>6</sub>. The solution was purged with argon for 5 minutes through a vial with dry MeCN over 4 Å molecular sieves. The electrode (> 0.5 cm<sup>2</sup>) was scanned at 100 mV/s three times to remove any trace unreacted FeTAPPCl and Dha. It was then transferred to a fresh electrolyte solution for further cyclic voltammetry studies. The electrode was scanned at 50, 75, 100, 125, 150, 175 and 200 mV/s. The solution was then purged with dry CO<sub>2</sub> for 5 minutes and several CV were collected at 100 mV/s. The effect of trifluoroethanol (TFE) as weak Brönsted acid for CO<sub>2</sub> reduction was also investigated.

#### **4.4.10 Controlled-potential electrolysis (CPE) studies.**

CPE experiments were carried out in a custom-made five-necked 89 mL pear-shaped flask, with three ground glass joints for electrodes and two joints capable of being sealed by septa for gas sparging. The working electrode was thoroughly rinsed, and cyclic voltammetry was conducted in a separate setup. The electrode was then transferred to the CPE cell, assembled by inserting a wire through a silicone rubber stopper and wrapping the wire of the carbon cloth electrode to it. The wire and epoxy parts of the carbon cloth electrode were covered with Teflon tape. A platinum wire counter electrode was separated from the bulk solution by a porous glass frit. BASi Ag/AgCl reference electrode was separated from the bulk solution by a glass sheath filled with 0.1 M TBAPF<sub>6</sub> in MeCN or DMF and capped with a CoralPor™ tip. The joints of the reference and counter electrodes were greased thoroughly and then inserted to the CPE cell and

clipped. The joints with silicone stoppers and rubber septa were sealed with electrical tape to avoid gas leakage. In the CPE cell, 20 mL of MeCN or DMF solution of 0.1 M TBAPF<sub>6</sub> and 0.5 M TFE was added and purged with dry CO<sub>2</sub> for 15 minutes prior to electrolysis. CVs were after the CPE. Gas analysis was performed using 1 mL sample injections on a Hewlett-Packard 7890A Series gas chromatograph with two molecular sieve columns (30m × 0.53mm i.d. × 25µm film). The 1 mL injection was split between the two columns, one with N<sub>2</sub> as the carrier gas and one with He to quantify both H<sub>2</sub> and CO simultaneously in each run. The amount of CO and H<sub>2</sub> gas produced was quantified by the peak areas in chromatograms.

## 4.5 Acknowledgement

**Chapter 4**, in full, comes directly from a manuscript entitled: “Facile Solvent-Free Synthesis of Thin Iron Porphyrin COFs on Carbon Cloth Electrodes for CO<sub>2</sub> Reduction.” by Cheung, P.L.; Lee, S.K. and Kubiak, C.P., which has been published in *Chem. Mater.* **2019**, *31*, 1908–1919. The dissertation author is a primary co-author of this manuscript. This work was supported by the Air Force Office of Scientific Research through AFOSR through a Basic Research Initiative (BRI) Grant (No. FA9550-12-1-0414).

## 4.6 Reference

1. Paris, REN21 Secretariat: *Renewables 2018 Global Status Report*; 2018.
2. Bhugun, I.; Lexa, D.; Savéant, J.-M., Catalysis of the Electrochemical Reduction of Carbon Dioxide by Iron(0) Porphyrins: Synergistic Effect of Weak Brønsted Acids. *J. Am. Chem. Soc.* **1996**, *118*, 1769–1776.
3. Bhugun, I.; Lexa, D.; Savéant, J.-M., Catalysis of the Electrochemical Reduction of Carbon Dioxide by Iron(0) Porphyrins. Synergistic Effect of Lewis Acid Cations. *J. Phys. Chem.* **1996**, *100*, 19981–19985.
4. Smieja, J. M.; Kubiak, C. P., Re(bipy-tBu)(CO)<sub>3</sub>Cl-improved catalytic activity for reduction of carbon dioxide: IR-spectroelectrochemical and mechanistic studies. *Inorg. Chem.* **2010**, *49* (20), 9283–9289.
5. Sampson, M.D.; Kubiak, C.P. , Manganese Electrocatalysts with Bulky Bipyridine Ligands: Utilizing Lewis Acids to Promote Carbon Dioxide Reduction at Low Overpotentials. *J. Am. Chem. Soc.* **2016**, *138* (4), 1386–1393.



6. Constant, L.A.; Davis, D.G., Electrochemical Characterization of Iron Porphyrin Complexes in Aprotic Solvents. *Anal. Chem.* **1975**, *47* (13), 2253–2260.
7. Costentin, C.;Drouet, S.;Robert, M.; Saveant, J. M., A local proton source enhances CO<sub>2</sub> electroreduction to CO by a molecular Fe catalyst. *Science* **2012**, *338* (6103), 90–94.
8. Costentin, C.;Robert, M.;Savéant, J.-M.; Tatin, A., Efficient and selective molecular catalyst for the CO<sub>2</sub> to CO electrochemical conversion in water. *Proc. Natl. Acad. Sci. U.S.A.* **2015**, *112* (22), 6882–6886.
9. Azcarate, I.;Costentin, C.;Robert, M.; Savéant, J.-M., Through-Space Charge Interaction Substituent Effects in Molecular Catalysis Leading to the Design of the Most Efficient Catalyst of CO<sub>2</sub>-to-CO Electrochemical Conversion. *J. Am. Chem. Soc.* **2016**, *138* (51), 16639–16644.
10. O'Hagan, M.;Shaw, W. J.;Raugei, S.;Chen, S.;Yang, J. Y.;Kilgore, U. J.;DuBois, D. L.; Bullock, R. M., Moving protons with pendant amines: proton mobility in a nickel catalyst for oxidation of hydrogen. *J. Am. Chem. Soc.* **2011**, *133* (36), 14301–14312.
11. Ostericher, A.L.;Waldie, K.M.; Kubiak, C.P., Utilization of Thermodynamic Scaling Relationships in Hydricity To Develop Nickel Hydrogen Evolution Reaction Electrocatalysts with Weak Acids and Low Overpotentials. *ACS Catal.* **2018**, 9596–9603.
12. Cabrera, C. R.; Abruña, H. D. , Electrocatalysis of CO<sub>2</sub> reduction at surface modified metallic and semiconducting electrodes. *J. Electroanal. Chem.* **1986**, *209* (101), 101–107.
13. O'Toole, T. R.;Sullivan, B. P.;Bruce, M. R.-M.;Margerum, L. D.;Murray, R. W.; Meyer, T. J. , Electrocatalytic reduction of CO<sub>2</sub> by a complex of rhenium in thin polymeric films. *J. Electroanal. Chem.* **1989**, *259* (217), 217–239.
14. Belanger, D.; Pinson, J., Electrografting: a powerful method for surface modification. *Chem. Soc. Rev.* **2011**, *40* (7), 3995–4048.
15. Yao, S.A.;Ruther, R. E.;Zhang, L.;Franking, R. A.;Hamers, R. J.; Berry, J. F., Covalent Attachment of Catalyst Molecules to Conductive Diamond: CO<sub>2</sub> Reduction Using “Smart” Electrodes. *J. Am. Chem. Soc.* **2012**, *134* (38), 15632–15635.
16. McCrory, C. C.;Devadoss, A.;Ottewill, X.;Lowe, R. D.;Stack, T. D.; Chidsey, C. E., Electrocatalytic O<sub>2</sub> reduction by covalently immobilized mononuclear copper(I) complexes: evidence for a binuclear Cu<sub>2</sub>O<sub>2</sub> intermediate. *J. Am. Chem. Soc.* **2011**, *133* (11), 3696–3699.
17. Sheridan, M. V.;Lam, K.; Geiger, W. E., An anodic method for covalent attachment of molecules to electrodes through an ethynyl linkage. *J. Am. Chem. Soc.* **2013**, *135* (8), 2939–2942.
18. Zhanaidarova, A.;Moore, C. E.;Gembicky, M.; Kubiak, C. P., Covalent attachment of [Ni(alkynyl-cyclam)]<sup>2+</sup> catalysts to glassy carbon electrodes. *Chem. Commun. (Camb., U.K.)* **2018**, *54* (33), 4116–4119.
19. Mann, J. A.;Rodriguez-Lopez, J.;Abruna, H. D.; Dichtel, W. R., Multivalent binding motifs for the noncovalent functionalization of graphene. *J. Am. Chem. Soc.* **2011**, *133* (44), 17614–17617.

20. Blakemore, J. D.;Gupta, A.;Warren, J. J.;Brunschwig, B. S.; Gray, H. B., Noncovalent immobilization of electrocatalysts on carbon electrodes for fuel production. *J. Am. Chem. Soc.* **2013**, *135* (49), 18288–18291.
21. Okabe, Y.;Lee, S. K.;Kondo, M.; Masaoka, S., Syntheses and CO<sub>2</sub> reduction activities of pi-expanded/extended iron porphyrin complexes. *J. Biol. Inorg. Chem.* **2017**, *22* (5), 713–725.
22. Maurin, A.; Robert, M., Noncovalent Immobilization of a Molecular Iron-Based Electrocatalyst on Carbon Electrodes for Selective, Efficient CO<sub>2</sub>-to-CO Conversion in Water. *J. Am. Chem. Soc.* **2016**, *138* (8), 2492–2495.
23. Shen, J.;Kortlever, R.;Kas, R.;Birdja, Y. Y.;Diaz-Morales, O.;Kwon, Y.;Ledezma-Yanez, I.;Schouten, K. J.;Mul, G.; Koper, M. T., Electrocatalytic reduction of carbon dioxide to carbon monoxide and methane at an immobilized cobalt protoporphyrin. *Nat. Commun.* **2015**, *6*, 8177–8184.
24. Maurin, A.; Robert, M., Catalytic CO<sub>2</sub>-to-CO conversion in water by covalently functionalized carbon nanotubes with a molecular iron catalyst. *Chem. Commun. (Camb., U.K.)* **2016**, *52* (81), 12084–12087.
25. Weng, Z.;Jiang, J.;Wu, Y.;Wu, Z.;Guo, X.;Materna, K. L.;Liu, W.;Batista, V. S.;Brudvig, G. W.; Wang, H., Electrochemical CO<sub>2</sub> Reduction to Hydrocarbons on a Heterogeneous Molecular Cu Catalyst in Aqueous Solution. *J. Am. Chem. Soc.* **2016**, *138* (26), 8076–8079.
26. Lin, S.;Diercks, C. S.;Zhang, Y. B.;Kornienko, N.;Nichols, E. M.;Zhao, Y.;Paris, A. R.;Kim, D.;Yang, P.;Yaghi, O. M.; Chang, C. J., Covalent organic frameworks comprising cobalt porphyrins for catalytic CO<sub>2</sub> reduction in water. *Science* **2015**, *349* (6253), 1208–1213.
27. Diercks, C. S.;Lin, S.;Kornienko, N.;Kapustin, E. A.;Nichols, E. M.;Zhu, C.;Zhao, Y.;Chang, C. J.; Yaghi, O. M., Reticular Electronic Tuning of Porphyrin Active Sites in Covalent Organic Frameworks for Electrocatalytic Carbon Dioxide Reduction. *J. Am. Chem. Soc.* **2018**, *140* (3), 1116–1122.
28. Liu, H.;Chu, J.;Yin, Z.;Cai, X.;Zhuang, L.; Deng, H., Covalent Organic Frameworks Linked by Amine Bonding for Concerted Electrochemical Reduction of CO<sub>2</sub>. *Chem* **2018**, *4* (7), 1696–1709.
29. Mandal, A.K.;Mahmood, J.; Baek, J.-B., Two-Dimensional Covalent Organic Frameworks for Optoelectronics and Energy Storage. *ChemNanoMat* **2017**, *3* (6), 373–391.
30. Payamyar, P.;King, B. T.;Ottinger, H. C.; Schluter, A. D., Two-dimensional polymers: concepts and perspectives. *Chem. Commun. (Camb., U.K.)* **2016**, *52* (1), 18–34.
31. Bisbey, R. P.; Dichtel, W. R., Covalent Organic Frameworks as a Platform for Multidimensional Polymerization. *ACS Cent. Sci.* **2017**, *3* (6), 533–543.
32. Chandra, S.;Kandambeth, S.;Biswal, B. P.;Lukose, B.;Kunjir, S. M.;Chaudhary, M.;Babarao, R.;Heine, T.; Banerjee, R., Chemically stable multilayered covalent organic nanosheets from covalent organic frameworks via mechanical delamination. *J. Am. Chem. Soc.* **2013**, *135* (47), 17853–17861.
33. Chen, X.;Addicoat, M.;Jin, E.;Zhai, L.;Xu, H.;Huang, N.;Guo, Z.;Liu, L.;Irlle, S.; Jiang, D., Locking covalent organic frameworks with hydrogen bonds: general and remarkable effects on crystalline structure, physical properties, and photochemical activity. *J. Am. Chem. Soc.* **2015**, *137* (9), 3241–3247.

34. Wan, S.;Gándara, F.;Asano, A.;Furukawa, H.;Saeki, A.;Dey, S. K.;Liao, L.;Ambrogio, M. W.;Botros, Y. Y.;Duan, X.;Seki, S.;Stoddart, J. F.; Yaghi, O. M., Covalent Organic Frameworks with High Charge Carrier Mobility. *Chem. Mater.* **2011**, *23* (18), 4094–4097.
35. Quezada, D.;Honores, J.;García, M.;Armijo, F.; Isaacs, M., Electrocatalytic reduction of carbon dioxide on a cobalt tetrakis(4-aminophenyl)porphyrin modified electrode in BMImBF<sub>4</sub>. *New J. Chem.* **2014**, *38* (8), 3606–3612.
36. Aoi, S.;Mase, K.;Ohkubo, K.; Fukuzumi, S., Selective electrochemical reduction of CO<sub>2</sub> to CO with a cobalt chlorin complex adsorbed on multi-walled carbon nanotubes in water. *Chem. Commun.* **2015**, *51* (50), 10226–10228.
37. Manbeck, G. F.; Fujita, E., A review of iron and cobalt porphyrins, phthalocyanines and related complexes for electrochemical and photochemical reduction of carbon dioxide. *J. Porphyr. Phthalocyanines* **2015**, *19* (01-03), 45–64.
38. Hu, X. M.;Ronne, M. H.;Pedersen, S. U.;Skrydstrup, T.; Daasbjerg, K., Enhanced Catalytic Activity of Cobalt Porphyrin in CO<sub>2</sub> Electroreduction upon Immobilization on Carbon Materials. *Angew. Chem., Int. Ed.* **2017**, *56* (23), 6468–6472.
39. Yao, C. L.;Li, J. C.;Gao, W.; Jiang, Q., An Integrated Design with new Metal-Functionalized Covalent Organic Frameworks for the Effective Electroreduction of CO<sub>2</sub>. *Chem. Eur. J.* **2018**, *24* (43), 11051–11058.
40. Nitta, N.;Wu, F.;Lee, J.T.; Yushin, G., Li-ion battery materials: present and future. *Mater. Today* **2015**, *18* (5), 252–264.
41. Allkgre, C.J.;Poirier, J.P.;Humler, E.; Hofmann, A.W., The chemical composition of the Earth *Earth Planet. Sci. Lett.* **1995**, *134*, 515–526
42. Singh, M.K.; Bandyopadhyay, D., Design and synthesis of nanoporous perylene bis-imide linked metalloporphyrin frameworks and their catalytic activity. *J. Chem. Sci.* **2016**, *128* (1), 1–8.
43. Huang, H.;Li, F.;Zhang, Y.; Chen, Y., Two-dimensional graphdiyne analogue Co-coordinated porphyrin covalent organic framework nanosheets as a stable electrocatalyst for the oxygen evolution reaction. *J. Mater. Chem. A* **2019**, *7*, 5575–5582.
44. Bhunia, S.;Das, S. K.;Jana, R.;Peter, S. C.;Bhattacharya, S.;Addicoat, M.;Bhaumik, A.; Pradhan, A., Electrochemical Stimuli-Driven Facile Metal-Free Hydrogen Evolution from Pyrene-Porphyrin-Based Crystalline Covalent Organic Framework. *ACS Appl. Mater. Interfaces* **2017**, *9* (28), 23843–23851.
45. Patra, B.C.;Khilari, S.;Manna, R.N.;Mondal, S.;Pradhan, D.;Pradhan, A.; Bhaumik, A., A Metal-Free Covalent Organic Polymer for Electrocatalytic Hydrogen Evolution. *ACS Catal.* **2017**, *7* (9), 6120–6127.
46. Xu, L.;Zhou, X.;Yu, Y.;Tian, W.Q.;Ma, J.; Lei, S., Surface-Confined Crystalline Two-Dimensional Covalent Organic Frameworks via on-Surface Schiff-Base Coupling. *ACS Nano* **2013**, *7* (9), 8066–8073.
47. Yu, Y.;Sun, J.; Lei, S., Surface-Confined Synthesis of One-Dimensional Schiff Base Polymers Investigated by Scanning Tunneling Microscopy. *J. Phys. Chem. C* **2015**, *119* (29), 16777–16784.

48. Xu, L.; Yu, Y.; Lin, J.; Zhou, X.; Tian, W. Q.; Nieckarz, D.; Szabelski, P.; Lei, S., On-surface synthesis of two-dimensional imine polymers with a tunable band gap: a combined STM, DFT and Monte Carlo investigation. *Nanoscale* **2016**, *8* (16), 8568–8574.
49. Yu, Y.; Zheng, Y.; Lei, S., From a Two-Dimensional Supramolecular Network to One-Dimensional Covalent Polymer at the Liquid/Solid Interface: Insight into the Role of the Stoichiometric Ratio of the Precursors. *J. Phys. Chem. C* **2017**, *121* (1), 593–599.
50. Gou, X.; Zhang, Q.; Wu, Y.; Zhao, Y.; Shi, X.; Fan, X.; Huang, L.; Lu, G., Preparation and engineering of oriented 2D covalent organic framework thin films. *RSC Adv.* **2016**, *6* (45), 39198–39203.
51. Yue, J. Y.; Liu, X. H.; Sun, B.; Wang, D., The on-surface synthesis of imine-based covalent organic frameworks with non-aromatic linkage. *Chem. Commun. (Camb., U.K.)* **2015**, *51* (76), 14318–14321.
52. Segura, J. L.; Mancheno, M. J.; Zamora, F., Covalent organic frameworks based on Schiff-base chemistry: synthesis, properties and potential applications. *Chem. Soc. Rev.* **2016**, *45* (20), 5635–5671.
53. Johnson, E. M.; Haiges, R.; Marinescu, S. C., Covalent Organic Frameworks Composed of Rhenium Bipyridine and Metal Porphyrins: Designing Heterobimetallic Frameworks with Two Distinct Metal Sites. *ACS Appl. Mater. Interfaces* **2018**, *10* (44), 37919–37927.
54. Kandambeth, S.; Shinde, D. B.; Panda, M. K.; Lukose, B.; Heine, T.; Banerjee, R., Enhancement of chemical stability and crystallinity in porphyrin-containing covalent organic frameworks by intramolecular hydrogen bonds. *Angew. Chem., Int. Ed.* **2013**, *52* (49), 13052–13056.
55. Fu, Z.; Xu, G., Crystalline, Highly Oriented MOF Thin Film: the Fabrication and Application. *Chem. Rec.* **2017**, *17* (5), 518–534.
56. Dong, R.; Zheng, Z.; Tranca, D. C.; Zhang, J.; Chandrasekhar, N.; Liu, S.; Zhuang, X.; Seifert, G.; Feng, X., Immobilizing Molecular Metal Dithiolene-Diamine Complexes on 2D Metal-Organic Frameworks for Electrocatalytic H<sub>2</sub> Production. *Chem.: Eur. J.* **2017**, *23* (10), 2255–2260.
57. Dong, R.; Pfeiffermann, M.; Liang, H.; Zheng, Z.; Zhu, X.; Zhang, J.; Feng, X., Large-area, free-standing, two-dimensional supramolecular polymer single-layer sheets for highly efficient electrocatalytic hydrogen evolution. *Angew. Chem., Int. Ed.* **2015**, *54* (41), 12058–12063.
58. Zhang, K. D.; Tian, J.; Hanifi, D.; Zhang, Y.; Sue, A. C.; Zhou, T. Y.; Zhang, L.; Zhao, X.; Liu, Y.; Li, Z. T., Toward a single-layer two-dimensional honeycomb supramolecular organic framework in water. *J Am Chem Soc* **2013**, *135* (47), 17913–17918.
59. Cui, D.; MacLeod, J. M.; Ebrahimi, M.; Perepichka, D. F.; Rosei, F., Solution and air stable host/guest architectures from a single layer covalent organic framework. *Chem. Commun. (Cambridge, U. K.)* **2015**, *51* (92), 16510–16513.
60. Lackinger, M., On-surface polymerization - a versatile synthetic route to two-dimensional polymers. *Polym. Int.* **2015**, *64* (9), 1073–1078.
61. Spitzer, S.; Rastgoo-Lahrood, A.; Macknapp, K.; Ritter, V.; Sotier, S.; Heckl, W. M.; Lackinger, M., Solvent-free on-surface synthesis of boroxine COF monolayers. *Chem. Commun. (Camb., U.K.)* **2017**, *53* (37), 5147–5150.

62. Dienstmaier, J.F.;Gigler, A.M.;Goetz, A.J.;Knochel, P.;Bein, T.;Lyapin, A.;Reichlmaier, S.;Heckl, W.M.; Lackinger, M., Synthesis of Well-Ordered COF Monolayers Surface Growth of Nanocrystalline Precursors versus Direct on surface polycondensation. *ACS Nano* **2011**, *5* (12), 9737–9745.
63. Liu, X. -H.;Yue, J.-Y.;Mo, Y.-P.;Yao, Y.;Zeng, C.;Chen, T.;Yan, H.-J.;Wang, Z.-H.;Wang, D.; Wan, L.-J., Surface Host–Guest Supramolecular Assemblies on Porphyrin-Based Covalent Organic Grids. *J. Phys. Chem. C* **2016**, *120* (29), 15753–15757.
64. Liu, X. H.;Guan, C. Z.;Wang, D.; Wan, L. J., Graphene-like single-layered covalent organic frameworks: synthesis strategies and application prospects. *Adv. Mater.* **2014**, *26* (40), 6912–6920.
65. Yu, L.;Li, Z. B.; Wang, D., Construction of boronate ester based single-layered covalent organic frameworks. *Chem. Commun. (Camb., U.K.)* **2016**, *52* (95), 13771–13774.
66. Chen, C.;Joshi, T.;Li, H;Chavez, A. D.;Pedramrazi, Z.;Liu, P.-N.;Li, H.;Dichtel, W. R.;Bredas, J.-L.; Crommie, M. F., Local Electronic Structure of a Single-Layer Porphyrin-Containing Covalent Organic Framework. *ACS Nano* **2017**, *12* (1), 385–391.
67. Huang, J-W.;Liu, Z.-L.;Gao, X.-R.;Yang, D.;Peng, X.-Y.; Ji, L.-N., Hydroxylation of cyclohexane catalyzed by iron(III)-metal-free porphyrin dimer with molecular oxygen: The effect of the steric hindrance and the intramolecular interaction between the two porphyrin rings *J. Mol. Catal. Chem. A: Chemical* **1996**, *111*, 261–266.
68. Gojković, S.L.;Gupta, S.; Savinell, R.F., Heat-Treated Iron(III) Tetramethoxyphenyl Porphyrin Supported on High-Area Carbon as an Electrocatalyst for Oxygen Reduction I. Characterization of the Electrocatalyst. *J. Electrochem. Soc.* **1998**, *145*, 3493–3499.
69. Di Giovannantonio, M.;Kosmala, T.;Bonanni, B.;Serrano, G.;Zema, N.;Turchini, S.;Catone, D.;Wandelt, K.;Pasini, D.;Contini, G.; Goletti, C., Surface–Enhanced Polymerization via Schiff-Base Coupling at the Solid–Water Interface under pH Control. *J. Phys. Chem. C* **2015**, *119* (33), 19228–19235.
70. Hu, Y.;Goodeal, N.;Chen, Y.;Ganose, A. M.;Palgrave, R. G.;Bronstein, H.; Blunt, M. O., Probing the chemical structure of monolayer covalent-organic frameworks grown via Schiff-base condensation reactions. *Chem. Commun.* **2016**, *52* (64), 9941–9944.
71. Nemykin, V. N.;Galloni, P.;Floris, B.;Barrett, C. D.;Hadt, R. G.;Subbotin, R. I.;Marrani, A. G.;Zanoni, R.; Loim, N. M., Metal-free and transition-metal tetraferrocenylporphyrins part 1: synthesis, characterization, electronic structure, and conformational flexibility of neutral compounds. *Dalton Trans.* **2008**, (32), 4233–4246.
72. Mahat, M. M.;Mawad, D.;Nelson, G. W.;Fearn, S.;Palgrave, R. G.;Payne, D. J.; Stevens, M. M., Elucidating the deprotonation of polyaniline films by X-ray photoelectron spectroscopy. *J. Mater. Chem. C* **2015**, *3* (27), 7180–7186.
73. Stevens, J. S.;Byard, S. J.;Seaton, C. C.;Sadiq, G.;Davey, R. J.; Schroeder, S. L., Proton transfer and hydrogen bonding in the organic solid state: a combined XRD/XPS/ssNMR study of 17 organic acid-base complexes. *Phys. Chem. Chem. Phys.* **2014**, *16* (3), 1150–1160.
74. Stevens, J. S.;Newton, L. K.;Jaye, C.;Muryn, C. A.;Fischer, D. A.; Schroeder, S. L. M., Proton Transfer, Hydrogen Bonding, and Disorder: Nitrogen Near-Edge X-ray Absorption Fine Structure and X-ray

- Photoelectron Spectroscopy of Bipyridine–Acid Salts and Co-crystals. *Cryst. Growth Des.* **2015**, *15* (4), 1776–1783.
75. Cornejo, G.;Ramírez, G.;Villagrán, M.;Costamagna, J.;Trollund, E.; Aguirre, M.J. , Electropolymerization and Electrocatalytic Behavior of Electrodes Modified with Fe and Non-Metalled Tetraaminophenylporphyrins: Effect of the Position of the Amino Group on the Ligand. *J. Chil. Chem. Soc.* **2003**, *48*, 49–55.
76. Tatin, A.;Comminges, C.;Kokoh, B.;Costentin, C.;M., Robert.; Savéant, J.-M., Efficient electrolyzer for CO<sub>2</sub> splitting in neutral water using earth-abundant materials. *Proc. Natl. Acad. Sci. U.S.A.* **2016**, *113* (20), 5526–5529.
77. Azcarate, I.;Costentin, C.;Robert, M.; Savéant, J.-M., Dissection of Electronic Substituent Effects in Multielectron–Multistep Molecular Catalysis. Electrochemical CO<sub>2</sub>-to-CO Conversion Catalyzed by Iron Porphyrins. *J. Phys. Chem. C* **2016**, *120* (51), 28951–28960.
78. Costentin, C.;Passard, G.;Robert, M.; Savéant, J.-M., Ultraefficient homogeneous catalyst for the CO<sub>2</sub>-to-CO electrochemical conversion. *Proc. Natl. Acad. Sci. U.S.A.* **2014**, *111* (42), 14990–14994.
79. Costentin, C.;Drouet, S.;Robert, M.; Saveant, J. M., Turnover numbers, turnover frequencies, and overpotential in molecular catalysis of electrochemical reactions. Cyclic voltammetry and preparative-scale electrolysis. *J. Am. Chem. Soc.* **2012**, *134* (27), 11235–11242.
80. Costentin, C.;Drouet, S.;Passard, G.;Robert, M.; Saveant, J. M., Proton-coupled electron transfer cleavage of heavy-atom bonds in electrocatalytic processes. Cleavage of a C-O bond in the catalyzed electrochemical reduction of CO<sub>2</sub>. *J. Am. Chem. Soc.* **2013**, *135* (24), 9023–9031.
81. Sinha, S.; Warren, J. J., Unexpected Solvent Effect in Electrocatalytic CO<sub>2</sub> to CO Conversion Revealed Using Asymmetric Metalloporphyrins. *Inorg. Chem.* **2018**, *57* (20), 12650–12656.
82. Romelt, C.;Song, J.;Tarrago, M.;Rees, J. A.;van Gastel, M.;Weyhermuller, T.;DeBeer, S.;Bill, E.;Neese, F.; Ye, S., Electronic Structure of a Formal Iron(0) Porphyrin Complex Relevant to CO<sub>2</sub> Reduction. *Inorg. Chem.* **2017**, *56* (8), 4746–4751.
83. Romelt, C.;Ye, S.;Bill, E.;Weyhermuller, T.;van Gastel, M.; Neese, F., Electronic Structure and Spin Multiplicity of Iron Tetraphenylporphyrins in Their Reduced States as Determined by a Combination of Resonance Raman Spectroscopy and Quantum Chemistry. *Inorg. Chem.* **2018**, *57* (4), 2141–2148.
84. Costentin, C.;Savéant, J.-M.; Tard, C., Ligand "noninnocence" in coordination complexes vs. kinetic, mechanistic, and selectivity issues in electrochemical catalysis. *Proc. Natl. Acad. Sci. U.S.A.* **2018**, *115* (37), 9104–9109.
85. Marboutin, L.;Desbois, A.; Berthomieu, C., Low-Frequency Heme, Iron-Ligand, and Ligand Modes of Imidazole and Imidazolate Complexes of Iron Protoporphyrin and Microperoxidase in Aqueous Solution. An Analysis by Far-Infrared Difference Spectroscopy. *J. Phys. Chem. B* **2009**, *113*, 4492–4499.
86. Kadish, K.M.;Larson, G.;Lexa, D.; Momenteau, M. , Electrochemical and Spectral Characterization of the Reduction Steps of *p*-Oxo-bis( iron tetraphenylporphyrin) Dimer in Dimethylformamide. *J. Am. Chem. Soc.* **1975**, *97* (2), 282–288.

87. Hu, C.;Noll, B.C.;Schulz, C.E.; Scheidt, W.R. , Four-Coordinate Iron(II) Porphyrinates: Electronic Configuration Change by Intermolecular Interaction. *Inorg. Chem.* **2007**, *46*, 619–621.
88. Hammouche, M.;Lexa, D.;Momenteau, M.; Savéant, J.-M., Chemical catalysis of electrochemical reactions. Homogeneous catalysis of the electrochemical reduction of carbon dioxide by iron(0) porphyrins. Role of the addition of magnesium cations. *J. Am. Chem. Soc.* **1991**, *113* (22), 8455–8466.
89. Sahabudeen, H.;Qi, H.;Glatz, B. A.;Tranca, D.;Dong, R.;Hou, Y.;Zhang, T.;Kuttner, C.;Lehnert, T.;Seifert, G.;Kaiser, U.;Fery, A.;Zheng, Z.; Feng, X., Wafer-sized multifunctional polyimine-based two-dimensional conjugated polymers with high mechanical stiffness. *Nat. Commun.* **2016**, *7*, 13461–13468.
90. Xu, X.L.;Lin, F.-W.;Xu, W.;Wu, J.; Xu, Z.K., Highly Sensitive INHIBIT and XOR Logic Gates Based on ICT and ACQ Emission Switching of a Porphyrin Derivative. *Chem. Eur. J.* **2014**, *21*, 984–987.
91. Bettelheim, A.;White, B.A.;Raybuck, S.A.; Murray, R.W., Electrochemical Polymerization of Amino-, Pyrrole-, and Hydroxy-Substituted Tetraphenylporphyrins *Inorg. Chem.* **1987**, *26*, 1009–1017.
92. Jin, F.;Cai, Z.-B.;Huang, J.-Q.;Li, S.-L.; Tian, Y.-P., Investigation of two-photon absorption properties in new A–D–A compounds emitting blue and yellow fluorescence. *J. Mol. Struct.* **2015**, *1093*, 33–38.
93. Jeon, S.;Park, S.;Nam, J.;Kang, Y.; Kim, J. M., Creating Patterned Conjugated Polymer Images Using Water-Compatible Reactive Inkjet Printing. *ACS Appl. Mater. Interfaces* **2016**, *8* (3), 1813–1818.

## 4.7 Appendix

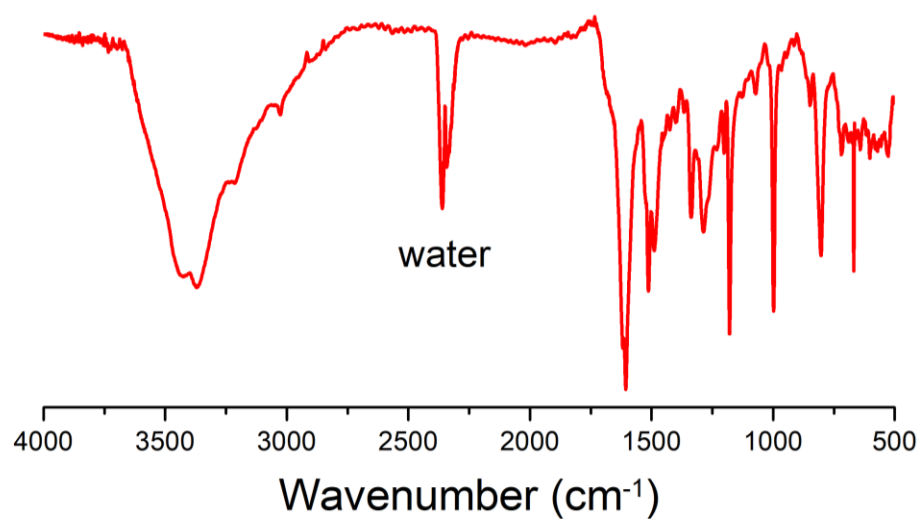


**Figure 4.13** FT-IR spectrum of iron(III) 5,10,15,20-tetrakis-(4'-aminophenyl)porphyrin chloride (FeTAPPCl) in KBr. FT-IR ( $\nu$ ;  $\text{cm}^{-1}$ ): 3427, 3370, 1700, 1617, 1606, 1513, 1488, 1286, 1179, 998 ( $\delta\text{Fe-N}$ ), 802, 722.

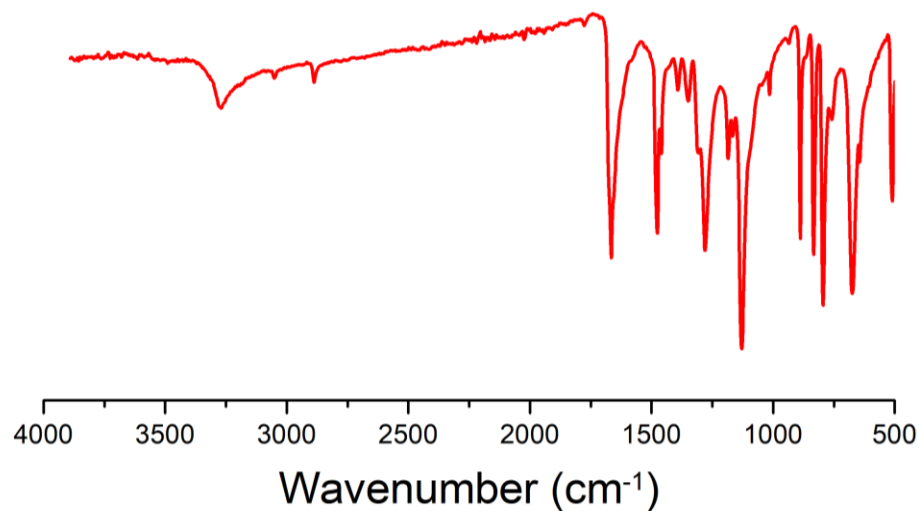


**Figure 4.14** ATR-IR spectrum of 2,5-dihydroxyterephthalaldehyde (Dha). ATR-IR ( $\nu$ ;  $\text{cm}^{-1}$ ): 3269, 1666, 1477, 1460, 1280, 1129, 888, 833, 795, 674.



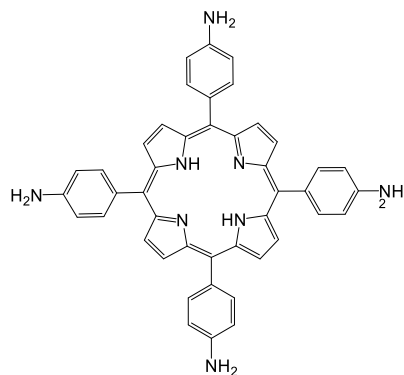
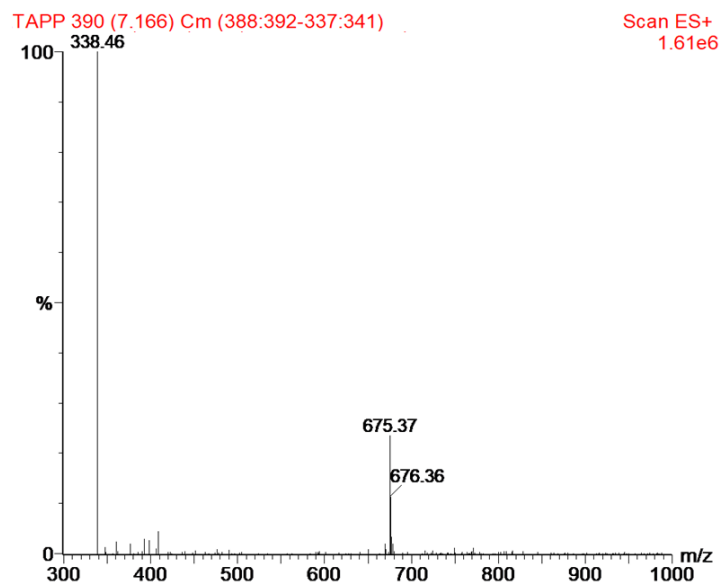


**Figure 4.15** Mass spectrum of 5,10,15,20-tetrakis(4'-aminophenyl)porphyrin (TAPP) m/z calcd for  $C_{44}H_{34}N_8$ , 675.30  $[M+H]^+$ ; found, 675.37  $[M+H]^+$ .

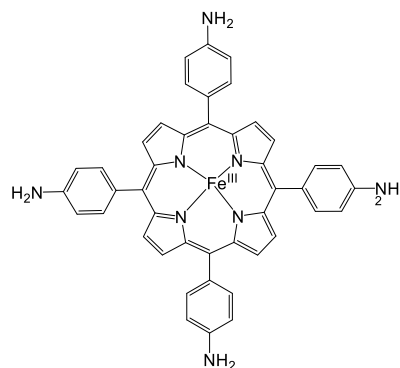
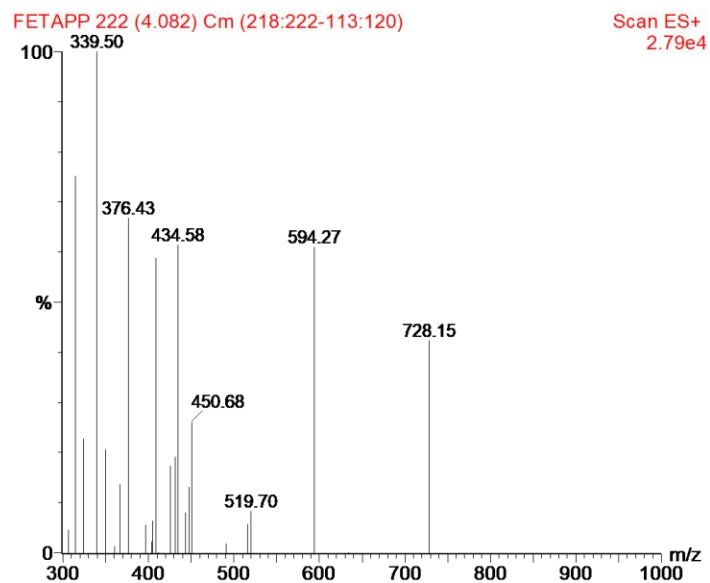


**Figure 4.16** Mass spectrum of FeTAPPCl m/z calcd for  $C_{44}H_{32}N_8Fe$ , 728.21  $[M-Cl]^+$ ; found, 728.15  $[M-Cl]^+$ .

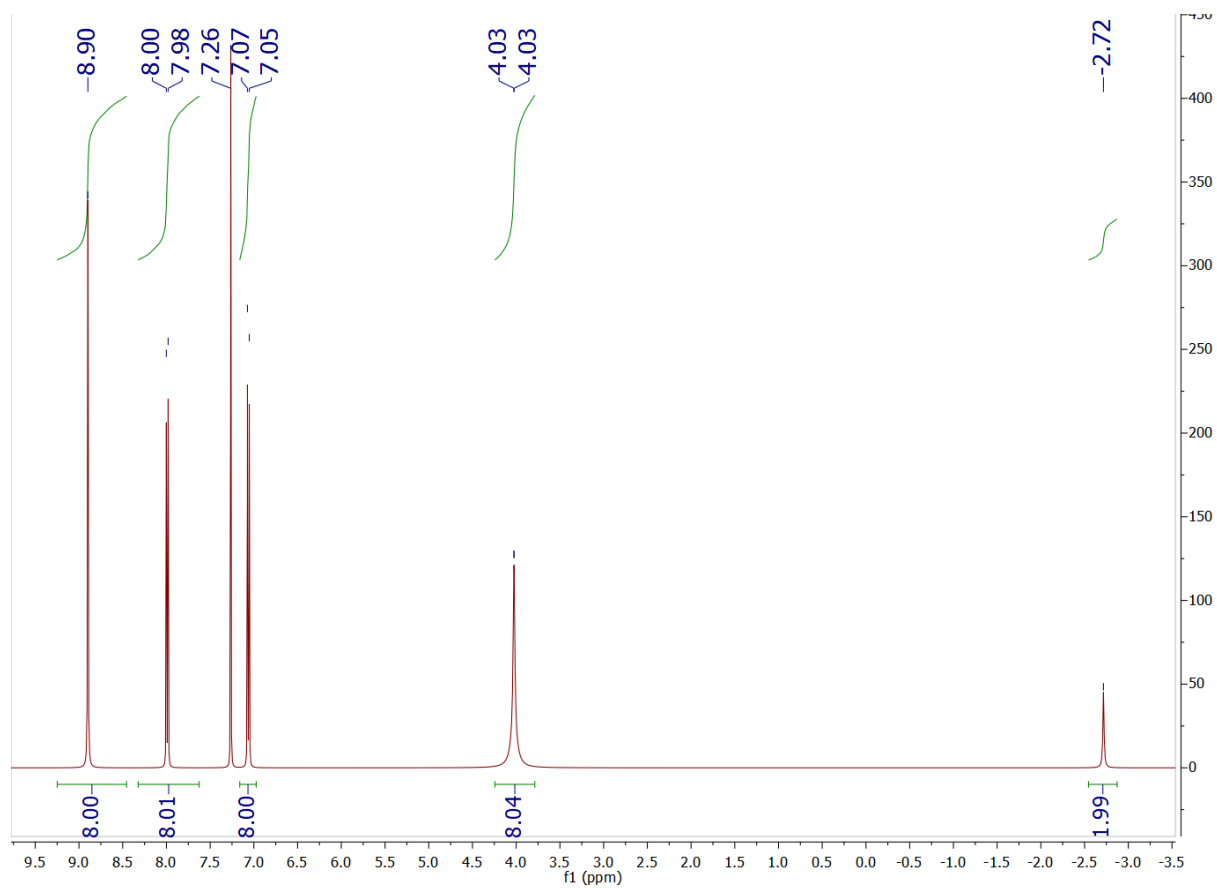


**Figure 4.17**  $^1\text{H}$  NMR ( $\text{CDCl}_3$ , 400 MHz) of FeTAPPCl:  $\delta$  (ppm)  $-2.72$ (s, 2H, NH), 4.02 (s, 8H,  $\text{NH}_2$ ), 7.05-.707 (d, 8H,  $J = 8.0$  Hz, aromatics), 7.98-8.00 (d, 8H,  $J = 8.0$  Hz, aromatics), 8.90 (s, 8H, H-pyrrole).

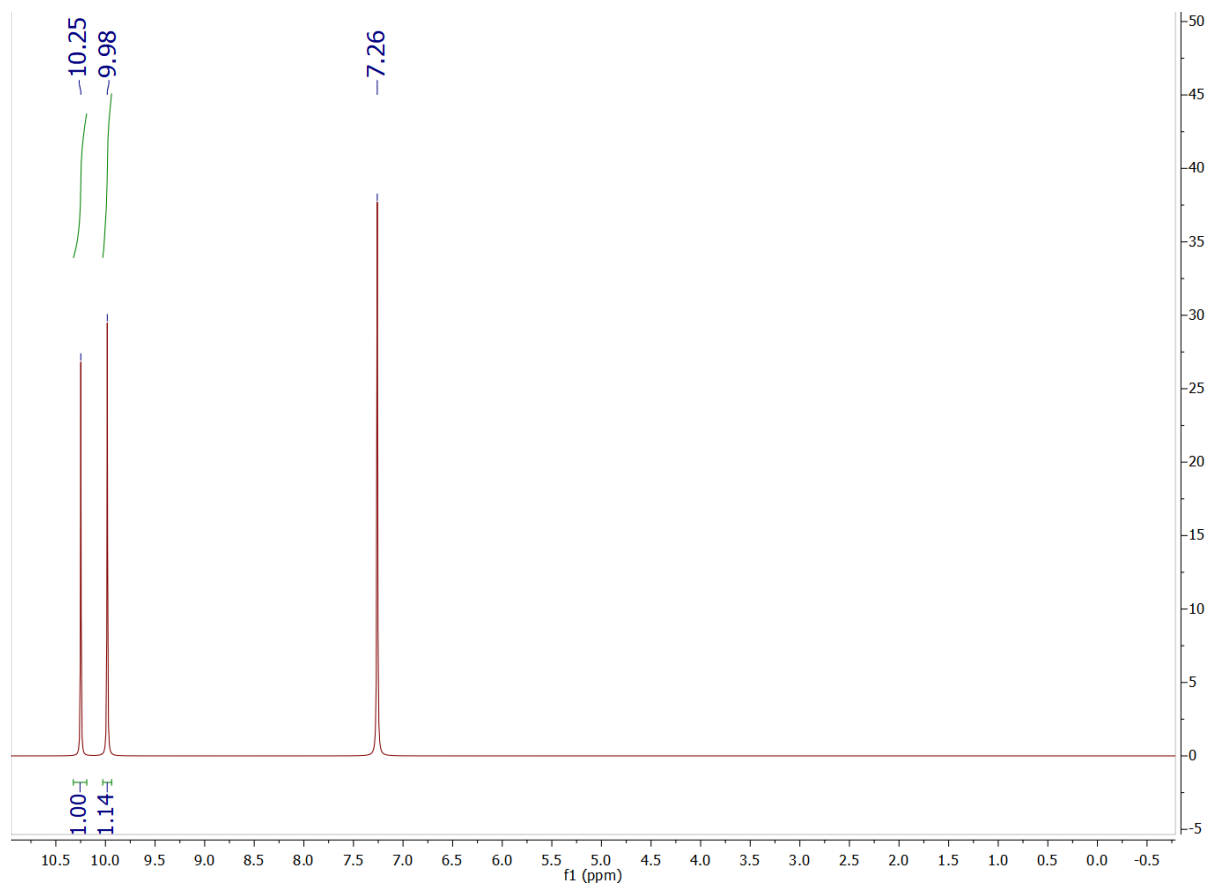


**Figure 4.18** <sup>1</sup>H NMR (CDCl<sub>3</sub>, 400 MHz) of Dha: δ (ppm) 10.23 (s, 1H), 9.96 (s, 1H), 7.24 (s, 1H).

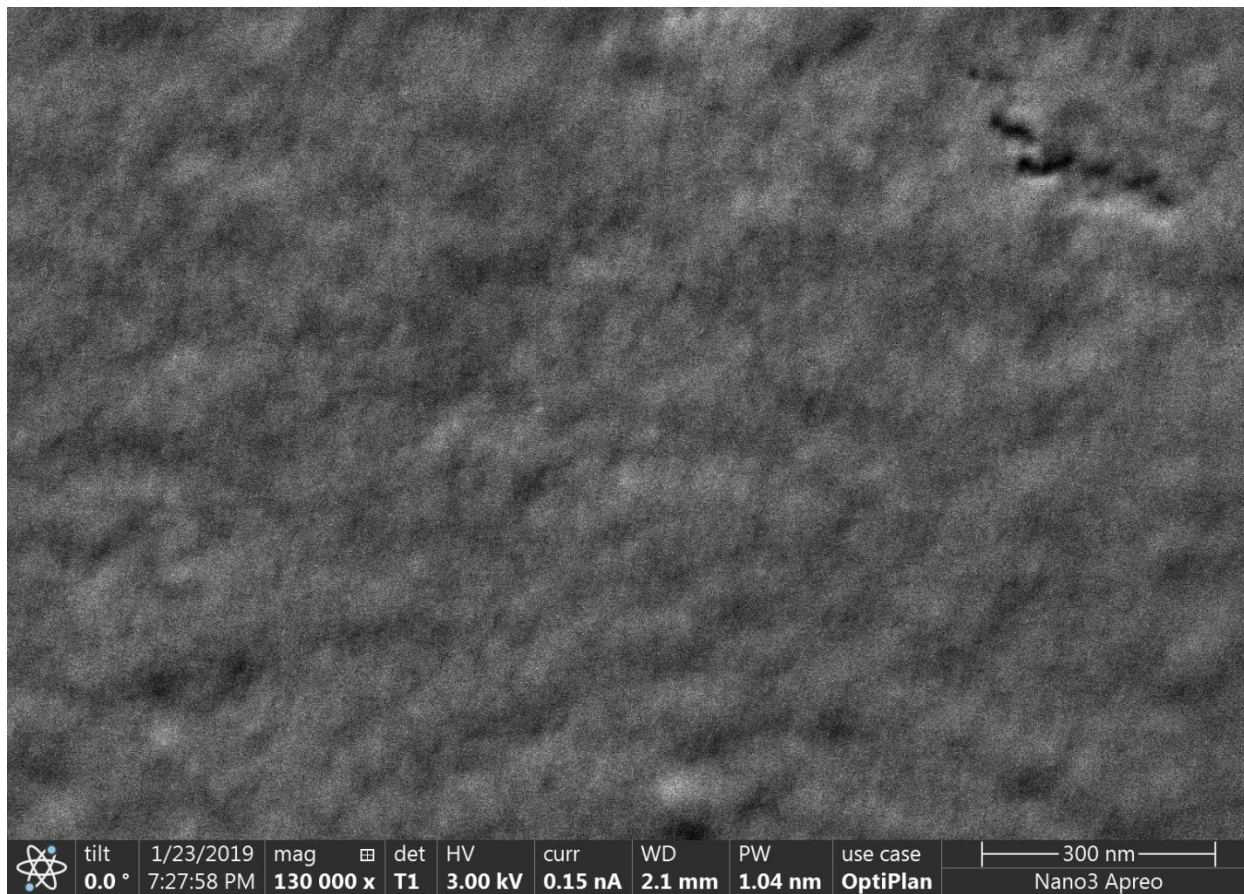


**Figure 4.19** SEM images of FeDhaTph-COF on Si wafer.

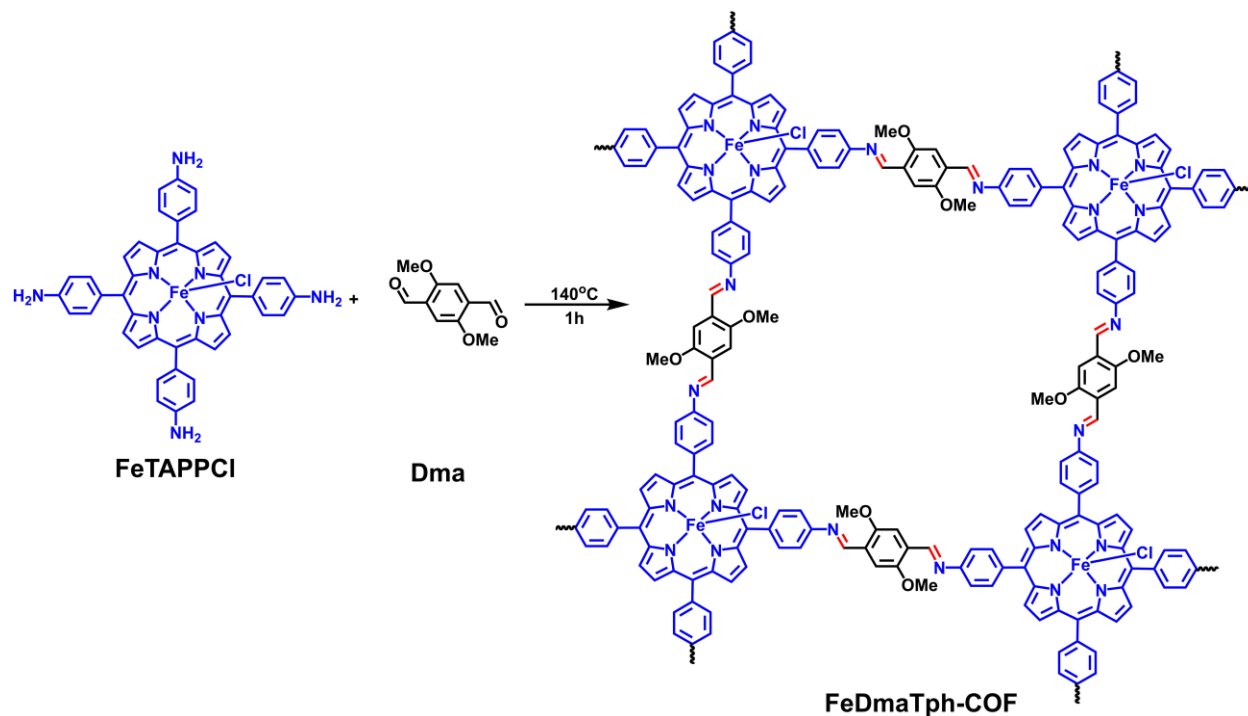


**Figure 4.20** Proposed structure of FeDmaTph-COF.

**Table 4.2** Percentage contributions of the different nitrogen species for FeTAPPCI, FeDhaTph-COF and FeDmaTph-COF.

N species	FeTAPPCI	FeDhaTph-COF	FeDmaTph-COF
	51.83	50.87	60.62
	48.17	24.78	15.66
	NA	24.36	23.72

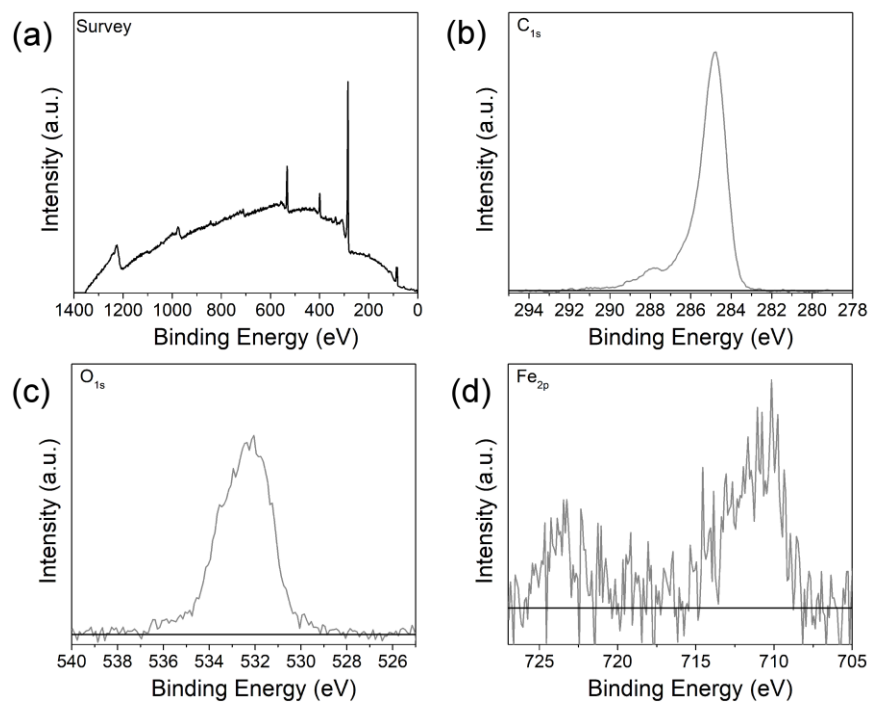


**Figure 4.21** Additional XPS spectra of FeTAPPCl on Au slides: (a) survey scan, (b) C<sub>1s</sub>, (c) O<sub>1s</sub> and (d) Fe<sub>2p</sub>.

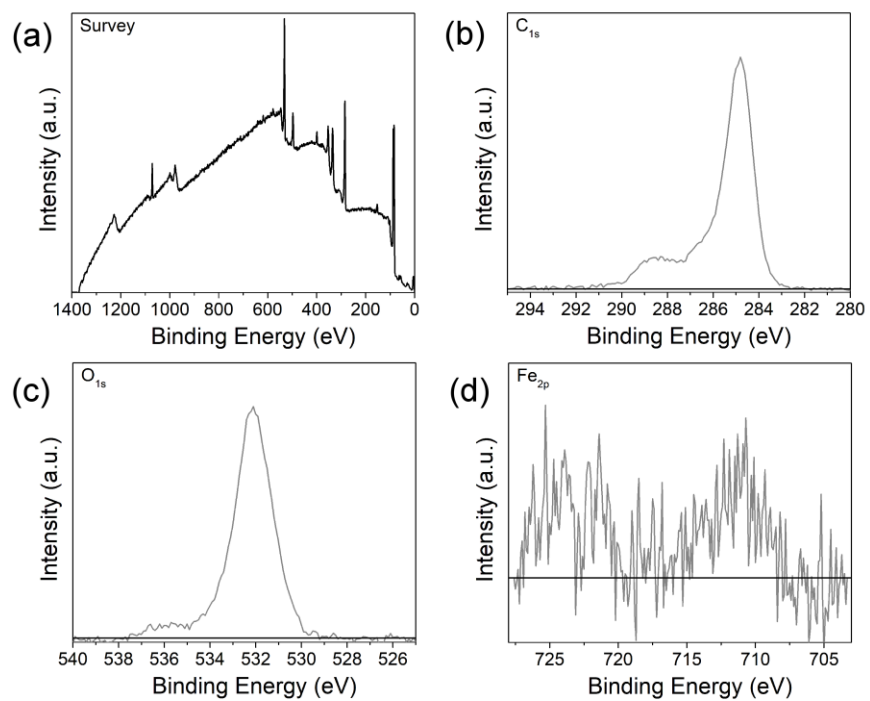


**Figure 4.22** Additional XPS spectra of FeDhaTph-COF on Au slides: (a) survey scan, (b) C<sub>1s</sub>, (c) O<sub>1s</sub> and (d) Fe<sub>2p</sub>.

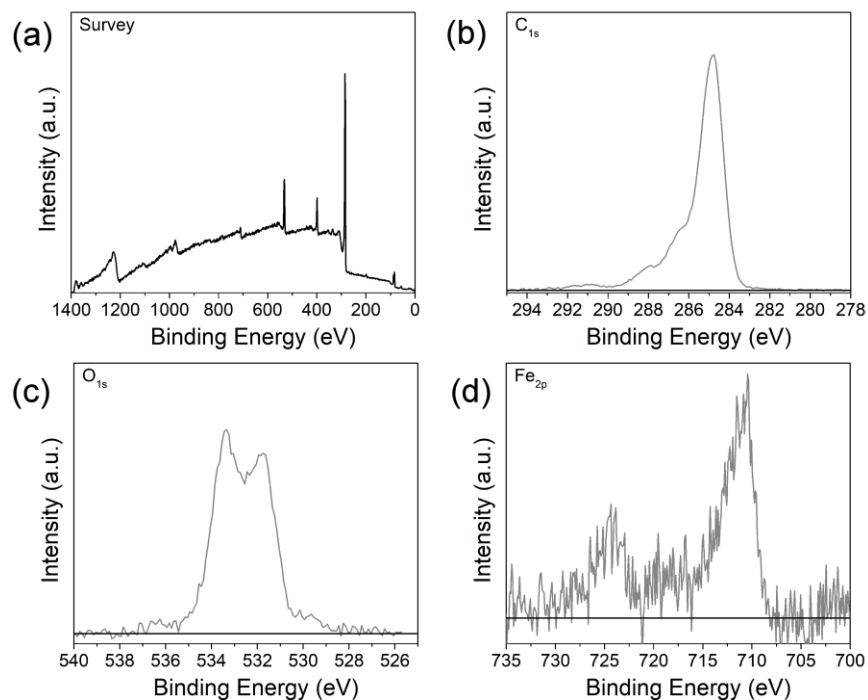


**Figure 4.23** Additional XPS spectra of FeDmaTph-COF on Au slides: (a) survey scan, (b) C1s, (c) O1s and (d) Fe2p. The two oxygen peaks correspond to the oxygen in the hemiaminal group and methoxy group.

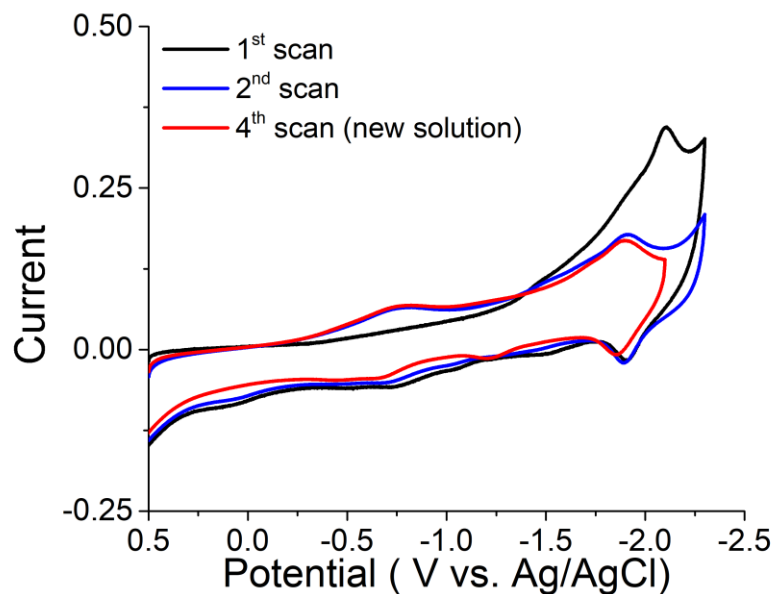


**Figure 4.24** CVs of FeDhaTph-COF electrode in original (black and blue) and new solutions (red) of dry MeCN containing 0.1 M TBAPF<sub>6</sub> under Ar at scan rate 100 mV/s.

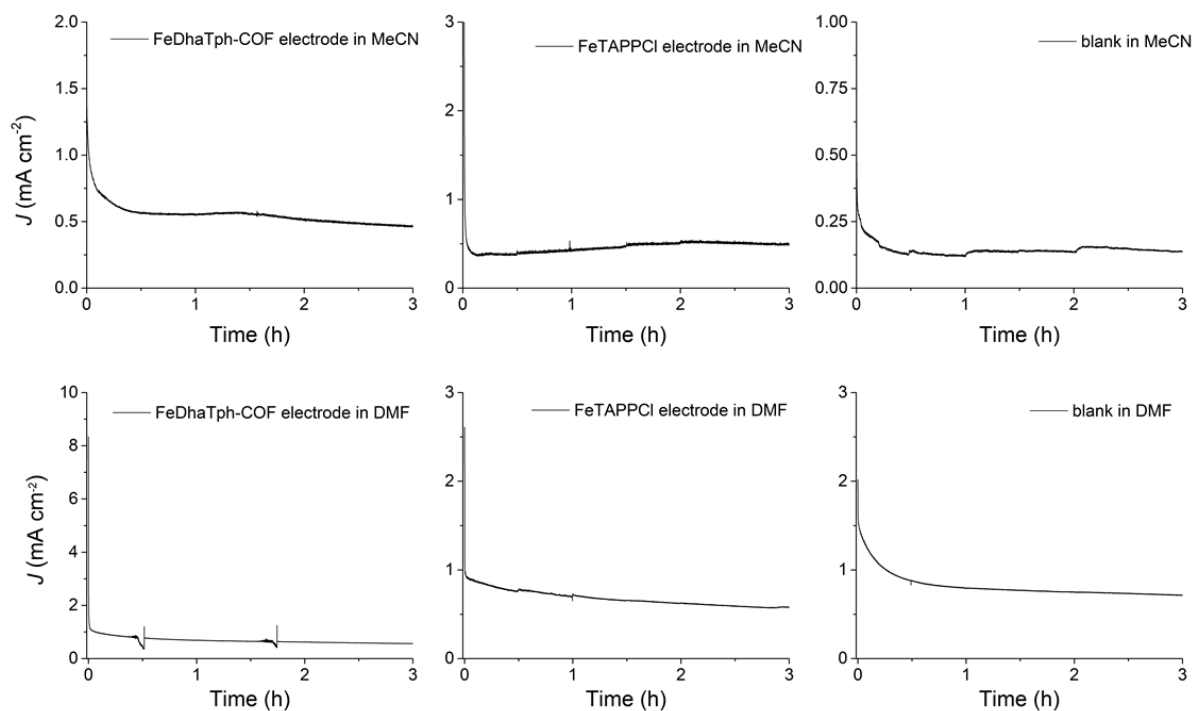


**Figure 4.25** Current of different electrodes during CPE at 2.2 V (vs. Ag/AgCl) in MeCN and 2.1 V in DMF containing 0.1 M TBAPF<sub>6</sub> and 0.5 M TFE under CO<sub>2</sub> for three hours.

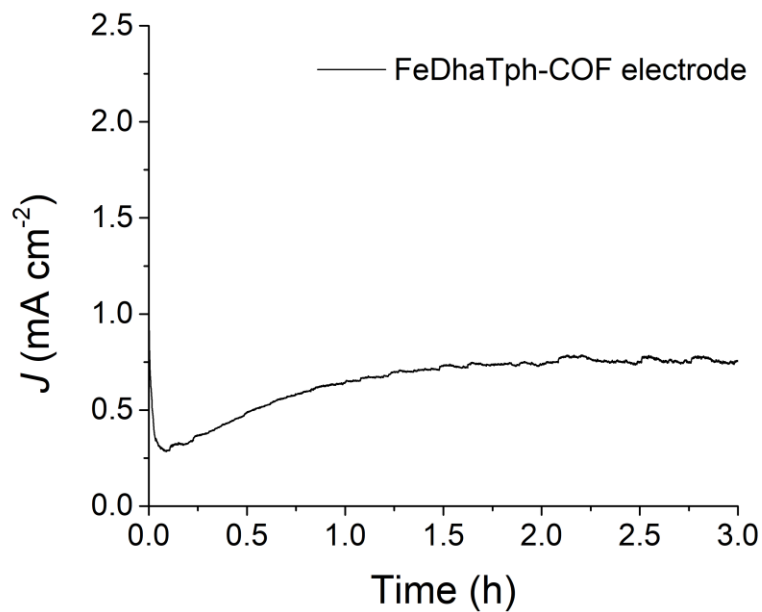


**Figure 4.26** Current of FeDhaTph-COF carbon cloth electrode during CPE at 1.3 V (vs. Ag/AgCl<sub>(3M NaCl)</sub>) in 0.5 M KHCO<sub>3</sub> under CO<sub>2</sub> for three hours.



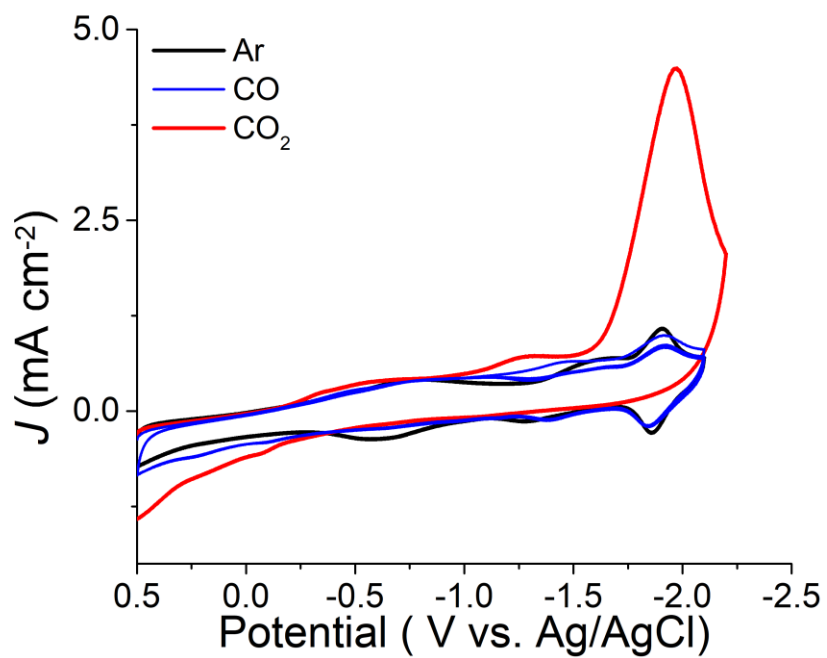


**Figure 4.27** CVs of FeDhaTph-COF electrode in dry MeCN containing 0.1 M TBAPF<sub>6</sub> under Ar (black), CO (blue) and CO<sub>2</sub> (red) at scan rate 100 mV/S.

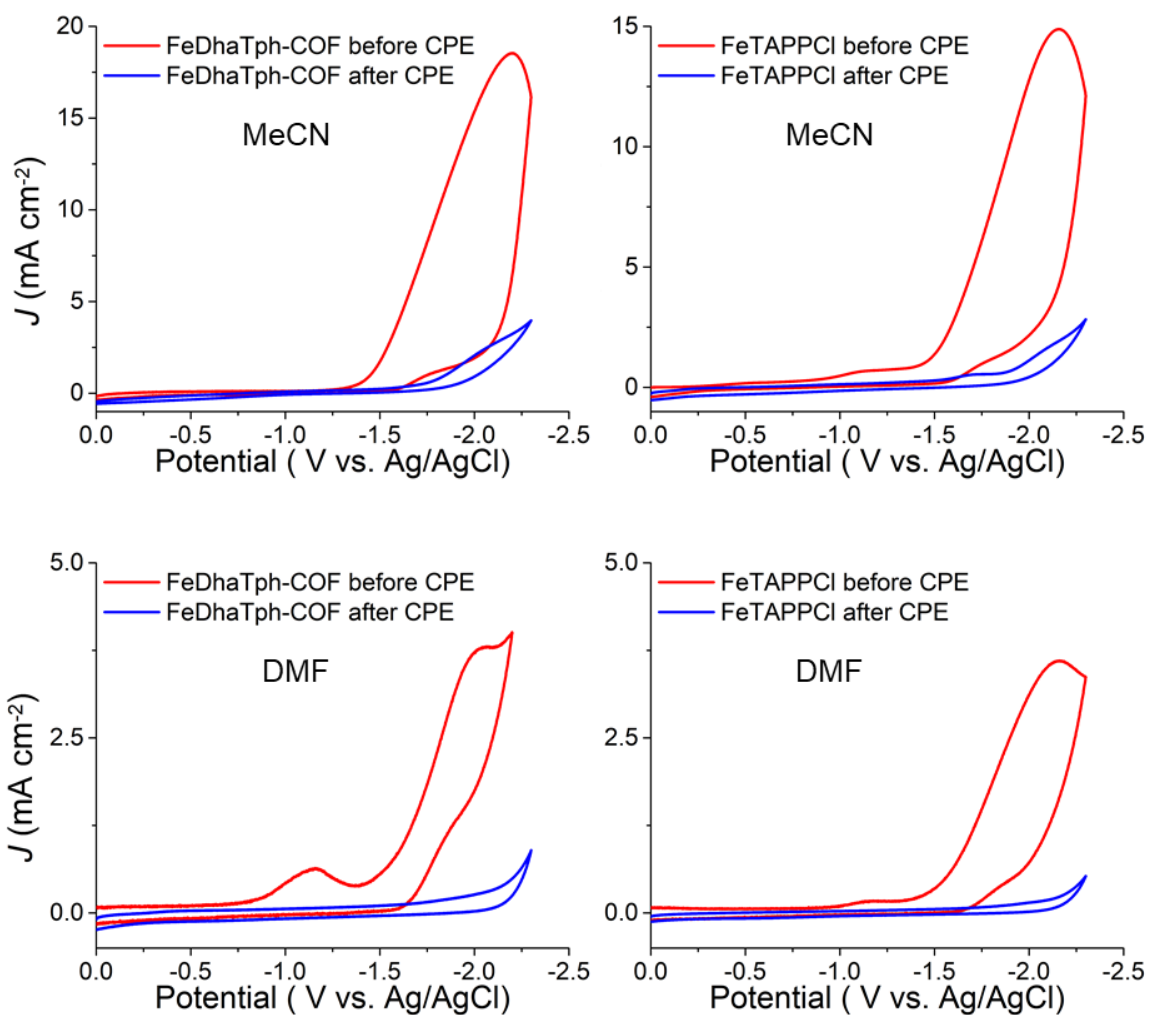


**Figure 4.28** Cyclic voltammograms of different electrodes before and after 3 h controlled-potential electrolysis at  $-2.2$  V (vs. Ag/AgCl) in MeCN and at  $2.1$  V in DMF solutions of  $0.1$  M TBAPF<sub>6</sub> under CO<sub>2</sub> with added TFE at scan rate  $50$  mV/s.

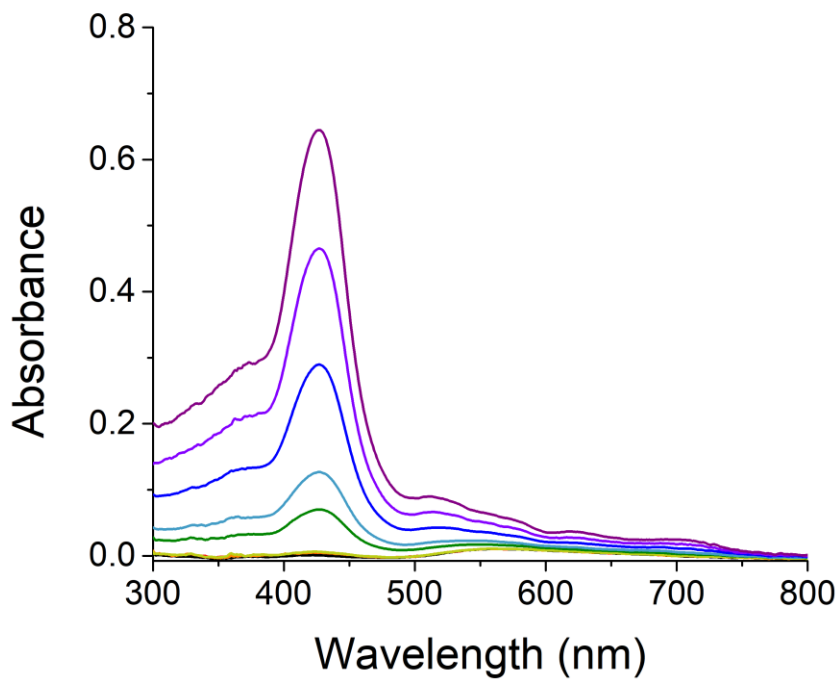


**Figure 4.29** UV-vis spectra of different concentration of FeTAPPCl in THF solution.

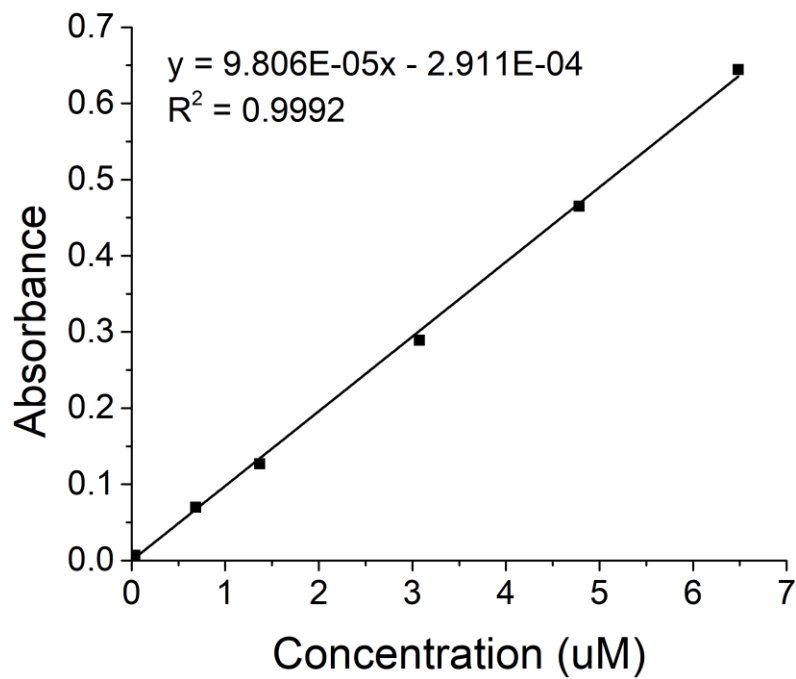


**Figure 4.30** Calibration curve of absorbance of soret band at 424 nm against concentration of FeTAPPCl in THF solution.

# Chapter 5

## Future Directions: New Areas to Be Explored

### 5.1 Summary

Despite the growth in renewable technologies, the world is still heavily dependent on fossil fuels for power and transportation. Carbon dioxide reduction has a pivotal role in the storage of excess electrical energy generated by solar panels and wind turbines and lowering the concentration of carbon dioxide in the atmosphere at the same time. The purpose of this dissertation was to investigate photochemical and electrochemical systems for practical carbon dioxide reductions.

The major findings in photochemical systems are the effects of ligand substitution and non-covalent interactions in second coordination sphere on rhenium and manganese bipyridine catalysts. As detailed in **Chapter 2**, the replacement of the Br<sup>-</sup> ligand to a CN<sup>-</sup> ligand has drastic change in reaction mechanism of Mn(bpy)(CO)<sub>3</sub>X catalyst, transforming from dimerization to disproportionation mechanism. The results of this investigation also show that the choice of solvent (MeCN vs. DMF) has a striking role in determining the selectivity of products (CO vs. HCOOH). Another piece of work in **Chapter 3** demonstrates that not only the ligands in the immediate coordination sphere (as shown in **Chapter 2**) but also the hydrogen bonding between ligands in second coordination sphere have significant influence on photocatalytic

activities of  $\text{Re}(\text{bpy-X})(\text{CO})_3\text{Cl}$  systems. Similarly, solvent effects were also studied. Surprisingly, the photocatalytic systems perform very well without the presence of proton source, which is believed to be a vital ingredient in photocatalysis. The proposed reason is that the hydrogen bonding rhenium bipyridine catalyst is able to catalyze the disproportionation of two carbon dioxide molecules to carbon monoxide and (bi)carbonate species. Taken together, these photochemical studies suggest that there are still many unexplored factors governing the performance of photocatalysis and more creative work should be done to examine them.

The investigation of heterogenization of molecular catalyst for electrochemical catalysis has shown that covalent organic frameworks (COFs) are good substrate for embedding iron porphyrins on carbon cloth electrodes (**Chapter 4**). It is unfortunate that the organic parts of immobilized iron porphyrins are degraded in electrocatalysis even though the COFs linkages are intact.

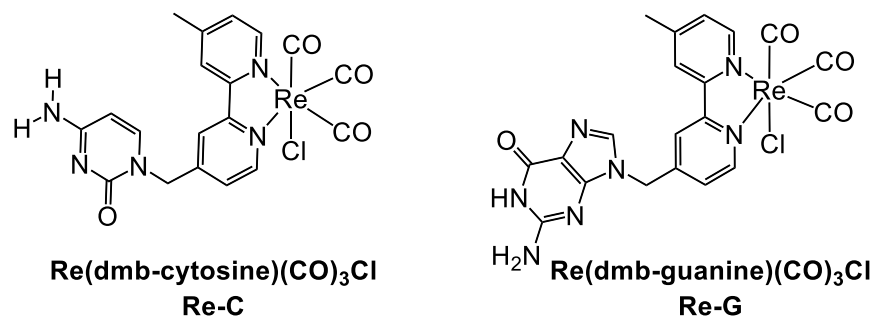
The following section includes some suggestions of further studies of the projects mentioned above.

## 5.2 Results and Discussion

### 5.2.1 Investigating Electrochemical and Photochemical Activities of Supramolecular Systems

#### Bonded by Guanine-Cytosine Base Pair

As a continuation of the work in **Chapter 3**, where non-specific hydrogen bonding is used to improve electron transfer between catalysts and photosensitizers, the next step is to use guanine and cytosine pairs to eliminate self-dimerization.



**Scheme 5.1** Molecular structure of  $\text{Re}(\text{dmb-cytosine})(\text{CO})_3\text{Cl}$  and  $\text{Re}(\text{dmb-guanine})(\text{CO})_3\text{Cl}$ .

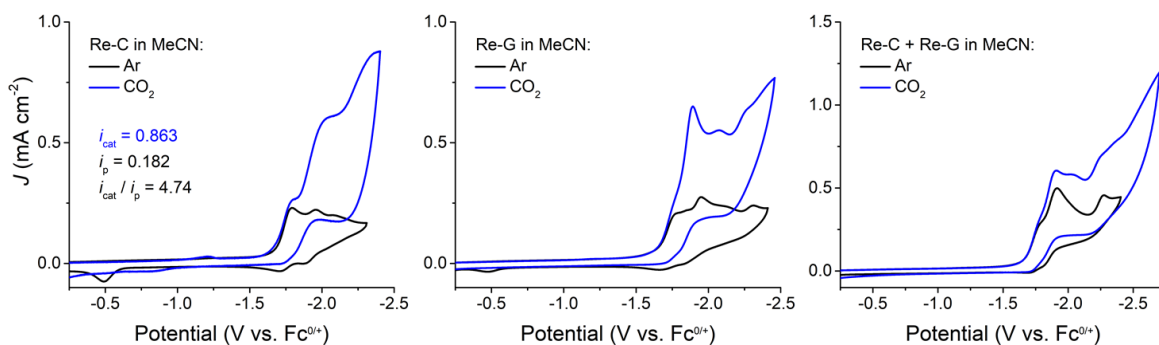


**Figure 5.1** Cyclic voltammograms of 1 mM of Re-C, Re-G and mixture of 1 mM Re-C and Re-G in dry MeCN under Ar or CO<sub>2</sub> at a scan rate of 100 mV/s.

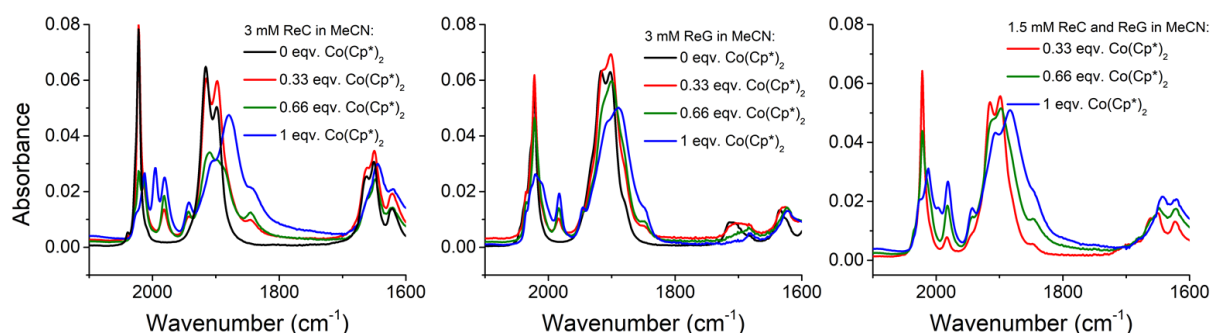
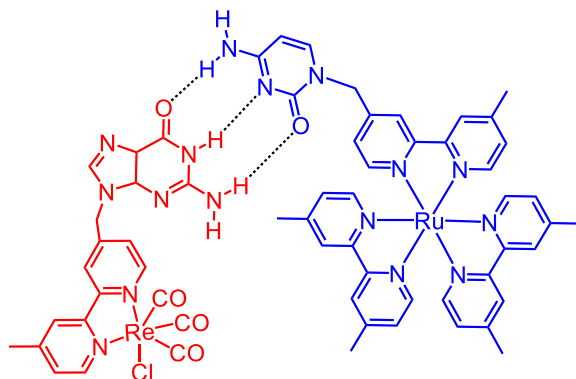


**Figure 5.2** IR spectrum of 3 mM Re-C, 3 mM Re-G and mixture of 1.5 mM Re-C and Re-G in MeCN upon chemical reduction of bis(pentamethylcyclopentadienyl)cobalt(II) (Co(Cp\*)<sub>2</sub>).

Before photochemical studies, electrochemical properties of Re(dmb-guanine)(CO)<sub>3</sub>Cl (Re-G, where 4-methyl-4'-methylguanine-2,2'-bipyridine = dmb-guanine) and Re(dmb-cytosine)(CO)<sub>3</sub>Cl (Re-C, where 4-methyl-4'-methylcytosine-2,2'-bipyridine = dmb-cytosine) were investigated in MeCN and DMF first (**Scheme 5.1**). As shown in the preliminary results in **Figure 5.1**, all three systems have redox features differ from the typical two-peak reduction in Re(bpy)(CO)<sub>3</sub>Cl or Re(tBu-bpy)(CO)<sub>3</sub>Cl. The Re-C and Re-G system also have an oxidative peak at 0.5 V vs. Fc<sup>0/+</sup>, which is believed to be the oxidation of Re-Re dimers. However, in the mixture of Re-C and Re-G, the oxidative peak disappears. The planarity in the cytosine-guanine dimer is likely able to avoid the formation of Re-Re metal dimer as the case of Re(dac)(CO)<sub>3</sub>Cl. From **Figure 5.2**, it is apparent that all Re-C, Re-G and mixture systems have peaks at 1982 and 1942 cm<sup>-1</sup>. These bands are close to the observed bands from metal–metal bound dimer [Re<sup>0</sup>(dac)(CO)<sub>3</sub>]<sub>2</sub> (1984, 1942, 1875, 1865, and 1842 cm<sup>-1</sup>)<sup>1</sup>. Preliminary NMR concentration studies also

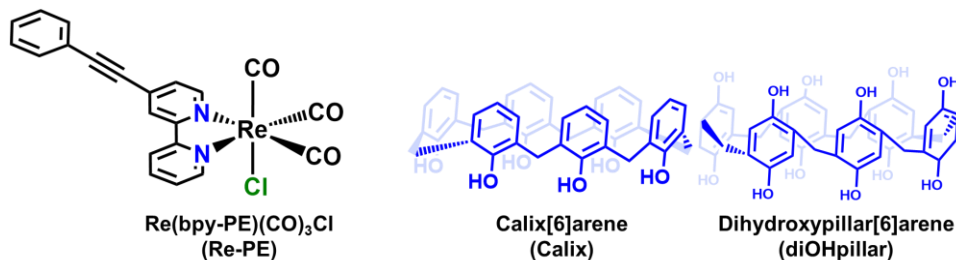
suggest that there is hydrogen bonding interaction ( $\sim 30 \text{ M}^{-1}$ ) between Re-C and Re-G in  $d_6$ -DMSO. More electrochemical and spectroscopic studies are required to reveal the interaction among molecules during electrocatalysis.



**Scheme 5.2** Schematic representation of proposed photochemical system with specific donor and acceptor pair for hydrogen bonding.

If the electrochemical studies show promising results, development of photocatalytic systems with Ru photosensitizers installed with guanine or cytosine substituents will be the next step (**Scheme 5.2**). Unlike the work in **Chapter 3**, in which proton source is avoided, triethanolamine (TEOA) or other proton sources can be used to further boost the catalytic performance. Computational studies are also suggested to observe the interaction between catalyst and photosensitizer.

### 5.2.2 Interrogating the Efficiency and Activity of Electrocatalysts for the Reduction of $\text{CO}_2$ Through Supramolecular Assembly with $\pi$ - $\pi$ Interaction



**Scheme 5.3** Molecular structure of  $\text{Re}(\text{bpy-PE})(\text{CO})_3\text{Cl}$ , calix[6]arene and dihydroxypillar[6]arene.

Besides hydrogen bonding,  $\pi$ - $\pi$  interaction is another important non-covalent interaction that is less studied. Even though  $\pi$ - $\pi$  interaction is used to immobilize molecular catalysts onto carbon electrodes<sup>2-4</sup>, the interaction between the molecular catalysts is still an area to be explored.

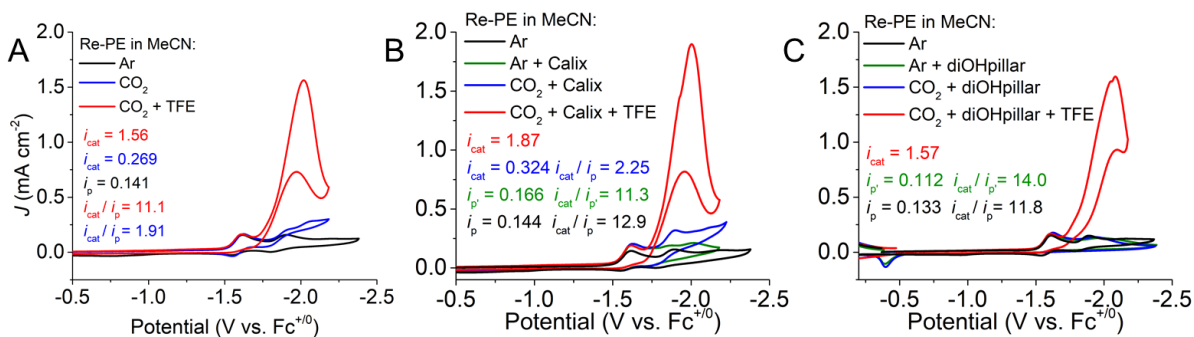


**Figure 5.3** Cyclic voltammograms of (a) 0.5 mM of Re(bpy-PE)(CO)<sub>3</sub>Cl, with addition of (b) 0.5 mM calix[6]arene or (c) 0.5 mM of dihydroxypillar[6]arene, in dry MeCN under Ar or CO<sub>2</sub> with or without addition of trifluoroethanol (TFE) at a scan rate of 100 mV/s.

A Re bipyridine catalyst was synthesized by installing a phenylethynyl group at the 4- position of one side of bipyridine ring, giving rise to Re(bpy-PE)(CO)<sub>3</sub>Cl (Re-PE, where 4-(phenylethynyl)-2,2'-bipyridine = bpy-PE). Initial electrochemical study of Re-PE shows interesting results. Re-PE itself demonstrates a typical two-reduction features as other Re bipyridine catalysts. The first reduction at 1.62 V vs. Fc<sup>+0</sup> is quasireversible while the second peak at 1.91 V is irreversible. There is a small enhancement in catalytic current under CO<sub>2</sub> without proton source ( $i_{cat} / i_p = 1.91$  in **Figure 5.3a**) while the catalytic current soars with addition of 0.5 mL (1.4 M) of trifluoroethanol (TFE) ( $i_{cat} / i_p = 11.1$ ). Interestingly, addition of calix[6]arene and dihydroxypillar[6]arene leads to changes in redox features of Re-PE under inert conditions (**Figure 5.4**). Furthermore, the presence of dihydroxypillar[6]arene turns off the catalytic activity of Re-PE under CO<sub>2</sub> when no proton source is added (**Figure 5.3c**). There are a couple speculated reasons for such observations. First, if  $\pi$ - $\pi$  interaction between the 4-(phenylethynyl)-2,2'-bipyridine substituents is vital for the catalytic activity of Re-PE, the blocking effect caused by the addition of rings (calix[6]arene or dihydroxypillar[6]arene) will slow down catalysis. Since calix[6]arene is a more opened cup shape and dihydroxypillar[6]arene is a narrower cylindrical shape, the blocking effect would be more prominent in the case with addition of dihydroxypillar[6]arene. This is consistent with the observation of



no drop in catalytic current in system with calix[6]arene but no current enhancement in system with dihydroxypillar[6]arene. The other possible explanation is the shifting of effective catalytic potential to more negative direction caused by strong host-guest interactions. 2D NMR (TOCSY and NOESY) experiments were conducted to elucidate the  $\pi$ - $\pi$  interaction. However, the overlapping of aromatic proton signals makes the NMR spectra very difficult to interpret.

These interesting findings worth further studies to explore the impact of  $\pi$ - $\pi$  interaction and potential host-guest interactions on electrocatalysis of Re bipyridine catalysts.

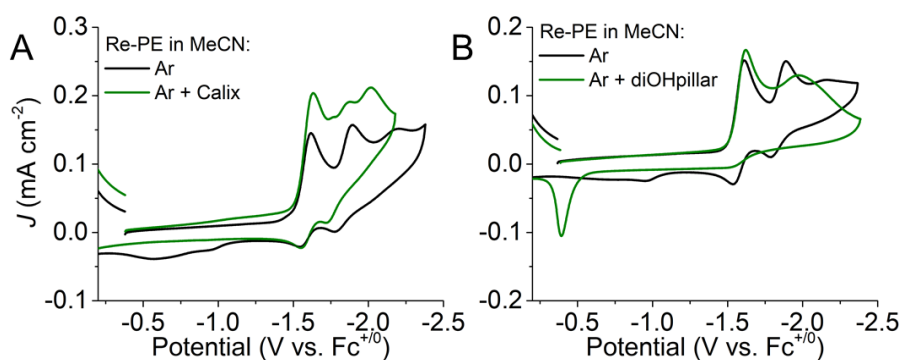


**Figure 5.4** Cyclic voltammograms of 0.5 mM of Re(bpy-PE)(CO)<sub>3</sub>Cl, with addition of (a) 0.5 mM calix[6]arene or (b) 0.5 mM of dihydroxypillar[6]arene in dry MeCN under Ar at a scan rate of 100 mV/s.

### 5.3 Conclusion and Final Suggestions

The research on non-covalent interactions, although being a popular field, is a rather unexplored area when it is applied to molecular catalysis. Hydrogen bonding,  $\pi$ - $\pi$  interaction, and columbic interactions could be useful tools to manipulate the catalytic activity of photocatalysts and electrocatalysts, in addition to the conventional modification of immediate ligands and metal centers. The research on non-covalent interactions is not as easy as the conventional molecular catalysis studies due to the very weak nature of those interactions. Techniques, like cyclic voltammetry, controlled-potential electrolysis, square wave voltammetry, IR-SEC, chemical reductions, UV-Vis absorption, fluorescence, 1D and 2D NMR spectroscopy, are common means to analyze the electrochemical and photochemical properties of these

catalysts with weak interactions. The biggest challenge of working with these catalysts is the solubility problem. Due to non-covalent interactions, the complexes with hydrogen bonding or  $\pi$ - $\pi$  interaction usually are too soluble or not soluble enough in solvents like MeCN or THF. The case is particularly serious for RuDAC (**Chapter 3**) and Re-PE. The former one is too soluble in most of solvents, so the complex has to be crashed out with a plethora of dry dimethyl ether in small batches. Otherwise, the orange powder will become gluey. The latter one, on the other hand, is easy to precipitate out, but it is not very soluble MeCN or THF. Also, calix[6]arene and Re-PE have different solubilities in different solvents, making the study difficult to progress. In spite of these obstacles, these research ideas could offer some insights into the fundamental and hence more applied studies of photocatalysts and electrocatalysts for carbon dioxide reduction.

The project in **Chapter 4** was a trail to attach molecular catalysts on cheap and robust electrodes. The synthesis method turned out to be surprisingly simple. The biggest limitation of the work is the unexpected degradation of organic part of iron porphyrins in the COFs. This project provided me a precious chance to learn various surface characterization techniques and made me realize that characterization of monolayers or ultrathin films of organometallic materials is a still a field needs substantial improvement. After communicating with other research groups, we believe that the conventional solvothermal synthesis of COFs is rather irreproducible and surface coverage of the electrode by drop-casting catalyst powder is always a problem. The exposure of carbon cloth to aqueous or organic solvents leads to significant production of hydrogen. It is necessary to find the balance between lowering catalyst loading and ensuring high surface coverage.

## 5.4 Experimental

All the raw data and data files can be found on the server Rhodium under my user folder.

#### 5.4.1 General

All solvents were obtained from Fisher Scientific. All solvents were deoxygenated and dried over alumina columns on a Grubbs style solvent system under an argon atmosphere. All compounds were obtained from Fisher Scientific or Sigma-Aldrich and used as obtained unless otherwise specified. The ferrocene was sublimed prior to use. 1.5 M solution of tetra-*N*-butylammonium hydroxide and calix[6]arene was obtained from Alfa Aesar and used without further purification. Tetrabutylammonium hexafluorophosphate (TBAPF<sub>6</sub>, Aldrich, 98%) was recrystallized from EtOH and dried at 90 °C overnight before use in electrochemical experiments.

#### 5.4.2 Synthesis of 4-methyl-4'-methyl(trimethylsilane)-2,2'-bipyridine (dmb-TMS)

The synthesis of dmb-TMS was adapted from the literature.<sup>5</sup> A solution of 1.3 M lithium diisopropylamide (LDA, 2.71 mL, 3.52 mmol) was added to another 50 mL of oven-dried Schlenk flask under nitrogen. A 50 mL of oven-dried Schlenk flask was charged with 4,4'-dimethyl-2,2'-dipyridine (0.5 g, 2.71 mmol) and 50 mL dry tetrahydrofuran (THF) under nitrogen. The bipyridine solution was cannulated dropwise to LDA solution over 15 minutes. The resulting dark brown suspension was stirred for 2 h at -78 °C. An excess of trimethylsilyl chloride (430  $\mu$ L, 3.39 mmol) was added quickly in one portion to the lithiated 4,4'-dimethyl-2,2'-dipyridine solution. After one minute of thorough stirring, the solution was quenched with 1 mL of ethanol and then 50 mL of saturated aqueous sodium bicarbonate solution. The solution was extracted with dichloromethane (DCM, 3  $\times$  50 mL). The organic fractions were combined, washed with brine, separated and then dried with anhydrous magnesium sulfate. Crude product was obtained by evaporation of the organic solvents. It was then further purified by flash column chromatography (1 % triethylamine (TEA) rinsed silica; ethyl acetate in hexane with a gradient of 0/100 to 10/90). The desired fractions were collected as first portion and the solvents evaporated in vacuo to yield 4-methyl-4'-methyl(trimethylsilane)-2,2'-bipyridine (0.6 g, 86% yield) as a white solid.

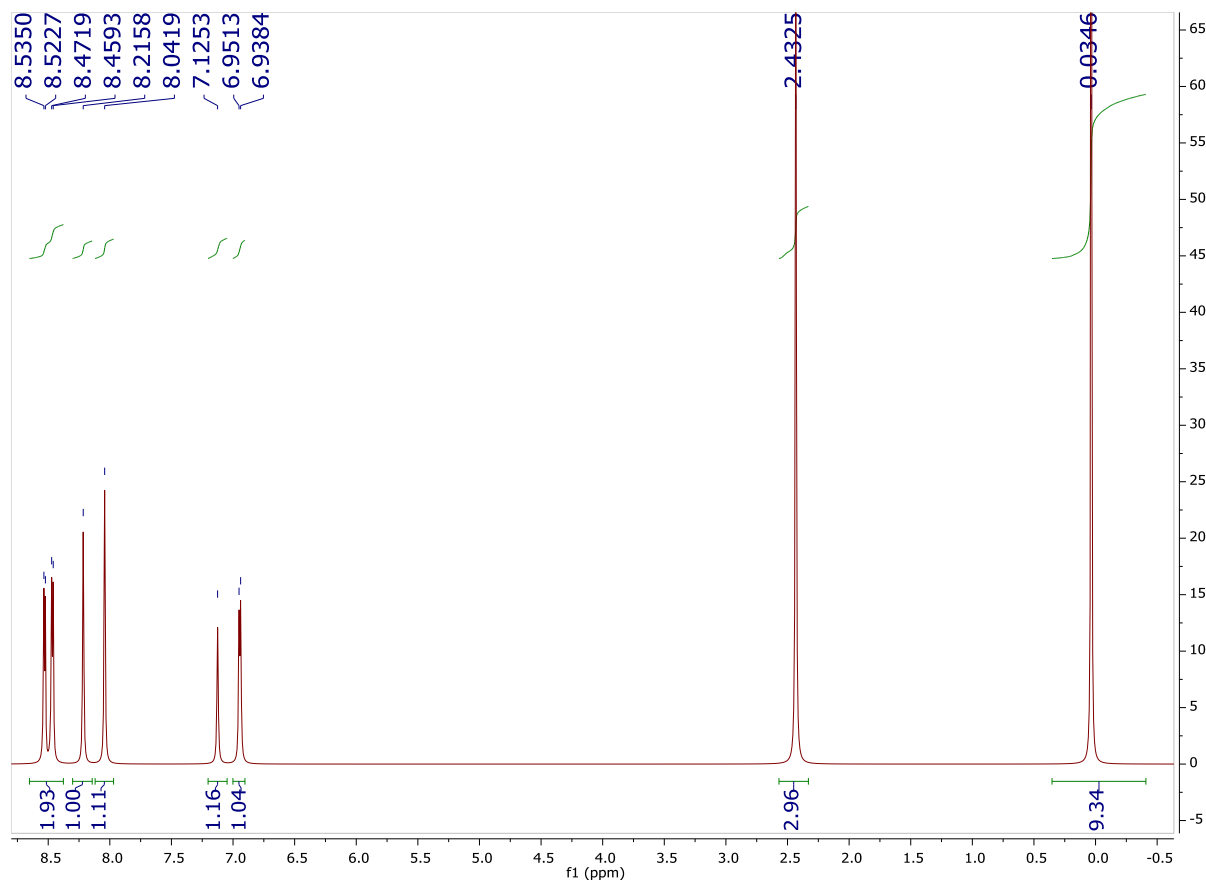


**Figure 5.5**  $^1\text{H}$  NMR of 4-methyl-4'-methyl(trimethylsilane)-2,2'-bipyridine in  $\text{CD}_3\text{Cl}$ .

#### 5.4.3 Synthesis of 4-methyl-4'-methylchloro-2,2'-bipyridine (dmb-Cl)

An oven-dried 50 mL Schlenk flask was charged with 4-methyl-4'-methyl(trimethylsilane)-2,2'-bipyridine (250 mg, 0.975 mmol), cesium fluoride (296 mg, 1.95 mmol), hexachloroethane (462 mg, 1.95 mmol), and 15 mL of dry MeCN under nitrogen. The mixture was heated to 65 °C for roughly 4 to 6 hours until completion, in which the progress was monitored by TLC. The reaction mixture was cooled to room temperature and then extraction with water/DCM ( $3 \times 30$  mL). The organic fraction was dried with anhydrous magnesium sulfate and then evaporated to dryness to give a off white solid. Hexachloroethane was sublimed and condensed at the bump trap of rotovap. The crude product was recrystallized with boiling pentane to remove remaining hexachloroethane and starting material to give a pale-yellow crystalline product (160 mg, 75% yield).

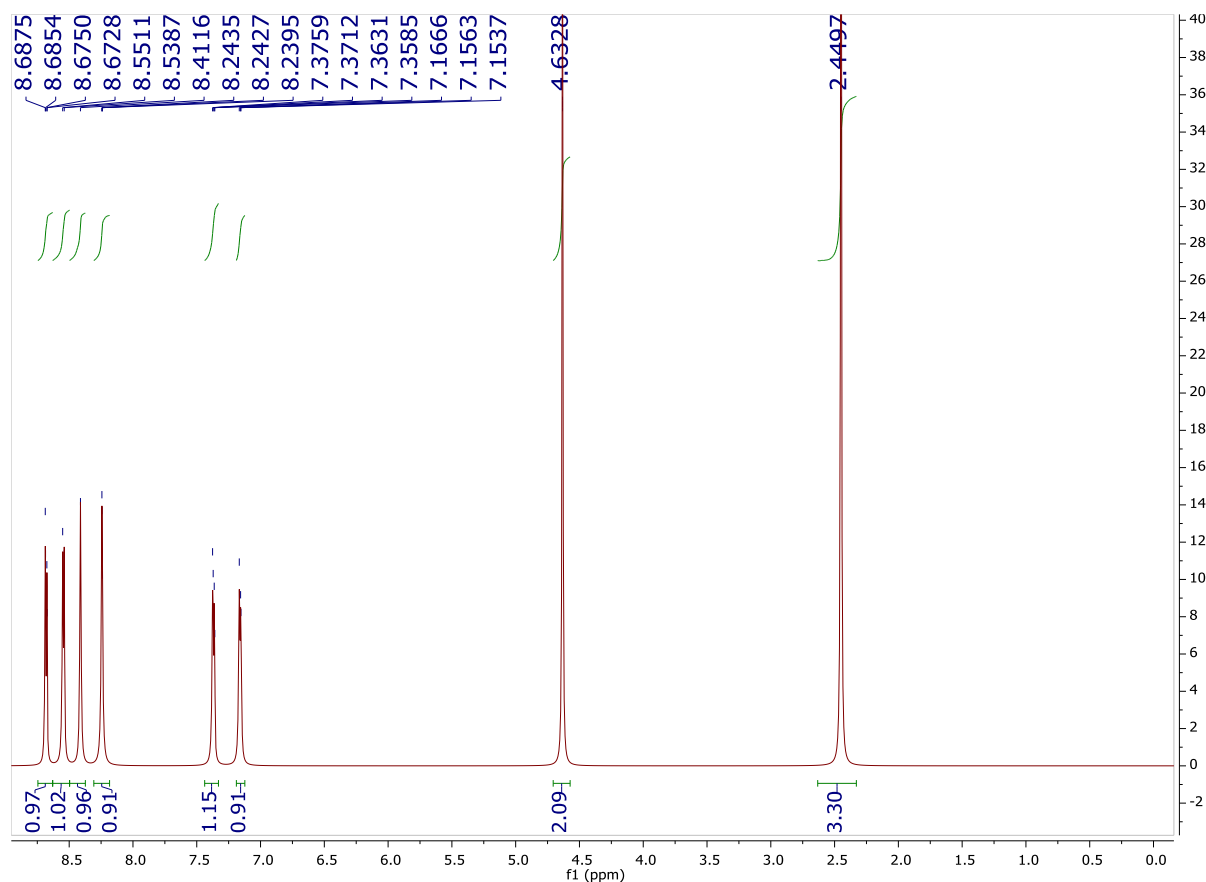


**Figure 5.6**  $^1\text{H}$  NMR of 4-methyl-4'-methylchloro-2,2'-bipyridine in  $\text{CD}_3\text{Cl}$ .

#### 5.4.4 Synthesis of $\text{Re}(\text{dmb-cytosine})(\text{CO})_3\text{Cl}$

The synthesis of 4-methyl-4'-methylcytosine-2,2'-bipyridine was adapted from the literature.<sup>6</sup> A 1.5 M solution of tetra-N-butylammonium hydroxide in MeOH (0.228 mL, 0.343 mmol) was added dropwise to a stirred suspension of cytosine (38.1 mg, 0.343 mmol) in MeCN (5 mL). The solution became clear and 4-methyl-4'-methylchloro-2,2'-bipyridine (50 mg, 0.229 mmol) dissolved in MeCN was added dropwise. The reaction mixture was stirred at room temperature overnight with formation of pale-yellow powder after half an hour of stirring. Then the solid was filtered out as the final 4-methyl-4'-methylcytosine-2,2'-bipyridine (38 mg, 57% yield).

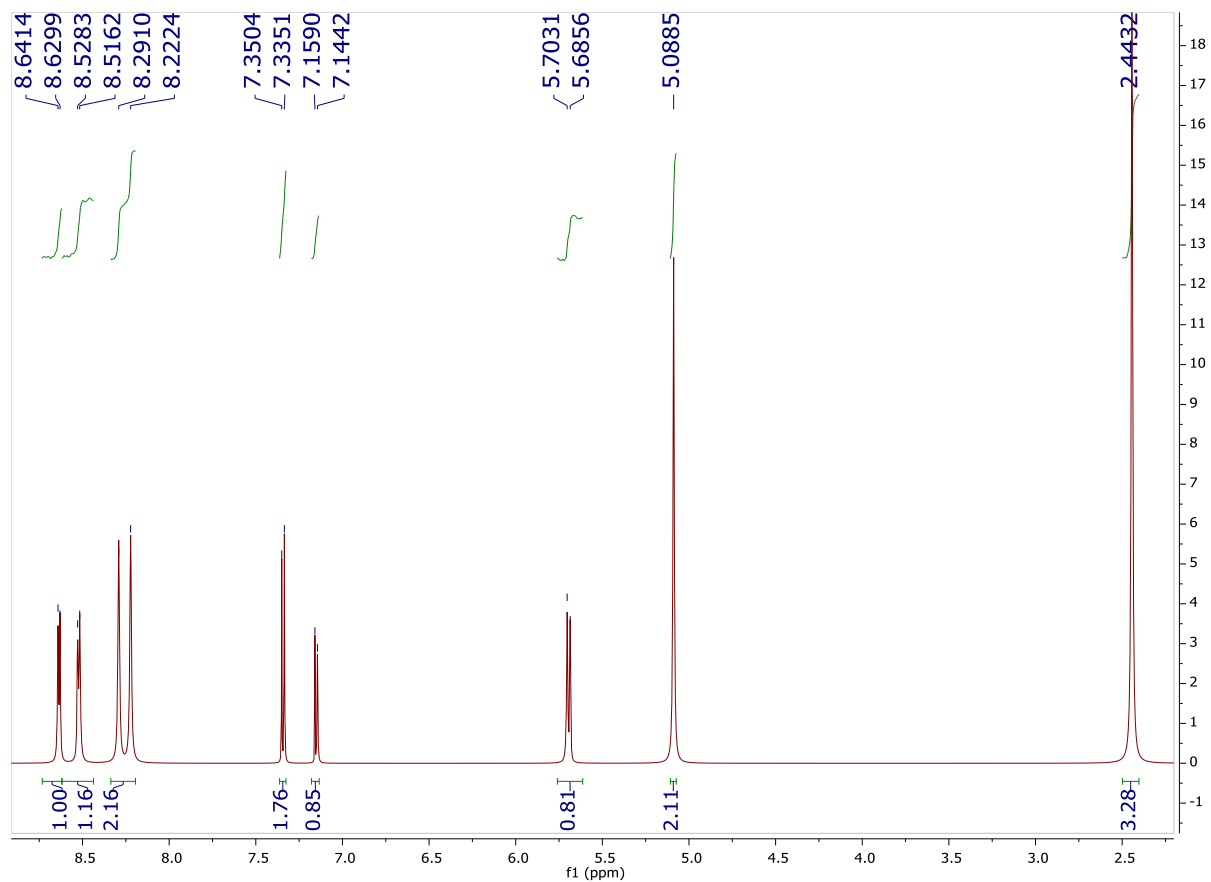


**Figure 5.7**  $^1\text{H}$  NMR of 4-methyl-4'-methylcytosine-2,2'-bipyridine in  $\text{CD}_3\text{Cl}$ .

4-methyl-4'-methylcytosine-2,2'-bipyridine (50 mg, 0.170 mmol) and pentacarbonylchlororhenium(I) (62 mg, 0.170 mmol) were added to a 25 mL pear-shaped flask filled with less than 3 mL of dry DMF. The solution was degassed with nitrogen for 5 minutes and then heated to above  $110^\circ\text{C}$  with stirring under nitrogen overnight. DMF was removed by rotovap. The crude product was dissolved in DMC, recrystallized with DCM/pentane to give dark yellow powder.

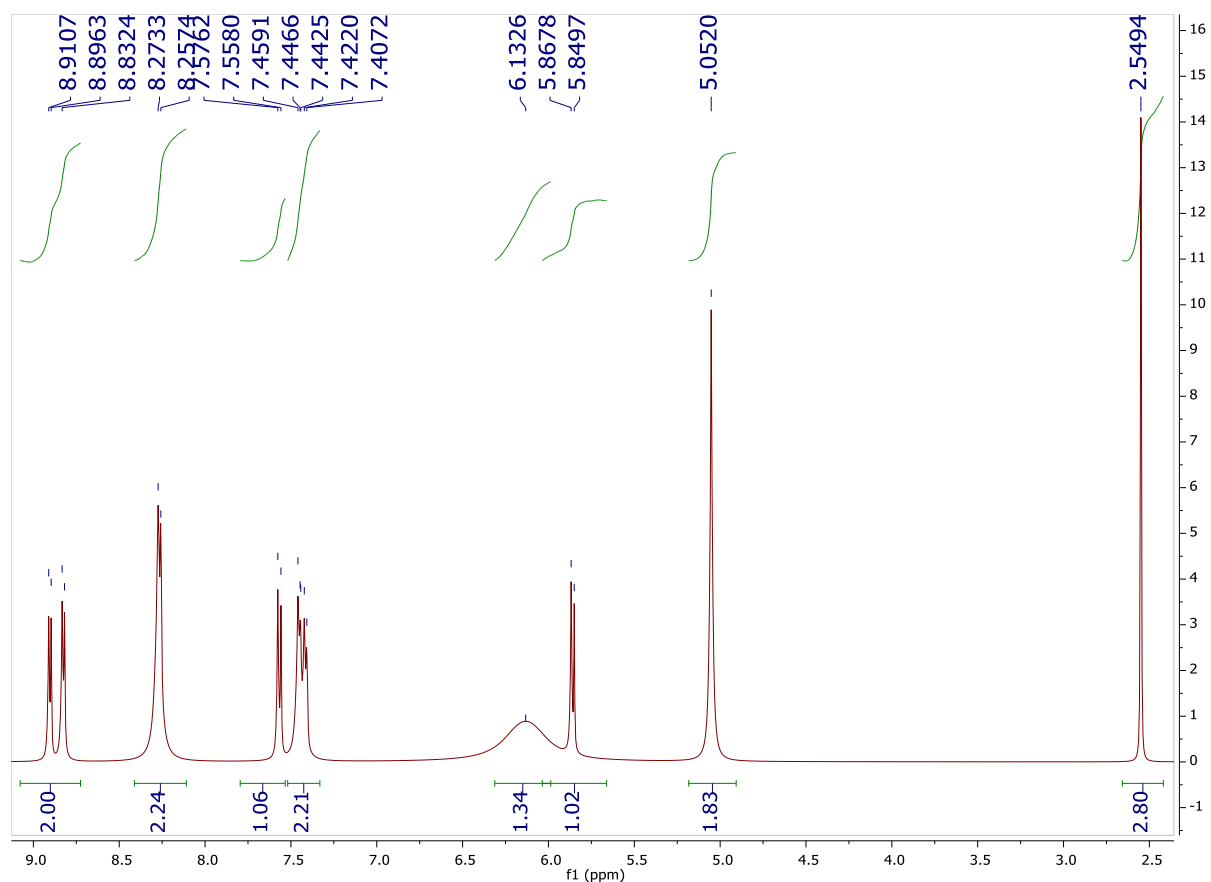


**Figure 5.8**  $^1\text{H}$  NMR of  $\text{Re}(\text{dmb-cytosine})(\text{CO})_3\text{Cl}$  in  $\text{CD}_3\text{CN}$ .

#### 5.4.5 Synthesis of $\text{Re}(\text{dmb-guanine})(\text{CO})_3\text{Cl}$

The synthesis of 4-methyl-4'-methylguanidine-2,2'-bipyridine was adapted from the literature.<sup>7</sup> A mixture of 2-amino-6-chloro purine (78.3 mg, 0.461 mmol) and 4-methyl-4'-methylchloro-2,2'-bipyridine (100 mg, 0.457 mmol), and potassium carbonate (126 mg, 0.914 mmol) were heated to reflux with stirring in 10 mL of dry MeCN at reflux temperature for 24 hours under nitrogen. The reaction process was monitored by TLC (DCM in MeOH with a gradient of 90/10) until completion. The solvent was removed to give a pale-yellow solid. Without further purification, the solid was dissolved in 5 mL of 1 M HCl. The solution was refluxed in air for two hours and then cooled to room temperature. The acidic solution was neutralized with 2 M NaOH solution until orange or white solid was precipitated out at neutral pH. The solid was filtered out as 4-methyl-4'-methylguanidine-2,2'-bipyridine (~ 50% yield).

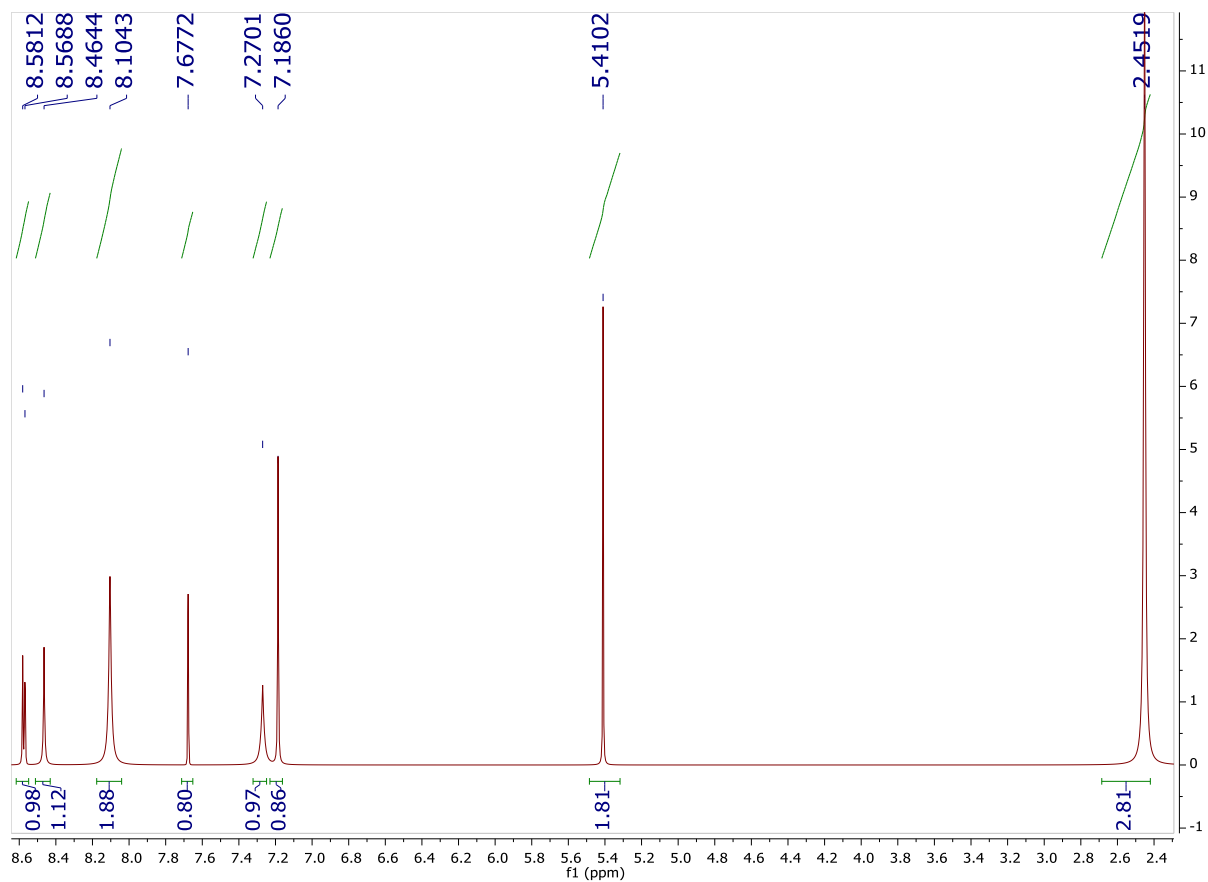


**Figure 5.9** <sup>1</sup>H NMR of 4-methyl-4'-methylguanine-2,2'-bipyridine in CD<sub>3</sub>Cl.

4-methyl-4'-methylcytosine-2,2'-bipyridine (100 mg, 0.3 mmol) and pentacarbonylchlororhenium(I) (109 mg, 0.3 mmol) were added to a 25 mL pear-shaped flask filled with less than 3 mL of dry DMF. The solution was degassed with nitrogen for 5 minutes and then heated to above 110 °C with stirring under nitrogen overnight. DMF was removed by rotovap. The crude product was dissolved in DCM, recrystallized with DCM/pentane to give brownish orange powder (60 mg, 32% yield).



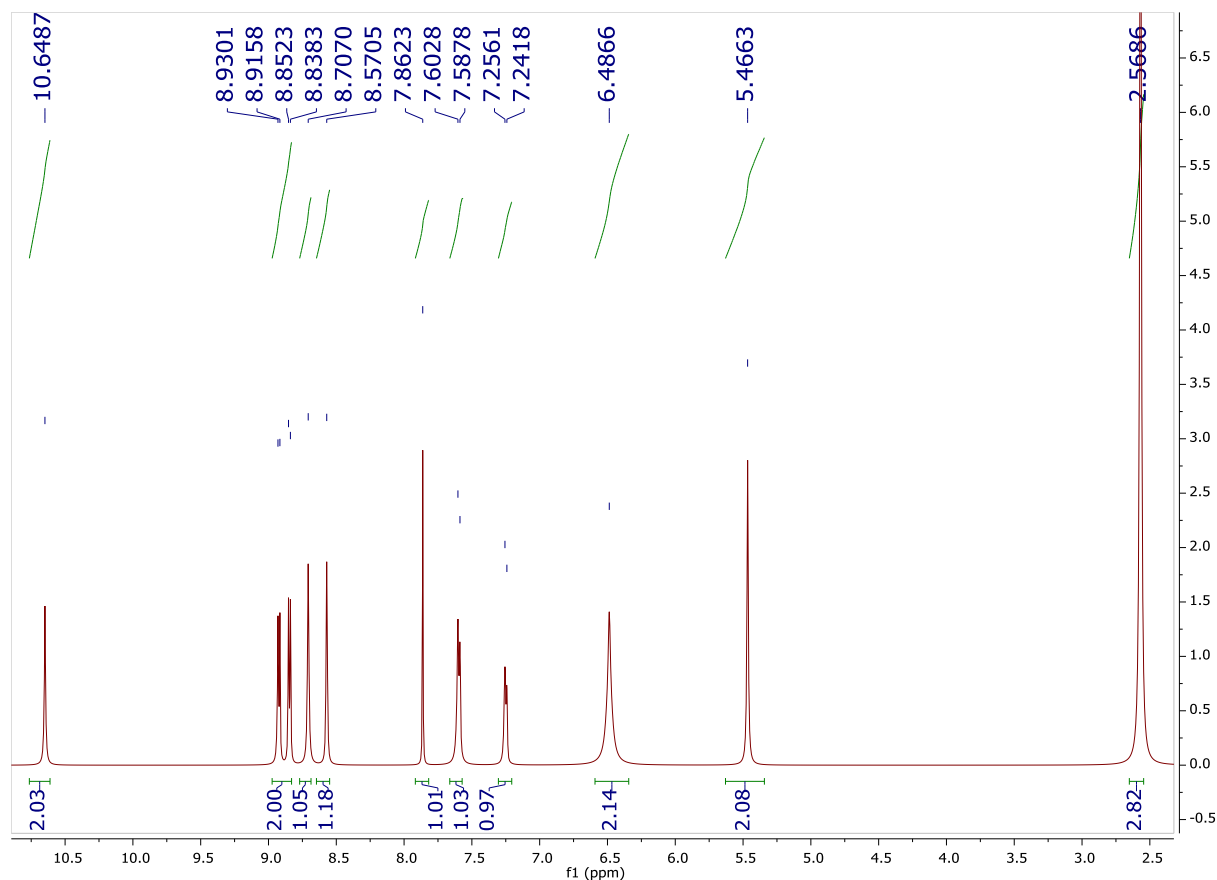


**Figure 5.10**  $^1\text{H}$  NMR of  $\text{Re}(\text{dmb-guanine})(\text{CO})_3\text{Cl}$  in  $\text{DMSO-d}_6$ .

#### 5.4.6 Synthesis of 4-(phenylethynyl)-2,2'-bipyridine

The synthesis of 4-(phenylethynyl)-2,2'-bipyridine was adapted from the literature.<sup>8-9</sup> The 4-bromo-2,2'-bipyridine (200 mg, 0.85 mmol),  $\text{Pd}(\text{PPh}_3)_2\text{Cl}_2$  (5 mol%),  $\text{CuI}$  (10 mol%), and phenylacetylene (113 mg, 1.11 mmol) were added to a 50 mL Schlenk flask with a stir bar under nitrogen. Then THF (10 mL) and triethylamine (TEA, 10 mL) were added sequentially. After stirring at room temperature overnight, 60 mL water were added and the reaction mixture was extracted with ethyl acetate ( $3 \times 15$  mL), washed with brine and dried over anhydrous magnesium sulfate. The residue was purified by recrystallization with hexane or DCM to give white or orange crystals (130 mg, 60%).

### 5.4.7 Synthesis of $\text{Re}(\text{bpy-PE})(\text{CO})_3\text{Cl}$

4-(phenylethynyl)-2,2'-bipyridine (150 mg, 0.585 mmol) and pentacarbonylchlororhenium(I) (212 mg, 0.585 mmol) were added to a 250 mL pear-shaped flask filled with 150 mL of dry toluene. The solution was degassed with nitrogen for 10 minutes and then heated to reflux with stirring under nitrogen overnight to give a deep red solution. The solvent was removed by rotovap to give a deep orange powder. The crude product was dissolved in DCM, recrystallized with DCM/ether to give brownish orange powder (260 mg, 80 % yield).

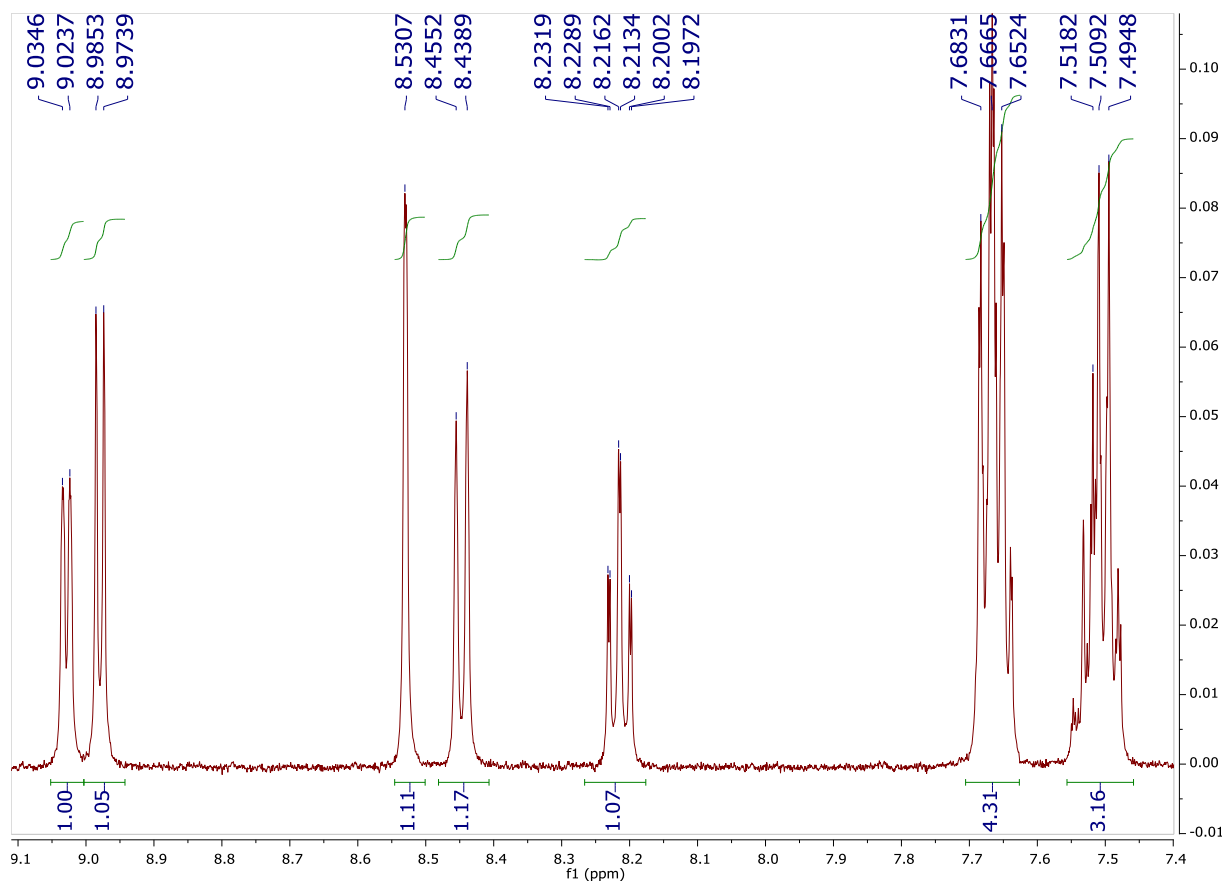


**Figure 5.11**  $^1\text{H}$  NMR of 5 mM  $\text{Re}(\text{bpy-PE})(\text{CO})_3\text{Cl}$  in  $\text{CD}_3\text{CN}$ .

### 5.4.8 Synthesis of Dihydroxypillar[6]arene

The synthesis of dihydroxypillar[6]arene was adapted from the literature.<sup>10</sup> The product should be stored in a desiccator.

### 5.4.9 Cyclic Voltammetry

CV studies were performed using a BASi Epsilon potentiostat. A 3 mm diameter glassy carbon working electrode (BASi), a platinum (Pt) wire counter electrode, and a silver/ silver chloride (Ag/AgCl) wire separated from the bulk solution by a CoralPor tip as a pseudoreference electrode were used in a single compartment cell for all experiments. Experiments were run with and without ferrocene as an internal reference. Electrolyte solutions were composed of dry MeCN or DMF, containing 0.5 or 1.0 mM of analyte, 0.1 M TBAPF<sub>6</sub> as supporting electrolyte. The electrolyte was purged with N<sub>2</sub> or CO<sub>2</sub> for before cyclic voltammograms were recorded and stirred between successive experiments.

## 5.5 Acknowledgments

**Chapter 5**, in part, consists of unpublished work. This work was supported by the Air Force Office of Scientific Research through AFOSR through a Basic Research Initiative (BRI) Grant (No. FA9550-12-1-0414).

## 5.6 Reference

1. Machan, C.W.;Chabolla, S.A.;Yin, J.;Gilson, M.K.;Tezcan, F.A.; Kubiak, C.P., Supramolecular Assembly Promotes the Electrocatalytic Reduction of Carbon Dioxide by Re(I) Bipyridine Catalysts at a Lower Overpotential. *J. Am. Chem. Soc.* **2014**, *136* (41), 14598–14607.
2. Zhanaidarova, A.;Jones, S.C.;Despagnet-Ayoub, E.;Pimentel, B.R.; Kubiak, C.P., Re(tBu-bpy)(CO)<sub>3</sub>Cl supported on multi-walled carbon nanotubes selectively reduces CO<sub>2</sub> in water. *J. Am. Chem. Soc.* **2019**, *141* (43), 17270–17277.
3. Sinha, S.;Sonea, A.;Shen, W.;Hanson, S.S.; Warren, J.J., Heterogeneous Aqueous CO<sub>2</sub> Reduction Using a Pyrene-Modified Rhenium(I) Diimine Complex. *Inorg. Chem.* **2019**, *58* (16), 10454–10461.
4. Leung, J.J.;Warnan, J.;Ly, K.H.;Heidary, N.;Nam, D.H.;Kuehnel, M.F.; Reisner, E., Solar-driven reduction of aqueous CO<sub>2</sub> with a cobalt bis(terpyridine)-based photocathode. *Nat. Catal.* **2019**, *2* (4), 354–365.
5. Ciana, L.D.;Hamachi, I.; Meyer, T.J., Synthesis of Side-Chain Derivatives of 2,2'-Bipyridine. *J. Org. Chem.* **1989**, *54*, 1731–1735.
6. Chhabra, S.;Barlow, N.;Dolezal, O.;Hattarki, M.K.;Newman, J.;Peat, T.S.;Graham, B.; Swarbrick, J.D., Exploring the Chemical Space around 8-Mercaptoguanine as a Route to New Inhibitors of the Folate Biosynthesis Enzyme HPPK. *PLoS ONE* **2013**, *8* (4), e59535.

7. Jeni, M.M.;Nathani, B.R.; Pandya, K.S., Synthesis, Characterization and Anti-microbial activity of some Novel Trisubstituted Purine Bearing Amino acid *Der Pharma Chem.* **2011**, 3 (5), 20–28.
8. Zhao, C.-Q.;Chen, Y.-G.;Qiu, H.;Wei, L.;Fang, P.; Mei, T.-S., Water as a Hydrogenating Agent: Stereodivergent Pd-Catalyzed Semihydrogenation of Alkynes. *Org. Lett.* **2019**, 21 (5), 1412–1416.
9. Farras, P. ;Waller, H.; Benniston, A.C., Enhanced Photostability of a Ruthenium(II) Polypyridyl Complex under Highly Oxidizing Aqueous Conditions by Its Partial Inclusion into a Cyclodextrin. *Chem. Eur. J.* **2016**, 22, 1133–1140.
10. Yuan, B.;Xu, J.-F.;Sun, C.-L.;Nicolas, H.;Schönhoff, M.;Yang , Q.-Z.; Zhang, X., Pillar[6]arene Containing Multilayer Films: Reversible Uptake and Release of Guest Molecules with Methyl Viologen Moieties. *ACS Appl. Mater. Interfaces* **2016**, 8 (6), 3679–3685.